

Quantum and Semiclassical Calculations of  
Electron Transport Through a Stochastic System

David Hardwick, MSci

*Thesis submitted to the University of Nottingham  
for the degree of Doctor of Philosophy*

*November 2007*

## ABSTRACT

In this thesis, I present a semiclassical and quantum mechanical study of a biased superlattice with a tilted magnetic field applied. This system exhibits non-KAM chaotic behaviour which can be controlled by the ratio between the cyclotron and Bloch frequencies. I will use a semiclassical model to show that electron trajectories become unbounded when this ratio takes an integer value. These extended electron trajectories cause peaks in the electron drift-velocity, which lead to current enhancements calculated using a drift-diffusion model. Furthermore, I will explain this current enhancement with reference to the electric field and charge carrier density across the superlattice. These results will then be compared to experimentally measured current-voltage characteristics.

A second superlattice is also studied, which has a high probability of interminiband tunnelling. I will outline several theoretical models to account for interminiband tunnelling and will ultimately use an empirical method. The current-voltage results obtained via this method will then be compared to experimental data.

Finally, I will use a quantum mechanical model to determine the electron eigenstates for the first superlattice. These quantum mechanical eigenstates will be compared to the semiclassical results to determine the degree of correspondence between the two models. Furthermore, I will use the eigenstates to calculate the energy level structure of the system and investigate how this varies for different applied field strengths. Ultimately, I will suggest a combined band transport plus scattering model to explain experimental current-voltage data obtained for high magnetic fields.

## ACKNOWLEDGEMENTS

There are a number of people at the University of Nottingham whose assistance has been invaluable in producing the work detailed in this thesis. These include, but are not limited to: Dave Fowler for the production of many experimental results and for interesting discussions on the consequences of the quantum work presented here. Jara Imbers for her invaluable help in explaining various mathematical problems to me. And everyone else in my office for help with physics, programming and latex related problems. I would also like to thank Jason Hogan O'Neill who kept the University of Nottingham Supercomputer running smoothly which enabled me to produce many of the results presented here. Most importantly, I would like to thank my supervisor, Mark Fromhold, who has patiently guided me toward producing this work via insightful guidance and suggestions. Finally, the production of this thesis would not have been possible without the support of my girlfriend, Kathy, without whom I never would have finished!

## CONTENTS

1. <i>Background</i> . . . . .	9
1.1 Superlattices . . . . .	10
1.1.1 Band Theory . . . . .	11
1.2 Superlattice Transport Models . . . . .	14
1.2.1 The Semiclassical Model . . . . .	14
1.2.2 Wannier-Stark Hopping . . . . .	17
1.2.3 Electron Scattering . . . . .	20
1.2.4 Electron Drift Velocity . . . . .	21
1.2.5 Negative Differential Velocity . . . . .	23
1.3 Superlattices in Electric and Tilted Magnetic Fields . . . . .	25
1.3.1 Semiclassical Equations of Motion . . . . .	28
1.4 Superlattice Samples . . . . .	30
1.4.1 Superlattice NU2293 . . . . .	31
1.4.2 Superlattice NU2299 . . . . .	32
1.4.3 Differences in the Miniband Structure of the Samples . . . . .	34
1.5 Electron Transport Properties . . . . .	34
1.5.1 Parameters of the Real Superlattices . . . . .	39
1.6 Compatibility of Assumptions Made . . . . .	39
2. <i>Chaos</i> . . . . .	42
2.1 Hamiltonian and Dissipative Systems . . . . .	43
2.2 Conserved Quantities . . . . .	44
2.3 Phase Space . . . . .	45
2.4 Integrable and Non-Integrable Systems . . . . .	45
2.4.1 Non-Integrable Systems . . . . .	48
2.4.2 Chaos . . . . .	49
2.5 Poincaré Sections . . . . .	49
2.6 KAM and non-KAM Chaos . . . . .	51
2.6.1 Non-KAM Chaos . . . . .	51
2.7 Quantum Chaos . . . . .	54
2.8 Phase Space in Quantum Chaos . . . . .	55
2.9 Summary . . . . .	57

---

3. Semiclassical Analysis of Superlattice NU2293 . . . . .	58
3.1 Introduction . . . . .	59
3.2 Motion through the Infinite Superlattice . . . . .	59
3.2.1 Effect of $r$ on Electron Orbits . . . . .	60
3.2.2 Effect of $\theta$ on Electron Orbits . . . . .	63
3.2.3 Effects of $B$ on Electron Orbits . . . . .	67
3.2.4 Phase Space Data . . . . .	67
3.2.5 $p_x = 0$ Poincaré Sections . . . . .	77
3.2.6 Frequency Analysis . . . . .	80
3.2.7 Summary of Single Electron Dynamics Excluding Scattering	82
3.2.8 Drift Velocity vs. Electric Field Data . . . . .	83
3.2.9 $v_d(F)$ Curves for $B = 11$ T at 4.2 K . . . . .	84
3.2.10 $v_d(F)$ Curves for other Magnetic Fields and Temperatures	86
3.3 Transport through a Finite Superlattice . . . . .	87
3.4 $I(V)$ and Electrostatic Data for $B = 11$ T . . . . .	93
3.5 Electrostatics at other Magnetic Fields . . . . .	98
3.5.1 Electrostatics at 300 K . . . . .	103
3.6 Conclusion . . . . .	106
4. Semiclassical Analysis of Superlattice NU2299 . . . . .	110
4.1 Introduction . . . . .	111
4.2 Electron Dynamics for Superlattice NU2299 . . . . .	111
4.3 Electrostatics for Superlattice NU2299 . . . . .	115
4.3.1 Probability of Interminiband Tunnelling . . . . .	117
4.4 Modifying the Drift-Diffusion Model . . . . .	119
4.5 Modifying Drift-Velocity . . . . .	121
4.5.1 Directly Modifying the $v_d(F)$ Curves . . . . .	121
4.5.2 Modifying $v_x$ . . . . .	124
4.5.3 Other Methods of Calculating $v_d$ . . . . .	125
4.6 Choice of Model . . . . .	126
4.7 Electrostatics Including Interminiband Tunnelling . . . . .	129
4.8 Conclusion . . . . .	131
5. Quantum Analysis of Superlattice NU2293 . . . . .	134
5.1 Introduction . . . . .	135
5.2 Quantum Mechanical Formulation of the Tilted Field System . .	135
5.3 Construction of the Hamiltonian Matrix . . . . .	138
5.3.1 Evaluation of Matrix Element due to $\hat{H}_x$ . . . . .	139
5.3.2 Evaluation of Matrix Element due to $\hat{H}_z$ . . . . .	140
5.3.3 Evaluation of Matrix Element due to $\Delta\hat{H}$ . . . . .	140

---

5.3.4	The Full Hamiltonian Matrix . . . . .	141
5.4	Solving the Eigenvalue Problem . . . . .	141
5.5	Wigner Functions . . . . .	142
5.6	Analysing the Quantum Data . . . . .	144
5.7	Energy Eigenvalues of the Superlattice . . . . .	145
5.8	Electron Probability Distributions for the Superlattice . . . . .	146
5.9	Explanation of the Steps in the On-Resonance $E(N)$ Curves . . . . .	150
5.10	Effect of $r$ on the Energy Eigenstates . . . . .	155
5.11	Summary of Comparison between the Quantum and Semiclassical Models	160
5.12	The Search for Scarring . . . . .	161
6.	<i>Analysis of Localised Bands in Superlattice NU2293</i> . . . . .	164
6.1	Probability Density Plots for Eigenstates on a Single Step in $E(N)$	165
6.1.1	Shorter Eigenstates . . . . .	170
6.1.2	Form of the Dynamical Barrier and Box . . . . .	176
6.1.3	What About the States We Skipped? . . . . .	183
6.1.4	Dynamical Potential Box Summary . . . . .	186
6.2	Semiclassical and Quantum Frequency Comparisons . . . . .	189
6.3	Band Structure . . . . .	197
6.3.1	Width of the Dynamical Bands . . . . .	203
6.3.2	Dynamic Band Summary . . . . .	210
6.4	A Hybrid Transport Model for the Dynamic Bands . . . . .	210
	<i>Appendix</i> . . . . .	215
A.	<i>Generation of Bloch states</i> . . . . .	216
A.1	Construction of the Hamiltonian Matrix for Bloch States . . . . .	216

*List of Commonly used Symbols*

Symbol	Meaning
$B$	Magnetic field magnitude.
$d$	Superlattice period.
$e$	Charge on an electron.
$E(p_x)$	Superlattice dispersion curve.
$F$	Electric field magnitude.
$G$	Differential conductance ( $G = \frac{dI}{dV}$ ).
$\hbar$	Planck's constant divided by $2\pi$ .
$I$	Electrical current (or action when discussing chaos).
$J_r$	$r^{\text{th}}$ Bessel function of the first kind.
$k$	Wavevector.
$M^*$	Reduced electron mass.
$p_x, p_z$	Momentum components along the $x$ and $z$ axes respectively.
$q_y$	Linear momentum along the $y$ axis.
$r$	ratio defined by $r = \omega_B / \omega_C \cos \theta$ .
$\rho$	Radial distance from the centre of phase space.
$\theta$	Magnetic field tilt angle relative to the $x$ axis.
$\tau$	Electron scattering time.
$\tau_{SL}$	Superlattice scattering time.
$V$	Voltage.
$V_{SL}$	Superlattice potential.
$x$	Axis aligned along the superlattice growth direction.

*Symbols Used in the Semiclassical Model*

Symbol	Meaning
$\alpha$	Quantum number indexing minibands.
$\Delta x_{orbit}$	Maximum displacement of an electron along the $x$ axis.
$E_{gap}$	Minibandgap energy.
$n$	Electron density or general index as indicated.
$T$	Probability of interminiband (Zener) tunnelling.
$\tau_{eff}$	Electron scattering time modified for elastic and inelastic scattering.
$v_d$	Electron drift velocity.
$v_{d,ET}$	Magnitude of the Esaki-Tsu peak in $v_d$ .
$\omega_B$	Block frequency ( $\omega_B = eFd/\hbar$ ).
$\omega_C$	Cyclotron frequency ( $\omega_C = eB/m^*$ ).

---

*Symbols Used in the Quantum Mechanical Model*

Symbol	Meaning
$\alpha$	Quantum number indexing Wannier functions for a given $m$ .
$\Delta E_D$	Dynamical bandwidth energy.
$\Delta E_G$	Dynamical bandgap energy.
$\Delta E_S$	Dynamical band spread ( $\Delta E_S = \Delta E_D / eFd$ ).
$\Delta x$	Spread of electron probability density along $x$ .
$\Delta x_D$	$x$ width of the dynamical box.
$E(N)$	Energy eigenvalue of eigenstate $N$ .
$g, N$	Quantum number for labelling eigenstates using a single index.
$m$	Quantum number indexing Wannier states shifted by $md$ along $x$ .
$n$	Landau level index.
$\Psi$	Eigenfunction ( $ \Psi ^2$ is probability density).
$W$	Wigner function quasiprobability.
$\omega_{LO}$	Longitudinal optic phonon frequency.
$\omega_S$	Slow frequency found in the semiclassical electron trajectories.

## 1. BACKGROUND

## 1.1 Superlattices

The idea of a one-dimensional semiconductor superlattice was considered by Esaki and Tsu in 1969 (1; 2). Such a structure would have a 1D periodic potential 'formed by a periodic variation of alloy composition or impurity density introduced during epitaxial growth'. A series of allowed and forbidden energy bands was predicted, similar to the bands occurring in semiconductor crystals but of much smaller width.

Since this original work, many different types of semiconductor superlattice have been created with a variety of electronic properties as well as magnetic and other types of superlattice.

Figure 1.1 shows the potential energy variation for an electron in a basic superlattice. The difference in energy is created by layering two types of semiconductor with different conduction band energies.

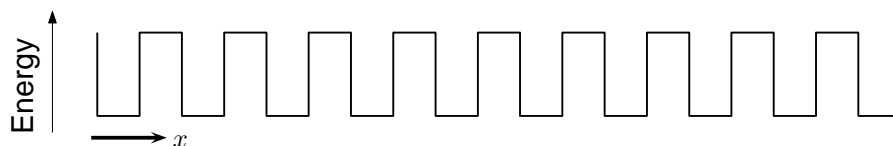


Fig. 1.1: Energy profile of a simple superlattice structure showing a series of potential energy wells and barriers in 1D.

This structure can be viewed as a set of adjacent 1D quantum wells which are coupled to one another via quantum mechanical tunnelling through the barriers. High or thick barriers cause the coupling between the wells to be weak and the structure can be effectively modelled as a series of independent quantum wells with a small probability of inter-well tunnelling. Such a structure is commonly referred to as a multiple quantum well (MQW) structure. However, if the coupling between the wells is sufficiently strong then the structure can no longer be adequately modelled by discrete wells and band theory must be used instead. These strongly coupled structures are known as superlattices. Superlattices have narrow bands of allowed electron energies which are known as minibands because they are much narrower than the bands which occur in semiconductors. Superlattices can also be divided into weakly and strongly coupled variants. In strongly coupled superlattices, the superlattice period is smaller than the coherence length ( $\sim 6$  nm) which leads to strong coupling between adjacent quantum wells and resulting minibands are 10s of meV wide. Conversely, weakly coupled superlattices have periods  $> 10$  nm which leads to minibands less than 1 meV wide. In these superlattices, electron transport operates via non-sequential tunnelling because the electrons dephase before they can move between quantum wells.(3)

The following sections will outline the band theoretical method for determining the behaviour of electrons moving perpendicular to the heterointerfaces (between the semiconductor layers) in a superlattice. This treatment will show the phenomena of Bloch oscillations and negative differential velocity.

### 1.1.1 Band Theory

For a 1D<sup>1</sup> system with a periodic potential and either an infinite extent or periodic boundary conditions, the electron probability density is expected to have the same periodicity. This statement is represented by:

$$|\psi(\mathbf{x})|^2 = |\psi(\mathbf{x} + \mathbf{X})|^2 \quad (1.1)$$

where  $\psi$  is the electron wavefunction,  $\mathbf{x}$  is a position vector and  $\mathbf{X}$  is a lattice vector given by:

$$\mathbf{X} = n\mathbf{a} \quad (1.2)$$

where  $\mathbf{a}$  is the primitive lattice vector and  $n$  is an integer. This lattice vector can be used to describe the position of any lattice point relative to any other lattice point. If condition 1.1 is true then it can be shown<sup>(4)</sup> that the wavefunction will have the following form:

$$\psi_{\mathbf{k}}(\mathbf{x}) = e^{i\mathbf{k}\cdot\mathbf{x}}u_{\mathbf{k}}(\mathbf{x}) \quad (1.3)$$

which is the product of a plane wave and a function  $u_{\mathbf{k}}(\mathbf{x})$  which has the periodicity of the lattice:

$$u_{\mathbf{k}}(\mathbf{x} + \mathbf{X}) = u_{\mathbf{k}}(\mathbf{x}) \quad (1.4)$$

where  $\mathbf{k}$  is known as the *wavevector*. Substituting 1.4 into 1.3 gives:

$$\psi_{\mathbf{k}}(\mathbf{x} + \mathbf{X}) = e^{i\mathbf{k}\cdot\mathbf{X}}\psi_{\mathbf{k}}(\mathbf{x}) \quad (1.5)$$

which, along with 1.3, is a statement of Bloch's Theorem.<sup>2</sup>

Reciprocal space is defined by the primitive reciprocal lattice vector  $\mathbf{b}$  which obeys:

$$\mathbf{b} \cdot \mathbf{a} = 2\pi. \quad (1.6)$$

The primitive cell in reciprocal space is also known as the *first Brillouin Zone*

---

<sup>1</sup> This work will only detail the 1D band theoretical model because the superlattices under investigation are periodic in one dimension. A full multidimensional treatment of periodic systems can be found in any good solid state text.

<sup>2</sup> For a proof of Bloch's theorem see (4) for example.

(BZ). The wavevector  $\mathbf{k}$  in reciprocal space is expressed as:

$$\mathbf{k} = l\mathbf{b}. \quad (1.7)$$

It can be shown that any wavevector  $\mathbf{k}$  can be described in the first Brillouin zone as follows. Consider the Bloch function:

$$\psi_{\mathbf{k}}(\mathbf{x} + \mathbf{X}) = e^{i\mathbf{k}\cdot\mathbf{X}}\psi_{\mathbf{k}}(\mathbf{x}) \quad (1.8)$$

where  $\mathbf{k}$  is outside the first BZ. We can express  $\mathbf{k}$  as:

$$\mathbf{k} = \mathbf{k}' + \mathbf{K} \quad (1.9)$$

where  $\mathbf{k}'$  is some wavevector in the first BZ and  $\mathbf{K}$  is a reciprocal lattice vector given by:

$$\mathbf{K} = m\mathbf{b} \quad (1.10)$$

where  $m$  is an integer. Substituting equation 1.9 into 1.8 gives:

$$\psi_{\mathbf{k}}(\mathbf{x} + \mathbf{X}) = e^{i\mathbf{k}'\cdot\mathbf{X}}e^{i\mathbf{K}\cdot\mathbf{X}}\psi_{\mathbf{k}}(\mathbf{x}) \quad (1.11)$$

and applying  $\mathbf{X} \cdot \mathbf{K} = 2nm\pi$  leaves

$$\psi_{\mathbf{k}}(\mathbf{x} + \mathbf{X}) = e^{i\mathbf{k}'\cdot\mathbf{X}}\psi_{\mathbf{k}}(\mathbf{x}). \quad (1.12)$$

Comparing equations 1.12 and 1.8 shows that  $\mathbf{k}$  is equivalent to  $\mathbf{k}'$ . Therefore only the first Brillouin zone needs to be considered.

The Bloch wavefunctions for a particular system can be determined from solving Schrödinger's equation:

$$\hat{H}\psi = E\psi. \quad (1.13)$$

The Hamiltonian of a periodic system of infinite extent is:

$$\hat{H} = -\frac{\hbar^2}{2m}\nabla^2 + V(\mathbf{r}) \quad (1.14)$$

where  $V(\mathbf{r})$  is the potential energy of the system and has the periodicity of the lattice. Appendix A details the construction of a Hamiltonian matrix in one dimension for this system which can be diagonalised to produce the Bloch wavefunctions. For each value of  $\mathbf{k}$  there are infinite solutions which are denoted by the quantum number  $\alpha$ <sup>3</sup>. Therefore the Bloch wavefunctions,  $\psi_{\mathbf{k},\alpha}$ , are the

<sup>3</sup> Note that this quantum number is conventionally denoted as  $n$  but we used  $\alpha$  to avoid

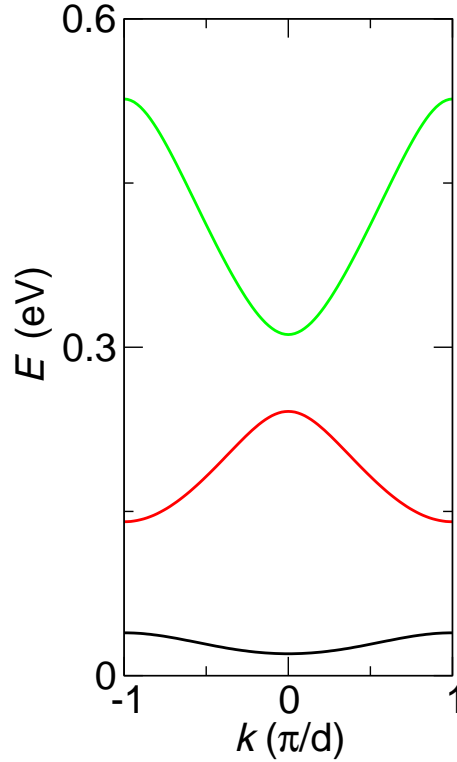


Fig. 1.2: Example 1D dispersion curves for a periodic potential plotted using the reduced zone scheme. The  $\alpha = 0$  (black),  $\alpha = 1$  (red) and  $\alpha = 2$  (green) dispersion curves are shown.

solutions of:

$$\hat{H}\psi_{k,\alpha} = E_{k,\alpha}\psi_{k,\alpha}. \quad (1.15)$$

A plot of the relationship between wavevector and energy is known as a dispersion curve  $E_{\mathbf{k},\alpha}$ . Figure 1.2 shows the three lowest energy ( $\alpha = 0, 1, 2$ ) dispersion curves obtained for a typical superlattice by solving the Schrödinger equation. If values of  $\mathbf{k}$  outside  $-\pi/d < k < \pi/d$  were considered then the dispersion relation would simply repeat as predicted by  $\mathbf{k} = \mathbf{k}' + \mathbf{K}$ .

From figure 1.2, it is clear that certain energies are not obtainable regardless of the wavevector or band index,  $\alpha$ . These regions are referred to as *band gaps* and the allowed energy regions are called *bands*, which are labelled by the quantum number  $\alpha$  which varies from 0 to  $\infty$ . It can be shown<sup>4</sup> that the number of possible  $k$  values allowed in each band is equal to the number of lattice sites in the superlattice and this limits the number of electrons that can inhabit a band because of the exclusion principle.

---

variable confusion.

<sup>4</sup> See any basic solid state text or (5) for example

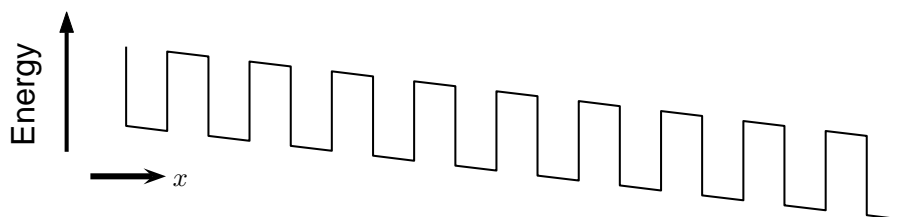


Fig. 1.3: Potential energy profile of a superlattice with an electric field applied in the negative  $x$  direction.

A superlattice is typically a one dimensional structure constructed of layered semiconductors. The semiconductor layers are periodic lattices of atoms and therefore have associated energy bands in three dimensions. However, the bands associated with the 1D superlattice periodicity are much smaller than these semiconductor bands and are therefore referred to as *minibands* with corresponding *miniband gaps*. The lower edge of the conduction bands of the semiconductors are the energy levels that determine the superlattice potential.

## 1.2 Superlattice Transport Models

This thesis will consider two main models to describe electron transport through a superlattice (or other periodic system). These models are miniband transport which uses a semiclassical model and Wannier-Stark hopping which uses a full quantum model. Other models such as non-equilibrium Green's function method can be used for this system(6) but will not be considered in this work.

### 1.2.1 The Semiclassical Model

Band theory and Bloch functions describe the state of an electron in a periodic potential. However, they cannot be used to model the time-dependant behaviour of the electron once an additional force, typically electric or magnetic, is applied. To calculate the time dependent electron behaviour, both the external forces and the influence of the dispersion relation must be considered. Figure 1.3 shows a new potential energy profile for a superlattice which has an electric field applied in the negative  $x$  direction.

The semiclassical model will not be described in detail here and the reader is directed to (4) and references therein for a complete derivation and description. However the approximations and important consequences of the model are outlined here.

The semiclassical model is intended to describe what happens to the position and wavevector of an electron under the influence of external fields, both electric,

$\mathbf{F}$ , and magnetic,  $\mathbf{B}$ . This model does not consider collisions or scattering of electrons which will be incorporated later in his chapter.

The semiclassical velocity of a wavepacket constructed from Bloch states is given by:

$$\mathbf{v}_\alpha(\mathbf{k}) = \frac{1}{\hbar} \frac{\partial E_\alpha(\mathbf{k})}{\partial \mathbf{k}} \quad (1.16)$$

where  $v_\alpha(\mathbf{K})$  is the velocity of a wavepacket in band  $\alpha$ . This equation is only valid for a wavepacket whose spread in real space is large compared to the periodic potential so that its spread in  $k$ -space is small and  $\mathbf{k}$  can be treated as constant over the wavepacket. This condition is the major requirement of the semiclassical model and it means that the wavepacket must be many times larger than the superlattice period. The response of the wavepacket to external fields is determined by classical mechanics through equations that are formally identical to Hamilton's equations and, for this to be valid, any change in the external field must be small over the extent of the wavepacket. In other words, the electric or magnetic field must be almost the same at any point of the wavepacket. Although classical mechanics are used to describe external fields, the form of  $E_\alpha(\mathbf{k})$  is derived from quantum mechanics and, for this reason, the model is known as **semiclassical**.

The non-relativistic equation of motion for  $\mathbf{k}$  is:

$$\hbar \dot{\mathbf{k}} = -e [\mathbf{F} + \mathbf{v}_\alpha(\mathbf{k}) \times \mathbf{B}] \quad (1.17)$$

where  $\hbar \mathbf{k}$  is known as the *crystal momentum* of the wavepacket. This crystal momentum is different to the total momentum of the wavepacket because its rate of change is only due to the electric and magnetic Lorentz force and not forces due to the lattice potential.

The semiclassical model omits specific details of the periodic potential and only incorporates indirect information about the lattice through the form of  $E_\alpha(\mathbf{k})$ . The model does not allow for transitions between different minibands and, because of this, only unfilled minibands need to be considered. In full bands, all the  $\mathbf{k}$  states are occupied and it can be shown that these filled bands will not contribute to any transport properties of the system(4).

In the limit of zero quantum well depth, the electrons become free and their kinetic energy will continually increase under a constant electric field. Because the semiclassical model does not allow interminiband tunnelling, it can only allow a finite energy increase. Therefore the semiclassical model is only applicable to a periodic potential with wells deeper than some minimum. Interminiband tunnelling can occur for any periodic potential given a high enough electric field and this is known as *electric breakdown*. An analogous *magnetic breakdown* can

also occur and this behaviour is even easier to cause given strong magnetic fields.

Now consider the behaviour of an electron in a 1D periodic potential of period  $d$  with an anti-parallel electric field of magnitude  $F$  (fig. 1.3). Assume that the band structure is given by the dispersion curves in figure 1.2 and that the electron is in the lowest ( $\alpha = 0$ ) band. For this system, the equations of motion are:

$$\hbar \dot{\mathbf{k}} = -eF \quad (1.18)$$

and

$$\dot{\mathbf{x}} = \frac{1}{\hbar} \frac{\partial E_\alpha(k)}{\partial k}. \quad (1.19)$$

The first equation of motion ensures that  $\mathbf{k}$  will change linearly with time. But, because  $\mathbf{k}$  can always be expressed in the first Brillouin zone (equation 1.9),  $\mathbf{k}(t)$  can also be treated as a sawtooth wave of amplitude  $\frac{2\pi}{d}$ . The second equation of motion states that the velocity in real space is proportional to the gradient of the dispersion curve.

Tracing the dispersion curve from  $k = 0$  shows that  $\dot{x}$  will increase from zero to some maximum at  $k = \pi/2d$  and then decrease back to zero at  $k = \pi/d$ . At this point, equation 1.9 states that  $k = \pi/d \equiv -\pi/d$  and, in the reduced zone scheme, we can continue to examine the behaviour of the electron by jumping to the left of the dispersion curve. The gradient now becomes negative and the electron moves backwards, attaining a peak negative speed at  $k = -\pi/2d$  and then slows to rest at  $k = 0$ . The cycle then repeats. Figure 1.4 overlays  $v(k)$  on  $E(k)$ . The change in electron velocity from positive to negative causes the electron to reverse its direction of motion and this is known as *Bragg-reflection*. The electrons motion is oscillatory because the dispersion curve is symmetrical about  $k = 0$  and these oscillations are known as *Bloch oscillations*. The frequency of the Bloch oscillations,  $\omega_B$ , is given by:

$$\omega_B = \frac{eFd}{\hbar}. \quad (1.20)$$

Although the semiclassical model predicts Bloch oscillations with an applied electric field, electron scattering still needs to be considered. In practice, it is found that electrons in crystal lattices scatter before Bloch oscillations can complete.

In this section we have shown how the semiclassical model can be used to predict the dynamic behaviour of electrons in a superlattice miniband (or other dispersion curve).

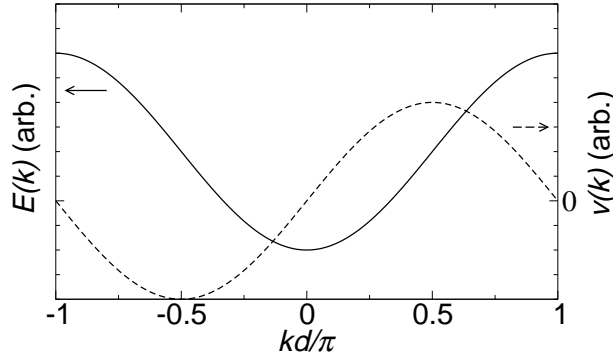


Fig. 1.4: Figure showing an example 1D dispersion curve (solid) and the corresponding velocity (dashed) of an electron moving in this dispersion curve under the influence of a constant electric field.

### 1.2.2 Wannier-Stark Hopping

One difficulty with the semiclassical model is that applying a constant field to a periodic potential destroys the periodicity. Therefore, the dispersion curve calculated for a superlattice is, strictly speaking, incorrect if a field is applied. The semiclassical model first begins to become invalid when the energy variation between states in additional quantum wells is greater than the thermal energy broadening of these states:

$$eFd > \frac{\hbar}{\tau} \quad (1.21)$$

where  $\tau$  is the scattering time of electrons in the lattice. This condition means that states in adjacent wells are no longer isoenergetic so treating the lattice as periodic is inaccurate. When this condition is true, a series of states are found in each quantum well and the set of states is known as a Wannier-Stark ladder. Adding a magnetic field causing the states to split further into Landau levels and this splitting is smaller than the principle quantum splitting. In chapter 5 we use a quantum model which incorporates the applied fields to calculate these states and figure 1.5 shows a set of Wannier-Stark-Landau (WSL) ladders in a superlattice.

Although the semiclassical model becomes invalid for  $\omega_B\tau > 1$ , in practice, we can use semiclassical dynamics provided that the width of the Bloch oscillations,  $\Delta x$ , spans several quantum wells:

$$\Delta x = \frac{\Delta}{eF} > d \quad (1.22)$$

where  $\Delta$  is the miniband width.

For transport to occur along the superlattice in the WSL model, an electron must be able to shift between different WSL ladders. Coherent transitions

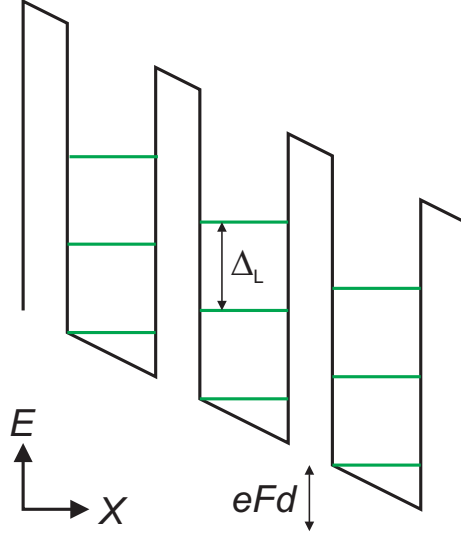


Fig. 1.5: Wannier-Stark-Landau ladder in a superlattice where  $\Delta_L$  is the Landau level spacing.

between any isoenergetic levels in different ladders is not possible because Landau levels have zero overlap for  $n \neq n'$ . Therefore, neglecting the possibility of photon assisted transitions, the transitions must be facilitated by a phonon scattering event. There are two major types of semiconductor phonon to consider: acoustic phonons, which are typically around 1 meV, and bulk longitudinal optic (LO) phonons, which have energies of tens of meV. The low energy acoustic phonons assist transitions between nominally isoenergetic states in adjacent periods in a quasi-elastic process. We use the terms “nominally” and “quasi” because the energy levels are thermally broadened (on the order of  $\hbar/\tau_{SL}$  where  $\tau_{SL}$  is the superlattice scattering time) so the electron can absorb a phonon and move to a state of the same average energy. States in adjacent periods are isoenergetic when the Landau level splitting is equal to the electric potential energy dropped in one period:

$$\Delta_L = \hbar\omega_C = eFd. \quad (1.23)$$

The LO phonons can scatter electrons between Landau levels in the same period which requires a second resonance condition to be met:

$$\Delta_L = \omega_C = \omega_{LO}, \quad (1.24)$$

where  $\omega_{LO}$  is the LO phonon frequency. This second condition is known as the magnetophonon resonance (MPR) condition and allows for vertical energy level

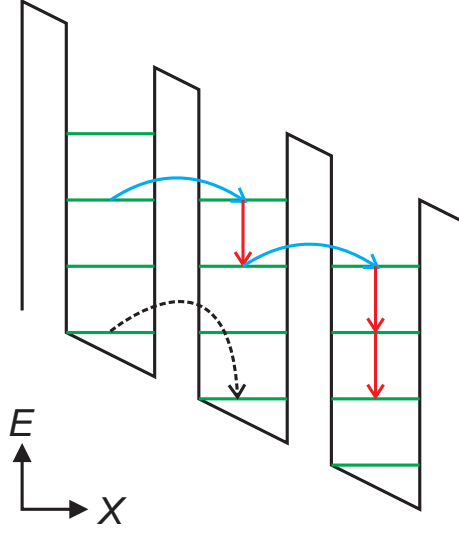


Fig. 1.6: Schematic of the energy level transitions mediated by phonons in MPR assisted transport. The blue arrow indicates low-energy acoustic phonon assisted quasi-elastic hopping and the red arrow shows LO phonon resonant hopping. The broken line indicates a single-phonon hopping transition which does not require the Stark-cyclotron resonance condition to be met.

transitions.

Figure 1.6 shows the scattering processes involved in Wannier-Stark hopping and, for this transport to be possible, conditions 1.23 and 1.24 must be met. Therefore, for Wannier-Stark hopping to occur,

$$\hbar\omega_C = eFd = \hbar\omega_{LO} \quad (1.25)$$

must be true. It is also possible for hopping to occur in a single scattering event as shown by the broken line on figure 1.6. A single scattering event hop removes the Stark-cyclotron resonance condition so only condition 1.24 need be met and such a transition can occur for any magnetic field.

Although the Wannier-Stark transport model is more valid at high  $F$ , it does not easily lead to a quantitative measure of electron dynamics. We will therefore use the semiclassical approximation in this chapter because it can easily be used to calculate properties such as drift-velocity for a range of applied fields. In chapter 5 we will incorporate the applied fields into our calculation of the electron eigenstates. We will then use the Wannier-Stark model to qualitatively explain some features in experimental data.

### 1.2.3 Electron Scattering

The Drude theory of metals<sup>(4)</sup> assumes that the predominant source of collisions and scattering within a conductor is interactions between electrons and the heavy lattice ions<sup>5</sup>. However, Bloch theory describes all the interactions of electrons with a periodic lattice of ions. Therefore results obtained using Bloch theory already have electron-ion scattering built in assuming that the lattice is perfectly perfect. Bloch theory relies on the quantum wavelike nature of electrons and thus was not understood in Drude's day.

A real semiconductor homostructure has two main sources of imperfection which prevent it from being a perfect lattice. The first type of deviation arises from structural defects in the lattice structure, which can either be growth defects or may arise from thermal, mechanical or other deformation of the lattice. In addition, localised structural defects such as missing or incorrect ions at a lattice site and larger defects such as slipped lattice planes can occur. These kind of defects may be present under any conditions but can be minimised by careful fabrication of the structures.

The second type of deviation in semiconductors arises from thermal vibrations of the ions. These vibrations occur at all temperatures but decrease in significance as the temperature approaches absolute zero. If the lattice ions are vibrating in different directions then the lattice is no longer perfectly periodic. This means that there will be scattering due to electron-ion interactions.

In superlattices, the large lattice that leads to the miniband structure is artificially created by depositing layers of different semiconductor material on a substrate. Therefore superlattice structures have all the defects of the underlying semiconductors as well as the defects associated with the superlattice periodicity. However, because superlattice periods are relatively large, the only significant source of additional scattering is due to imperfections at the semiconductor heterointerfaces known as *interface roughness*. Interface roughness can also arise if the adjoining semiconductors have different lattice constants which will stretch or compress the two layers at the point of contact. This distortion in the periodicity of each semiconductor can lead to electron-ion scattering events.

Electron-electron scattering events can occur but the *independent electron approximation*<sup>(4)</sup> can be used which treats these scattering events as unimportant. This approximation removes the need for a complex self-consistent approach to scattering times. The *Fermi liquid theory* shows that this neglect of electron-electron interactions is valid if dealing with electrons close to the Fermi level and the carriers are treated as quasi-particles rather than true electrons. In this thesis, the independent electron approximation is used and the

---

<sup>5</sup> At the time, the concept of electrons and ions was not understood in as much detail as it is today but the general idea is the same.

carriers are still treated as electrons for simplicity.

This thesis will use a simple representation of scattering time and incorporate all the possible scattering events described above into a single variable  $\tau$  where  $dt/\tau$  is the probability of a scattering event occurring in time  $dt$ . This scattering time must be inferred from experiments, although scattering times for some of the simpler defects can be accounted for analytically.

Analytically, two types of scattering process can be identified: *elastic* and *inelastic* scattering. Inelastic scattering processes allow both the energy and momentum of the electron to change. Phonon scattering is an example of inelastic scattering where energy is transferred to or from the lattice. Elastic scattering can only change the momentum of the electron. Ignatov *et al*(7) replace  $\tau$  with an effective scattering time (also see section 3.1.2 of (8)):

$$\tau_{eff} = \tau_i \sqrt{\frac{\tau_e}{\tau_i + \tau_e}} \quad (1.26)$$

which includes contributions from the inelastic,  $\tau_i$  and elastic,  $\tau_e$ , scattering times. A correction of  $\delta = \tau_{eff}/\tau_i$  is required to the electron drift velocity if this effective scattering time is used. We will use this effective scattering time because it does not significantly increase the complexity of any calculations once  $\tau_{eff}$  and  $\delta$  are known.

#### 1.2.4 Electron Drift Velocity

This section will derive an equation for electron drift velocity which will then be altered to use  $\tau_{eff}$  as described in the previous section.

Consider what happens to electrons in a superlattice with dispersion curve  $E(\mathbf{k})$  and scattering time  $\tau$ . Two major assumptions will be made which constitute the *relaxation time approximation*.

1. It is assumed that scattered electrons forget about their behaviour prior to the scattering event.
2. Any point in the system is assumed to have an equilibrium electron distribution appropriate to the temperature at that point.

Other approximations will be made in addition to the relaxation time approximation:

1. The scattering time is independent of position,  $\mathbf{k}$  and  $\epsilon(\mathbf{k})$  and is therefore constant.
2. The temperature,  $T$ , and chemical potential,  $\mu$ , are independent of position and time.

3. The electric and magnetic field strengths are constant.
4. The electrons are not allowed to move between bands or minibands by scattering or otherwise.

To formulate an expression for the electron drift velocity, consider  $N_0$  electrons starting from time  $t = 0$ . If the number of electrons that remain unscattered by time  $t$  is  $N(t)$ , then the probability of an electron scattering in the time interval  $dt$  can be calculated as follows. The number of electrons unscattered by time  $t + dt$  is:

$$N(t + dt) = N(t) - N(t) \frac{dt}{\tau} \quad (1.27)$$

where  $N(t) \frac{dt}{\tau}$  is the number of electrons that scatter in time  $dt$ . Therefore the rate of change of electrons not having scattered is:

$$\frac{dN}{dt} = \frac{N(t + dt) - N(t)}{dt} = -\frac{N(t)}{\tau}. \quad (1.28)$$

Integrating gives the number of electrons that have travelled for time  $t$  without scattering:

$$N(t) = N_0 e^{-t/\tau}. \quad (1.29)$$

The probability of an electron scattering in time  $dt$  is now given by the the number of electrons that scatter divided by the total number of electrons:

$$P(t)dt = \frac{N(t)dt}{N_0} \quad (1.30)$$

and substituting in equation 1.29 gives:

$$P(t)dt = \frac{1}{\tau} e^{-t/\tau} dt. \quad (1.31)$$

Because of assumption one of the relaxation time approximation, only the behaviour of the electrons after their most recent scattering event will affect the average or drift electron velocity. For example, the drift velocity component due to electrons which last scattered one second ago is:

$$v_d(t = 1) = v_x(t = 1)P(t = 1)dt \quad (1.32)$$

which is simply the electron velocity after one second multiplied by the proportion of electrons that scattered one second ago. The full electron drift velocity equation is obtained by integrating over all past times to give:

$$v_d = \int_0^\infty v_x(t)P(t)dt. \quad (1.33)$$

We can now apply the two scattering time correction and substitute in equation 1.31 to give:

$$v_d = \delta \int_0^\infty \frac{dt}{\tau_{eff}} v(t) e^{-t/\tau_{eff}} \quad (1.34)$$

where

$$\tau_{eff} = \tau_i \sqrt{\frac{\tau_e}{\tau_i + \tau_e}}, \quad (1.35)$$

$\delta = \tau_{eff}/\tau_i$  and  $\tau_e$  and  $\tau_i$  are the elastic and inelastic scattering times respectively.

The initial spread of electron momenta can be characterised by an effective temperature. To incorporate this spread into  $v_d$ , we average over a number of initial states:

$$v_d = \frac{\delta}{I} \sum_{i=0}^I \int_0^\infty \frac{dt}{\tau_{eff}} v_i(t) e^{-t/\tau_{eff}} \quad (1.36)$$

where  $i$  is one of  $I$  initial conditions and  $v_i(t)$  is the velocity of an electron after starting from initial state  $i$  after time  $t$ . The initial states are regularly spaced points in a region of 3D momentum space whose boundaries are determined by the effective temperature:

$$E_{max} = E(p_x) + \frac{q_y^2 + p_z^2}{2m^*} \quad (1.37)$$

where  $E_{max}$  is the electron energy set by the effective electron temperature.

Equation 1.36 is the final definition of the electron's drift velocity used in this thesis.

### 1.2.5 Negative Differential Velocity

Combining the semiclassical equations of motion with the electron drift velocity formula allows the average electron velocity to be calculated. Consider the simple case of electrons in a 1D periodic system characterised by the dispersion curve  $E(k_x) = \Delta/2 (\cos(k_x d))$  with an applied electric field. This system is identical to that considered at the end of section 1.2.1 in which the electrons are localised in real space by Bloch oscillations of frequency  $\omega_B = \frac{eFd}{\hbar}$ . We can now incorporate electron scattering into the model using equation 1.36 and hence calculate the electron drift velocity as a function of electric field strength,  $v_d(F)$ .

As  $F$  increases, the Bloch frequency increases and the Bloch period correspondingly decreases. Substituting the dispersion curve into the semiclassical equations of motion,

$$v_x = \frac{1}{\hbar} \frac{dE}{dk_x}, \quad \text{and} \quad \hbar \frac{dk_x}{dt} = eF, \quad (1.38)$$

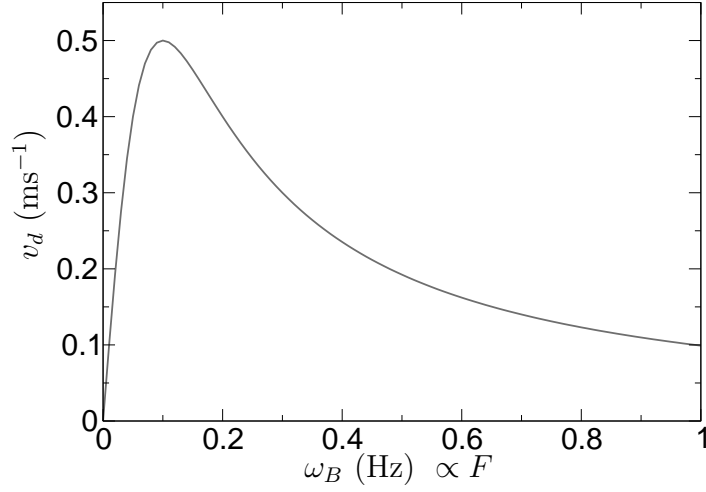


Fig. 1.7: Drift velocity vs. electric field curve for an electron in a periodic potential with a cosinusoidal dispersion curve and an applied electric field. The scattering time is  $\tau = 10$  and negative differential velocity clearly occurs for  $\omega_B\tau > 1$ .

gives:

$$v_x = \frac{\Delta d}{2\hbar} \sin(k_x d), \quad \text{and} \quad k_x = \frac{eFt}{\hbar} \quad (1.39)$$

assuming that the electron starts from the bottom of the miniband ( $k_x = 0$ ). Substituting these equations into 1.33 gives:

$$v_d = \frac{\Delta d}{2\hbar} \int_0^\infty \sin(\omega_B t) \exp(-t/\tau) dt / \tau. \quad (1.40)$$

This integral evaluates to:

$$v_d = \frac{\Delta d}{2\hbar} \frac{\omega_B \tau}{(\omega_B \tau)^2 + 1} \quad (1.41)$$

which is plotted in figure 1.7.

Figure 1.7 shows that drift velocity reaches a maximum at  $\omega_B\tau = 1$ . For  $\omega_B\tau \ll 1$  the drift velocity increases linearly with electric field because the electrons can only explore the parabolic lower part of the dispersion curve before scattering. Therefore no Bloch oscillations occur and ohmic behaviour is observed. When  $\omega_B\tau > 1$  the Bloch period decreases with increasing  $F$  which causes  $v_d(F)$  to decrease. This is because the electron has an increasing chance of performing one or more Bloch oscillations and so the localising effects of these oscillations become stronger with increasing field. This phenomenon is known as *negative differential velocity* (NDV). This result is only valid for a single electric field aligned anti-parallel to the superlattice.

It has been shown (9; 10) that the presence of negative differential velocity can cause the conduction electrons in a bulk structure to perform collective high frequency oscillations whose frequency is in the GHz to THz range.

### 1.3 Superlattices in Electric and Tilted Magnetic Fields

The previous sections considered electron transport through a periodic superlattice with an electric field applied anti-parallel to the superlattice growth direction. This section will consider how the electron motion changes due to the addition of a magnetic field tilted at an angle ( $0^\circ \leq \theta \leq 90^\circ$ ) to the growth direction. Figure 1.8 shows a schematic of this system.

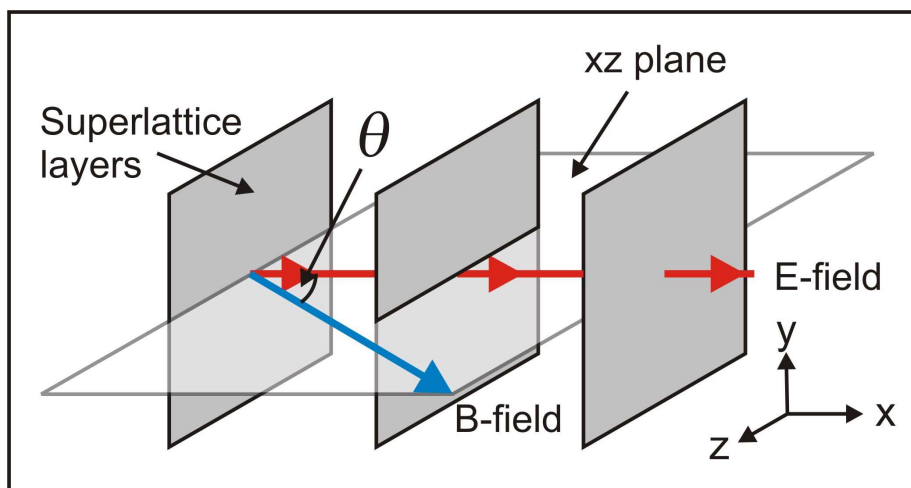


Fig. 1.8: Diagram showing orientation of the external electric and magnetic fields applied to the superlattice. The superlattice layers are represented by the grey planes. The  $xz$  plane, in which the magnetic field vector lies, is shown in white.

When  $\theta = 0$ , the two types of motion which will occur in this system are Bloch oscillations due to the electric field, with angular frequency  $\omega_B = eEd/\hbar$ , and cyclotron oscillations about the magnetic field, with angular frequency  $\omega_C = eB/m^*$ . Figure 1.9 shows the form of the 2D potential that an electron experiences in these fields.

We will now construct a Hamiltonian to describe the electron dynamics. The Hamiltonian of a 3-dimensional system with a periodic potential along the  $x$ -axis but no applied fields is:

$$H_0 = E(p_x) + \frac{p_y^2}{2m^*} + \frac{p_z^2}{2m^*} \quad (1.42)$$

which combines the dispersion curve  $E(p_x)$  of the periodic potential in  $x$  with

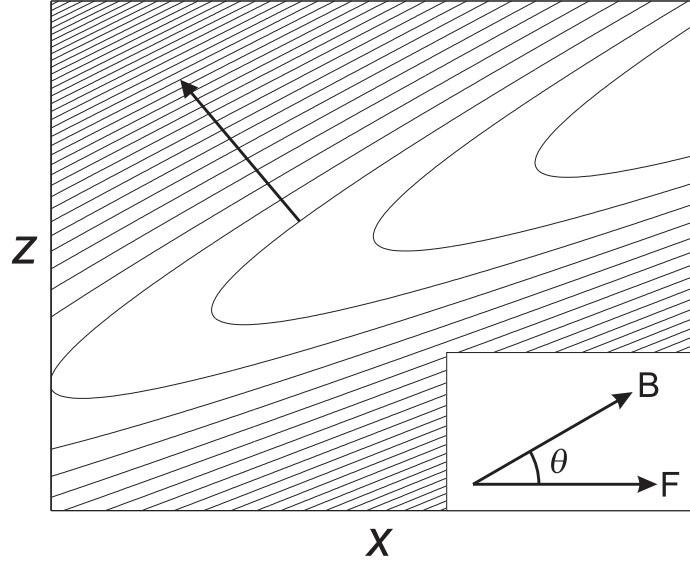


Fig. 1.9: Contour plot of the 2D potential energy due to electric and magnetic fields tilted at  $30^\circ$  to each other. The arrow shows the direction of increasing potential energy and the inset shows the direction of the applied fields.

parabolic dispersion curves in  $y$  and  $z$ . Note that the mass is replaced with the effective mass,  $m^*$ , of an electron in the semiconductor material forming the superlattice. Making this replacement incorporates the effects of the *semiconductor* dispersion curves within the Hamiltonian. The superlattice dispersion curve will be represented as a Fourier series for generality:

$$E(p_x) = \frac{\Delta}{2} \left( a_0 - \sum_{n=1}^{\infty} a_n \cos \left( n \frac{p_x d}{\hbar} \right) \right) \quad (1.43)$$

where  $\Delta$  is the width of the miniband and  $a_{n=0,1,2,3,\dots}$  are a set of coefficients which define the shape of the dispersion curve. For the cosinusoidal dispersion curve considered previously,  $a_1 = 1$  and  $a_{n>1} = 0$ . References (11) and (12) detail the construction of these coefficients.

The semiclassical model states that the change in crystal momentum of an electron is given by the external forces acting on that electron:

$$\dot{\mathbf{p}} = \hbar \dot{\mathbf{k}} = \mathbf{Force} \quad (1.44)$$

and its velocity is given by:

$$\mathbf{v} = \frac{\partial E(\mathbf{p})}{\partial \mathbf{p}}. \quad (1.45)$$

Therefore the classical Hamiltonian of an electron in a periodic potential with

an electric field anti-parallel to  $x$  is:

$$H_e = H_0 - eFx. \quad (1.46)$$

Including a magnetic field does not directly alter the total (kinetic plus potential) energy of an electron but it does change the direction of its motion. It is therefore convenient to incorporate this effect into the momentum operator rather than the Hamiltonian:

$$\mathbf{p} \rightarrow \mathbf{p} + e\mathbf{A} = m\mathbf{v} = \mathbf{q} \quad (1.47)$$

where  $\mathbf{A}$  is the magnetic vector potential and the canonical momentum  $\mathbf{p}$  has been replaced with the linear momentum  $\mathbf{q}$  (13). For our system, the magnetic field vector is  $\mathbf{B} = (B \cos \theta, 0, B \sin \theta)$  and the simplest (14) choice for the magnetic vector potential is  $\mathbf{A} = (0, B(x \sin \theta - z \cos \theta), 0)$ . This leads to a linear momentum of:

$$\begin{aligned} q_y &= p_y + e\mathbf{A}_y(x, z) \\ &= p_y + eB(x \sin \theta - z \cos \theta) \end{aligned} \quad (1.48)$$

in  $y$  and leaves the  $x$  and  $z$  momentum components unchanged. The full Hamiltonian is now be written as

$$H = E(p_x) + \frac{q_y^2}{2m^*} + \frac{p_z^2}{2m^*} - eFx \quad (1.49)$$

and substituting in equation 1.48 for  $q_y$  gives:

$$\begin{aligned} H &= E(p_x) + \frac{k_y^2}{2m^*} + \frac{\hbar e B k_y}{m^*} (x \sin \theta - z \cos \theta) \\ &+ \frac{e^2 B^2}{2m^*} (x \sin \theta - z \cos \theta)^2 - eFx \\ &= E. \end{aligned} \quad (1.50)$$

This can be simplified to:

$$H = E(p_x) + \frac{1}{2} m^* \omega_C^2 (x \sin \theta - (z - z_0) \cos \theta)^2 - eFx = E. \quad (1.51)$$

where  $\omega_C = eB/m^*$  and  $z_0 = p_y/eB \cos \theta$ . This equation is the final semiclassical Hamiltonian for an electron in a superlattice of dispersion curve  $E(p_x)$  with applied electric and magnetic fields as depicted in figure 1.8.

## 1.3.1 Semiclassical Equations of Motion

Equations of motion can be formed from the Hamiltonian of a system using Hamiltonian mechanics and Hamilton's equations in particular. These equations define the equations of motion for a particle which is described by the conjugate coordinates  $\{\mathbf{r}, \mathbf{p}\}$ :

$$\frac{dr_i}{dt} = \frac{\partial H(\mathbf{r}, \mathbf{p}, t)}{\partial p_i} \quad (1.52)$$

and

$$\frac{dp_i}{dt} = -\frac{\partial H(\mathbf{r}, \mathbf{p}, t)}{\partial r_i} \quad (1.53)$$

where degrees of freedom are indexed by  $i$ . A single electron in a superlattice with electric and tilted magnetic fields has 3 degrees of freedom. However, the equations of motion for  $x$  and  $z$  are independent of  $y$  so only  $i = x$  and  $z$  need to be considered for Hamiltonian 1.51. Therefore the four Hamilton's equations for this system are:

$$\dot{x} = \frac{\partial H}{\partial p_x}, \quad \dot{p}_x = -\frac{\partial H}{\partial x} \quad (1.54)$$

$$\dot{z} = \frac{\partial H}{\partial p_z}, \quad \dot{p}_z = -\frac{\partial H}{\partial z}. \quad (1.55)$$

It needs to be shown that Hamilton's equations lead to the semiclassical equations of motion,  $\dot{\mathbf{p}} = \mathbf{Force}$  and  $\mathbf{v} = \frac{\partial E(\mathbf{p})}{\partial \mathbf{p}}$ , in order for Hamiltonian mechanics to be applicable to our system. Simply substituting  $\mathbf{p} = \hbar \mathbf{k}$  into equations 1.54 and 1.55 gives:

$$\dot{x} = v_x = \frac{1}{\hbar} \frac{\partial H}{\partial k_x} \quad (1.56)$$

$$\dot{z} = v_z = \frac{1}{\hbar} \frac{\partial H}{\partial k_z} \quad (1.57)$$

which are equivalent to the semiclassical velocity equation. Substituting Hamiltonian 1.49 into Hamilton's equation for  $p_x$  gives:

$$\begin{aligned} \dot{p}_x &= eF - \frac{q_y}{m^*} \frac{\partial q_y}{\partial x} \\ &= e \left[ F - \frac{q_y}{m^*} B \sin \theta \right] \end{aligned} \quad (1.58)$$

which shows that the change in crystal momentum along  $x$  is given by the Lorentz force. A similar argument can be made for  $p_z$  which demonstrates the equivalence of Hamilton's and the semiclassical equations of motion. Therefore Hamilton's equations can be used to obtain semiclassical equations of motion for our system.

The four equations of motion that emerge from applying equations 1.54 and

1.55 to the Hamiltonian 1.51 are:

$$\dot{x} = \sum_{n=1}^{\infty} \frac{nda_n}{\hbar} \sin\left(\frac{ndp_x}{\hbar}\right) \quad (1.59)$$

$$\dot{z} = \frac{p_z}{m^*} \quad (1.60)$$

$$\dot{p}_x = -m^* \omega_C^2 (x \sin^2 \theta - z \sin \theta \cos \theta) + eF \quad (1.61)$$

$$\dot{p}_z = -m^* \omega_C^2 (z \cos^2 \theta - x \cos \theta \sin \theta). \quad (1.62)$$

The second time derivative of  $p_z$  is given by:

$$\ddot{p}_z = -m^* \omega_C^2 (\dot{z} \cos^2 \theta - \dot{x} \cos \theta \sin \theta) \quad (1.63)$$

which is equal to:

$$\ddot{p}_z + \omega_C^2 \cos^2 \theta p_z = -\frac{m^* \Delta \omega_C^2 \cos \theta \sin \theta d}{2\hbar} \sum_{n=1}^{\infty} na_n \sin\left(\frac{nd}{\hbar} p_x\right). \quad (1.64)$$

An expression for  $p_x$  in equation 1.64 can be calculated from 1.61 and 1.62:

$$\dot{p}_z \sin \theta + \dot{p}_x \cos \theta = eF \cos \theta \quad (1.65)$$

integrating with respect to time gives:

$$p_z \sin \theta + p_x \cos \theta = eF \cos \theta t + \beta \quad (1.66)$$

where  $\beta$  is a constant of integration. Setting  $t = 0$ , we find that:

$$\beta = p_x(0) \cos \theta + p_z(0) \sin \theta. \quad (1.67)$$

Substituting 1.67 into 1.66 and simplifying gives:

$$p_x(t) = p_x(0) + eFt - (p_z - p_z(0)) \tan \theta. \quad (1.68)$$

Substituting equation 1.68 into 1.64 gives the final equation of motion for  $p_z$ :

$$\begin{aligned} \ddot{p}_z + \omega_C^2 \cos^2 \theta p_z &= -\frac{m^* \Delta \omega_C^2 \cos \theta \sin \theta d}{2\hbar} \\ &\times \sum_{n=1}^{\infty} na_n \sin\left[\frac{nd}{\hbar} (p_{x_0} + eFt - (p_z - p_{z_0}) \tan \theta)\right] \end{aligned} \quad (1.69)$$

This equation of motion uniquely determines  $p_z(t)$  and is independent of  $x$ ,  $z$  and  $p_x$ . Conversely, the equations of motion for  $x$ ,  $z$  and  $p_x$  (eqns. 1.59, 1.60

and 1.68) are dependant on  $p_z$  after some simple substitution. Therefore it can be concluded that the behaviour of the system is characterised by equation 1.69.

If only the  $n = 1$  term is considered, equation 1.69 can be rewritten as:

$$\ddot{p}_z + \omega_C^2 \cos^2 \theta p_z = -\frac{m^* \Delta \omega_C^2 \cos \theta \sin \theta d}{2\hbar} \sin(Kp_z - \omega_B t - \phi) \quad (1.70)$$

where  $K = \frac{d \tan \theta}{\hbar}$ ,  $\phi = \frac{d}{\hbar} (p_x(0) + p_z(0) \tan \theta)$  and  $a_1 = 1$ . The left-hand side of this equation has the form of a simple harmonic oscillator with angular frequency  $\omega_C \cos \theta$  and the right-hand side is a plane wave driving term with a different frequency of  $\omega_B$  that can be controlled independently of  $K$ . A theoretical treatment of the driven harmonic oscillator problem will be carried out in chapter 2.

The electron velocity in the  $x$  direction,  $v_x(t)$ , is given by substituting equation 1.68 into equation 1.59 to give:

$$v_x(t) = \dot{x}(t) = \sum_{n=1}^{\infty} \frac{nda_n}{\hbar} \sin \left[ \frac{nd}{\hbar} (p_x(0) + eFt - (p_z - p_z(0)) \tan \theta) \right]. \quad (1.71)$$

Substituting this equation into:

$$v_d = \frac{\delta}{I} \sum_{i=0}^I \int_0^{\infty} \frac{dt}{\tau_{eff}} v_{x,i}(t) e^{-t/\tau_{eff}} \quad (1.72)$$

gives the final expression for electron drift velocity where  $p_x(0)$  and  $p_z(0)$  are used to set the initial states,  $i$ . This equation has been corrected for effective temperature and the two scattering time model as described in section 1.2.4.

## 1.4 Superlattice Samples

This section will focus on the parameters of the actual superlattices used in this thesis. Two types of superlattice are used which differ in one important feature that alters their dynamics. The first superlattice, known as sample NU2293, was engineered to have a large miniband gap between the first and second minibands which reduces interminiband tunnelling and so the semiclassical approximation introduced in section 1.2.1 can be used. The second superlattice, sample NU2299, was designed with a much smaller miniband gap to allow interminiband tunnelling to occur far more readily. Consequently, for this second sample, the semiclassical model will need to be revised to include the effects of inter-miniband tunnelling.

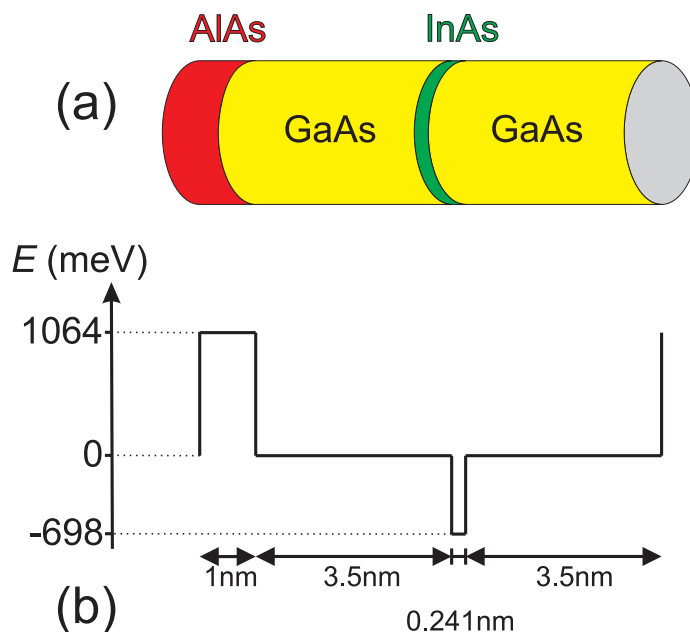


Fig. 1.10: (a) Sketch of the structure of superlattice NU2293 showing a single unit cell. (b) Variation of the electron potential energy with position  $x$  through the unit cell. Arrows show the widths of each layer.

#### 1.4.1 Superlattice NU2293

Sample NU2293 is a superlattice composed of three different semiconductor materials arranged in four layers. The semiconductors are AlAs, GaAs and InAs and the arrangement of these layers is shown in figure 1.10(a). The InAs layer has an average width of 0.8 monolayers and is included to lower the energy of the first miniband to facilitate electron injection into this miniband in experiments(15).

The band structure can be calculated from the lattice parameters summarised in table 1.1 by solving the Schrödinger equation constructed in section 1.1.1. To do this we use the matrix diagonalisation method outlined in appendix A. Although the matrix method is technically less accurate than an exact analytical calculation such as the Kronig-Penny model it produces results that are functionally identical for a sufficiently large basis set. The advantage of the numerical method is that it can calculate the wavefunctions for an arbitrarily complex symmetric superlattice potential and the method could be easily modified to also handle non-symmetric potentials. Modifying the analytical Kronig-Penny method to handle more complex superlattices would involve calculating a new, larger, set of simultaneous equations.

Figure 1.11 shows the miniband structure calculated for this superlattice

Layer	AlAs	GaAs	InAs	GaAs
Conduction Band Energy (meV)	1064	0	-698	0
Layer Width (nm)	1	3.5	0.241	3.5
Start Position (nm)	0	1	4.5	4.741

Table 1.1: Summary of the layer structure and potential energy variation for superlattice NU2293.

Miniband Index, $\alpha$	0	1	2	3	4
$E_{lower}$ (meV)	20.0	240.6	511.6	985.4	1529.3
$E_{upper}$ (meV)	39.1	341.4	726.8	1362.9	2087.0

Table 1.2: Energies of the lower and upper edges of the lowest five minibands in superlattice NU2293.

illustrating the large energy gap between the first and second minibands. Table 1.2 summarises the energies of the top and bottom of the five lowest minibands of superlattice NU2293.

Owing to the large miniband gap, it is expected that sample NU2293 will be effectively described by the single band semiclassical dynamics described in this chapter. Chapter 3 will describe the behaviour of this superlattice in detail.

#### 1.4.2 Superlattice NU2299

Superlattice NU2299 is constructed from similar materials to NU2293 but has only two layers per unit cell and a very different miniband structure. Basically the InAs layer has been removed and the AlAs layer now contains Gallium and is proportionally thicker than in NU2293. Figure 1.12(a) shows the composition of this second superlattice and (b) shows its potential energy structure which is summarised in table 1.3.

The dispersion curves are again calculated using the matrix method. Figure 1.13 shows the first three dispersion curves for this superlattice and the energy gap between the first and second minibands is calculated as 66.1meV. Table 1.4

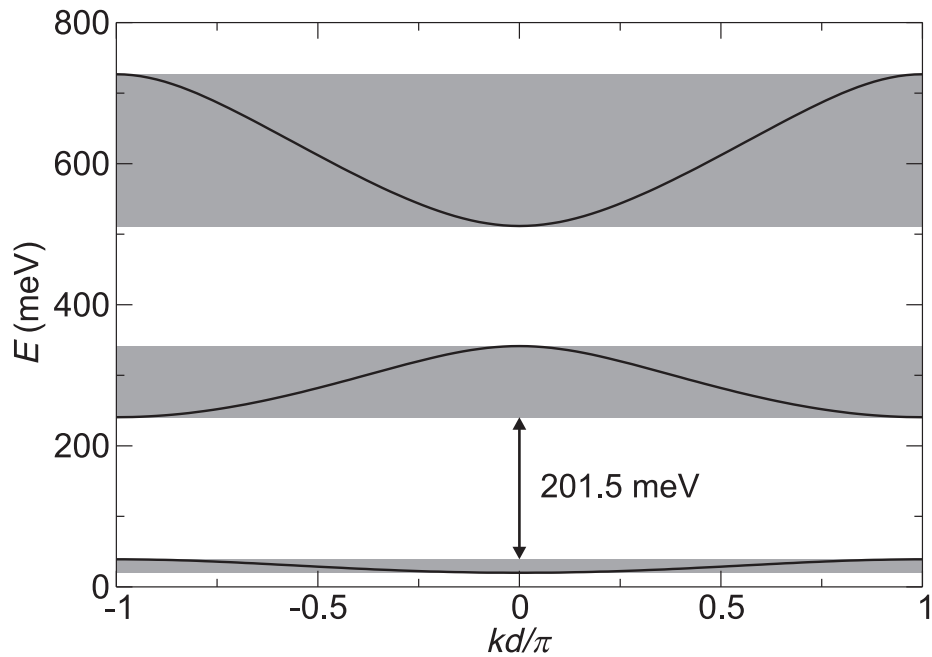


Fig. 1.11: First three dispersion curves calculated for superlattice NU2293. The large 201.5meV miniband gap between the  $\alpha = 0$  and  $\alpha = 1$  minibands is marked.

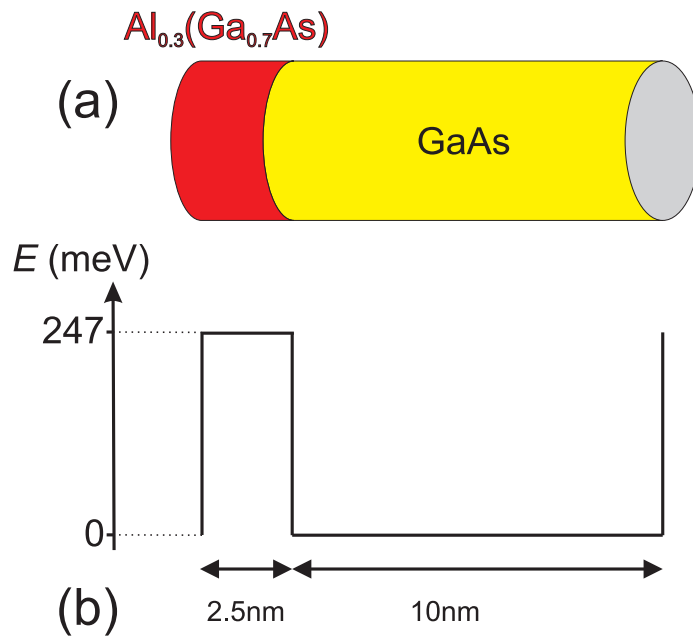


Fig. 1.12: (a) Sketch of the structure of superlattice NU2299 showing a single unit cell. (b) Variation of the electron potential energy with position  $x$  through the unit cell. Arrows show the widths of each layer.

Layer	Al <sub>0.3</sub> (Ga <sub>0.7</sub> As	GaAs
Conduction Band Energy (meV)	247	0
Layer Width (nm)	2.5	10
Start Position (nm)	0	2.5

Table 1.3: Summary of the layer structure and potential energy variation for superlattice NU2299.

Miniband Index, $\alpha$	0	1	2	3	4
$E_{lower}$ (meV)	26.6	104.7	231.9	410.5	648.9
$E_{upper}$ (meV)	38.6	153.9	344.7	609.0	944.5

Table 1.4: Energies of the lower and upper edges of the lowest five minibands in superlattice NU2299.

lists the positions of the first five minibands for superlattice NU2299.

#### 1.4.3 Differences in the Miniband Structure of the Samples

The first,  $\alpha = 0$ , minibands are of comparable width in the two structures, 19.1meV for NU2293 and 12.0meV for NU2299, although the dispersion curve for NU2293 is more sinusoidal. However, there is a large difference in the gap between the first and second minibands for these two structures, 201.5meV for NU2293 and 66.1meV for NU2299, a difference of 300%. The small miniband gap for superlattice NU2299 means that the no interminiband tunnelling assumption made by the semiclassical approximation may no longer be valid and this tunnelling will have to be accounted for at some point in the model. Chapter 4 deals with superlattice NU2299 and interminiband tunnelling in more detail.

## 1.5 Electron Transport Properties

The semiclassical model describes the behaviour of a single electron in an infinite periodic potential, such as a superlattice, under the influence of electric and

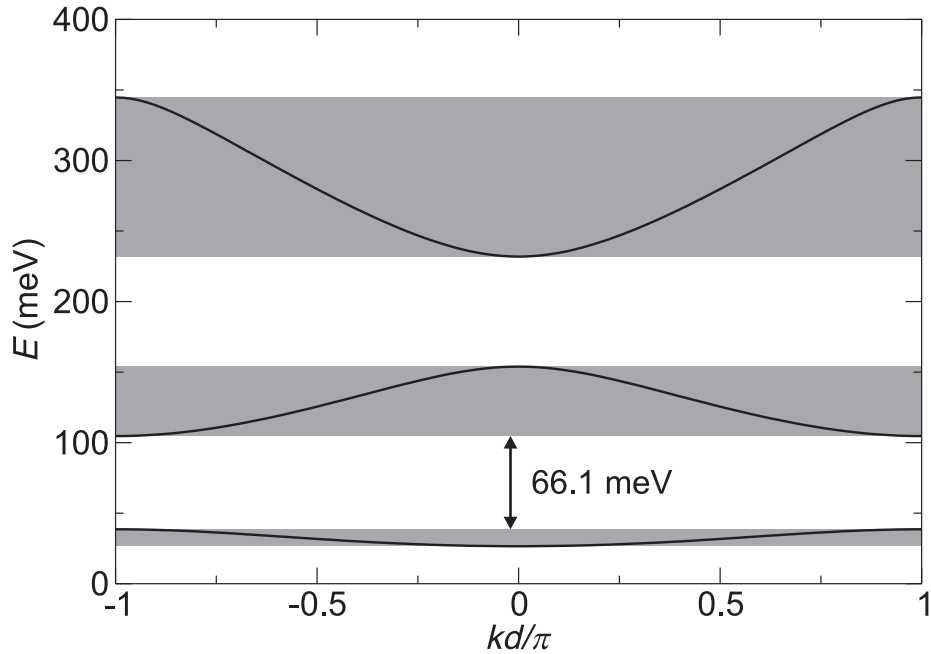


Fig. 1.13: First three dispersion curves calculated for superlattice NU2299. The 66.1meV miniband gap between the  $\alpha = 0$  and  $\alpha = 1$  minibands (marked) is clearly smaller than that for NU2293. Note the difference in the energy axis scaling between this and figure 1.11.

tilted magnetic fields. This model can describe the evolution of an electron's position and momentum in the absence of scattering. The concept of a scattering time was introduced to describe the average velocity of an electron with a given initial condition and this can be further averaged over a number of electrons with different starting conditions to account for thermal broadening. However, these models cannot determine any experimentally observable properties of the superlattice system<sup>6</sup>.

The most usable transport property is the current-voltage relationship ( $I(V)$ ) for the device. This transport data needs to correspond to a finite superlattice to have physical significance, rather than the infinite superlattice used in band theory. The transport properties must also deal with a large number of electrons and allow the electric field to be non-linear.

To deal with a very large number of electrons we define a local electron density rather than deal with individual electrons. The behaviour of a classical bulk current carrier can be determined using the Poisson and current continuity

<sup>6</sup> Some three-terminal-superlattice experiments can measure the drift velocity of an electron but such experiments have not yet been performed for the samples discussed here.

equations. The Poisson equation,

$$\nabla \cdot \mathbf{F} = \frac{\rho}{\epsilon}, \quad (1.73)$$

where  $\rho$  is the charge density and  $\epsilon$  permittivity, relates the net charge at a particular point to the rate of change of electric field at that point. The current continuity equation,

$$I(n) = I(n + 1), \quad (1.74)$$

where  $n$  indexes a section of the circuit, simply ensures that the current,  $I$ , is the same at all points in a circuit.

The transport properties of electrons in a real, finite superlattice can be predicted using a drift-diffusion model. This model involves solving the classical Poisson and current continuity equations through the superlattice by dividing it into  $N$  discrete sections. Figure 1.14 shows this division with an additional four sections (A through D) representing the ohmic contacts used for electron injection and collection. The following assumptions are made:

- For a given applied voltage, the electric field is constant in sections (A) and (D) (the ends of the device).
- The width,  $\Delta x$ , of the superlattice sections will be small enough so that changes in electric field and charge density across them will be unimportant.

This second assumption allows the  $v_d(F)$  curves predicted for the infinite superlattice to be used to describe electron velocity in each superlattice section. However, this then makes the assumption that the electron's maximum  $x$  displacement is less than  $\Delta x$  which will only ever be an approximation because scattering events are random.

To construct a set of simultaneous equations describing the device, we first consider behaviour in the superlattice sections. The two variables to consider are local charge density and local electric field which can be determined by applying the current continuity and Poisson's equation to each superlattice section. Current continuity is expressed by:

$$\begin{aligned} I(i) &= I(i + 1) \\ n(i)v_d(i)eA &= n(i + 1)v_d(i + 1)eA \end{aligned} \quad (1.75)$$

where  $I(i)$ ,  $n(i)$  and  $v_d(i)$  are the current, charge density, and drift-velocity respectively in section  $i$ , and  $A$  is the cross-sectional area of the conductor.  $v_d(i)$  is the electron drift velocity corresponding to the average electric field in

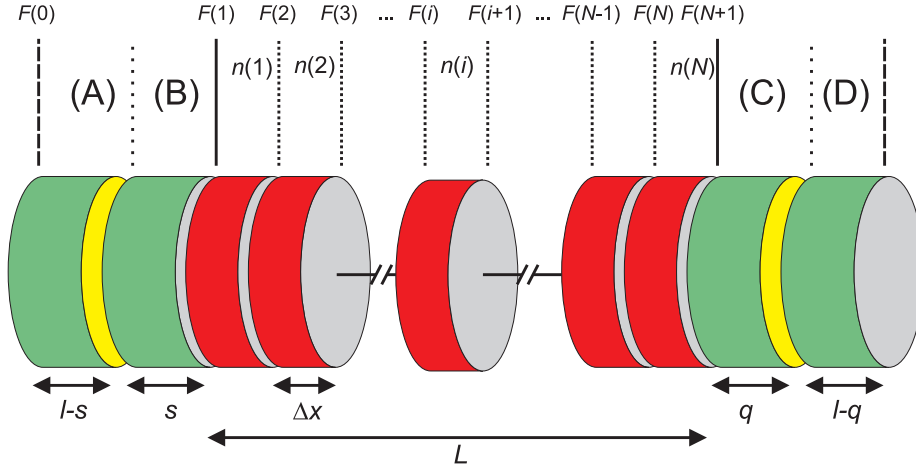


Fig. 1.14: Schematic of the division of the real superlattice device into sections for the purpose of determining its electrostatic properties. The contacts are split into the four green sections (A-D) and the superlattice region is divided into the  $N$  red sections. The electric field magnitude at the interface between the  $i^{\text{th}}$  and  $(i-1)^{\text{th}}$  layers is written as  $F(i)$  where  $i = 1, 2, \dots, (N+1)$ . Note that the direction of the electric field is always assumed to be in the negative  $x$  direction.

region  $i$ :

$$v_d(i) = v_d \left( \frac{F(i) + F(i+1)}{2} \right). \quad (1.76)$$

This average field is used because electric field is defined at the boundaries of sections whereas charge density is defined at the centre.

Equation 1.75 can be simplified to:

$$n(i)s_d(i) = n(i+1)s_d(i+1) \quad (1.77)$$

where the scaled variable  $s_d(i) = \frac{v_d(i)}{v_{d,max}}$  has been introduced and  $v_{d,max}$  is the maximum drift-velocity for the system.

Poisson's equation simply states:

$$F(i+1) - F(i) = \left( \frac{e\Delta x}{\epsilon_0\epsilon_r} \right) [n(i) - n_D(i)] \quad (1.78)$$

where  $n_D(i)$  is the density of ionised donors in  $i^{\text{th}}$  superlattice section which is included to account for the positively charged donor ions. The proportion of ionised donors is, in our model, assumed to be exponentially related to the local electric field,

$$n_D(i) = n_D \exp \left( -\frac{2F_{ion}}{F(i) + F(i+1)} \right) \quad (1.79)$$

where  $F_{ion}$  is the characteristic electric field required to ionise the donors and

$n_D$  is the overall doping density.

The superlattice contacts are heavily doped and the electric field is constant in regions (A) and (D). We can therefore relate current and conductivity by:

$$I = \sigma F(0)A \quad (1.80)$$

where

$$\sigma = \frac{n_0 e^2 \tau_c}{m^*} \quad (1.81)$$

and  $\tau_c$  and  $n_0$  are the scattering time and doping density respectively for the contacts.

Regions (A) and (B) are divided by a sheet of negative charge or electron accumulation layer, which serves to alter the constant electric field,  $F(0)$ , in region (A) to the field at the LHS of the superlattice,  $F(1)$ . Poisson's equation gives the charge density of this sheet,  $n_L$ , as,

$$F(1) - F(0) = \frac{en_L}{\varepsilon_0 \varepsilon_r}. \quad (1.82)$$

In a similar way, region (C) becomes depleted (loses electrons) in order to change the field  $F(N + 1)$  at the end of the superlattice region back to  $F(0)$ . Poisson's equation shows that the relationship between the length,  $q$ , and electron depletion density,  $n_0$ , in this region is:

$$F(0) = F(N + 1) - \frac{en_0 q}{\varepsilon_0 \varepsilon_r}. \quad (1.83)$$

By integrating the field change across the depletion region, it can be shown that the voltage drop across region (C) is,

$$V(C) = F(N + 1)q - \frac{en_0 q^2}{2\varepsilon_0 \varepsilon_r}. \quad (1.84)$$

The total voltage drop across the system can be calculated by assuming that the electric field in each section is constant except in region (C), for which equation 1.84 is used:

$$\begin{aligned} V = & F(0)(l - s) + F(0)(l - q) + F(1)s + F(N + 1)q \\ & + V(C) + \frac{\Delta x}{2} \sum_{i=1}^N (F(i) + F(i + 1)) + \sigma F(0)AR_{ext} \end{aligned} \quad (1.85)$$

where  $R_{ext}$  is a resistance describing the remaining circuit and its connections to the actual superlattice device at (A) and (D).

For given values of  $s$  and  $n_0$ , which we take to be the nominal values specified during the MBE growth process, there are  $2N + 4$  unique unknowns in this problem.  $N + 2$  local electric fields,  $N$  local charge densities, the sheet density,  $n_L$ , of the electron accumulation layer between regions (A) and (B), and the width,  $q$ , of region (C). A set of  $2N + 4$  non-linear equations have also been defined:

1. The first  $N - 1$  equations arise from current continuity through the superlattice - see equation 1.77.
2. There are  $N$  Poisson's equation - one for each section of the superlattice - see equation 1.78.
3. Two equations maintain current continuity between regions (B) and (C) and the superlattice:

$$\sigma F_0 = n(1)ev_d(1) \quad (1.86)$$

$$\sigma F_0 = n(N)ev_d(N). \quad (1.87)$$

4. Eqns 1.82 and 1.85 provide two further equations for the set.
5. The final equation arises from ensuring that there is no net charge in the structure. This requires that the electric field is equal in regions (A) and (D) and so equation 1.83 is needed.

Solving the  $2N + 4$  coupled non-linear equations will give information on the current-voltage characteristics of the device as well as more fundamental electrostatic properties such as the electric field and charge density at any point through the superlattice.

### 1.5.1 Parameters of the Real Superlattices

The drift-diffusion model requires a number of parameters to characterise the superlattice devices used in experiments. Table 1.5 summarises these parameters for both superlattices samples. The doping density of the superlattice layers is given as an average because it varies between the different semiconductor materials. Note that the contact parameters were estimated from bulk semiconductor experiments at 4.2 K

## 1.6 Compatibility of Assumptions Made

A number of assumptions were made in formulating the drift-diffusion and semi-classical drift velocity models. This section will summarise and discuss the implications of these assumptions and identify areas where they may not hold.

Parameter	Symbol	Value	
		NU2293	NU2299
Contact length	$l$	500 Å	300 Å
Contact doping density	$n_0$	$10^{17} \text{ cm}^{-3}$	$3.2 \times 10^{16} \text{ cm}^{-3}$
Contact scattering time	$\tau_c$	90 fs	27 fs
Position of accumulation layer	$s$	150 Å	150 Å
Mean SL doping density	$n_D$	$3 \times 10^{16} \text{ cm}^{-3}$	$1.88 \times 10^{16} \text{ cm}^{-3}$
Characteristic ionising field	$F_{ion}$	$150 \text{ KVm}^{-1}$	$80 \text{ KVm}^{-1}$
External resistance	$R_{ext}$	$17 \Omega$	$(2 < R_{ext} < 20) \Omega$

Table 1.5: Parameters used to define the real superlattice devices. Note that the external resistance used for NU2299 was varied depending on the magnetic field.

Bloch theory assumes an infinite length superlattice and this assumption conflicts with the finite length superlattice used in the bulk transport model. However, Rauch has shown(16) that even a five quantum well structure exhibits minibands so Bloch theory should be valid for our 14 period structure. Therefore, the infinite superlattice assumption will only be invalid if size of the electron orbits in the  $x$  direction exceeds the length of the superlattice. Chapter 3 will show that the spatial extent of the electron orbits is generally determined by the angle and strength of the magnetic field and the applied voltage. However, the most significant limit on the distance travelled by an electron is the electron scattering time. We find that even the most extended electron trajectories do not exceed five superlattice periods over a period of  $3\tau$ . Therefore the infinite superlattice assumption is valid for the determination of drift velocity.

Bloch theory also assumes a perfectly periodic superlattice, which will not be correct for a real superlattice. The introduction of a scattering time is used to account for this aperiodicity.

The semiclassical model makes two main assumptions - a wavepacket size of many periods and no change in the magnitudes of any fields over the extent of this wavepacket. The large wavepacket assumption does not directly conflict with any other assumptions but, in the bulk transport model, the electric field is allowed to vary over the finite superlattice and there are no guarantees that this variation will be small enough to satisfy the semiclassical model. In addition, the field needs to be constant over the mean free electron path for the constant field used in equation 1.17 to be valid.

The assumptions made in the scattering model were discussed in section 3.2.8 and these assumptions do not directly conflict with any other assumptions made.

The drift-diffusion model uses the local electron drift velocity and there-

---

fore explicitly uses all the assumptions made in the Bloch, semiclassical and scattering models.

The superlattice is modelled as a series of discrete slices which approaches the real situation as the number of slices goes to infinity. It is assumed that the electric field is constant over one slice and this can lead to problems if the electric field changes rapidly over the width of the slices. Some of the results in chapter 3 are affected by this limitation for high magnetic and electric field strengths.

Finally, a number of the parameters used to model the real superlattice, especially those defining the contacts, are only inferred from experimental results. Parameters such as the contact resistance could take a range of values which can alter the positions of significant features substantially. However, it is unlikely that the real parameters are significantly different from the inferred ones.

## 2. CHAOS

The usual definition of chaos refers to systems which have an extreme sensitivity to initial conditions. This means that the evolution of a system with an initial state denoted by  $I$  would be very different to that of the same system with initial state  $I + dI$ . This difference can be characterised by:

$$d(t) = d(0)e^{\lambda t} \quad (2.1)$$

where  $d(t)$  is some measure of the difference in the states of the two systems at time  $t$ . The parameter  $\lambda$  is known as the Lyapunov exponent and when  $\lambda$  is real and positive then the system is chaotic i.e. it has exponential divergence. A system with periodic or quasi-periodic system behaviour cannot have this exponential divergence.

Because of this extreme sensitivity to initial conditions it is very difficult to predict the evolution of chaotic systems but they are still deterministic. By this it is meant that, for a particular set of initial conditions, a chaotic system will always evolve in the same manner. However, in practice, such uniformity is unlikely to exist for numerical simulations. This is because the level of precision to which a parameter is taken as well as computational rounding errors can lead to a divergence between two different simulations of the same system.

## 2.1 Hamiltonian and Dissipative Systems

There are two major types of system studied in relation to chaos: dissipative and Hamiltonian systems. A Hamiltonian system must contain no dissipation and, conversely, a dissipative system cannot generally<sup>1</sup> be described by a Hamiltonian. A dissipative system converges on some limiting set or *attractor* as  $t \rightarrow \infty$  while a Hamiltonian system does not. The system developed in Chapter 1 and described by Hamiltonian 1.51 is therefore not expected to converge.

Hamiltonian systems are described by pairs of variables which relate to a value and its derivative, typically position and momentum, which, for the purposes of this chapter, will be referred to as  $q_i$  and  $p_i$  respectively. The subscript on these variables is an integer that ranges from 1 to  $N$  where  $N$  is the number of degrees of freedom of the system and there is a unique pair  $\{p_i, q_i\}$  for each degree of freedom. Therefore, a Hamiltonian system with  $N$  degrees of freedom is described by  $2N$  variables. As outlined in the previous chapter, there are  $2N$  Hamilton's equations that can be defined for a classical Hamiltonian:

$$\frac{dp_i}{dt} = -\frac{\partial H(\mathbf{p}, \mathbf{q}, t)}{\partial q_i} \quad (2.2)$$

---

<sup>1</sup> A dissipative system can be described by a Hamiltonian provided a mechanism for dissipation is also incorporated into the Hamiltonian.

and

$$\frac{dq_i}{dt} = \frac{\partial H(\mathbf{p}, \mathbf{q}, t)}{\partial p_i}. \quad (2.3)$$

The time derivative of energy is given by:

$$\frac{dH}{dt} = \sum_i \left\{ \frac{\partial H}{\partial p_i} \frac{dp_i}{dt} + \frac{\partial H}{\partial q_i} \frac{dq_i}{dt} \right\} + \frac{\partial H}{\partial t}, \quad (2.4)$$

which contains terms for the explicit and implicit time dependence of  $H$ . The Hamiltonian of the system considered in this work has no explicit time dependence (equation 1.51) so the final term in the above equation is zero. Using Hamilton's equations 2.2 and 2.3 to replace the time derivatives of  $p_i$  and  $q_i$  in equation 2.4 gives:

$$\frac{dH}{dt} = \sum_i \left\{ \frac{\partial H}{\partial p_i} \left( -\frac{\partial H}{\partial q_i} \right) + \frac{\partial H}{\partial q_i} \frac{\partial H}{\partial p_i} \right\} = 0. \quad (2.5)$$

Equation 2.5 shows that a Hamiltonian with no explicit time dependence is a constant of motion. For conservative systems,  $H$  is the total energy of the system and therefore is also conserved. This is not an automatic consequence of defining a Hamiltonian as non-dissipative: even though energy cannot be lost via dissipation it can be added or removed from the system - for example by an external force.

## 2.2 Conserved Quantities

Hamiltonian systems are also known as *conservative systems* because they often have one or more quantities that are conserved. It has already been shown that Hamiltonian 1.51 corresponds to a constant energy and therefore describes a conservative system. A test to see whether a particular quantity is conserved can be performed in a similar way to the above analysis of energy. If  $f$  is the quantity to be tested for conservation then if:

$$\frac{df(\mathbf{p}, \mathbf{q}, t)}{dt} = \frac{\partial f}{\partial t} + \frac{\partial f}{\partial \mathbf{q}} \cdot \frac{d\mathbf{q}}{dt} + \frac{\partial f}{\partial \mathbf{p}} \cdot \frac{d\mathbf{p}}{dt} \quad (2.6)$$

is zero the quantity is conserved. Using Hamilton's equations 2.2 and 2.3 to substitute for the time derivatives of  $\mathbf{p}$  and  $\mathbf{q}$  in equation 2.6 gives:

$$\frac{df(\mathbf{p}, \mathbf{q}, t)}{dt} = \frac{\partial f}{\partial t} + [f, H] \quad (2.7)$$

where

$$[f, H] = \frac{\partial f}{\partial \mathbf{q}} \cdot \frac{\partial H}{\partial \mathbf{p}} + \frac{\partial f}{\partial \mathbf{p}} \cdot \frac{\partial H}{\partial \mathbf{q}} \quad (2.8)$$

and the quantity  $[f, H]$  is known as the Poisson bracket of  $f$  and  $H$ . It follows from equation 2.7 that if:

$$[f, H] = \frac{\partial f}{\partial t} \quad (2.9)$$

is true then  $f$  is conserved. Note that if  $H$  is time dependent then the Poisson bracket may also be time dependent and condition 2.9 must be true at all times to ensure that  $f$  is conserved.

### 2.3 Phase Space

Because Hamiltonian systems are described by pairs of vectors  $\{\mathbf{p}, \mathbf{q}\}$  it is useful to define a space with dimensions of *both* of these vectors, which is known as *phase space*. Phase space therefore has  $2N$  dimensions where  $N$  is the number of degrees of freedom of the system. Thus a system with one dimension in real space such as a simple harmonic oscillator has a 2D phase space with axes of position and momentum. Phase space is an extremely useful tool because it provides information on the dynamics of the system in a single point. This is in contrast to a real space plot where the momentum can only be determined by looking at the time evolution of position.

The phase space for a system with  $k$  unique conserved quantities is  $2N - k$  dimensional. A conserved quantity is only unique if the Poisson bracket of it with all the other conserved quantities is zero:

$$[f_i, f_j] = 0 \quad (2.10)$$

where  $i \neq j$  and  $i$  and  $j$  index the conserved quantities. A set of unique conserved quantities is said to be “*in involution*”.

### 2.4 Integrable and Non-Integrable Systems

First a definition:

*An integrable system is a system where the number of conserved quantities is the same or greater than the number of degrees of freedom.*

This means that a system with  $N$  degrees of freedom must have  $k \geq N$  conserved quantities to be integrable. Therefore, the phase space of an integrable system will have  $N$  or fewer independent dimensions. A simple example of an integrable system is a simple harmonic oscillator which has varying  $x$  and  $p_x$  but fixed energy. The phase space of such a system is two dimensional but the trajectories are confined to an ellipse of constant energy as shown in figure 2.1.

For an integrable system with more than one degree of freedom and  $k = N$ , the trajectories are confined to an  $N$  dimensional *torus* in  $2N$  dimensional

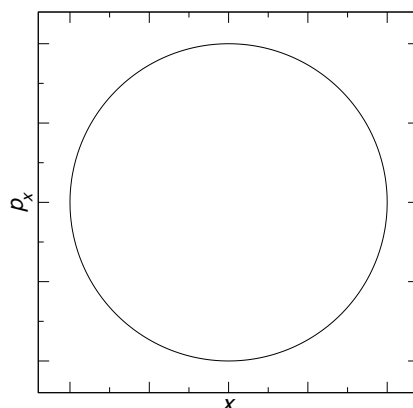


Fig. 2.1: Phase space plot (position  $x$  vs. momentum  $p_x$ ) of a simple harmonic oscillator with constant energy. This shows that the motion is confined to a 1D curve (an ellipse) in 2D phase space.

phase space. This torus represents all the points in phase space that have the initial conditions of the  $k$  conserved quantities. Figure 2.2(a) shows an example 2D torus for an integrable system with two degrees of freedom. An  $N$  dimensional torus can be described by  $N$  radii (see figure 2.2(a)) which give rise to  $N$  possible distinct frequencies for motion on this torus. Any actual trajectory around this torus must consist of a linear combination of these fundamental frequencies - if any fundamental frequency is not included then the system must have additional conserved quantities. Therefore, for the torus sketched in figure 2.2(a), a trajectory can be specified by the frequencies of motion around the small radius,  $f_2$  and the large radius,  $f_1$ . A winding number can be defined which is the ratio of these frequencies:

$$\omega = \frac{f_2}{f_1}, \quad (2.11)$$

which means the trajectories will be periodic if  $\omega$  is rational and quasi-periodic if  $\omega$  is irrational.

Because we are now dealing with motion on the surface of a torus it is convenient to perform a change of coordinate systems. This system, known as *action-angle* variables, will define a point on the torus in terms of vectors of magnitude  $I_i$  (action) with direction  $\phi_i$  (angle). Figure 2.2(b) shows the action-angle coordinates for a 2D torus. Because motion is constrained to the surface of the torus, the action coordinates are constant for a given integrable system and define the initial conditions. The angle coordinates vary with time and give the current state of the system at time  $t$ . An important property that has to be satisfied by this coordinate transform is that the form of Hamilton's equations

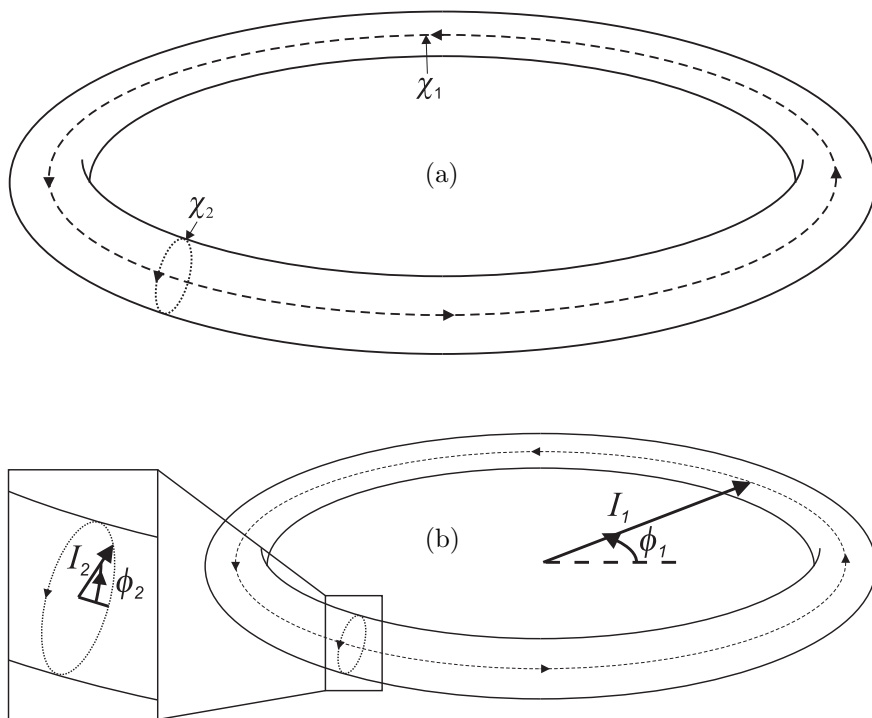


Fig. 2.2: (a) is a representation of a 2D torus showing the fundamental circumferences  $\chi_1$  and  $\chi_2$  which have radii  $r_1$  and  $r_2$  respectively. (b) shows the two sets of action-angle  $(I_i, \phi_i)$  coordinates for this torus.

should remain unaltered so that:

$$\frac{d\phi_i}{dt} = \frac{\partial H}{\partial I_i}, \quad (2.12)$$

and

$$\frac{dI_i}{dt} = -\frac{\partial H}{\partial \phi_i}, \quad (2.13)$$

which simplifies the use of these coordinates.

Using these new action-angle coordinates, the winding number,  $\omega$ , can be defined as:

$$\omega = \frac{\omega_2}{\omega_1} \quad (2.14)$$

where  $\omega_1$  and  $\omega_2$  are the angular frequencies of the  $\phi_1$  and  $\phi_2$  angle coordinates respectively. For a system with more than two degrees of freedom there is a set of winding numbers which must all be rational for the system to have periodic behaviour.

This description of action-angle variables is brief because it does not directly affect the main thrust of this work. The theoretical results obtained numerically in this thesis will be compared to experimental results rather than analysed with respect to the mathematics of chaos. A more comprehensive treatment of these concepts can be found in any basic chaos text, see refs (17)(18) for example.

#### 2.4.1 Non-Integrable Systems

The above discussion relates to integrable systems, which exhibit either periodic or quasi-periodic behaviour but not chaotic behaviour. Chaotic behaviour can only occur in non-integrable systems where the number of conserved quantities is smaller than the number of degrees of freedom of the system. The 1D simple harmonic oscillator would become non-integrable if the energy conservation condition were removed - for example by an external driving force. Under such a force, the trajectory would no longer be confined to a single elliptical path in phase space. The system can now behave aperiodically as well as periodically or quasi-periodically but there is still no guarantee that its behaviour will be chaotic.

It is more difficult to visualise the transition of a larger system from integrable to non-integrable because the multidimensional phase space is impossible to plot effectively. A simple example of a system with two degrees of freedom and one conserved quantity can be obtained by taking the integrable system in figure 2.2 and removing the energy quantisation condition. In this case, the ‘‘fatness’’ of the torus, which is related to energy, will change with time but the trajectories will still lie on its surface. A coupled system has now been created

with the  $f_2$  frequency coupled to the energy variation, as in a double pendulum system. The double pendulum is a classic example of a non-linear system that can be chaotic for certain initial conditions.

### 2.4.2 Chaos

At the start of this chapter it was stated that chaos is defined by the exponential divergence of two trajectories starting from almost identical initial conditions. This divergence is characterised by the Lyapunov exponent (eqn. 2.1). If the Lyapunov exponent is real and positive then the system's behaviour is chaotic. However this chaotic behaviour does not necessarily occur over the whole of phase space and it is possible to have *weak chaotic* systems where some regions of phase space behave in a chaotic manner and other regions retain periodic or quasi periodic behaviour. The contrasting case is *strong chaos* where the whole of phase space behaves in a chaotic manner.

To illustrate these concepts of strong and weak chaos it is necessary to use phase space. However, it has become increasingly difficult to illustrate phase space for systems with more than one degree of freedom so it is necessary to reduce the dimensionality of phase space. This is achieved by taking a Poincaré section as is explained in the next section.

## 2.5 Poincaré Sections

A Poincaré section is typically a 2D slice through  $2N$  dimensional phase space, chosen to reveal the dynamics of the system. The advantage of taking such a section is that the behaviour of the system can be effectively plotted in 2D. The challenge with defining a Poincaré section lies in choosing the conditions to limit the plot to 2D.

Consider a system with two degrees of freedom described by the Hamiltonian:

$$H = H_0(x, z, p_x, p_z = 0) + \epsilon \Delta H(x, z, p_x, p_z = 0, t) \quad (2.15)$$

where  $\epsilon$  will be varied to change the system. In this Hamiltonian, the  $H_0$  term is integrable because it has no explicit time dependence and therefore has conserved energy as well as a second conserved quantity ( $p_z = 0$ ). However, the  $\Delta H$  term is time dependent and is therefore non-integrable. If  $\epsilon \neq 0$ , the full Hamiltonian will also be non-integrable.

Even if  $\epsilon = 0$  the  $(\mathbf{p}, \mathbf{q})$  phase space is still 3D and an additional constraint is required to construct a 2D Poincaré section. Looking at phase space whenever  $z$  has some fixed value is an example of such a constraint. Figures 2.3(a) and (b) show Poincaré sections for  $\epsilon = 0$  where the trajectory has rational and irrational

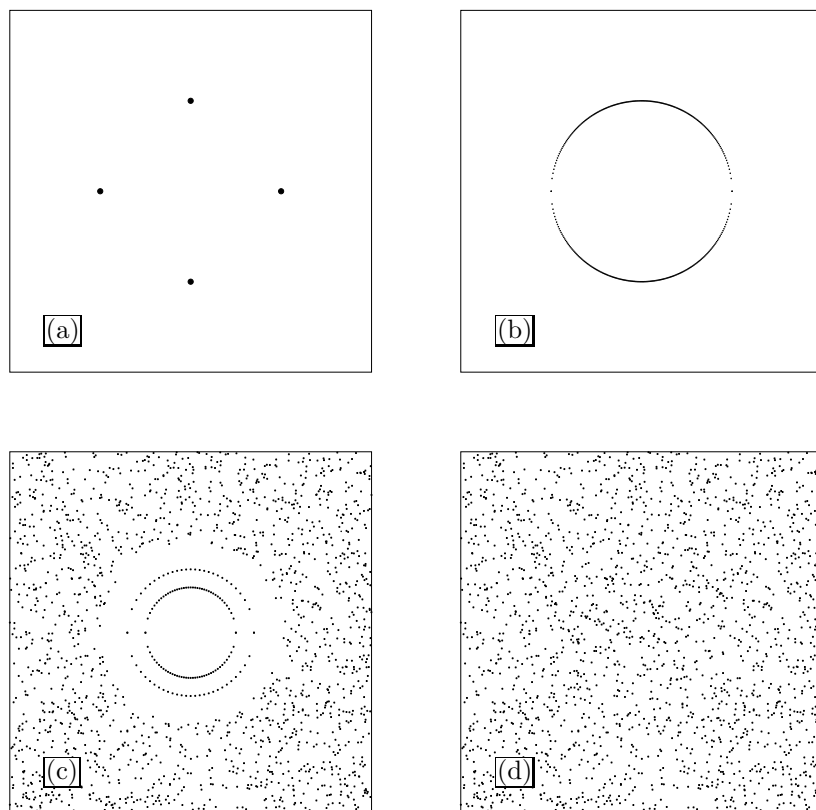


Fig. 2.3: Example Poincaré sections. (a) and (b) show periodic and quasi-periodic trajectories respectively for the system shown in figure 2.2. (c) and (d) show chaotic Poincaré sections which can occur for a non-integrable system. (c) displays weak chaos and (d) strong chaos.

winding numbers respectively. It can be seen that the Poincaré sections show the small cross-section of the torus. As  $\epsilon$  is increased the system becomes non-integrable and the trajectories can leave the surface of the torus. This leads to figures 2.3(c) and (d) which display regions of chaotic behaviour - i.e. the Lyapunov exponent is positive. In figure 2.3(c) there are regions of phase space which still display regular behaviour known as *stable islands* and such a mix of stable and chaotic behaviour is referred to as *weak chaos*. Figure 2.3(d) is chaotic across all the Poincaré section and this region is referred to as a *chaotic sea* and the system displays *strong chaos*.

Although a Poincaré section may display a certain type of behaviour there is no guarantee that this behaviour holds across all of phase space - there may be addition islands of stability or regions of chaos. However, a Poincaré section is usually chosen with a consideration of the likely dynamics and should therefore give a good representation of the system's overall behaviour in phase space.

## 2.6 KAM and non-KAM Chaos

Given a system:

$$H(\mathbf{I}, \phi, t) = H_0(\mathbf{I}) + \epsilon \Delta H(\mathbf{I}, \phi, t), \quad (2.16)$$

the KAM theorem states(18):

If  $\epsilon$  is small and  $H_0$  is non-degenerate such that:

$$\left| \frac{\partial^2 H_0}{\partial \mathbf{I} \partial \phi} \right| \neq 0 \quad (2.17)$$

for a sufficiently irrational set of trajectories, there exists a torus for  $H$  close to the invariant torus of  $H_0$ .

Essentially this means that, for such a system, as the parameter  $\epsilon$  is increased from zero the rational trajectories are destroyed but there can still exist islands of stability consisting of trajectories with irrational frequency ratios. Increasing  $\epsilon$  further will destroy these stable islands. This means that there is a gradual transition to chaos as the perturbation of the system is increased - the behaviour changes from stable to weakly chaotic and finally to strongly chaotic.

However, the system that is considered in this work is degenerate so condition 2.17 does not hold and KAM theory cannot be applied. This work focuses on a system formally identical to a driven harmonic oscillator and the following will consider the behaviour of such a system.

### 2.6.1 Non-KAM Chaos

The one dimensional driven harmonic oscillator with natural frequency  $\omega$  and driving frequency  $\omega_D$  is described by:

$$H = \frac{1}{2} \dot{x}^2 + \frac{1}{2} \omega^2 x^2 + \epsilon \frac{\omega^2}{K^2} \cos(Kx - \omega_D t) \quad (2.18)$$

where  $\epsilon$  is a dimensionless coefficient governing the strength of the perturbing plane wave and  $K$  is the wavevector of this wave. Applying Hamilton's equations gives the equation of motion:

$$\ddot{x} + \omega^2 x = -\epsilon \frac{\omega^2}{K} \sin(Kx - \omega_D t). \quad (2.19)$$

We will consider the case when the driving term is resonant with the integrable harmonic oscillation which occurs when  $r = \omega_D/\omega$  is an integer and gives the strongest possible perturbation. For all integer  $r$  values, the Hamiltonian 2.18 can be converted to polar coordinates using  $x = \rho \sin \theta$  and  $\dot{x} = \omega \rho \cos \theta$

giving:

$$H = \frac{1}{2}\omega^2\rho^2 + \frac{1}{K^2}\epsilon\omega^2 \sum_m J_m(K\rho) \cos(m\theta - r\omega t) \quad (2.20)$$

where  $J_m$  is an  $m^{\text{th}}$  order Bessel function of the first kind. Separating out the term with  $m = r$  gives:

$$\begin{aligned} H &= \frac{1}{2}\omega^2\rho^2 + \frac{1}{K^2}\epsilon\omega^2 J_r(K\rho) \cos(r\theta - r\omega t) \\ &+ \frac{1}{K^2}\epsilon\omega^2 \sum_{m \neq r} J_m(K\rho) \cos(m\theta - r\omega t). \end{aligned} \quad (2.21)$$

The system can now be converted to action-angle coordinates using

$$I = \frac{\omega\rho^2}{2r} \quad \phi = r\theta - r\omega t. \quad (2.22)$$

A new Hamiltonian will be defined:

$$\tilde{H} = H - r\omega I, \quad (2.23)$$

which can be separated into time dependent and time independent parts:

$$\tilde{H} = \tilde{H}_0(I, \phi) + \tilde{V}(I, \phi, t) \quad (2.24)$$

thus

$$\begin{aligned} \tilde{H}_0 &= \frac{1}{K^2}\epsilon\omega^2 J_r(K\rho) \cos \phi \\ \tilde{V} &= \frac{1}{K^2}\epsilon\omega^2 \sum_{m \neq r} J_m(K\rho) \cos \left[ \frac{m}{r}\phi - \left(1 - \frac{m}{r}\right)r\omega t \right]. \end{aligned} \quad (2.25)$$

where  $\rho = \sqrt{2rI/\omega}$ . If we treat the time dependent part,  $\tilde{V}$ , as a perturbation then the stationary points of the system can be found by differentiating the time-independent Hamiltonian,  $\tilde{H}_0$ :

$$\frac{\partial \tilde{H}_0}{\partial I} = 0 \quad \frac{\partial \tilde{H}_0}{\partial \phi} = 0. \quad (2.26)$$

Solving these equations gives a set of elliptic points:

$$J'_n(K\rho) = 0 \quad \phi = 0, \pi \quad (2.27)$$

which will define the centres of stable trajectories in phase space and a set of hyperbolic points:

$$J_n(K\rho) = 0 \quad \phi = \pm\pi/2 \quad (2.28)$$

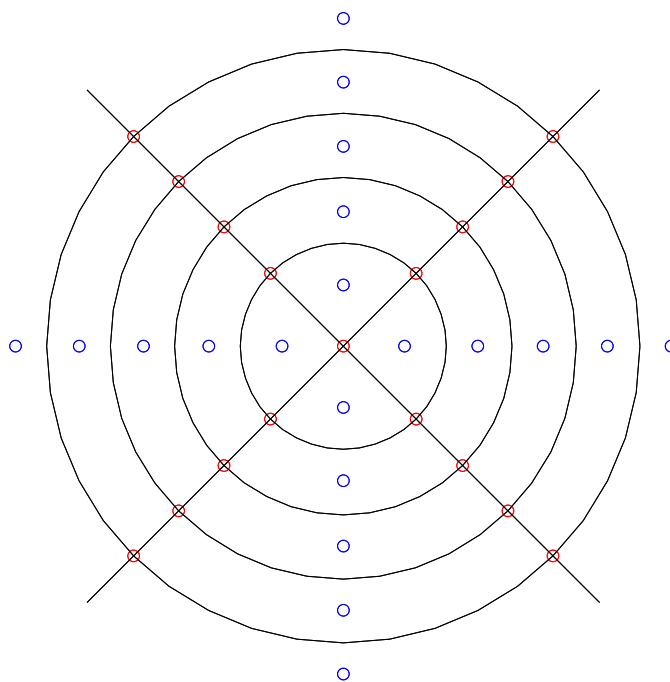


Fig. 2.4: Hyperbolic points (red) and elliptic points (blue) of the driven harmonic oscillator where  $r = 2$ . The black lines are a sketch of the separatrices connecting the hyperbolic points.

which will be unstable points in phase space. Figure 2.4 shows the location of these hyperbolic and elliptic points.

The hyperbolic points are connected by an infinitely thin web-like structure of separatrices while the elliptical points are the centres of a series of closed orbits within the cells of this web.

Including the time-dependent term into this analysis will destroy the separatrices which form in the static system and replace them with stochastic channels of finite width. In this context a stochastic layer is defined as “a region of many overlapping trajectories whose width varies linearly with perturbation strength” (19). Essentially these stochastic channels display chaotic behaviour and diffusion can occur throughout this web structure along both the radial and circular stochastic filaments. Including this perturbation term is complex and the analysis will not be reproduced here. See chapter 4 of (20) for full details. This treatment shows that the width of the stochastic filaments drops off exponentially in the radial direction:

$$\Delta_C \propto A\rho^{1/2} \exp\{B\rho^{1/2}\} \quad (2.29)$$

where  $\Delta_C$  is the width of the stochastic channels and  $A$  and  $B$  are constants.

This analysis has considered the case where the natural frequency of the oscillator is resonant with the driving frequency. If the ratio between these frequencies is irrational, the web of stochastic channels or *stochastic web* does not form and motion is generally confined to stable orbits or a chaotic sea. These different behaviours will be considered in Chapter 3.

Therefore the parameter  $r$ , which sets the ratio between the driving and natural frequencies of the system, is vital in determining whether or not a stochastic web can form and how extended it is in phase space. This system differs to KAM systems because there is a parameter that can turn the chaotic stochastic web on and off abruptly rather than gradually.

## 2.7 Quantum Chaos

It is possible to formulate a quantum model of the driven harmonic oscillator system. This quantum system should display similar behaviour to the classical system and should have identical behaviour for sufficiently large quantum numbers or as  $\hbar \rightarrow 0$ . This is known as the *correspondence principle*. However, there are several general difficulties(17) with this correspondence:

1. Schrödinger's equation is linear which means that wavefunctions cannot diverge exponentially. Therefore it appears as if the quantum system cannot converge on the classical system as  $\hbar \rightarrow 0$ . However, it is possible for the mean position of the wavefunctions to diverge exponentially so the correspondence principle holds.
2. The Heisenberg Uncertainty Principle precludes knowledge of the particles position and momentum to an accuracy greater than  $\hbar/2$ :

$$\Delta\mathbf{p}\Delta\mathbf{q} > \hbar/2. \quad (2.30)$$

This means that it is impossible to define two trajectories with arbitrarily close starting points so the classical test of chaos cannot be applied.

3. The Uncertainty Principle also means that areas of  $2N$ -dimensional phase space smaller than  $\hbar^N$  cannot be resolved and classical features that are smaller than this will not appear in the quantum system.

Points 2 and 3 do reduce to the classical limit when  $\hbar = 0$  because the uncertainty in position and momentum drops to zero.

Therefore, a quantum system cannot directly display many of the properties that are attributed to classical chaotic systems and the term “quantum chaos” is a misnomer(21). Quantum chaos is really a study of the quantum properties

of systems whose classical counterparts exhibit chaos. Although the above limitations may suggest that these quantum systems will be uninteresting from a chaotic standpoint it must be remembered that the quantum solutions approach the classical solutions in the limit of high quantum numbers or as  $\hbar \rightarrow 0$ . In addition, “large” features will still appear in the quantum phase space and chapter 5 will show that there is a striking correspondence between results obtained using the quantum and classical models.

## 2.8 Phase Space in Quantum Chaos

In classical systems, the features which are distinctive to chaos such as chaotic seas and stochastic channels are best viewed in phase space. It would therefore be useful to view the corresponding quantum states in phase space for the purpose of comparison. The solutions to Schrödinger’s equation are usually particle wavefunctions,  $\Psi$ , where  $|\Psi|^2$  gives the probability density of the particle in real space. Thus, to look at the phase space probability of the particle it is necessary to obtain information about the momentum of the particle. However, introducing momentum means that resolution is limited to  $\hbar^N$  for a system with  $N$  degrees of freedom because of the Uncertainty Principle. One common method used to look at the properties of two non-commuting variables simultaneously is Wigner mechanics(22)(23). In general, Wigner mechanics involves a transformation of both operators and variables. But in this section we will only consider the transformation of a quantum mechanical wavefunction  $\Psi(\mathbf{q})$  into a Wigner quasi-probability function  $W(\mathbf{q}, \mathbf{p})$ .

The Wigner function was designed to be an analogue of the classical phase space distribution and has the following form:

$$W(\mathbf{q}, \mathbf{p}) = \frac{1}{\pi\hbar} \int_{-\infty}^{\infty} \psi^*(\mathbf{q} + \lambda)\psi(\mathbf{q} - \lambda)e^{2i\mathbf{p}\lambda/\hbar} d\lambda \quad (2.31)$$

where  $\mathbf{q}$  is position,  $\mathbf{p}$  is momentum and  $\lambda$  is a spatial displacement. The Wigner function is a measure of the *quasi*-probability of the particle which means that the resolution constraint imposed by the Uncertainty Principle is removed but the function is now no longer a measure of true probability.

The Wigner function obeys the following desirable conditions which make it a good analogue of the classical phase space.

1. The Wigner function  $W(x, p_x)$  is real.
2. The integral of the Wigner function over all momenta is equal to the the

electron probability density at that point in real space:

$$\int_{-\infty}^{\infty} W(x, p_x) dp_x = |\Psi(x)|^2. \quad (2.32)$$

3. The integral of the Wigner function over all position is equal to the the Fourier transform of the electron probability density at that point in momentum space:

$$\int_{-\infty}^{\infty} W(x, p_x) dx = |\Phi(p_x)|^2 \quad (2.33)$$

where  $\Phi(p_x)$  is the Fourier transform of  $\Psi(x)$ .

There are a number of different functions that would satisfy these conditions but equation 2.31 was chosen by Wigner because it doesn't increase the complexity of  $\Psi(\mathbf{q})$  and because in his words "*it seems to be the simplest*". However, this simplicity comes at a cost and the formulation has the following problems.

1. The Wigner quasi-probability can have negative values which is an impossible concept in classical mechanics, however no all positive function would satisfy the conditions above and leave  $\Psi(\mathbf{q})$  simple.
2. The Wigner function only gives quasi-probability values which can be accurately defined to greater resolution than true probability values. Therefore any behaviour in quasi-probability smaller than  $\hbar^N$  will not be a good representation of true probability.

It has also been shown analytically(24) that, in the classical limit, the Wigner function of an integrable system reduces to a delta function following the classical torus. This provides strong evidence that the Wigner function is a valid analogue of an integrable classical phase space. Many numerical comparisons have also been performed (25)(26) in which Wigner functions for non-integrable systems have been compared to both classical phase spaces and Husimi functions, which are another candidate for quantum phase space plots. In all of these studies it has been found that quantum Wigner functions show a striking similarity to classical phase spaces. The work performed by the Theory Group at the University of Nottingham has also compared Wigner functions to semi-classical Poincaré sections (27)(28) and this has shown good correspondence between the two. Chapter 5 shows some of these comparisons.

Therefore the Wigner function will be used in this work to describe the phase space of the quantum system. However, this phase space will generally consist of more than two dimensions so it will be necessary to apply some constraints to produce a 2D plot. These conditions should be chosen to produce a plot analogous to the semiclassical Poincaré sections. It is difficult to define a

---

stroboscopic Wigner function so a new constraint must be chosen to construct the 2D sections. We will choose this to be  $p_x = 0$  because it corresponds to a simple slice of phase space and to when the electron is at the bottom of the miniband. So, to compare Wigner functions to Poincaré sections, it will be necessary to construct Poincaré sections with  $p_x = 0$  rather than at strobed time intervals.

## 2.9 Summary

This chapter has introduced the concept of chaos, which is crucial for understanding the superlattice systems considered in this thesis because the Hamiltonian 2.18 will potentially display chaotic behaviour. However, more importantly, this chapter has developed tools for looking at the phase space of the system which will give a more detailed insight into the system's dynamics. The classical and quantum phase spaces can be compared through Poincaré sections and 2D projections of quantum Wigner functions. In a similar way, the classical and quantum real space behaviours can be compared by examining classical electron trajectories and quantum electron probability densities.

### 3. SEMICLASSICAL ANALYSIS OF SUPERLATTICE NU2293

### 3.1 Introduction

Chapter 1 formulated a semiclassical model describing the behaviour of an electron in a superlattice system with an electric field,  $F$ , applied antiparallel to the superlattice axis and a magnetic field,  $B$ , applied at an angle  $\theta$  to the superlattice axis. Here we use this model to analyse superlattice NU2293 (described in section 1.4.1). The first half of this chapter uses Hamiltonian 1.51 to model the superlattice as an infinite structure and will investigate the behaviour of a single electron. We show electron orbits in both real and phase space and also investigate how the electron drift-velocity varies as a function of electric field. The second half of the chapter will use these drift-velocity results to model the superlattice as a finite system within an electrical circuit. We investigate the variation in current as a function of applied voltage and the change in electric field and charge carrier density across the superlattice. Finally, we compare our numerical results to experimental results taken for the real NU2293 superlattice system.

### 3.2 Motion through the Infinite Superlattice

An electron's motion through our infinite superlattice system with applied electric and tilted magnetic fields (section 1.3) can be determined from its equations of motion:

$$\dot{x} = \sum_{n=1}^{\infty} \frac{nda_n}{\hbar} \sin\left(\frac{ndp_x}{\hbar}\right) \quad (3.1)$$

$$\dot{z} = \frac{p_z}{m^*} \quad (3.2)$$

$$p_x = p_x(0) + eFt - (p_z - p_z(0)) \tan \theta \quad (3.3)$$

$$\begin{aligned} \ddot{p}_z = & -\omega_C^2 \cos^2 \theta p_z - \frac{m^* \Delta \omega_C^2 \cos \theta \sin \theta d}{2\hbar} \\ & \times \sum_{n=1}^{\infty} na_n \sin \left[ \frac{nd}{\hbar} (p_{x_0} + eFt - (p_z - p_{z_0}) \tan \theta) \right]. \end{aligned} \quad (3.4)$$

where the variables are specified in chapter 1. In this thesis, a fourth-order Runge-Kutta method(29) is used to integrate these equations to determine the evolution of  $x$ ,  $z$ ,  $p_z$  and  $\dot{p}_z$  with time.

When the magnetic field is applied antiparallel to the electric field ( $\theta = 0^\circ$ ), the Bloch and cyclotron oscillations are orthogonal. This causes equation 3.4, which describes  $p_z$ , to reduce to that of a simple harmonic oscillator (SHO):

$$\ddot{p}_z + \omega_C^2 \cos^2 \theta p_z = 0. \quad (3.5)$$

Consequently, electron motion along the  $x$  and  $z$  directions is separable and corresponds to periodic Bloch and cyclotron oscillations respectively. Figure 3.1 shows sample electron trajectories for  $\theta = 0^\circ$ . Although these trajectories are stable, their precise form depends on the initial momentum,  $p_z(t = 0)$ , which, for  $\theta = 0^\circ$ , uniquely determines motion in the  $yz$  plane. Figure 3.1(a) shows that, when  $\omega_B = \omega_C$ , the resulting motion is periodic and takes the form of an ellipse whose shape depends on the initial momentum of the electron. Figures 3.1(b-d) show electron orbits for  $\omega_B \neq \omega_C$ , which are quasi-periodic. These are the two types of behaviour characteristic of an integrable system, as described in chapter 2. It should be noted that the system is only integrable when  $\theta = 0^\circ$ .

The ratio between the Bloch frequency and  $x$  component of the cyclotron frequency, corresponding to the  $x$ -component of magnetic field, is denoted by  $r$ :

$$r = \frac{\omega_B}{\omega_C \cos \theta} = \frac{Fdm^*}{\hbar B \cos \theta}. \quad (3.6)$$

For  $\theta = 0^\circ$ , an electron's maximum displacement along its orbit in  $x$ ,  $\Delta x_{orbit}$ , is inversely proportional to  $F$ , and hence  $r$ . This proportionality can be seen by comparing figure 3.1(a-d), as  $r$  and thus  $F$  decrease the orbits are more extended. Physically, it occurs because decreasing  $F$  decreases the Bloch frequency and the electron can travel for a longer time before it undergoes Bragg reflection.

When examining the electron behaviour for  $\theta \neq 0^\circ$ , there are a number of parameters that can be varied. These parameters include the tilt angle,  $\theta$ , and magnitude,  $B$ , of the magnetic field as well as the frequency ratio,  $r$ , which defines the electric field magnitude. Figure 3.2 shows the parameter space ( $F, B$ ) for an arbitrary  $\theta > 0$  indicating the points of interest that will be studied in detail. We will also investigate the effects of varying  $\theta$ .

### 3.2.1 Effect of $r$ on Electron Orbits

Figure 3.3 shows the effects of keeping  $B$  and  $\theta$  constant but varying  $r$ . These plots correspond to the circular points on figure 3.2. At low electric field,  $r = 0.1$ , the electron orbit resembles those for  $\theta = 0^\circ$  (fig. 3.1) but aligned along the direction of the magnetic field. The length of this orbit along  $x$ ,  $\Delta x_{orbit}$ , is determined by the size of a single Bloch oscillation. Therefore, at low  $F$ , the change in electron trajectory as  $\theta$  changes from  $0^\circ$  to  $\theta \neq 0^\circ$  can be viewed as a perturbation along the direction of the angled magnetic field.

When  $r$  is an integer meaning that the Bloch and cyclotron frequencies are resonant, we find (fig. 3.3) that the electron performs small local oscillations which have a general drift in the  $x$  direction. As  $x$  increases these local oscillations have a larger amplitude along  $z$  and a smaller amplitude along  $x$ . At some

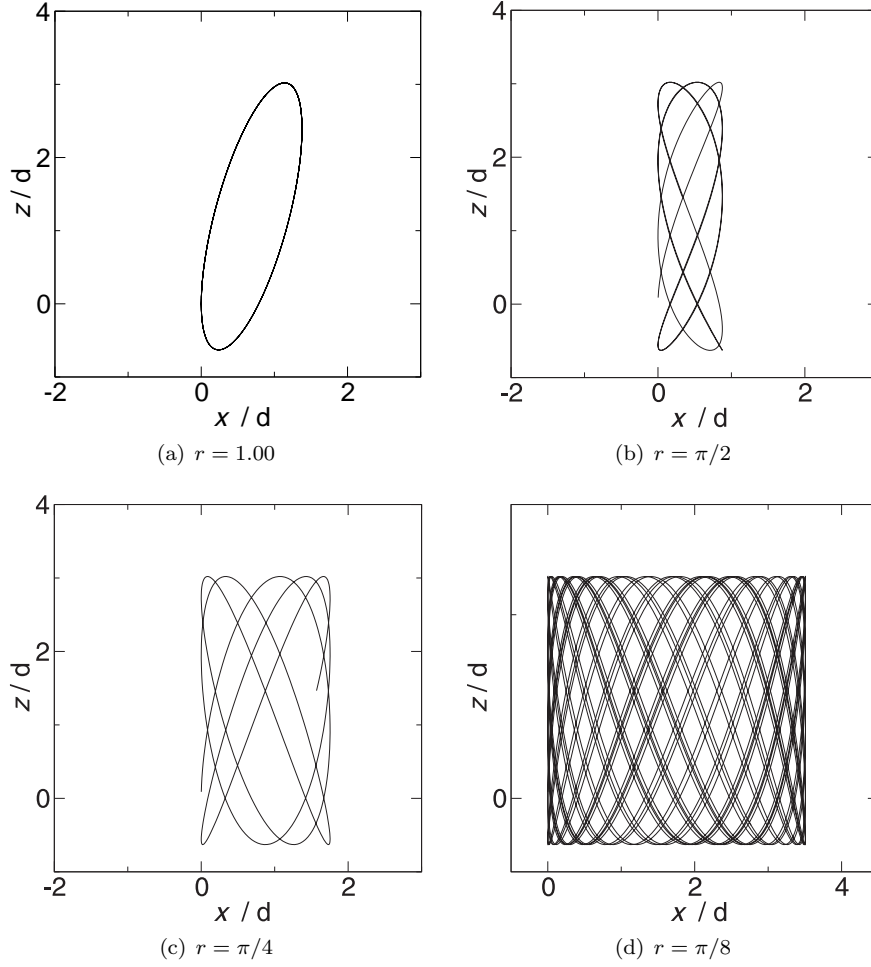


Fig. 3.1: Sample electron trajectories for a range of different ratios between the Bloch and cyclotron oscillations,  $r$ . In all cases,  $B = 11$  T,  $\theta = 0^\circ$  and the time of flight is 1 ps for (a)-(c) and 10 ps for (d). The size of the Bloch oscillations in the  $x$ -direction increases as  $r$ , and thus  $F$ , decreases. (a) is periodic and (c-d) are quasi-periodic and these types of motion are characteristic of an integrable system.

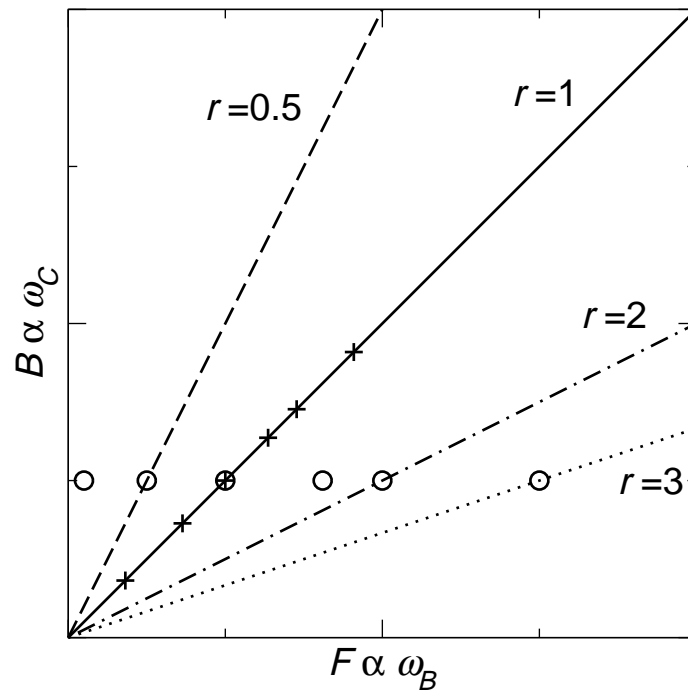


Fig. 3.2: Key points in the parameter space  $(F, B)$  which is a plane of fixed  $\theta$  in the full  $(F, B, \theta)$  parameter space. For a fixed  $r$ , the coordinates  $(F, B)$  lie on lines whose gradient is  $\propto \frac{1}{r}$ . These lines are shown for  $r = 0.5, 1, 2, 3$  as indicated. The effects of varying  $F \propto r$  at fixed  $B$  (circles) and varying  $B$  at fixed  $r$  ( $+$ ) will be investigated in figures 3.3 and 3.7 respectively.

critical  $x$  value, the  $x$  drift reverses direction leading to a quasi-periodic orbit and we find that  $\Delta x_{orbit}$  is much larger than the extent of a single Bloch oscillation. This complex behaviour can no longer be explained by treating  $\mathbf{B}$  as a perturbation and will be discussed using phase space plots in section 3.2.4. The electron orbits are similar for both  $r = 1$  and  $r = 2$  (fig. 3.3) although moving to these higher integer values of  $r$  increases the amplitude of the oscillations in the  $z$  direction for a given value of  $x$  ( $\Delta z_{orbit}(x)$ ) and changes the form of the high frequency oscillations. The orbit for  $r \geq 3$  is highly localised.

The  $r = 0.5$  subharmonic resonance electron orbit is also extended but only to half the extent as that of  $r = 1$  or 2. When  $r$  takes the irrational value of  $\frac{1+\sqrt{5}}{2}$  the orbit is highly localised compared to orbits for rational values of  $r$ .

The reason for these extended electron orbits will be discussed in section 3.2.4 by considering the electron phase space.

### 3.2.2 Effect of $\theta$ on Electron Orbits

Figure 3.4 shows the effect of increasing the magnetic field tilt angle,  $\theta$ , on electron orbits for  $B = 11$  T and  $r = 1$  or  $r = 2$ . Figures 3.4(a,c,e) clearly show that, for  $r = 1$ ,  $\Delta x_{orbit}$  decreases with increasing  $\theta$ . Figures 3.4(b) and 3.4(d) show this same trend for  $r = 2$  but when  $\theta$  is increased to  $60^\circ$  (fig. 3.4(f))  $\Delta x_{orbit}$  increases again. A closer look at figure 3.4(f) reveals that the orbit consists of two distinct regions: the orbit is significantly denser when  $x \lesssim 5d$ . The less dense region does not appear at lower  $\theta$  and is the cause of the additional  $\Delta x_{orbit}$  extension at  $\theta = 60^\circ$ .

Figure 3.5 shows the effect of increasing  $\theta$  on the electron orbit at  $r = 2$  on a single set of axes for clarity. There is a general decrease in  $\Delta x_{orbit}$  between  $\theta = 15^\circ$  and  $\theta = 45^\circ$  but then an increase from  $\theta = 45^\circ$  to  $\theta = 75^\circ$ . This increase occurs because the electron can “break out” of the previous limit on  $\Delta x_{orbit}$  and enter a new region of motion.

The electron orbits also change with  $\theta$  when  $r$  is not an integer. Figure 3.6 shows electron orbits for  $r = 0.5$  (fig. 3.6(a,b)) and  $r = \frac{1+\sqrt{5}}{2}$  (fig. 3.6(c,d)) for both  $\theta = 30^\circ$  and  $\theta = 60^\circ$ . These orbits clearly show that  $\Delta x_{orbit}$  is greater for the higher magnetic field tilt angle. For both  $r = 0.5$  and  $r = \frac{1+\sqrt{5}}{2}$ , increasing the magnetic field tilt angle changes the trajectories from regular to non-regular and for  $r = 0.5$  at  $\theta = 60^\circ$  there are two distinct regions as occurred for  $r = 2$  at  $\theta = 60^\circ$  (figure 3.4(f)).

Again, all the behaviour noted in this section will be discussed via an examination of the electron phase space in section 3.2.4.

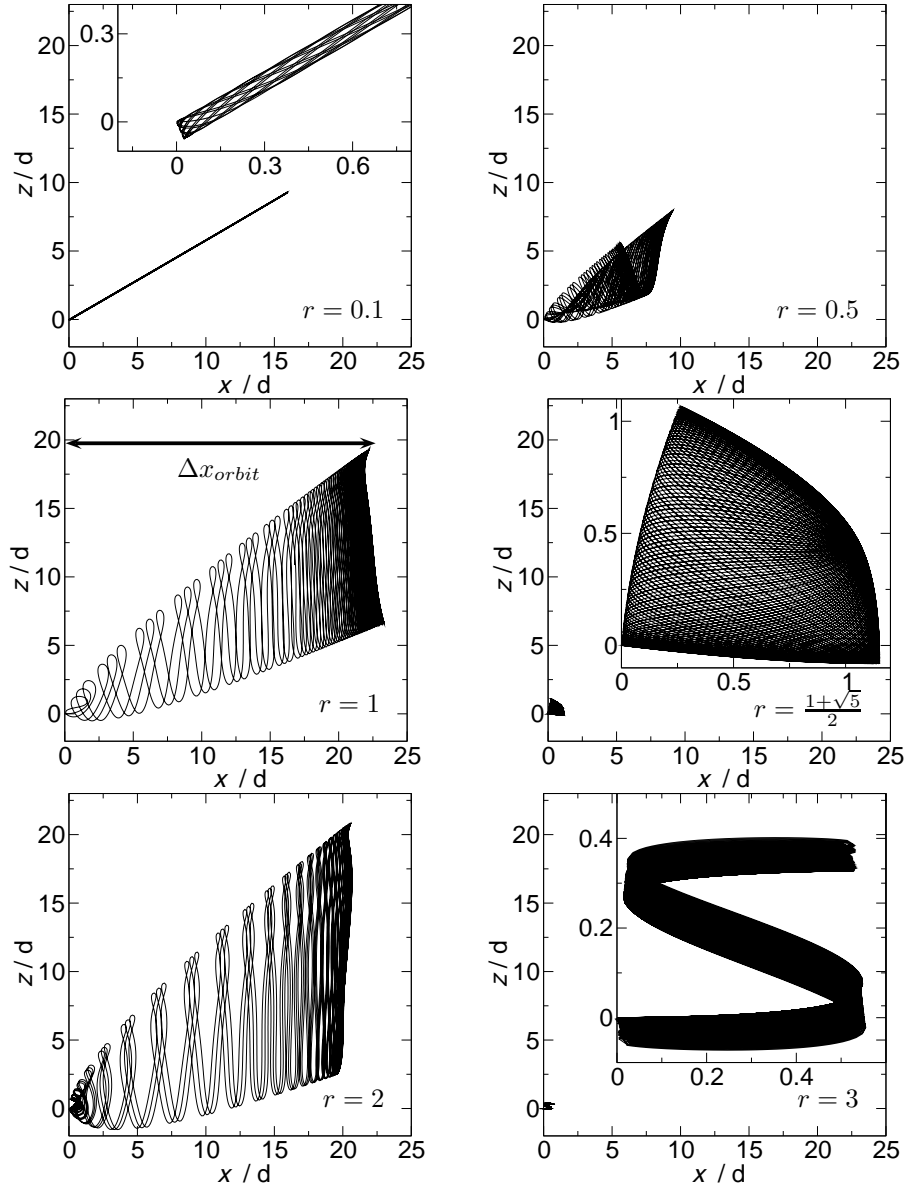


Fig. 3.3: Electron trajectories calculated over 20 ps starting from rest for  $\theta = 30^\circ$  and  $B = 11$  T. The electric field is chosen such that  $r$  is equal to the values shown which correspond to the circles in figure 3.2. The plot for  $r = 1$  indicates  $\Delta x_{orbit}$ , the width of the electron orbit in the  $x$ -direction.

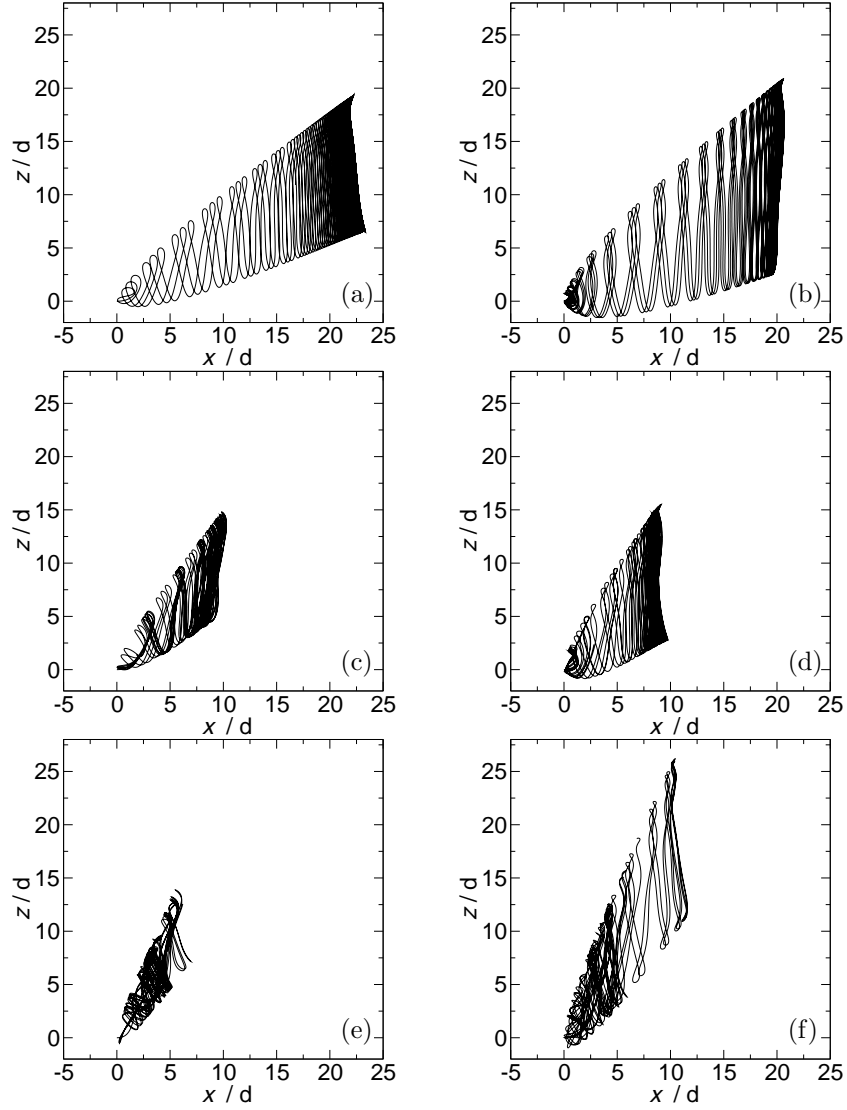


Fig. 3.4: Electron orbits calculated over 20 ps starting from rest with an applied magnetic field of  $B = 11$  T. (a,b)  $\theta = 30^\circ$ , (c,d)  $\theta = 45^\circ$  and (e,f)  $\theta = 60^\circ$ .  $r = 1$  for the left hand column (a,c,e) and  $r = 2$  for the right hand column (b,d,f).

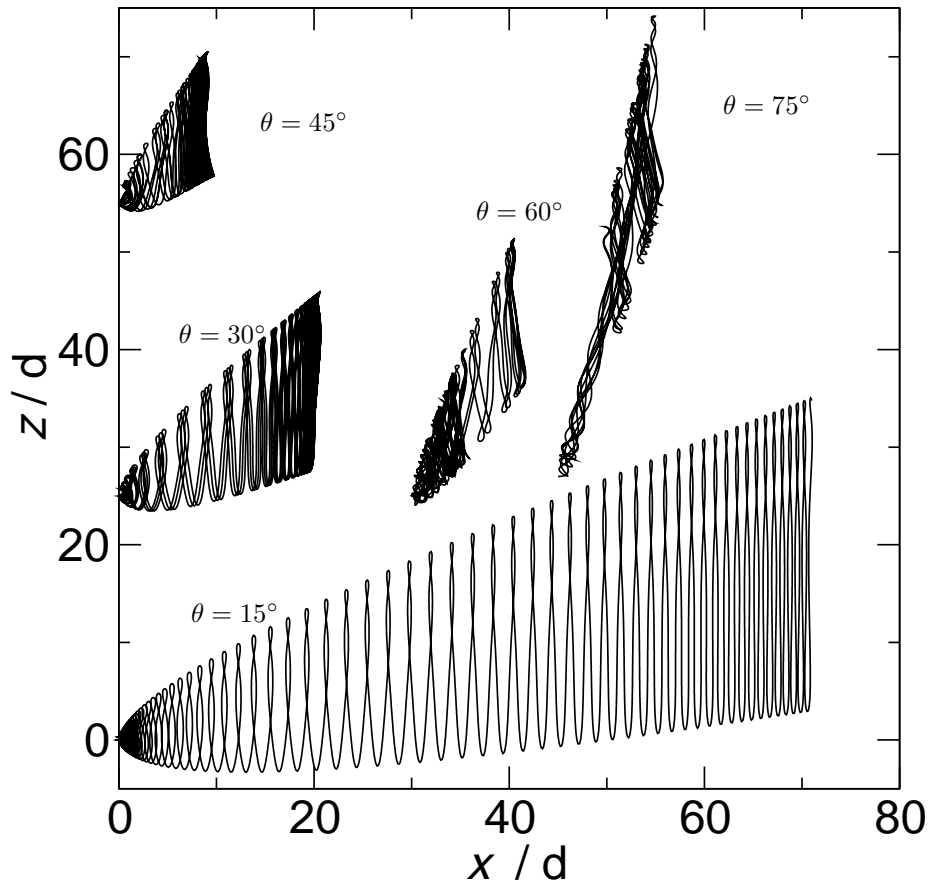


Fig. 3.5: Variation in electron orbit with  $\theta$  values as specified. These orbits are shown on the same scale and calculated over 20 ps starting from rest with  $B = 11$  T and  $r = 2$ .  $\Delta x_{orbit}$  decreases with increasing  $\theta$  from  $15^\circ$  to  $45^\circ$  but then increases with increasing  $\theta$  up to  $75^\circ$ .

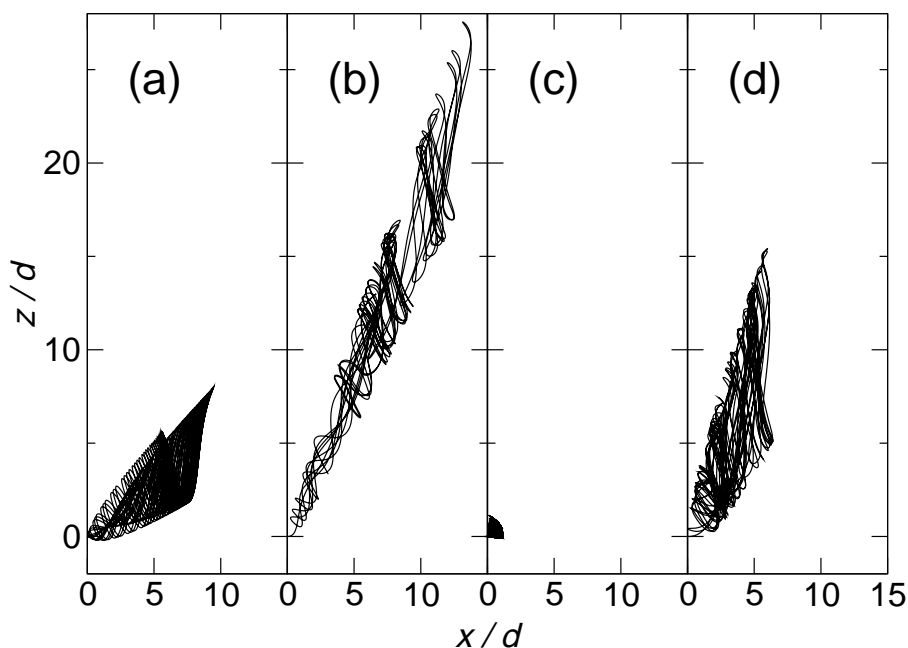


Fig. 3.6: Electron orbits calculated over 20 ps starting from rest with an applied magnetic field of  $B = 11$  T. (a,c)  $\theta = 30^\circ$  and (b,d)  $\theta = 60^\circ$ . (a,b)  $r = 0.5$  and (c,d)  $r = \frac{1+\sqrt{5}}{2}$ . The increase in the extent of the electron orbits is clearly visible as  $\theta$  is increased to  $60^\circ$ .

### 3.2.3 Effects of $B$ on Electron Orbits

Figure 3.7 shows the effects of increasing  $B$  for  $\theta = 30^\circ$  and  $r = 1$  from (a-f). This figure clearly shows that the electron orbits decrease in extent along both axes as  $B$  is increased. The reasons for this decrease will be examined in the next section which explores the electron's phase space.

### 3.2.4 Phase Space Data

Section 1.3.1 showed that  $p_z$  is the fundamental variable that determines the dynamics of this system. The equation of motion for this variable, equation 3.4, is formally identical to a driven harmonic oscillator (DHO), which was studied analytically for several integer values of  $r$  in section 2.6.1. This work showed that a DHO gives rise to a so-called *stochastic web* in phase space through which an electron can diffuse. This section will show numerical calculations of the stochastic web and also that stochastic web formation is the cause of the extended electron orbits seen in the previous section.

The numerically calculated behaviour of the electron orbits viewed in 2D ( $p_z, q_y = \dot{p}_z / \omega_C \cos \theta$ ) phase space can be compared to the analytical treatment of the DHO (section 2.6.1). To display this phase space, a stroboscopic

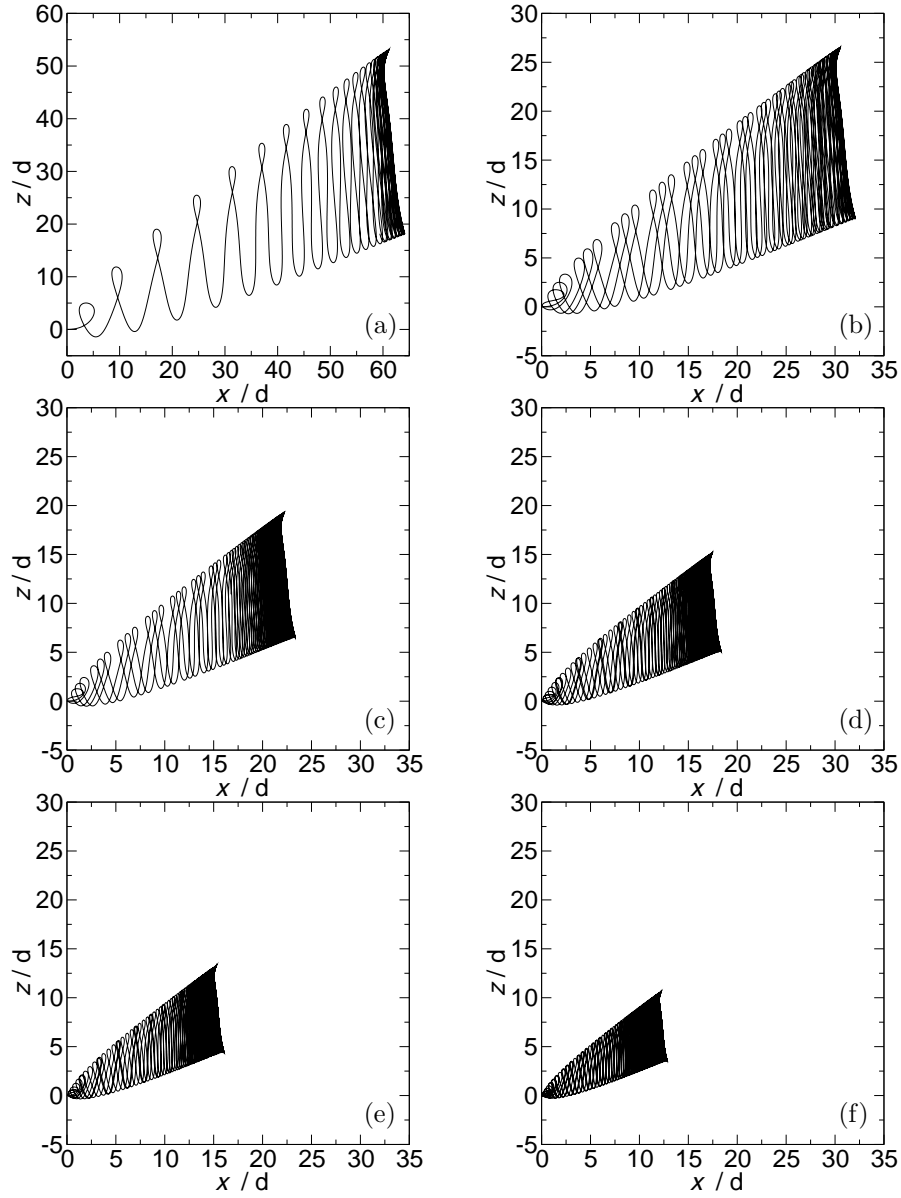


Fig. 3.7: Effect of changing  $B$  in the sequence  $B = 4, 8, 11, 14, 16, 20 \text{ T}$  from (a-f) for  $\theta = 30^\circ$  and  $r = 1$  on electron trajectories calculated over a 20 ps interval starting from rest. Note that the axes on (a) have a different scale to the other figures.

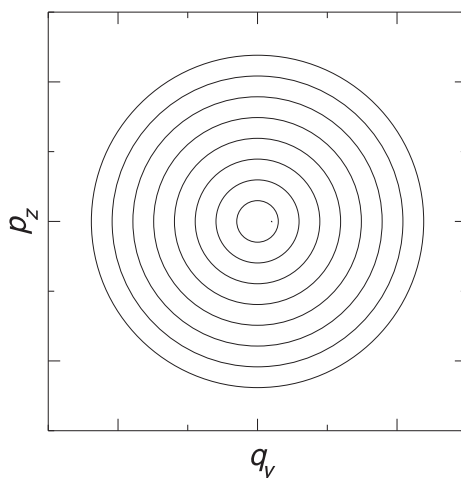


Fig. 3.8: Phase space for  $\theta = 0$  and  $r = 1$ . A full phase space plot rather than a Poincaré section is shown because both types of section will only produce one identical point per oscillation.

Poincaré section will be used, which is formed by plotting points at a time interval of  $\frac{2\pi}{\omega_C \cos \theta}$ . This type of Poincaré section can be directly compared with the analytical expressions for the location of the web filament junctions (eqn. 2.28).

The  $p_z$  and  $q_y$  data required for these Poincaré sections can be determined from equation 3.4 and data over a long time interval is required to produce a well-defined Poincaré section. In addition, multiple initial conditions in  $(p_z, q_y)$  space will be used so that the phase space structure away from the stochastic web can also be seen.

When  $\theta = 0^\circ$  the system is integrable and  $p_z$  behaves as a simple harmonic oscillator as figure 3.8 shows. Consequently, the electron orbits in phase space lie on ellipses (fig. 3.8) whose areas depend on the initial electron energy and these orbits determine the associated regular motion in the  $xz$  plane. Note that figure 3.8 shows continuous time trajectories in phase space rather than a discrete time Poincaré section.

When  $\theta > 0$  and  $r$  is an integer, we expect from section 2.6.1 that the stroboscopic Poincaré sections will reveal a stochastic web consisting of  $2r$  radial filaments and an infinite number of circular filaments. The radii of these circular filaments should be near the zeros of:

$$J_r\left(\rho \frac{d \tan \theta}{\hbar}\right) \quad (3.7)$$

where  $\rho^2 = p_z^2 + \dot{p}_z^2$  and  $J_r$  is the  $r^{\text{th}}$  Bessel function of the first kind. Therefore, the spacing of the circular filaments in the web will increase as  $\theta$  decreases. Also,

for a given  $r$ , the  $2r$  radial filaments should be evenly distributed in angle from the centre of the web. The part of the web extending out to the first circular filament will be referred to as the first ring of the web, the area between the first and second circular filaments as the second ring and so on.

Figures 3.9 and 3.10 show that, when  $r$  is an integer, there exists a stochastic web in phase space through which electrons move chaotically. In the cells of this web there are islands of stability where electrons display regular motion. Figure 3.9 confirms that the number and angular distribution of radial filaments is  $2r$  by plotting stroboscopic Poincaré sections for  $B = 11$  T and  $r = 1, 2, 3, 4$ . The effect of varying  $\theta$  is shown in figure 3.10 which confirms that the circular filaments become more closely spaced as  $\theta$  increases. In addition, the chaotic sea seen at the centre of the stochastic web expands with increasing  $\theta$  and the stochastic filaments also increase in thickness. These effects can be predicted from the Hamiltonian of the system, as briefly mentioned in section 2.6.1. Because of this increase in filament thickness, it is expected that the electron can diffuse further in the radial direction at higher  $\theta$ .

In section 3.2.2 we noted that  $\Delta x_{orbit}$ , the maximum electron displacement along  $x$ , initially decreased with increasing  $\theta$  for  $\theta \leq 45^\circ$  but then increased with increasing  $\theta$  for  $\theta > 45^\circ$  and  $r = 2$ . To understand this behaviour, we plot stroboscopic Poincaré sections and highlight the points corresponding to the first 20 ps of the trajectory starting from rest. Figure 3.11 shows this data for  $B = 11$  T,  $r = 1$  and  $\theta = 15^\circ$  to  $75^\circ$  which corresponds to the real space electron orbits shown in figure 3.5. For  $\theta \leq 45^\circ$  (fig. 3.11(a-c)) electrons starting from rest are confined within the first ring of the stochastic web and the decreasing size radius of this ring leads to the decrease in  $\Delta x_{orbit}$ . When  $\theta$  is increased to  $60^\circ$  (fig. 3.11(d)) an electron starting from rest can explore both the first and part of the second rings of phase space. For  $\theta = 75^\circ$  (fig. 3.11(e)), the first few rings of the web merge because of the thicker stochastic filaments and the electron explores much of the resulting chaotic sea.

Figure 3.11 shows that electrons starting from rest tend to be confined to a circular region of phase space comprising of one or more rings of the stochastic web whose radius varies with  $\theta$ . It is possible to use maximum radius of phase space explored to calculate  $\Delta x_{orbit}$ . More comprehensively, it is possible to determine the outer perimeter of the electron trajectory in the  $xz$  plane of real space using phase space data. Starting from the semiclassical Hamiltonian:

$$H = E(p_x) + \frac{\rho^2}{2m^*} - eFx, \quad (3.8)$$

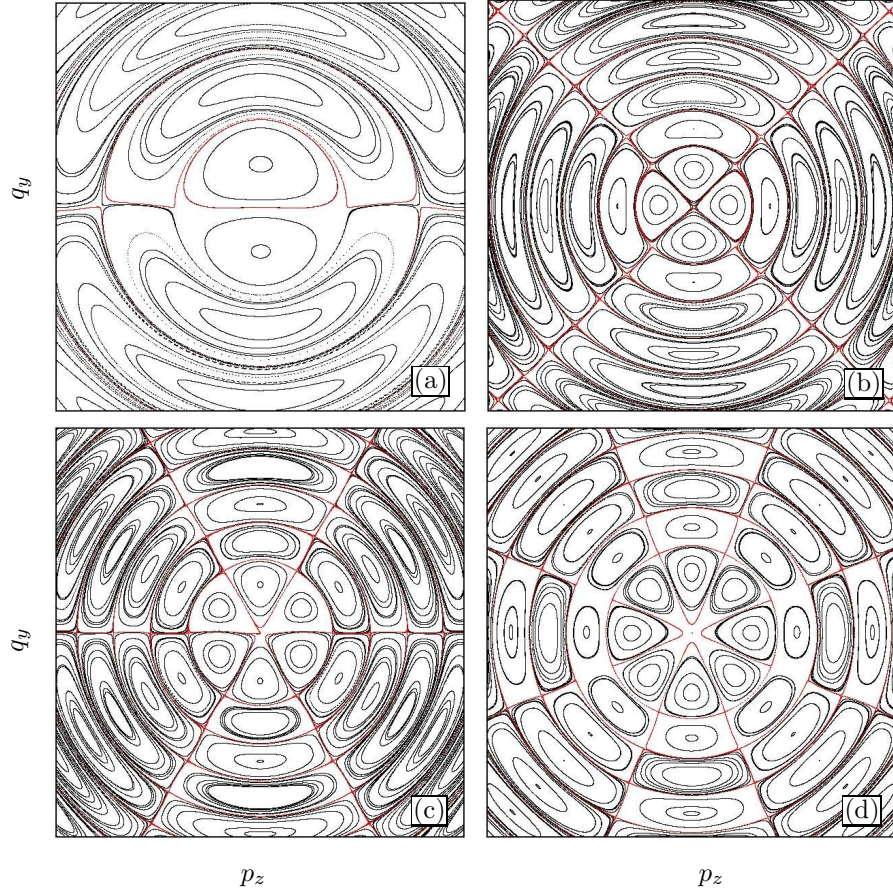


Fig. 3.9: Stroboscopic Poincaré sections calculated for  $\theta = 30^\circ$ ,  $B = 11$  T and (a)  $r = 1$ , (b)  $r = 2$ , (c)  $r = 3$ , and (d)  $r = 4$ . The red points correspond to data from initial conditions located on the web filaments and the black points correspond to initial conditions taken from an evenly spaced grid in the  $(p_z, q_y)$  plane. The axis range is  $(-4 \rightarrow 4) \times 10^{-25}$  kg ms $^{-1}$  for both  $q_y$  and  $p_z$ .

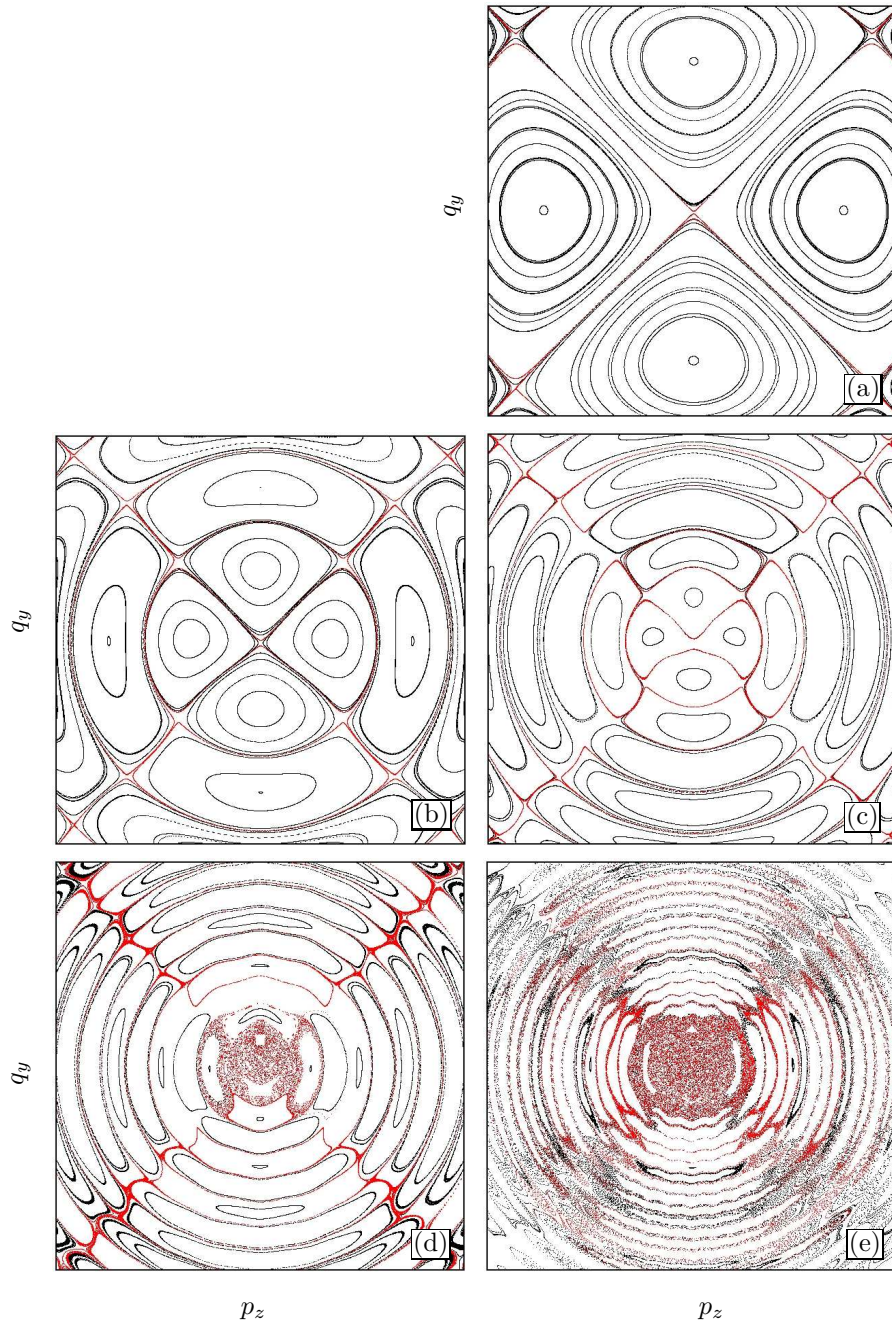


Fig. 3.10: Effect of increasing  $\theta$  on stroboscopic Poincaré sections calculated for  $B = 11$  T,  $r = 2$  and (a)  $\theta = 15^\circ$ , (b)  $\theta = 30^\circ$ , (c)  $\theta = 45^\circ$ , (d)  $\theta = 60^\circ$  (e)  $\theta = 75^\circ$ . The red points correspond to data from initial conditions located on the web filaments and the black points correspond to initial conditions taken from an evenly spaced grid in the  $(p_z, q_y)$  plane. Note that the axis range is  $(-2 \rightarrow 2) \times 10^{-25}$  kg ms $^{-1}$  for both  $q_y$  and  $p_z$ .

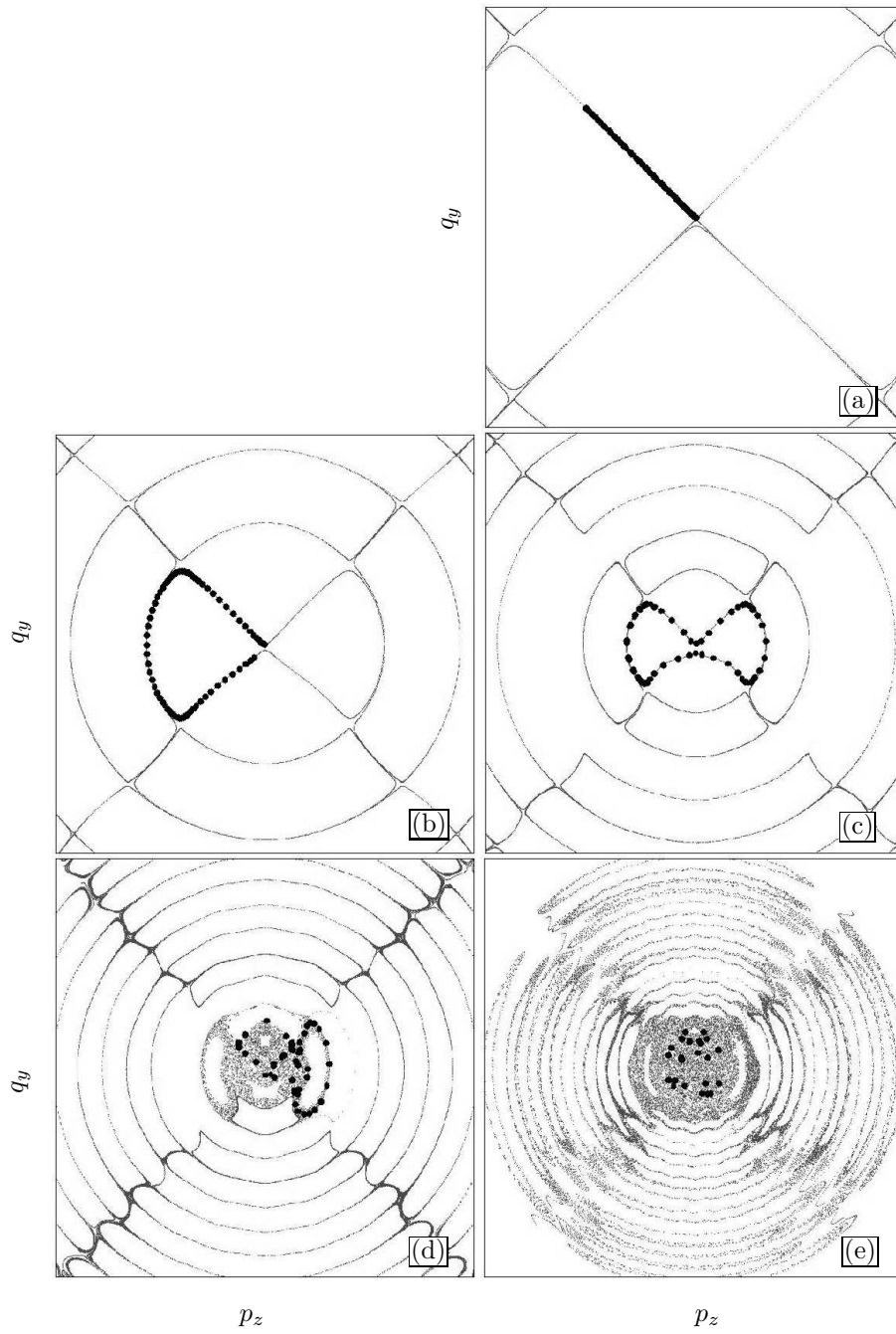


Fig. 3.11: Large black points: stroboscopic Poincaré sections calculated for a single electron starting from rest and travelling for a time interval of 20 ps. The smaller grey points show the form of the full stochastic web for comparison. This data is plotted for  $B = 11$  T,  $r = 2$  and  $\theta$  increasing from  $15^\circ$  to  $75^\circ$  in  $15^\circ$  increments from (a) to (e). Note that the axis range is  $(-2 \rightarrow 2) \times 10^{-25}$  kg ms $^{-1}$  for both  $q_y$  and  $p_z$ .

where  $\rho^2 = p_z^2 + q_y^2$  is the radial position in phase space and rearranging leaves:

$$x = \frac{1}{eF} \left( -H + \frac{\rho^2}{2m^*} + E(p_x) \right) \quad (3.9)$$

where  $H$  is the total electron energy. At  $t = 0$ ,  $\rho = 0$  and  $E(p_x = 0) = 0$  which means that the electron's  $x$ -coordinate at  $t = 0$  is

$$x_{min} = -\frac{H}{eF} \quad (3.10)$$

which is the smallest possible  $x$  value for any  $t$ . If the electron is confined to a circular region of radius  $\rho_{max}$  in the Poincaré section, then the maximum possible  $x$ -coordinate is given by

$$x_{max} \sim -\frac{H}{eF} + \frac{\rho_{max}^2}{2m^*eF}. \quad (3.11)$$

Therefore,

$$\Delta x_{orbit} = x_{max} - x_{min} = \frac{\rho_{max}^2}{2m^*eF}. \quad (3.12)$$

More comprehensively, the boundary of the electron trajectory with a given energy can be calculated from the definition of  $q_y$  (equation 1.48):

$$q_y = p_y = eB(x \sin \theta - z \cos \theta). \quad (3.13)$$

At the perimeter of the electron trajectory  $p_y = 0$  so

$$z = \frac{1}{\cos \theta} \left( -\frac{q_y}{eB} + x \sin \theta \right). \quad (3.14)$$

The minimum and maximum values of  $q_y$  are equal to  $\rho_{max}(x)$  and  $-\rho_{max}(x)$  respectively for a given  $x$  and, from equation 3.11,

$$\rho_{max}(x) = \sqrt{2m^*eF \left( x + \frac{H}{eF} \right)}. \quad (3.15)$$

Therefore, the the electron trajectory must exist within the limits of

$$z = \frac{1}{\cos \theta} \left( \pm \sqrt{\frac{2m^*F}{eB^2} \left( x + \frac{H}{eF} \right)} + x \sin \theta \right) \quad (3.16)$$

Figure 3.12(a) shows that the form of these limits clearly has the same characteristic shape as the electron trajectories seen in sections 3.2.1 to 3.2.3. Figure 3.12(b) overlays a numerical electron trajectory on this boundary which fits exactly within the  $z$  limits. The calculated trajectory overlaps the  $x$  limit slightly

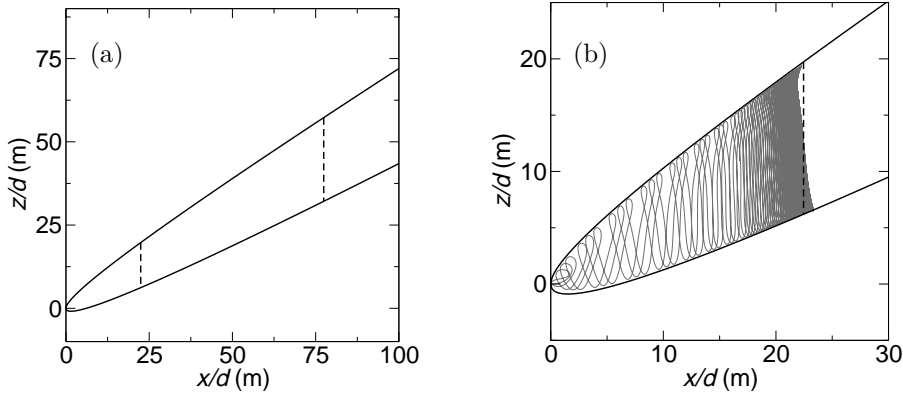


Fig. 3.12: (a) Solid lines show the locus of an electron orbit with  $\theta = 30^\circ$ ,  $B = 11$  T and  $r = 1$  starting from rest as given by equation 3.16. The broken lines show the  $x_{orbit}$  limits assuming the electron stays within the first and second rings of phase space from left to right respectively determined using equation 3.11. (b) Show an enlargement of (a) but also include an electron trajectory overlaid in grey for the same parameters. This trajectory is identical to that shown in figure 3.4(a).

because the analytical calculation of  $\rho_{max}$  doesn't account for the slightly non-circular shape of the circular stochastic web filaments.

Thus, the behaviour of an electron in phase space can be easily used to determine the limits of its orbit in real space. The boundaries given by equation 3.16 can be analytically determined for any set of parameters. However, the right-hand  $x$  limit on the electron trajectory needs information on how far the electron disperses through phase space. Thus a numerical simulation is required to determine the essentially random motion through the stochastic web. We find that radial motion through phase space leads to extended electron orbits which are larger in  $x$  than simple Bloch oscillations would account for.

The analysis in section 2.6.1 only predicts stochastic web formation when  $r$  is an integer so we do not expect such a web to form when this is not the case. Figure 3.13 shows stroboscopic Poincaré sections for  $r = 0.5$  and  $\frac{1+\sqrt{5}}{2}$  and angles of  $\theta = 30^\circ$  and  $60^\circ$  and, as expected, these sections show no stochastic web of the type seen in figure 3.9.

The electron trajectory for  $r = 0.5$  and  $\theta = 30^\circ$  (fig. 3.6(a)) shows that the electron behaves regularly at  $\theta = 30^\circ$  but is more extended along the  $x$ -axis than the  $r = \frac{1+\sqrt{5}}{2}$  trajectory (figure 3.6(c)). The Poincaré sections for these parameters (fig. 3.13(a,c) respectively) explain this difference. When  $r = 0.5$  the Poincaré section (fig. 3.13(a)) shows some of the characteristics of a stochastic web. Like the Poincaré sections when  $r$  is an integer, there are circular filaments enclosing stable islands but there are no radial filaments connecting the circular ones to produce the full web pattern. The extended electron orbit for  $r = 0.5$

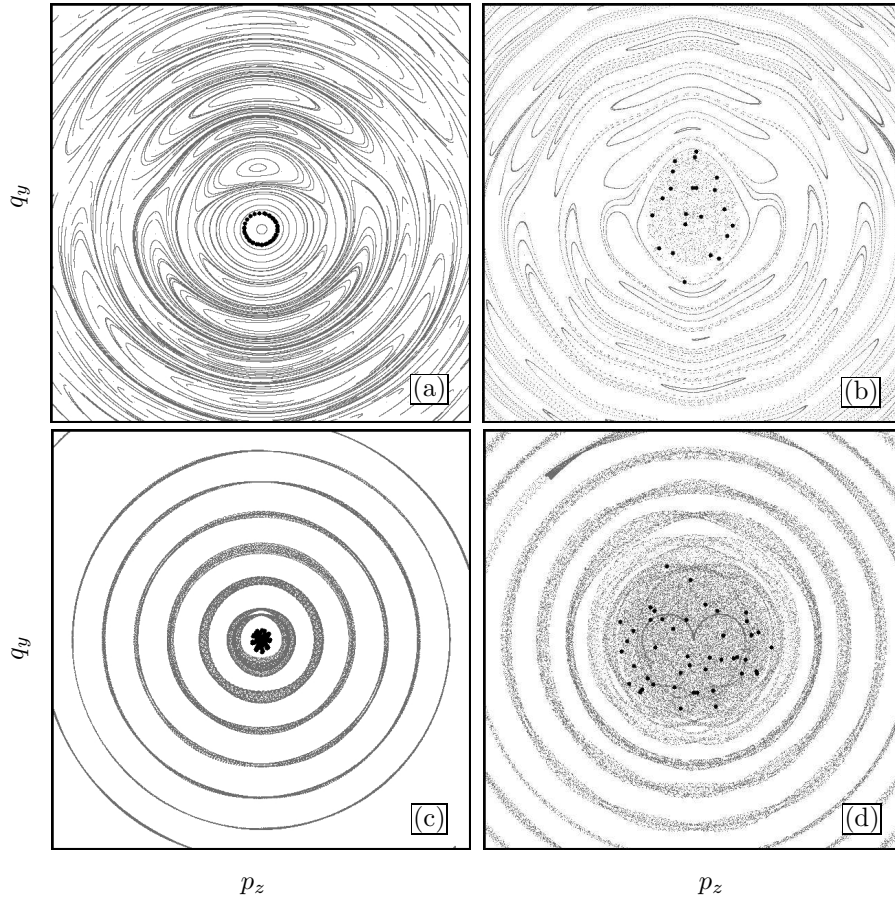


Fig. 3.13: Poincaré sections calculated for  $B = 11$  T and (a,c)  $\theta = 30^\circ$  or (b,d)  $\theta = 60^\circ$ .  $r = 0.5$  for (a,b) and  $r = 0.5(1 + \sqrt{5})$  for (c,d). The large black points show data taken over a time interval of 20 ps for an electron starting from rest. The axis range for  $\theta = 30^\circ$  (a,c) is  $(-2 \rightarrow 2) \times 10^{-25}$  kg ms $^{-1}$  and for  $\theta = 60^\circ$  (b,d) is  $(-1 \rightarrow 1) \times 10^{-25}$  kg ms $^{-1}$  for both  $q_y$  and  $p_z$ .

and  $\theta = 30^\circ$  (fig. 3.6(a)) occurs because the stable island at the centre of phase space is not centred on the origin. Consequently, as the electron moves around the stable island it moves away from  $(p_z, q_y) = (0, 0)$  thus increasing its in-plane momentum and transporting it spatially through the superlattice.

In contrast, the Poincaré section for  $r = \frac{1+\sqrt{5}}{2}$  and  $\theta = 30^\circ$  (figure 3.13(c)) shows trajectories that are regular, centred on the origin and broadly circular with a small radial component. This means that an electron starting from rest does not move far through phase space and its real space  $x$  displacement is correspondingly small. The stroboscopic Poincaré sections do not show this behaviour well and the next section will look at  $p_x = 0$  Poincaré sections which are better for examining non-integer values of  $r$ .

When  $\theta$  is increased to  $60^\circ$  a chaotic sea forms at the centre of phase space for both  $r = 0.5$  and  $\frac{1+\sqrt{5}}{2}$  (fig. 3.13(b,d)). This allows an electron starting from rest to move radially through phase space and gain in-plane momentum leading to extended real space orbits (fig. 3.6(b,d)). However, there is a maximum limit to this radial diffusion because of the finite size of the chaotic sea, which is bounded by stable orbits, so the electron trajectories cannot be infinitely extended along  $x$ .

### 3.2.5 $p_x = 0$ Poincaré Sections

The stroboscopic Poincaré sections are not a good tool for examining phase space when  $r$  takes a non-integer value. They often show closely packed trajectories which give the appearance of chaotic behaviour in a regular system. Figure 3.13(c) is a good example of this and appears to show rings of chaotic behaviour centred on the origin. However, enlarging the Poincaré section or examining the real space electron trajectories shows that it behaves regularly (figure 3.3 for example).

However, we can also examine phase space using a second type of Poincaré section which plots the in-plane momentum components  $(q_y, p_z)$  whenever  $p_x = 0$  rather than at equally spaced time intervals. Figure 3.14 compares the stroboscopic (a) and  $p_x = 0$  (b) Poincaré sections for  $\theta = 45^\circ$ ,  $B = 11$  T and  $r = 2$ . This figure shows that both types of Poincaré section have circular filaments that appear in the same location although the form of the other filaments is different. This second type of Poincaré section has a gap at  $q_y = eF/\omega_C \sin \theta$  because the electron would be stationary at this point since both  $p_x = 0$  and  $\dot{p}_x = 0$  (see equation 1.58).

Figure 3.15 shows this second type ( $p_x = 0$ ) of Poincaré section for same non-integer  $r$  parameters shown in figure 3.13 using the stroboscopic Poincaré sections. For  $r = 0.5$  both types of Poincaré section (figs. 3.13(a,b) and 3.15(a,b))

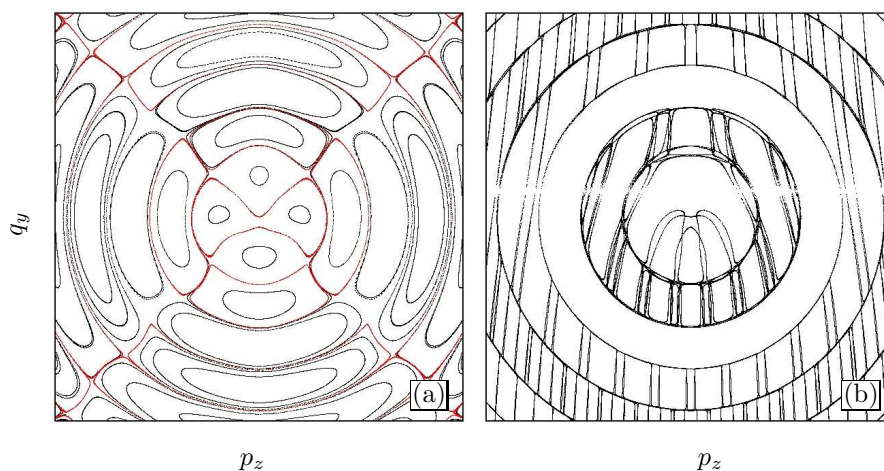


Fig. 3.14: Comparison of stroboscopic (a) and  $p_x = 0$  (b) types of Poincaré section for  $\theta = 45^\circ$ ,  $B = 11$  T and  $r = 2$ . The axis range is  $(-2 \rightarrow 2) \times 10^{-25}$  kg ms $^{-1}$  for both  $q_y$  and  $p_z$ .

show the same general behaviour - regular trajectories encircling the origin with smaller stable islands in-between. Both types of Poincaré section show stable behaviour for  $\theta = 30^\circ$  and a chaotic sea surrounded by stable trajectories for  $\theta = 60^\circ$ .

In contrast, the two types of Poincaré section show different behaviour when  $r = \frac{1+\sqrt{5}}{2}$  (figs. 3.13(c,d) and 3.15(c,d)). As noted previously, the stroboscopic sections appear to show chaotic behaviour even when  $\theta = 30^\circ$  (fig. 3.15(c)) but each of these rings actually consisted of a closely packed stable trajectory and is therefore an artifact of the stroboscopic Poincaré section. The  $p_x = 0$  Poincaré section show these stable trajectories clearly (fig. 3.15(c)) and is therefore a better choice for displaying the phase space of systems with non-integer values of  $r$ . When  $\theta = 60^\circ$  the situation is similar and the Poincaré section clearly consists of a central chaotic sea surrounded by regular trajectories.

Figure 3.16 shows what happens when the system is shifted off resonance to  $r = 1.01$  for  $B = 11$  T and  $\theta = 30^\circ$  (a) or  $\theta = 60^\circ$  (b). From these Poincaré sections, it is clear that moving the system off resonance destroys the radial stochastic filaments but the structure of the central region is left unchanged. Therefore the system is highly sensitive to the resonance condition  $r$  and shifting it slightly away from an integer value leads to the destruction of the stochastic web.

Figures 3.9 to 3.16 have shown that the appearance of a chaotic sea at the origin of phase space depends on the magnetic field tilt angle  $\theta$  but is independent of  $r$ . However radial filaments, which create a stochastic web, only appear for integer values of  $r$  and their appearance is independent of  $\theta$ .

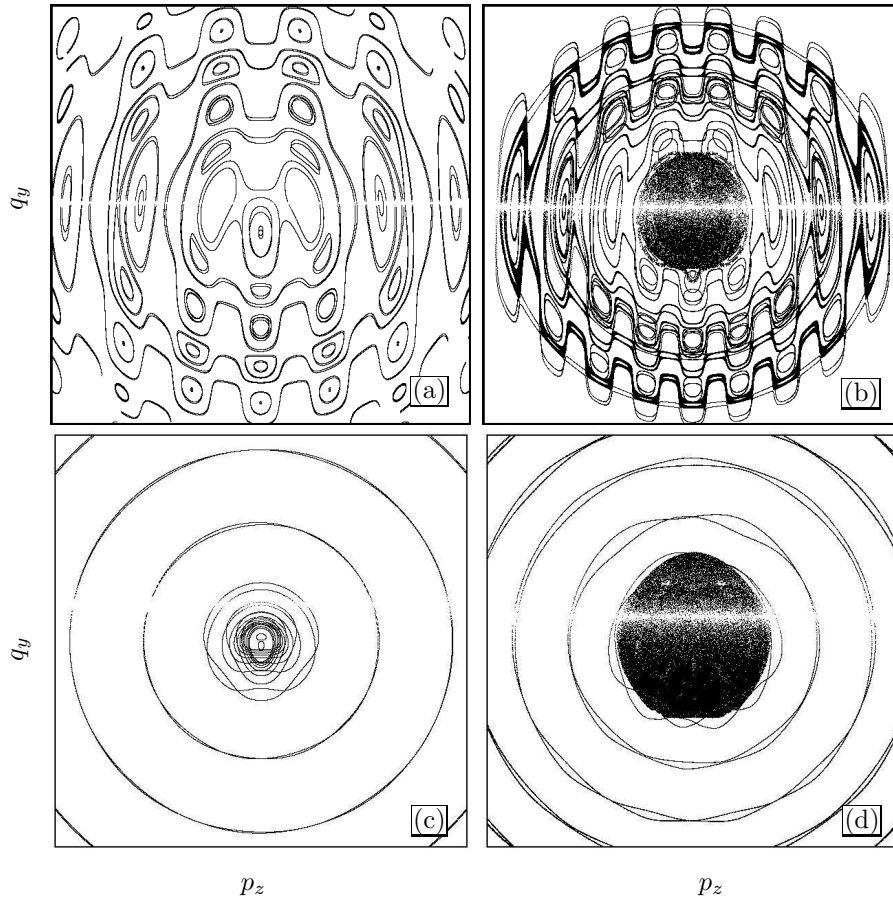


Fig. 3.15:  $p_x = 0$  Poincaré sections for  $B = 11$  T and (a,c)  $\theta = 30^\circ$  or (b,d)  $\theta = 60^\circ$ .  $r = 0.5$  for (a,b) and  $r = 0.5(1 + \sqrt{5})$  for (c,d). The axis range for  $\theta = 30^\circ$  is  $(-2 \rightarrow 2) \times 10^{-25}$  kg ms $^{-1}$  and for  $\theta = 60^\circ$  is  $(-1 \rightarrow 1) \times 10^{-25}$  kg ms $^{-1}$  for both  $q_y$  and  $p_z$ .

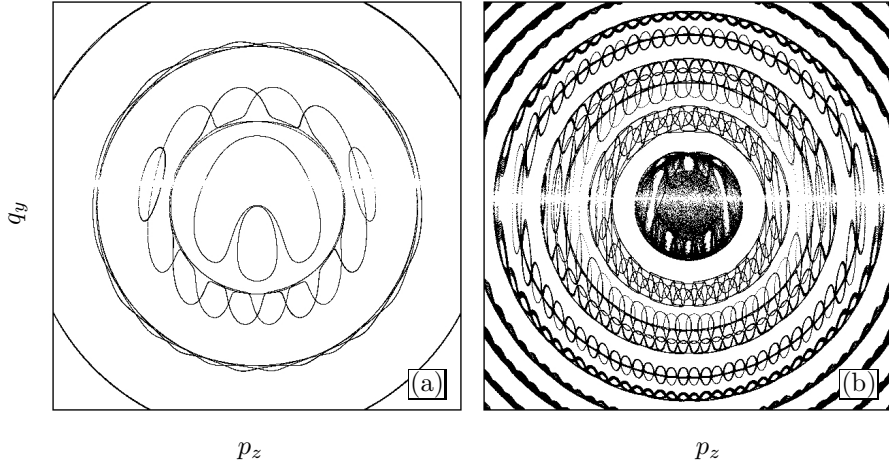


Fig. 3.16:  $p_x = 0$  Poincaré sections for  $B = 11$  T and  $r = 1.01$ . (a) is for  $\theta = 30^\circ$  and (b) for  $\theta = 60^\circ$ . Note that the axis range is  $(-2 \rightarrow 2) \times 10^{-25}$  kg ms $^{-1}$  for both  $q_y$  and  $p_z$ .

### 3.2.6 Frequency Analysis

We can examine the electron's behaviour in frequency space by calculating the Fourier transform:

$$\mathbb{F}(\omega) = \frac{1}{T} \int_0^T [x(t) + z(t)] e^{-i\omega t} dt. \quad (3.17)$$

We take the Fourier transform of  $x + z$  so that the Fourier transform reveals frequencies associated with motion along both  $x$  and  $z$ . The electron is started from rest so that it always falls on the stochastic web (if present), however, this does mean that frequency components due to orbits in stable islands will not be present in the Fourier transform. Figure 3.17 plots  $\mathbb{F}(\omega, B)$  for fixed values of  $\theta$  ((a)  $\theta = 30^\circ$ , (b)  $\theta = 45^\circ$  and (c)  $\theta = 60^\circ$ ) and  $F$ .  $F$  is chosen such that  $r = 1$  at  $B = 10$  T and  $r$  varies linearly with  $1/B$  according to:

$$r = \frac{\omega_B}{\omega_C \cos \theta} = \frac{F dm^*}{\hbar B \cos \theta}. \quad (3.18)$$

In addition, because  $F$  is constant, the Bloch frequency  $\omega_B$  is fixed for all  $B$  and this frequency can be seen as a peak at  $\sim 23 \times 10^{12}$  rad s $^{-1}$  in figure 3.17(a) (and at differing frequencies in figs. 3.17(b,c)). The cyclotron frequency  $\omega_C$  varies linearly with  $B$  and is the origin of the diagonal peak going through  $(\omega, B) = (0, 0)$  in figure 3.17(a).

For  $\theta = 30^\circ$  (figure 3.17(a)), when  $B$  is such that  $r$  takes a non-integer value (e.g.  $B = 7$  T) there are only two main non-zero frequency peaks - corresponding to the Bloch and cyclotron frequencies. But, when  $r = 1$  ( $B = 10$  T), a

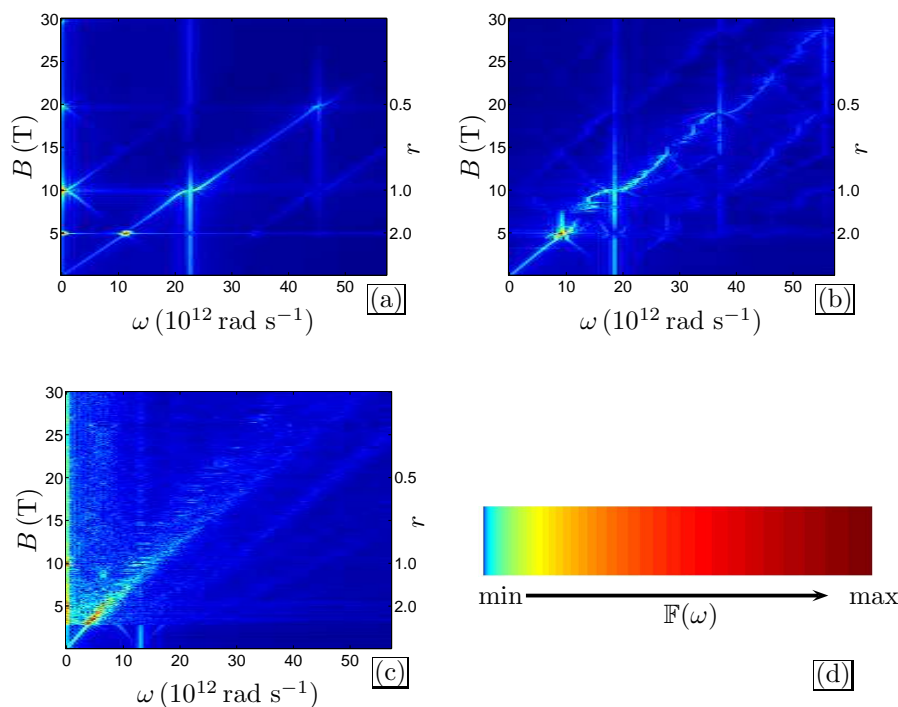


Fig. 3.17: Intensity plot of  $\mathbb{F}(\omega)$  calculated as a function of  $B$  for  $\theta =$  (a)  $30^\circ$ , (b)  $45^\circ$  and (c)  $60^\circ$  with the electron starting from rest. For each angle the electric field,  $F$ , is chosen so that  $r = 1$  when  $B = 10$  T. The colours are determined linearly from the fourth root of  $\mathbb{F}$  so that a wide range of intensities can be clearly seen. (d) shows this choice of colour scaling as a linear colourmap.

stochastic forms through which the electron can diffuse and its behaviour characterised by a wide range of frequencies seen as a horizontal stripe in the Fourier transform. Similar behaviour is seen for  $r = 2$  ( $B = 5$  T). When  $r$  is shifted slightly from an integer there are large peaks in  $\mathbb{F}(\omega)$  because the phase space trajectories are very regular (see figure 3.16(a)). However, when  $r$  is exactly an integer, this regular behaviour is destroyed by appearance of the stochastic web and the peaks in the Fourier transform vanish. When  $r = 0.5$  ( $B = 20$  T), there are a several frequencies present, but a relatively large peak occurs at  $\omega = \omega_C \cos \theta \sim 7.2$  THz because motion is still stable (see figure 3.15(a)).

As  $\theta$  increases (compare figures 3.17(a-c)), the regular features seen at  $\theta = 30^\circ$  are gradually blurred out and, at  $\theta = 60^\circ$ , a wide range of frequencies are present for any value of  $B$ . This effect is caused by the emergence of a chaotic sea for all values of  $r$  which causes the electron trajectories to be irregular with no dominant frequencies.

### 3.2.7 Summary of Single Electron Dynamics Excluding Scattering

The preceding sections on single electron dynamics have investigated electron trajectories in real, frequency and phase space. This analysis has shown a number of trends which depend of the parameters of the fields applied to the infinite NU2293 superlattice.

In general, we find that radial motion from the origin of phase space gives rise to electron orbits which are extended beyond the size of a single Bloch oscillation.

When the resonance parameter  $r = \omega_B/\omega_C \cos \theta$  is an integer, a stochastic web, with  $2r$  radial filaments, is formed in phase space. This web allows electrons to diffuse radially through phase space which results in extended electron orbits in real space. These orbits can theoretically extend an infinite distance in  $x$ , however, in practice, they are limited by the thickness of the stochastic filaments which can impede electron transport or by the mean time before an electron scattering event occurs.

Increasing  $\theta$  decreases the radial separation of the rings in phase space. However, increasing  $\theta$  also thickens the stochastic web so radial diffusion can occur more easily. Therefore, the extension of the electron orbits tends to decrease as  $\theta$  is increased from  $15^\circ$  to  $45^\circ$  where the electrons are confined to a single ring of phase space. At higher  $\theta$  the stochastic filaments are thicker so the electrons can explore more rings of the stochastic web in phase space and the orbits increase in extension with increasing  $\theta$ .

When  $r = 0.5$ , electron orbits are still extended because low energy stable islands exist in phase space which are not centred on the origin. At high  $\theta$  these stable trajectories merge into a chaotic sea, which also allows for radial diffusion. However, there is always a fixed limit on this radial diffusion so electron orbits can never be infinitely extended in  $x$  for  $r = 0.5$ .

If  $r$  takes some irrational non-integer value, such as  $\frac{1+\sqrt{5}}{2}$ , the electron's motion is always stable at high momentum initial conditions (far from  $(q_y = 0, p_z = 0)$ ) but a chaotic sea does form at the centre of phase space for high  $\theta$ . This can lead to extended electron orbits whose spatial width depends on the dimensions of this chaotic sea.

We have therefore found that the formation of a chaotic sea occurs at high  $\theta$  and is independent of  $r$ . Conversely, a stochastic web can occur for any integer value of  $r$  provided  $\theta > 0^\circ$ . Therefore both of these parameters can have a large effect on the motion of an electron through the superlattice system.

## 3.2.8 Drift Velocity vs. Electric Field Data

Solving the equations of motion for a single electron reveal the intricate underlying dynamics of the system. However, equivalent experimental data cannot be obtained for comparison. In general, experiments measure the bulk transport properties of superlattice systems so we need to understand the mean behaviour of electrons in our system. The simplest mean property that can be determined from real space electron motion is drift velocity which will be calculated as a function of electric field,  $v_d(F)$ , at various values of  $\theta$  and  $B$ .

Section 1.2.4 detailed how to calculate electron drift velocity and this requires knowledge of the scattering time of electrons in the superlattice,  $\tau_{SL}$ . This scattering time is mainly determined by semiconductor impurities and interface roughness (see section 1.2.3) but the exact value of  $\tau_{SL}$  also depends on the experimental setup. Thus, we estimate  $\tau_{SL}$  from experimental current voltage characteristics as follows. Figure 3.18 shows an example experimental  $I(V)$  relation for the superlattice with  $\theta = 0^\circ$  which exhibits a linear region at low  $V$  terminating at  $I_L(V_L)$ . This linear region corresponds to ohmic behaviour which occurs when  $\omega_B \tau_{SL} \leq 1$  (see section 1.2.5). Therefore, at  $I_L(V_L)$ , we know that  $\omega_B \tau_{SL} = 1$ . If we further assume that  $F$  is proportional to the voltage dropped over the superlattice<sup>1</sup>,  $V_{SL}$ , then

$$\tau_{SL} = \frac{1}{\omega_B} = \frac{\hbar}{eFd} \simeq \frac{\hbar L_{SL}}{ed V_{SL}} \quad (3.19)$$

where  $L_{SL}$  is the length of the superlattice.  $V_{SL}$ , the voltage dropped over the superlattice, is given by

$$V_{SL} = V_L - I_L R_{ext} \quad (3.20)$$

where  $R_{ext}$  is the resistance of the non-superlattice parts of the circuit. Therefore,  $\tau_{SL}$  can be estimated using the above equations from an experimental  $I(V)$  relation if  $R_{ext}$  is known.

The correction,  $\delta$ , for the elastic-inelastic scattering time model (section 1.2.3) (7)(8) can also be calculated here. We know that  $I_L$  is related to the peak drift-velocity by:

$$I_L \simeq eA\delta v_{d,u} n_{D,ionised} \quad (3.21)$$

where  $A$  is the cross-sectional area of the superlattice,  $v_{d,u}$  is the maximum uncorrected drift velocity at  $\theta = 0$  and  $n_{D,ionised}$  is the total number of ionised donors across the superlattice.  $\delta$  can thus be determined by a simple rearrangement of this equation:

$$\delta \simeq \frac{I_L}{eA v_{d,u} n_{D,ionised}}. \quad (3.22)$$

<sup>1</sup> which is the case in the ohmic region as will be seen in section 3.3

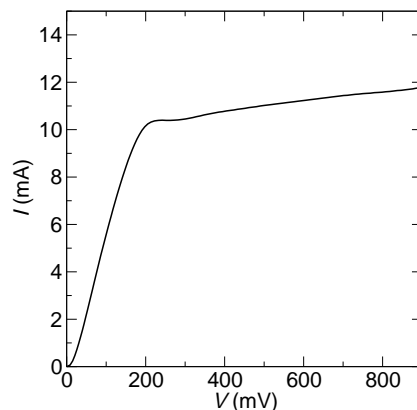


Fig. 3.18: Experimentally measured  $I(V)$  curve taken for the NU2293 superlattice with an 11 T magnetic field aligned parallel to the superlattice direction. Note the approximately linear region below  $V = 200$  mV where the superlattice is behaving ohmically.

For superlattice NU2293, we find that the average scattering time is 175 fs which will be used for all  $B$  and  $\theta$ .  $\delta$  was found to be  $1/8.5$ . Finally, because the drift-velocity is averaged over a range of initial conditions, we need the average temperature of the electrons to set these initial conditions. When the experimental temperature is 4.2 K the thermal energy is  $kT \simeq 0.36$  meV, however, the electrons also receive kinetic energy from the electric field which gives them a maximum kinetic energy of  $\sim 10$  meV. At 300 K the thermal energy contribution is dominant and the electrons receive up to  $\sim 30$  meV of kinetic energy thermally. Therefore there is a transition from voltage heating at 4.2 K to thermal heating at 300 K.

### 3.2.9 $v_d(F)$ Curves for $B = 11$ T at 4.2 K

Plots of  $v_d(F)$  are shown in figure 3.19 for  $B = 11$  T and a range of  $\theta$  values. When  $\theta < 45^\circ$ , the feature occurring at the lowest electric field in the  $v_d(F)$  curves is an Esaki-Tsu-like peak at  $F = 0.45$  MVm $^{-1}$ . These peaks are obscured by other features for  $\theta \geq 45^\circ$ . This initial peak, known as the main superlattice peak, occurs when  $\omega_B \tau_{SL} = 1$  as predicted by Esaki and Tsu (see section 1.2.5). There are also a range of other features, which we now discuss.

Peaks in  $v_d(F)$  other than the main SL peak are clearly visible (fig. 3.19) for  $10^\circ \geq \theta \geq 55^\circ$ . These peaks are caused by the extended electron orbits discussed at the beginning of this chapter and occur at electric fields corresponding to  $r = 0.5, 1, 2, 3, \dots$  as expected. For example, when  $\theta = 45^\circ$ , peaks corresponding to  $r = 0.5, 1, 2$  are clearly visible. These peaks have a finite width so there is still some enhancement of electron velocity when  $r$  takes a value which is close

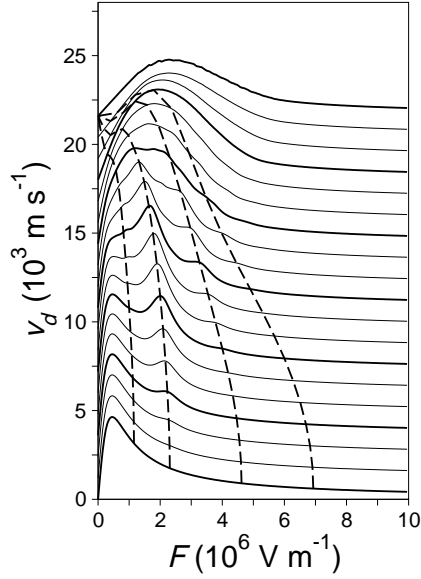


Fig. 3.19: Drift velocity vs. electric field curves calculated at 4.2K for  $B = 11$  T.  $\theta$  increases from  $0^\circ$  to  $90^\circ$  in  $5^\circ$  intervals from bottom to top. Adjacent curves are offset vertically by  $1.2 \times 10^3 \text{ ms}^{-1}$  for clarity. Curves for  $\theta = 0^\circ, 15^\circ, 30^\circ, 45^\circ, 60^\circ, 75^\circ$  and  $90^\circ$  are shown in bold. The dashed lines pass through the points on each curve where  $r = 0.5, 1, 2, 3$  from left to right respectively.

to an integer.

The intensity of the additional or resonance<sup>2</sup> peaks in  $v_d(F)$  increases with increasing  $\theta$  until  $\theta \approx 45^\circ$ , thereafter the main superlattice peak and additional peaks begin to merge into a single peak in  $v_d(F)$ . The  $r = 1$  peak is always the most intense and widest. We will first link some of these observations into the previous discussion of Poincaré sections (section 3.2.4) and then go on to examine  $v_d(F)$  for other values of  $B$ .

The finite width of the resonance peaks in  $v_d(F)$  can be explained by the Poincaré sections in figure 3.16 which show that the central region of the stochastic web still exists when  $r$  is close to an integer value.

In section 3.2.4 we observed that for sufficiently high  $\theta$  a chaotic sea appears in the centre of the Poincaré section independently of  $r$  (e.g. fig. 3.15 shows this for  $\theta = 60^\circ$  and two different  $r$  values). This chaotic sea allows all electrons with initial conditions close to rest to explore a non-zero radial distance in phase space and hence have a large  $\Delta x_{orbit}$ . This observation explains the gradual loss of well-defined  $v_d(F)$  peaks in figure 3.19 with increasing  $\theta$ . At low  $\theta$  the electron orbits can only be extended when  $r \propto F$  takes an integer value so peaks in  $v_d(F)$  occur. However, as  $\theta$  increases the orbits are extended for any all values of

<sup>2</sup> Because the extended electron orbits occur when  $\omega_B$  and  $\omega_C$  are resonant, the additional peaks in  $v_d(F)$  will also be known as *resonance peaks*.

$r \propto F$  and the well defined peaks are lost.

We can also use Poincaré sections to understand the increasing intensity of the  $r = 1$  peaks in  $v_d(F)$  with increasing  $\theta < 45^\circ$  (fig. 3.19). As  $\theta$  increases, the circular stochastic web filaments become more closely spaced and all the stochastic filaments become thicker (see figure 3.10 for example). In section 3.2.4 we showed that these changes lead to a decrease in  $\Delta x_{orbit}$  with increasing  $\theta \leq 45^\circ$  for a single electron starting from rest. However, we now have multiple non-rest initial conditions so as  $\theta$  increases, and a greater proportion of phase space is covered by the stochastic web, more initial conditions fall on the web. Therefore, the increasing intensity of the resonance peaks in  $v_d(F)$  with increasing  $\theta$  is caused by an increasing number of electrons having an extended orbit rather than the same number of electrons having increasingly extended orbits. Finally, it must be remembered that the calculation of  $v_d(F)$  includes an exponential term to approximate scattering which is impossible to consider in this qualitative analysis using Poincaré sections.

### 3.2.10 $v_d(F)$ Curves for other Magnetic Fields and Temperatures

Figure 3.20 shows  $v_d(F)$  curves calculated at 4.2 K for a range of  $\theta$  and  $B$  values. The  $v_d(F)$  curves for each different  $B$  have broadly similar features to those discussed for  $B = 11$  T in the preceding section. Each  $v_d(F)$  curve has a main superlattice peak occurring at the same electric field for a given  $B$ . This peak is visible for  $\theta$  up to at least  $35^\circ$  and is visible for larger  $\theta$  as  $B$  increases. The  $r = 1, 2, \dots$  resonance peaks occur at higher  $F$  as  $B$  increases which is a simple consequence of the ratio:

$$r = \frac{\omega_B}{\omega_C \cos \theta} = \frac{Fdm^*}{\hbar B \cos \theta}. \quad (3.23)$$

At low  $B$  the resonance peaks occur at lower  $F$  and are less well defined because they overlap with the main superlattice peak. The  $r > 1$  resonance peaks become larger as  $B$  increases. Both of these effects can be seen more clearly in figure 3.21 which shows  $v_d(F)$  for  $\theta = 45^\circ$  for a range of  $B$  values. It is not immediately obvious why the peak intensity increases with increasing magnetic field because the extended electron orbits decrease in size with increasing  $B$  (fig. 3.7). To explain this observation we can look at the ratio:

$$\gamma = \frac{\Delta x_{orbit}(r = 1)}{\Delta x_{orbit}(r = \frac{1+\sqrt{5}}{2})} \quad (3.24)$$

for electron orbits starting from rest and travelling for a time of  $\tau_{SL}$ . This ratio incorporates two new factors. Firstly, it considers the proportional extension of

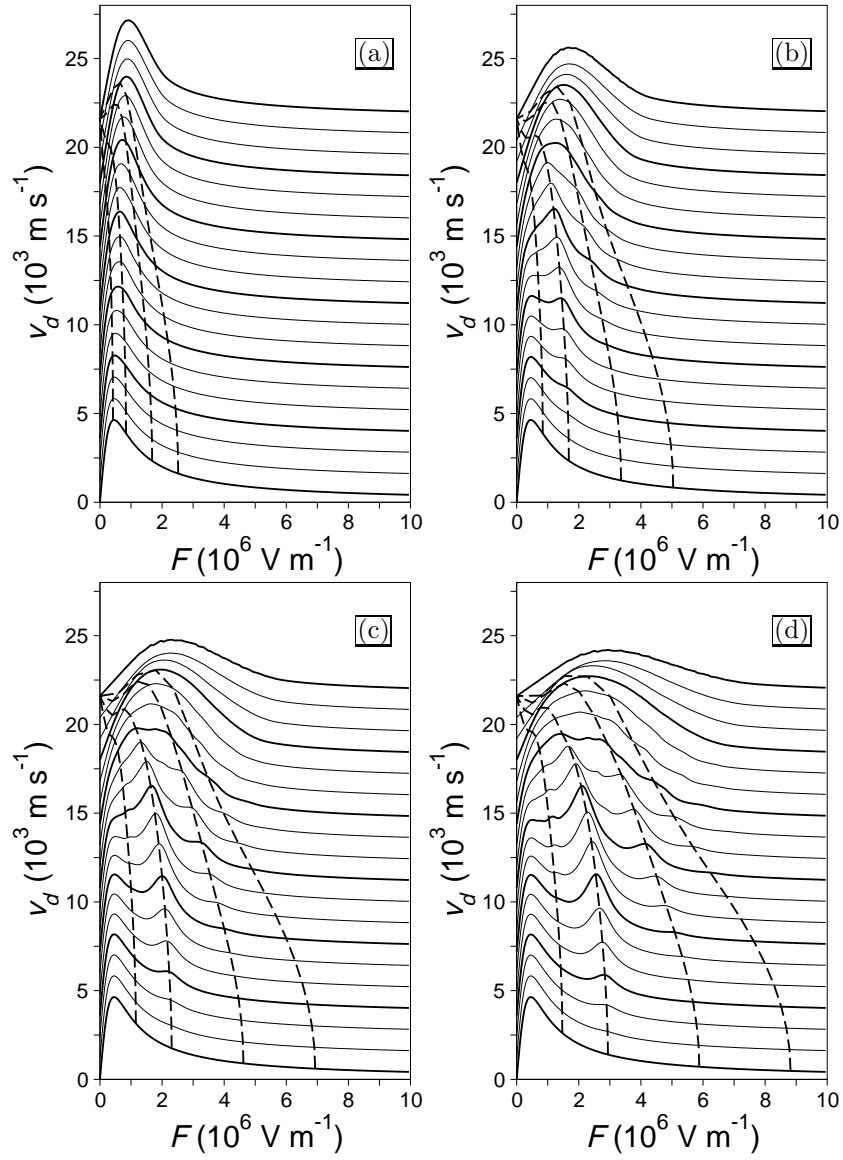
the electron orbits rather than the absolute extension. Secondly, it calculates the maximum extension over a time of  $\tau_{SL}$  because the electron might not reach its maximum displacement before a scattering event occurs. Figure 3.22 shows the change in  $\gamma$  with increasing  $B$  and this data shows that the resonant electron orbits are progressively extended over the off-resonance orbits as  $B$  increases. Although the results of this simple model correlate with the  $v_d(F)$  results,  $\gamma$  ignores all the non-rest initial conditions that had a large effect on  $v_d(F)$  for changing  $\theta$ .

We can also calculate  $v_d(F)$  curves for the superlattice system at room temperature by changing the initial electron momenta which simply involves extending the spread of initial conditions in equation 1.37 by increasing  $E_{max}$  from 10 meV to 30 meV. Figure 3.23 shows  $v_d(F)$  data calculated at 300 K for (a)  $B = 11$  T and (b)  $B = 14$  T (comparable to figure 3.20(c-d) at 4.2 K). All of the parameters affecting  $r$  are independent of temperature so the only possible changes should be in the intensities of the resonance and main superlattice peaks. In general, we find that for the higher temperature, all the peaks decrease in intensity and the resonance peaks tend to be wider and so appear less well defined. The  $v_d(F)$  curves provide the simplest measure of the effects of changing system temperature, which primarily influences the distribution of initial electron velocities since scattering time is limited by elastic scattering and is therefore insensitive to temperature. Because temperature has no effect on the Poincaré sections, it is difficult to account for these results in any meaningful way.

In summary, the extended electron motion discussed at the start of the chapter gives rise to a series of additional resonant peaks appearing in  $v_d(F)$ . These peaks occur for characteristic values of  $F$  which correspond to integer values of  $r$ . Increasing  $B$  increases the size of these peaks, which also depends on  $\theta$ . The second half of this chapter will use these  $v_d(F)$  curves to help model the bulk behaviour of an experimentally realised finite superlattice system.

### 3.3 Transport through a Finite Superlattice

The  $v_d(F)$  curves from the previous section can be used as the basis for determining the current voltage,  $I(V)$ , characteristics of the system. To do this, we divide the superlattice into a number of slices and self-consistently solve Poisson's and the current continuity equations as detailed in section 1.5. The set of equations obtained is highly non-linear and we solve it using a sequential quadratic programming algorithm such as (30). As well as determining  $I(V)$ , the drift-diffusion equations also determine the electric field and charge density variation across the superlattice system.



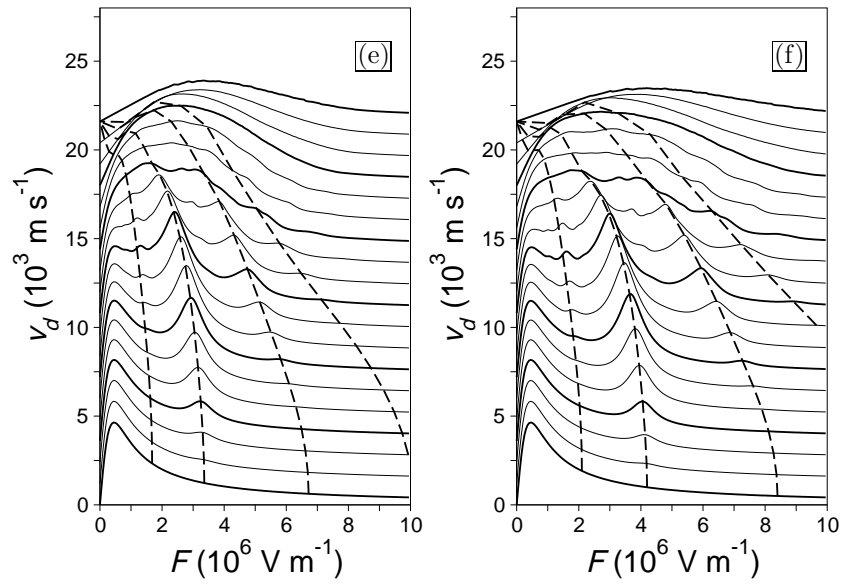


Fig. 3.20: Drift velocity vs. electric field curves calculated at 4.2 K for (a)  $B = 4$  T, (b)  $B = 8$  T, (c)  $B = 11$  T, (d)  $B = 14$  T, (e)  $B = 16$  T and (f)  $B = 20$  T. In each panel  $\theta$  increases from  $0^\circ$  to  $90^\circ$  in  $5^\circ$  intervals from bottom to top. Adjacent curves are offset vertically by  $1.2 \times 10^3 \text{ m s}^{-1}$  for clarity. Curves for  $\theta = 0^\circ, 15^\circ, 30^\circ, 45^\circ, 60^\circ, 75^\circ$  and  $90^\circ$  are shown in bold. The dashed lines pass through the points on each curve where  $r = 0.5, 1, 2, 3$  from left to right respectively.

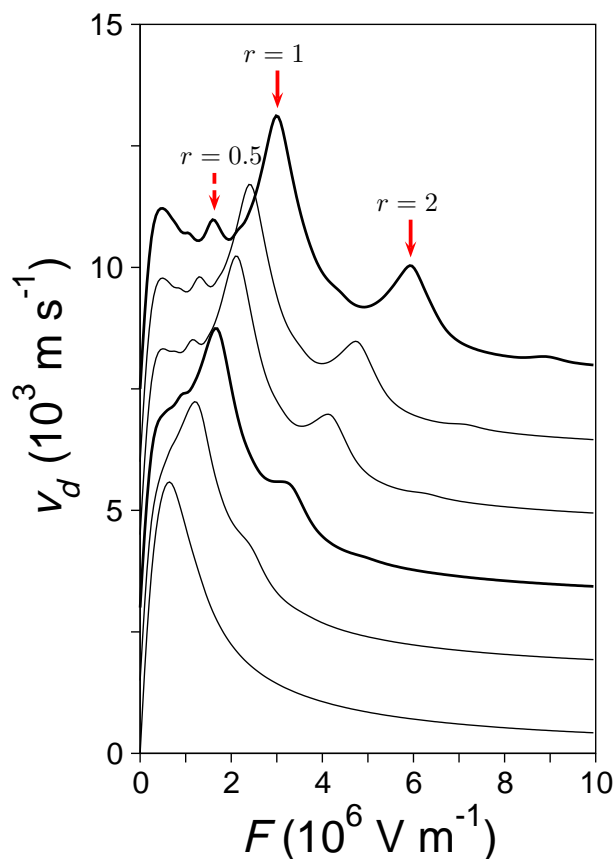


Fig. 3.21:  $v_d(F)$  curves calculated for  $\theta = 45^\circ$  and  $B = 4, 8, 11, 14, 16, 20$  T from the lower curve to the upper. Adjacent curves are vertically offset by  $1.5 \times 10^3 \text{ m s}^{-1}$  for clarity. This figure clearly shows that the intensity of the resonance peaks (labelled) increases with  $B$ .

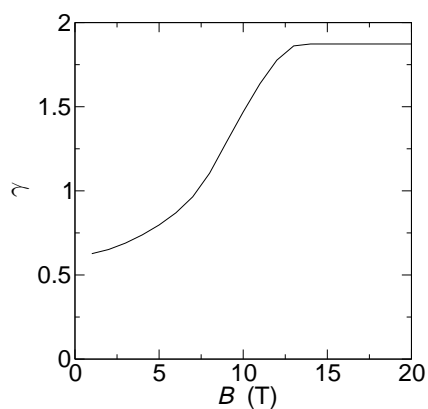


Fig. 3.22: Ratio  $\gamma$  (equation 3.24) plotted a function of  $B$  for  $\theta = 45^\circ$ . The electron trajectories used to produce this ratio we calculated over a time interval of  $\tau_{SL}$  starting from rest. The change in this ratio roughly correlates with the change in  $v_d(r = 2)$  peak intensity seen in figure 3.21.

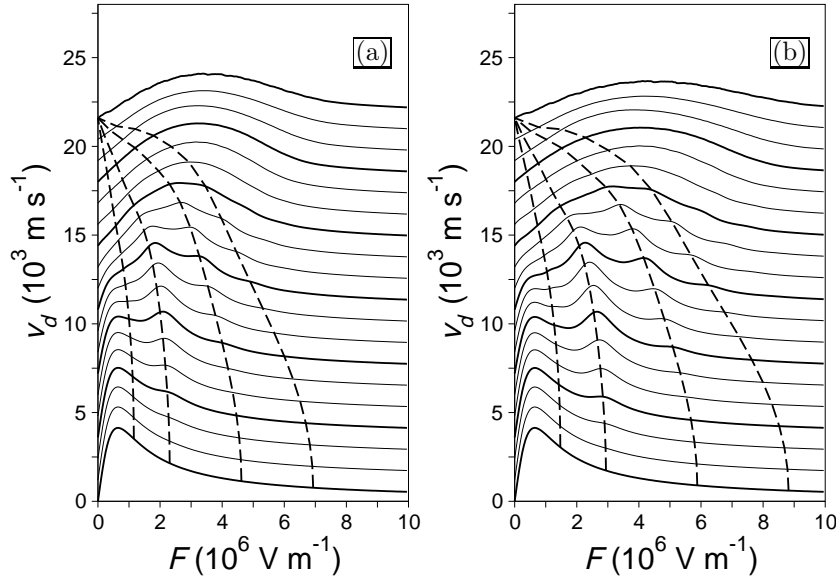


Fig. 3.23:  $v_d(F)$  curves calculated at 300 K for (a)  $B = 11$  T and (b)  $B = 14$  T. In each panel  $\theta$  increases from  $0^\circ$  to  $90^\circ$  in  $5^\circ$  intervals from bottom to top. Adjacent curves are offset vertically by  $1.2 \times 10^3 \text{ ms}^{-1}$  for clarity. Curves for  $\theta = 0^\circ, 15^\circ, 30^\circ, 45^\circ, 60^\circ, 75^\circ$  and  $90^\circ$  are shown in bold. The dashed lines pass through the points on each curve where  $r = 0.5, 1, 2, 3$  from left to right respectively.

Figure 3.24(a) plots the electric field profile calculated using this method for  $B = 11$  T and  $\theta = 0^\circ$  as a function of position  $x$  through the superlattice and voltage  $V$ . Figure 3.24(b) shows the same data but has  $r$  on the vertical axis rather than  $F$  (recall that  $F \propto r$ ). Figure 3.24(c) shows the corresponding electron density profile,  $n(x, V)$ . In all three figures, the solid contours indicate when  $r$  takes an integer value and the broken contour indicates  $r = 0.5$ . From these figures, it is clear that the electric field is not constant across the superlattice and, for high voltages, a high field domain forms towards the collector contact. High field domains occur in devices which exhibit negative differential velocity (NDV) because, in the NDV region, the electrons slow as the electric field increases. Therefore, more electrons are required to maintain current continuity which causes an increase in electric field. This constitutes a positive feedback loop so a sharp increase in electric field and electron density in regions of NDV is observed. In contrast, the electric field at voltages  $\leq 200$  mV is approximately constant across the bulk of the superlattice as figure 3.24 shows with more clarity for  $V = 10, 100, 200, 300$  mV. This result validates the constant  $F$  assumption made in the formulation of equation 3.19.

The presence of a large high field domain means that the semiclassical assumption of a slowly varying electric field is incorrect at high voltages. Therefore

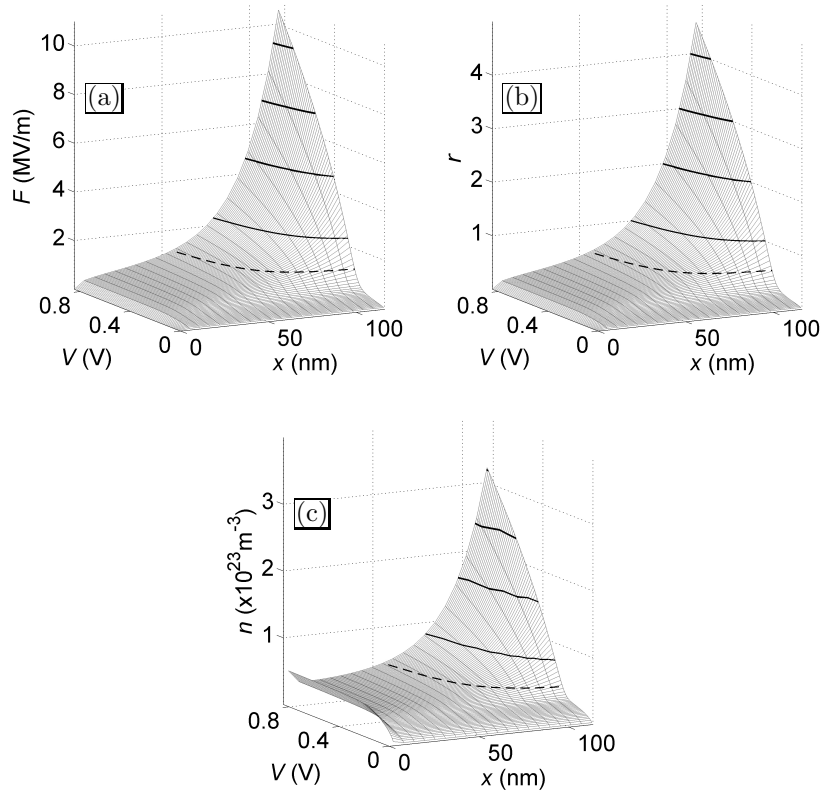


Fig. 3.24: Surfaces showing the electrostatics of superlattice NU2293 with  $B = 11$  T and  $\theta = 0^\circ$ . (a-c) respectively show the change in  $F$ ,  $r$  and  $n$  as functions of  $x$  and  $V$ . The solid contours on each surface indicate when  $r$  takes an integer value and the broken contour indicates  $r = 0.5$ . Note that positioning the  $r$  contours on (c) is not exact because  $n$  is not necessarily single valued along these contours.

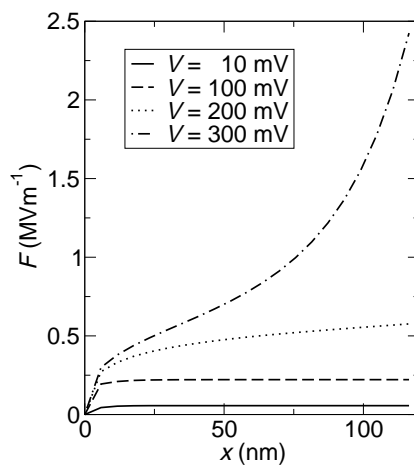


Fig. 3.25: Plots of  $F$  as a function of  $x$  for  $B = 11$  T and  $\theta = 0^\circ$ . These plots show that the electric field is approximately constant across the bulk of the superlattice for  $V < 200$  mV.

stochastic webs may not form and the electron's  $x$  displacement would be reduced meaning that  $v_d(F)$  may be over estimated. However, the model is still applicable provided that  $F$  varies slowly over the mean free path of the electron.

The next section will explore the electrostatics and  $I(V)$  relationships for  $B = 11$  T and a range of  $\theta$  values. Then the effect of changing  $B$  will be investigated.

### 3.4 $I(V)$ and Electrostatic Data for $B = 11$ T

Figures 3.26(a) and (b) show calculated and experimental current voltage,  $I(V)$ , relationships respectively for superlattice NU2293 with an applied magnetic field of  $B = 11$  T and a range of  $\theta$ . The theoretical results agree well with the experimental data for  $\theta < 45^\circ$  but, for higher  $\theta$ s, the current tends to be underestimated at high voltages. In both sets of data an additional feature appears which causes an increase in current as  $\theta$  is increased. This increase is shown more clearly in the corresponding differential conductance,  $G(V) = dI(V)/dV$ , (figs. 3.26(c) and (d)) as a peak (highlighted area). The initial rapid increase in  $G$  at very low  $V$  occurs because many of the donor ions are not ionised at  $V = 0$  V and 4.2 K. As  $V$  increases, the donor ions become ionised by the increasing electric field. This process is known as field ionisation. Therefore  $I$  increases more slowly in the ohmic region because the number of charge carriers is initially low.

For  $\theta = 45^\circ$ , the highlighted peak in  $G(V)$  is positioned at  $V \sim 400$  mV in both the numerical and experimental results. However, the width of the peak

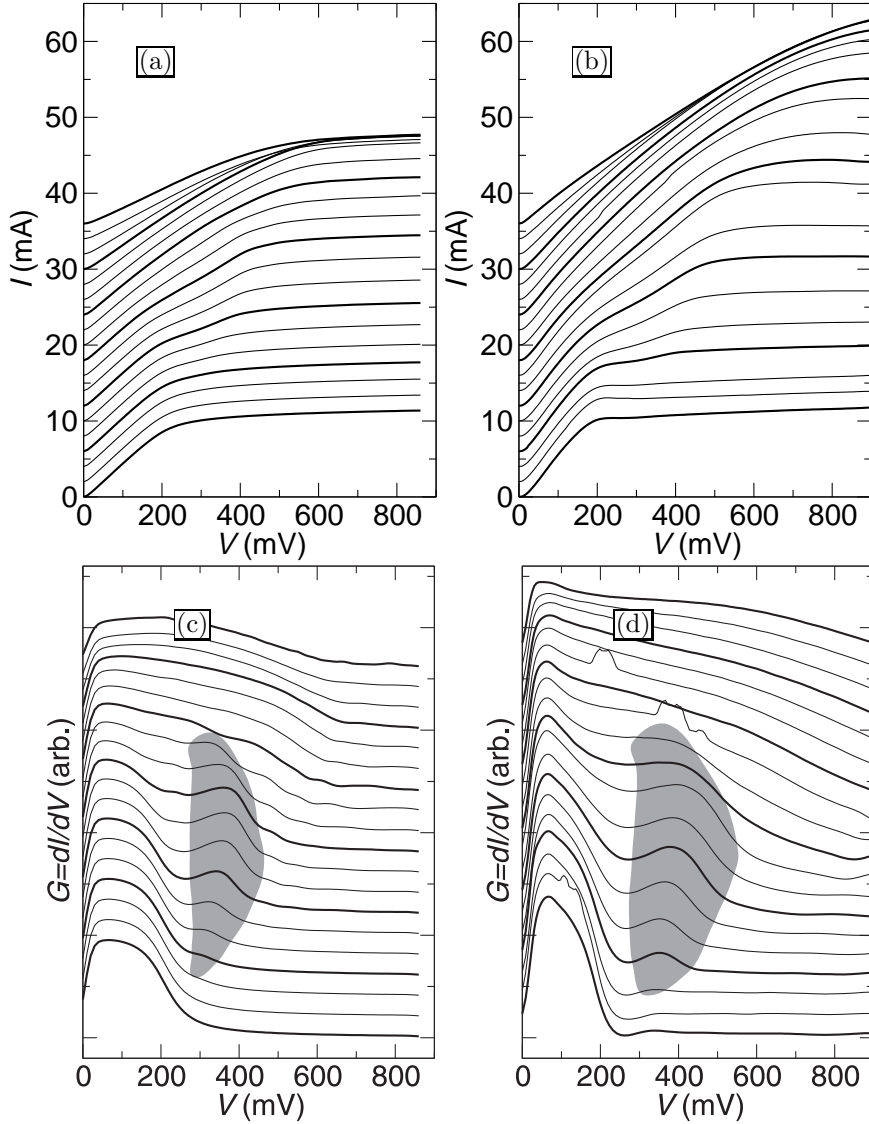


Fig. 3.26: Comparison of (a,c) theoretical and (b,d) experimental plots of (a,b)  $I(V)$  and (c,d)  $G(V) = dI(V)/dV$  at  $B = 11$  T.  $\theta$  increases from  $0^\circ$  to  $90^\circ$  in  $5^\circ$  intervals from bottom to top. Adjacent curves are vertically offset by 2 mA in (a,b) and by a varying amount in (c,d) for clarity. In (c,d) peaks due to the  $r = 1$  resonance are highlighted by the grey shaded region. All experimental data in this chapter are provided by Dr D. Fowler and Dr A. Patanè.

is greater in the experimental data. Any differences between experiment and theory can be attributed to the large number of assumptions made in the various models used as well as to inaccuracies in our estimates of the parameters used to model the superlattice. However, the qualitative and quantitative correspondence between theory and experiment supports the validity of our models. We can therefore give a good quantitative account of the features in  $G(V)$  using our semiclassical and drift-diffusion models.

To verify that this additional peak in differential conductance is due to the resonance peak in  $v_d(F)$  we look at the electric field profile across the superlattice when  $\theta \neq 0^\circ$  to ascertain if the electron is subject to electric fields which correspond to peaks in  $v_d(F)$ . Figures 3.27 and 3.28 show the change in  $r$ ,  $F$  and  $n$  as 2D functions of  $x$  and  $V$  for  $B = 11$  T and  $\theta = 15^\circ, 30^\circ, 45^\circ$  and  $60^\circ$ . The bold contours on all these figures indicate where  $r$  takes integer values and the broken contour indicates where  $r = 0.5$ . This data shows that when  $V < 0.2$  V the electric field is below that required for both the main superlattice peak and the  $r = 1$  resonance in  $v_d(F)$ . Therefore, the superlattice should exhibit ohmic behaviour for  $V < 0.2$  V, as seen in figure 3.26. As  $V$  increases beyond 0.2 V,  $F$  varies more rapidly with position along the superlattice (figs. 3.27 and 3.28) and a large high field domain forms for voltages  $> 0.6$  V, which causes  $F$  to increase rapidly near the collector contact. These high field domains occur for the same reason as those at  $\theta = 0^\circ$  discussed in the previous section.

The main difference between the  $F(x, V)$  surface at  $\theta = 0^\circ$  and, for example, that at  $\theta = 45^\circ$  is the plateau of approximately constant  $F$  which occurs for  $45^\circ$  (fig. 3.28(b)). The contour lines show that this plateau corresponds to  $r = 1$  and is thus a consequence of the first resonant peak in  $v_d(F)$ . Assuming that the plateau extends between  $0.9 \leq r \leq 1.1$ , the contour plot (fig. 3.28(a)) shows that it occurs for  $V > 0.4$  V for  $\theta = 45^\circ$ . The emergence of this plateau means that the  $r = 1$  resonance condition is satisfied across an appreciable fraction of the superlattice for a range of voltages. Similar plateaux are visible for  $\theta \geq 30^\circ$  (figs. 3.27 and 3.28) which occur when  $V > 0.35$  V and  $V > 0.35$  V for  $\theta = 30^\circ$  and  $60^\circ$  respectively.

The plateaux in  $F(x, V)$  appear as minima in  $n(x, V)$  (figs. 3.27(c) and 3.28(c)) because Poisson's equation (eqn. 1.78) states that regions of low electron density result in a slowly varying electric field. The contours of integer  $r$  plotted on these surfaces help confirm that the minima in  $n(x, V)$  occur at the same point in  $(x, V)$  space as the plateaux in  $F(x, V)$ .

Because the plateaux correspond to peaks in  $v_d(F)$  they have a large effect on electron transport through the superlattice. The electrons move rapidly through the plateaux which causes  $I(V)$  (fig. 3.26(a)) to increase faster with increasing  $V$ . This increased gradient appears as a peak in  $G(V)$  (fig. 3.26(c))

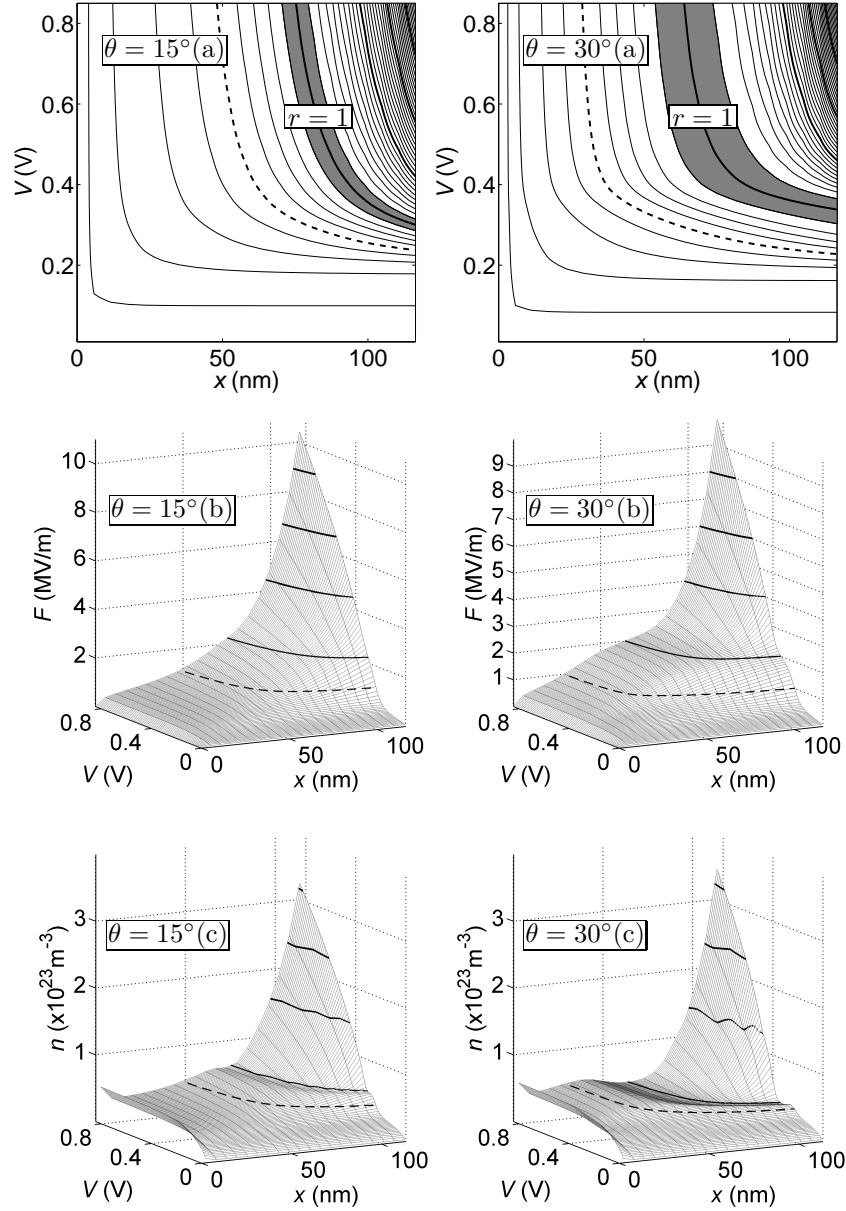


Fig. 3.27: Contour plots (a) showing  $r$  as a function of  $x$  and  $V$ . The contours are in steps of 0.1 with the broken contour indicating  $r = 0.5$  and the bold contours indicating when  $r$  is an integer. Finally,  $0.9 \leq r \leq 1.1$  is shaded in grey. (b-c) show 2D surface plots of  $F$  and  $n$  respectively as functions of  $x$  and  $V$ . The solid contours indicate when  $r$  is an integer and the broken contour indicates  $r = 0.5$ . This data is calculated for  $B = 11$  T and (left hand column)  $\theta = 15^\circ$  or (right hand column)  $\theta = 30^\circ$  as indicated.

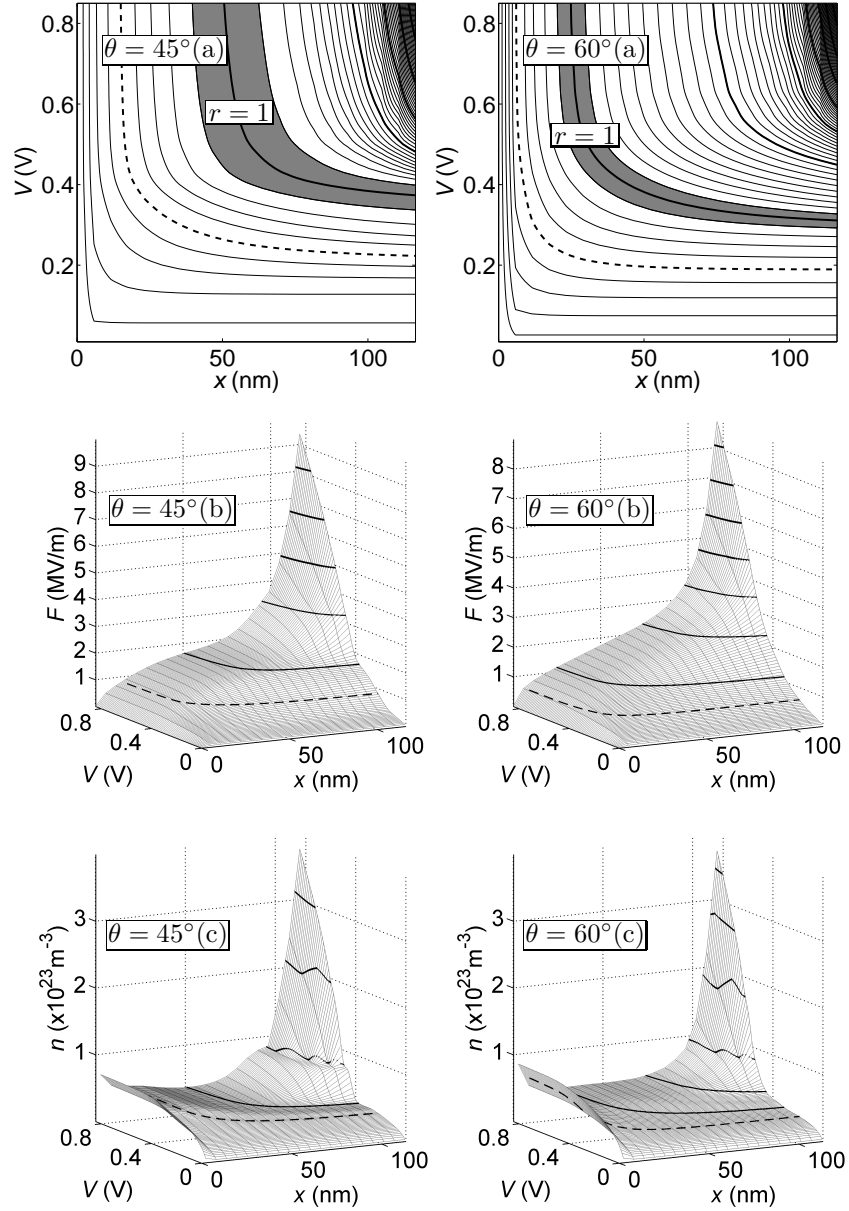


Fig. 3.28: Contour plots (a) showing  $r$  as a function of  $x$  and  $V$ . The contours are in steps of 0.1 with the broken contour indicating  $r = 0.5$  and the bold contours indicating when  $r$  is an integer. Finally,  $0.9 \leq r \leq 1.1$  is shaded in grey. (b-c) show 2D surface plots of  $F$  and  $n$  respectively as functions of  $x$  and  $V$ . The solid contours indicate when  $r$  is an integer and the broken contour indicates  $r = 0.5$ . This data is calculated for  $B = 11$  T and (left hand column)  $\theta = 45^\circ$  or (right hand column)  $\theta = 60^\circ$  as indicated.

corresponding to the small range of voltages for which the plateaux extend across most of the superlattice.

The formation of these plateau in  $F$  can be explained by the following logic. For  $F$  just below  $F(r = 1)$  there is a high positive differential velocity (PDV) (fig. 3.26) as opposed the usual NDV seen for  $\theta = 0^\circ$ . This positive gradient causes an opposite effect to that which produced the high field domain. Increasing  $F$  slightly causes the drift-velocity to increase sharply. Therefore the number of electrons required to maintain current continuity decreases significantly which in turn reduces any increase in electric field. This effect tends to make  $F$  increase very slowly because increasing  $F$  even slightly produces a large resistance to this change. Thus  $F$  changes very slowly over the region of PDV.

So, in summary, when  $r = 1$  and  $\theta$  is large enough, stochastic webs form in phase space (fig. 3.9) along which electrons can diffuse radially. This extends the distance the electrons can move through the superlattice (fig. 3.3) which causes a peak in the electron drift-velocity (fig. 3.20). This peak leads to a plateau of  $F \equiv r = 1$  forming in  $F(x)$  across a real superlattice (figs. 3.27 and 3.28) which finally leads to an enhanced current through the superlattice (fig. 3.26).

### 3.5 Electrostatics at other Magnetic Fields

In this section we consider the effects of  $B$  on the electrostatics of the system for  $\theta = 45^\circ$ . The electrostatics for  $B = 4$  T to 20 T are shown in figures 3.29 to 3.31 and these plots show the same general features as were observed for  $B = 11$  T in the previous section. However, as  $B$  increases, we can identify several trends in the strength and position of these features as  $B$ .

Figures 3.29(b), 3.30(b) and 3.31(b) shows that the minimum voltage at which a high field domain near the collector contact can form increases with increasing  $B$ . The contour plots (figs. 3.29(a), 3.30(a) and 3.31(a)) show that the  $r = 1$  contour shifts to higher  $V$  and  $x$  values with increasing  $B$  and that the corresponding plateau becomes broader. The increase in the size of the plateau can be explained by the  $v_d(F)$  curves (fig. 3.21) which show that increasing  $B$  increases the intensity of the  $r = 1$  peak. Therefore, the resistance to increasing  $F$  as described in the previous section becomes greater with increasing  $B$  and the plateau of slowly varying  $F$  becomes larger. We therefore predict the peaks in  $G(V)$  to be progressively larger, wider and shifted to higher  $V$  as  $B$  increases. These changes are expected because the plateau covers more of the superlattice, does this for a wider range of voltages and begins at a higher voltage respectively. Figure 3.32 clearly shows that all three of these changes occur in both the theoretical and experimental data as predicted.

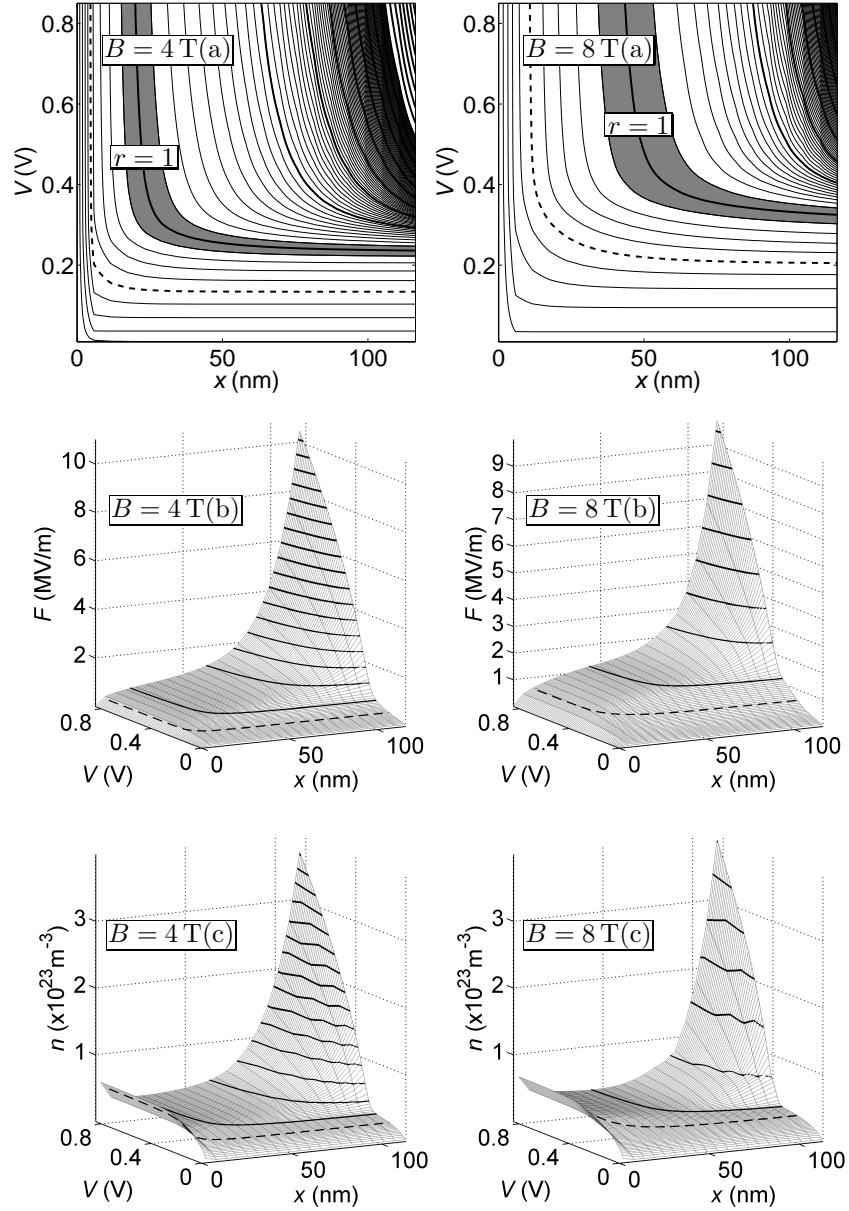


Fig. 3.29: Contour plots (a) showing  $r$  as a function of  $x$  and  $V$ . The contours are in steps of 0.1 with the broken contour indicating  $r = 0.5$  and the bold contours indicating when  $r$  is an integer. Finally,  $0.9 \leq r \leq 1.1$  is shaded in grey. (b-c) show 2D surface plots of  $F$  and  $n$  respectively as functions of  $x$  and  $V$ . The solid contours indicate when  $r$  is an integer and the broken contour indicates  $r = 0.5$ . This data is calculated for  $\theta = 45^\circ$  and (left hand column)  $B = 4$  T or (right hand column)  $B = 8$  T as indicated.

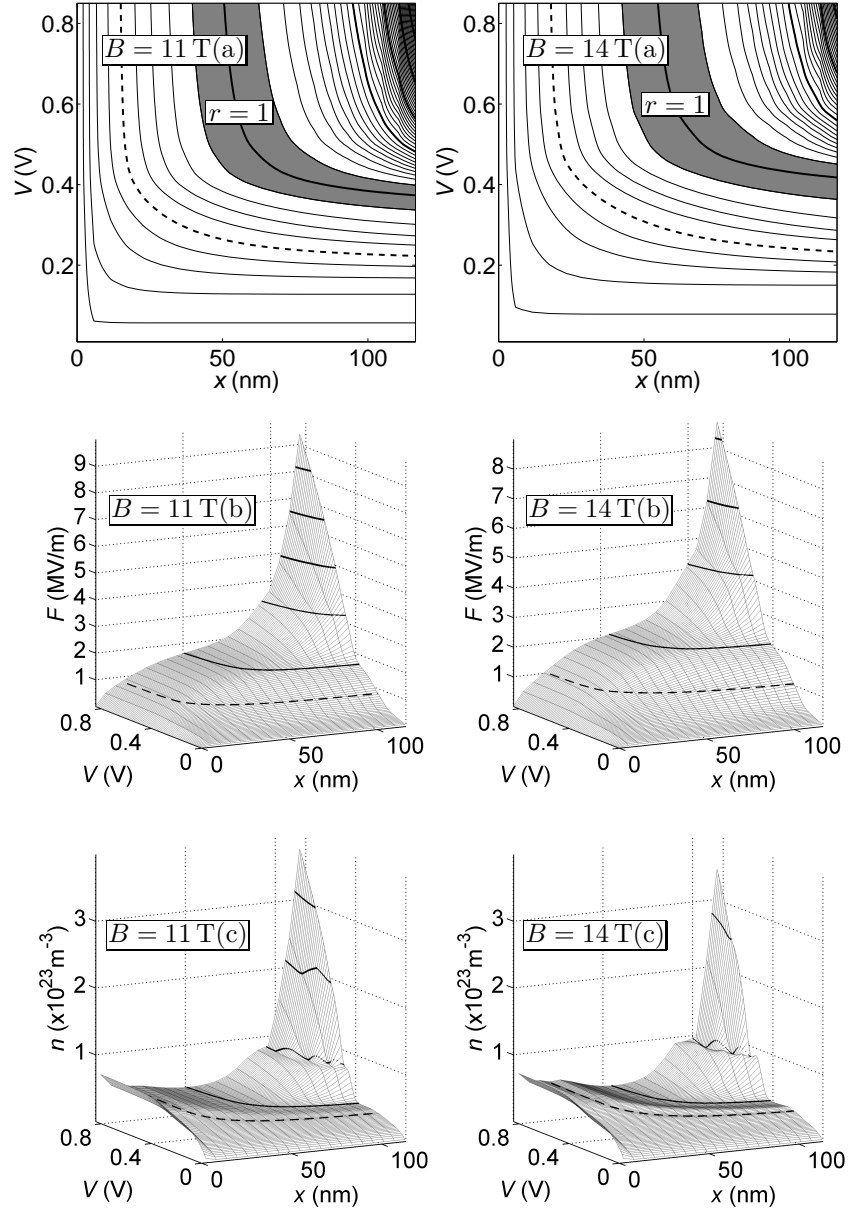


Fig. 3.30: Contour plots (a) showing  $r$  as a function of  $x$  and  $V$ . The contours are in steps of 0.1 with the broken contour indicating  $r = 0.5$  and the bold contours indicating when  $r$  is an integer. Finally,  $0.9 \leq r \leq 1.1$  is shaded in grey. (b-c) show 2D surface plots of  $F$  and  $n$  respectively as functions of  $x$  and  $V$ . The solid contours indicate when  $r$  is an integer and the broken contour indicates  $r = 0.5$ . This data is calculated for  $\theta = 45^\circ$  and (left hand column)  $B = 11$  T or (right hand column)  $B = 14$  T as indicated.

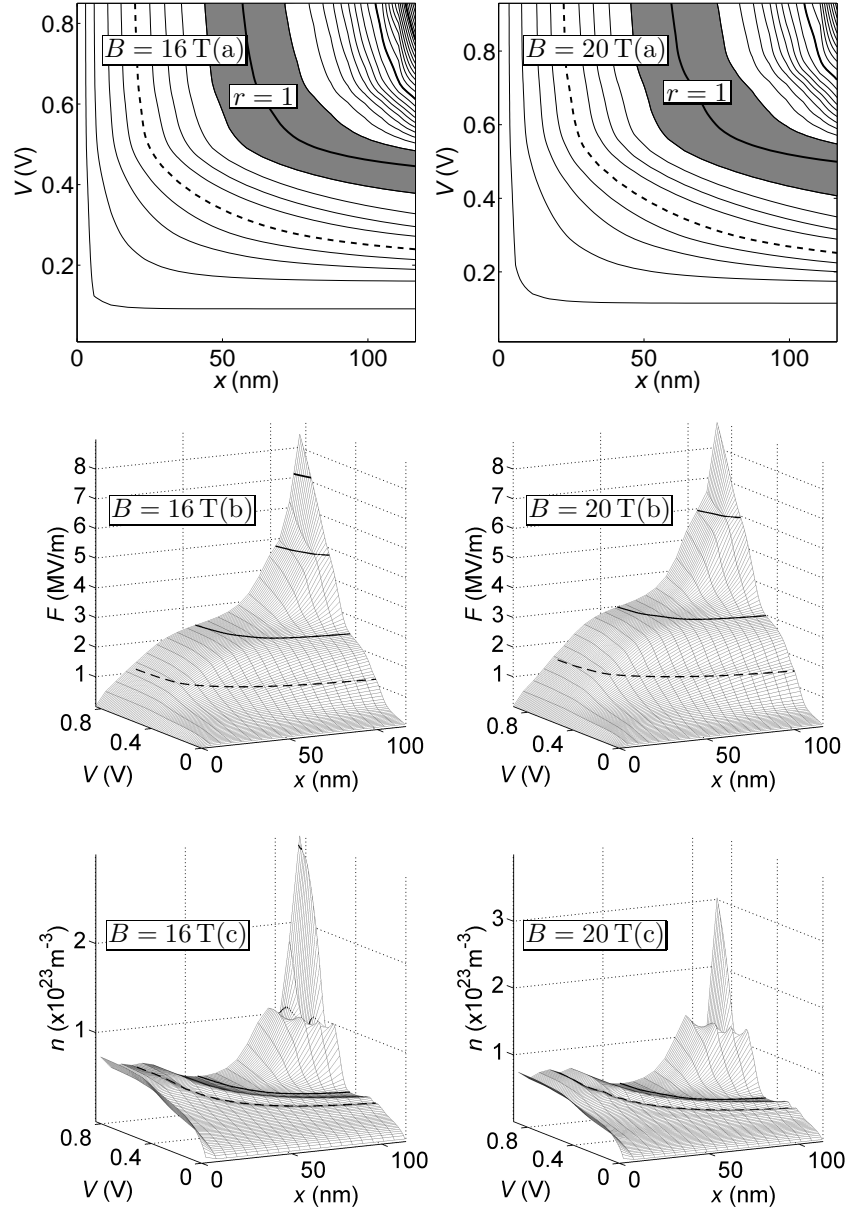


Fig. 3.31: Contour plots (a) showing  $r$  as a function of  $x$  and  $V$ . The contours are in steps of 0.1 with the broken contour indicating  $r = 0.5$  and the bold contours indicating when  $r$  is an integer. Finally,  $0.9 \leq r \leq 1.1$  is shaded in grey. (b-c) show 2D surface plots of  $F$  and  $n$  respectively as functions of  $x$  and  $V$ . The solid contours indicate when  $r$  is an integer and the broken contour indicates  $r = 0.5$ . This data is calculated for  $\theta = 45^\circ$  and (left hand column)  $B = 16$  T or (right hand column)  $B = 20$  T as indicated.

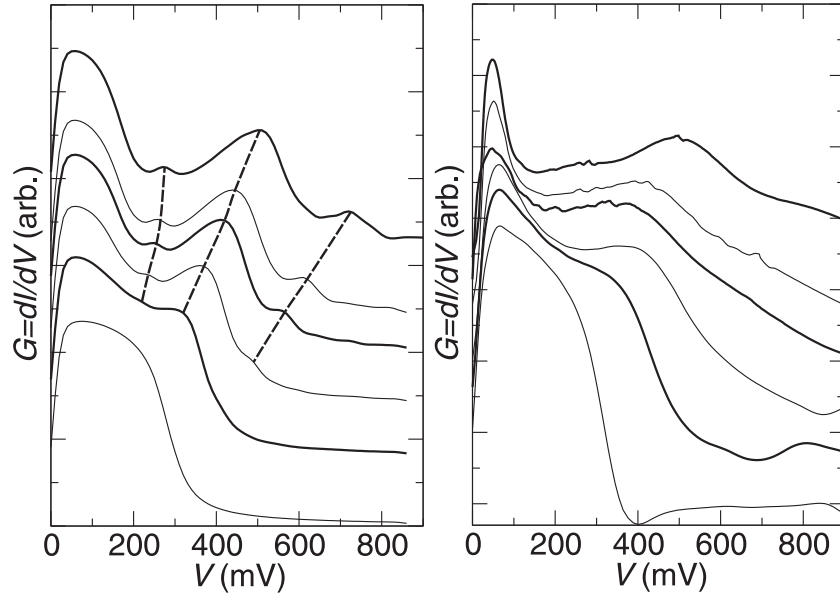


Fig. 3.32: Theoretical (left) and experimental (right)  $G(V) = dI(V)/dV$  curves for  $\theta = 45^\circ$ . The vertically offset curves show  $B = 4, 8, 14, 16$  and  $20$  T from bottom to top. The broken lines (from left to right) indicate the  $r = 0.5, 1$  and  $2$  resonant peaks.

Figure 3.32 shows that the  $r = 2$  peak in  $G(V)$  first appears for  $B = 11$  T at  $V \sim 0.5$  V and is most clearly visible for  $B = 20$  T at  $V = 0.75$  V. This peak occurs for the same reason as the  $r = 1$  peak but is much weaker. The lack of an  $r = 2$   $G(V)$  peak at  $B = 4$  T or  $8$  T is explained by the  $v_d(F)$  curves in figure 3.21. These curves show that there is no region of positive differential velocity (PDV) on the leading edge of the  $r = 2$  resonance peak because this peak is merged into the  $r = 1$  peak. Therefore there is no negative feedback loop to slow the increase of  $F$  and no  $r = 2$  plateau forms. The same reasoning explains the strength of the  $r = 2$   $G(V)$  peaks relative to the  $r = 1$  peaks and the increase in  $G(V)$  peak strength with increasing  $B$ . Basically, the longer and steeper the region of PDV on the leading edge of a resonance peak in  $v_d(F)$ , the stronger the resistance to an increase in  $F$  so a larger plateau forms. This larger plateau then causes a larger peak in  $G(V)$ .

No  $r = 2$  peaks are present in the experimental data. To explain this, we note that the numerical  $r = 2$  peaks in  $G(V)$  arise from a plateau that is less than  $0.5d$  in length. This distance is shorter than the electron's mean free path along  $x$  so our calculations of  $v_d(F)$  would overestimate the magnitude of the  $r = 2$  resonant peak. So if we reduced the magnitude of the  $r = 2$   $v_d(F)$  peak then the peak in  $G(V)$  would become smaller or vanish for the reasons described in the previous paragraph.

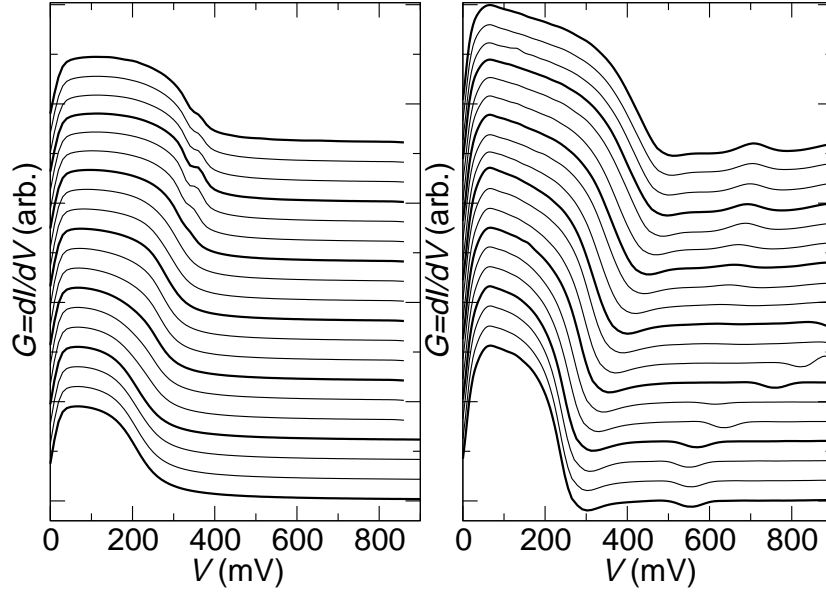


Fig. 3.33: Comparison of theoretical (left) and experimental (right)  $G(V) = dI(V)/dV$  curves for  $B = 4$  T.  $\theta$  increases from  $0^\circ$  to  $90^\circ$  in  $5^\circ$  intervals from bottom to top. Adjacent curves are vertically offset by a varying amount for clarity.

Finally, figures 3.33, 3.34, 3.35, 3.36 and 3.37 show the full comparison between calculated and experimental  $G(V)$  results for  $B = 4, 8, 14, 16$  and  $20$  T respectively for  $\theta = 0^\circ$  to  $90^\circ$  in  $5^\circ$  increments. These figures show that the theoretical model tends to correctly predict the position of the  $r = 1$  peaks in  $G(V)$  but underestimates their width. The theoretical results also show  $r = 2$  resonant peaks, which are not seen in the experimental data, for the reason explained above.

### 3.5.1 Electrostatics at 300 K

We can use the 300 K  $v_d(F)$  curves (fig. 3.23) to predict the current voltage characteristics of the superlattice at room temperature. Figures 3.38 and 3.39 show the comparison between this theoretical and experimental  $I(V)$  data for  $B = 11$  T and  $14$  T respectively. The calculated data slightly underestimates the initial current gradient but the resonance peaks appear in approximately the same positions as in the experimental data.

When compared to the 4.2 K data (figs. 3.26 and 3.35), we see that  $G(V = 0)$  is high at room temperature but low at 4.2 K. This is because at 300 K the donors are all thermally ionised and the conductance increase associated with field ionisation does not occur (see section 3.4). The other difference between  $G(V)$  at the two temperatures is that the  $r = 1$  peaks appear at a lower voltage

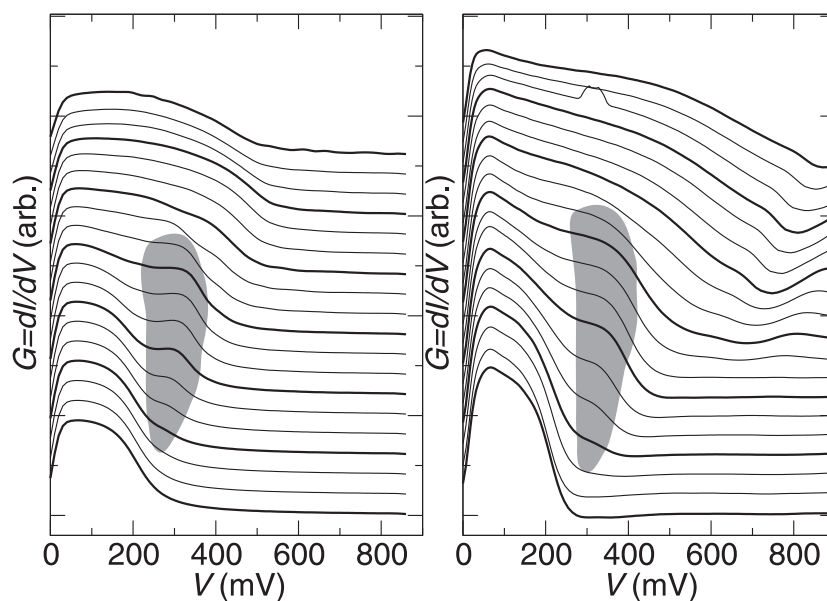


Fig. 3.34: Comparison of theoretical (left) and experimental (right)  $G(V) = dI(V)/dV$  curves for  $B = 8$  T.  $\theta$  increases from  $0^\circ$  to  $90^\circ$  in  $5^\circ$  intervals from bottom to top. Adjacent curves are vertically offset by a varying amount for clarity. The peaks due to the  $r = 1$  resonance are highlighted by the grey shaded region.

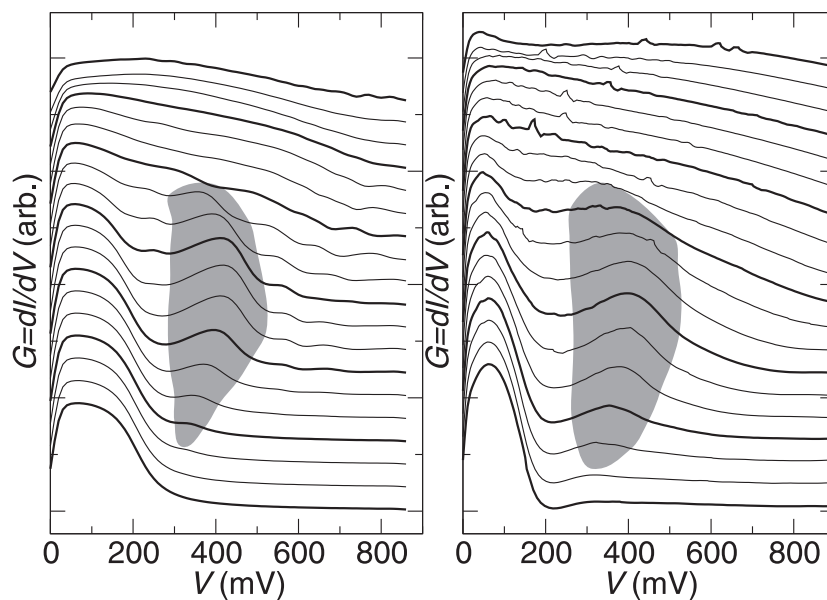


Fig. 3.35: Comparison of theoretical (left) and experimental (right)  $G(V) = dI(V)/dV$  curves for  $B = 14$  T.  $\theta$  increases from  $0^\circ$  to  $90^\circ$  in  $5^\circ$  intervals from bottom to top. Adjacent curves are vertically offset by a varying amount for clarity. The peaks due to the  $r = 1$  resonance are highlighted by the grey shaded region.

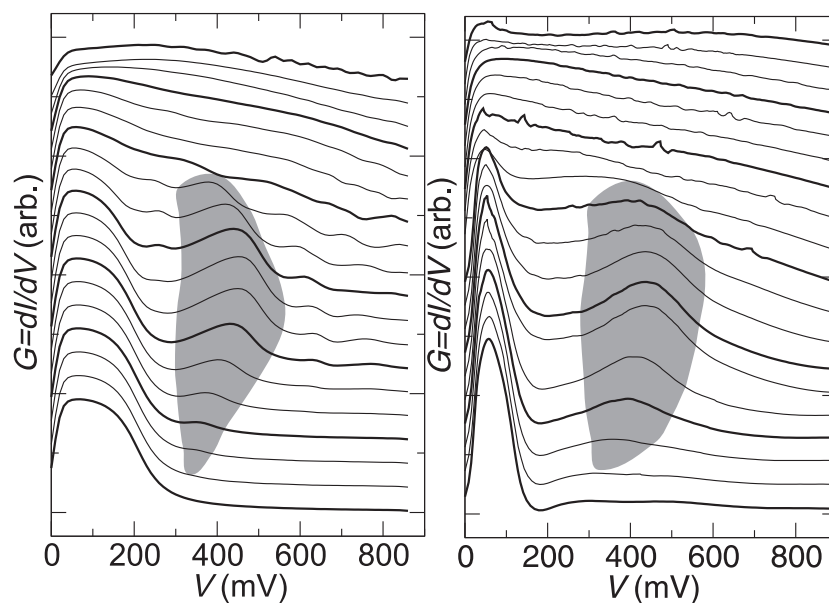


Fig. 3.36: Comparison of theoretical (left) and experimental (right)  $G(V) = dI(V)/dV$  curves for  $B = 16$  T.  $\theta$  increases from  $0^\circ$  to  $90^\circ$  in  $5^\circ$  intervals from bottom to top. Adjacent curves are vertically offset by a varying amount for clarity. The peaks due to the  $r = 1$  resonance are highlighted by the grey shaded region.

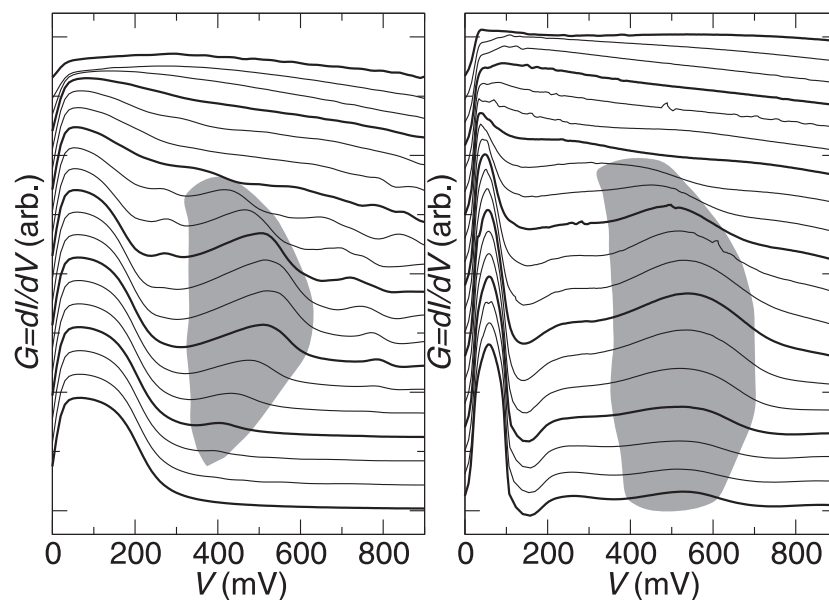


Fig. 3.37: Comparison of theoretical (left) and experimental (right)  $G(V) = dI(V)/dV$  curves for  $B = 20$  T.  $\theta$  increases from  $0^\circ$  to  $90^\circ$  in  $5^\circ$  intervals from bottom to top. Adjacent curves are vertically offset by a varying amount for clarity. The peaks due to the  $r = 1$  resonance are highlighted by the grey shaded region.

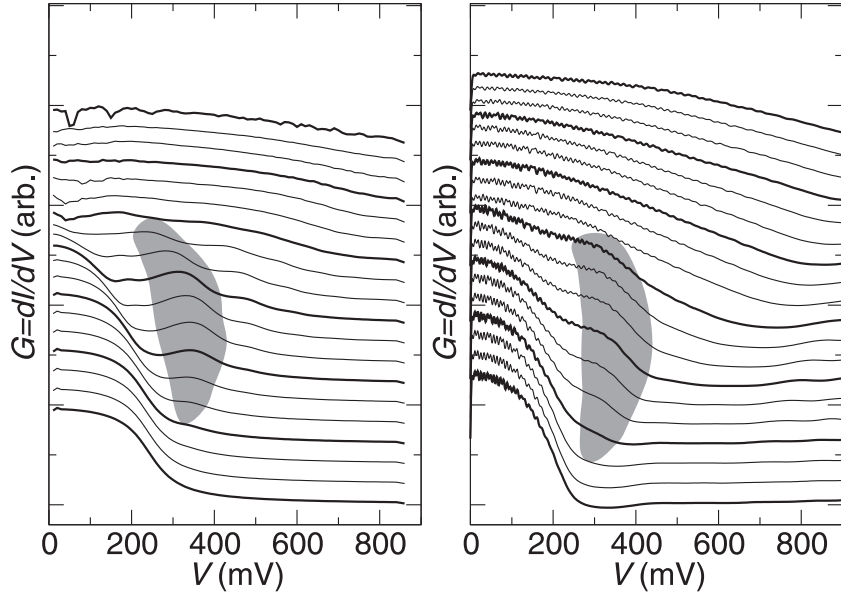


Fig. 3.38: Comparison of theoretical (left) and experimental (right)  $G(V) = dI(V)/dV$  curves at 300 K for  $B = 11$  T.  $\theta$  increases from  $0^\circ$  to  $90^\circ$  in  $5^\circ$  intervals from bottom to top. Adjacent curves are vertically offset by a varying amount for clarity. The peaks due to the  $r = 1$  resonance are highlighted by the grey shaded region.

for 300 K and are less intense. Figure 3.40 shows plots of  $r(x, V)$ ,  $F(x, V)$  and  $n(x, V)$  for 300 K which, as expected from the changes in  $G(V)$ , show that the plateaux in  $F$  occur for lower  $x$  and  $V$  values and are thinner than the corresponding plateaux for 4.2 K (fig. 3.30). Thus, following the logic set out in the previous section, we would expect these smaller plateaux to be the result of a smaller or wider  $r = 1$  resonance peaks in  $v_d(F)$ . Comparing the  $v_d(F)$  data in figures 3.38 (300 K) to 3.26 (4.2 K) shows that this is the case.

### 3.6 Conclusion

This chapter investigated the behaviour of superlattice NU2293 with an applied electric and tilted magnetic field using a variety of numerical models. This system forms a driven harmonic oscillator with Bloch oscillations caused by the electric field coupled to cyclotron oscillations caused by the magnetic field.

In the first half of this chapter, we assumed that the superlattice was infinite and used a semiclassical model to predict the behaviour of a single electron. We observed that a stochastic web forms in the phase space of our system when the Bloch oscillations are resonant with the  $x$  component of the cyclotron oscillations ( $r = \text{integer}$ ). We also saw a mixed chaotic/stable phase space appearing for

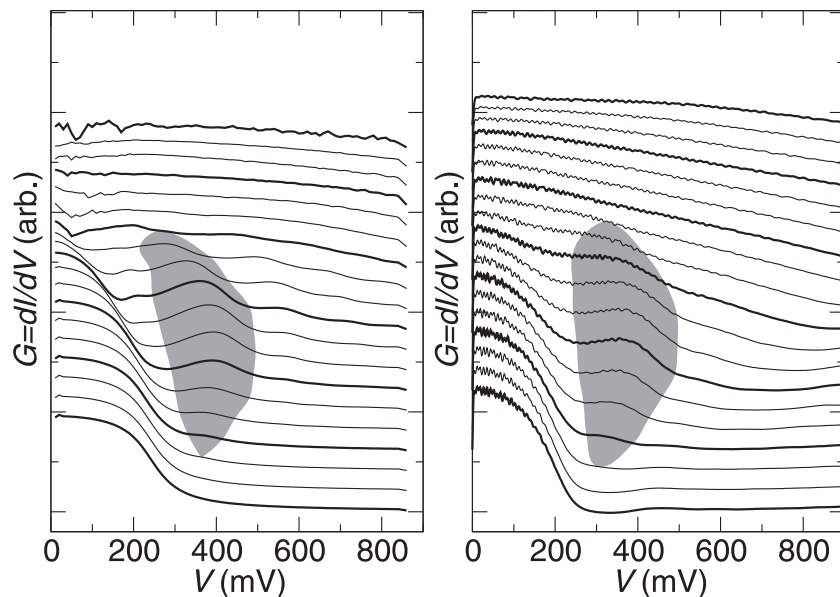


Fig. 3.39: Comparison of theoretical (left) and experimental (right)  $G(V) = dI(V)/dV$  curves at 300 K for  $B = 14$  T.  $\theta$  increases from  $0^\circ$  to  $90^\circ$  in  $5^\circ$  intervals from bottom to top. Adjacent curves are vertically offset by a varying amount for clarity. The peaks due to the  $r = 1$  resonance are highlighted by the grey shaded region.

high magnetic fields tilt angles,  $\theta$ , independently of  $r$ . These features allow an electron to diffuse in the radial direction through phase space which corresponds to a large  $x$  displacement in real space. This large displacement along  $x$  means that the electron drift velocity,  $v_d(F)$ , is enhanced both when  $r \propto F$  is close to an integer and when  $\theta$  is sufficiently large. This enhancement leads to additional peaks appearing in  $v_d(F)$  which we dubbed resonance peaks.

In the second half of this chapter, we input the  $v_d(F)$  relations to a drift-diffusion model to calculate electrostatic and  $I(V)$  data for a finite superlattice system. We found that the electric field across the superlattice was often highly non-linear and that a high field domain occurs at high voltages near the collector contact which is a consequence of negative differential velocity.

Conversely, we also found plateaux of slowly varying  $F$  in  $F(x)$  which are a result of the regions of positive differential velocity on the leading edge of the resonant peaks in  $v_d(F)$ . These plateaux lead to enhanced current because the electrons can move across them swiftly due to  $v_d(F)$  being maximised. This increased current is best viewed via a  $G(V) = dI(V)/dV$  plot which shows the enhancements as peaks. We observed such peaks, and the corresponding plateaux, for both  $r = 1$  and  $r = 2$  although the validity of the  $r = 2$  peaks is doubtful due to the small size of their plateaux.

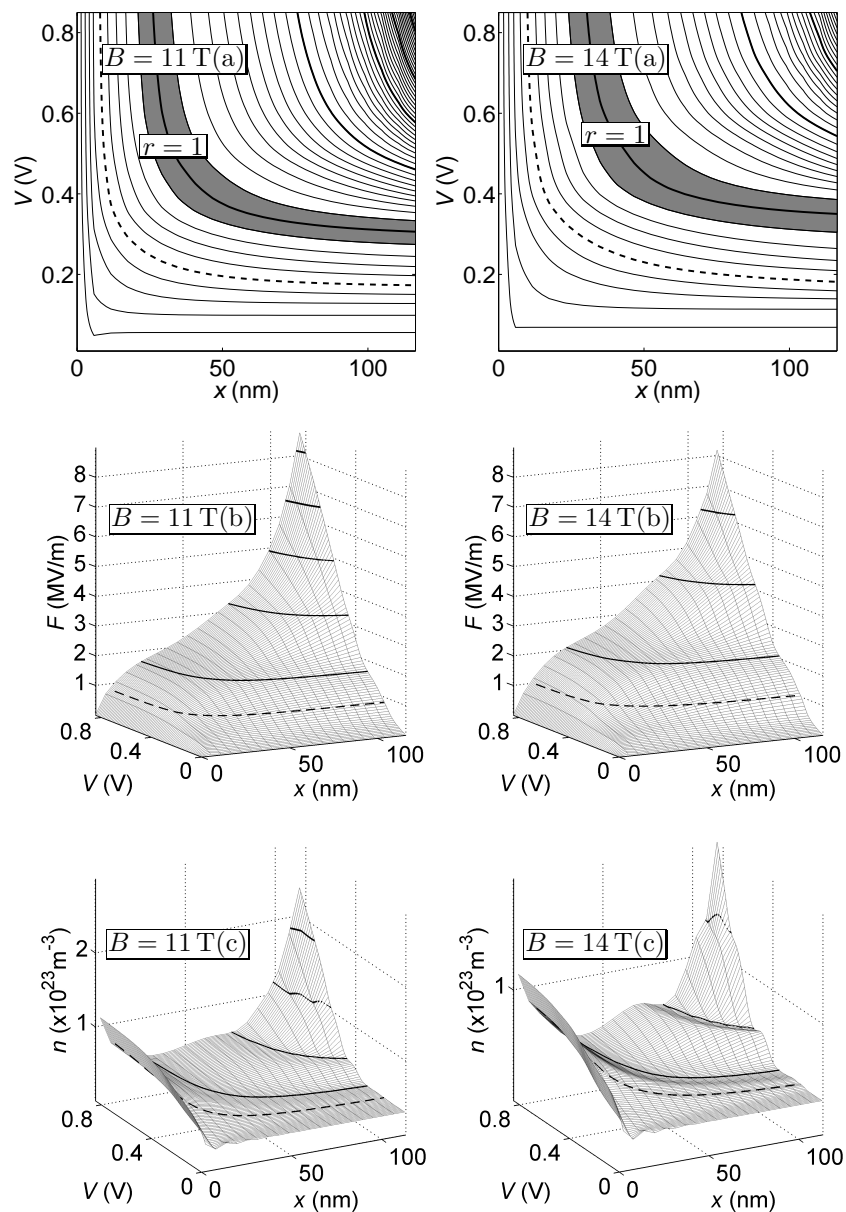


Fig. 3.40: Contour plots (a) showing  $r$  as a function of  $x$  and  $V$ . The contours are in steps of 0.1 with the broken contour indicating  $r = 0.5$  and the bold contours indicating when  $r$  is an integer. Finally,  $0.9 \leq r \leq 1.1$  is shaded in grey. (b-c) show 2D surface plots of  $F$  and  $n$  as functions of  $x$  and  $V$  respectively. The solid contours indicate when  $r$  is an integer and the broken contour indicates  $r = 0.5$ . This data is calculated at 300 K for  $\theta = 45^\circ$  and (left hand column)  $B = 11$  T or (right hand column)  $B = 14$  T as indicated and can be directly compared to the 4.2 K data in figure 3.30.

Our numerical  $G(V)$  plots are in good agreement with experimental data for the real superlattice NU2293. This agreement validates our models.

#### 4. SEMICLASSICAL ANALYSIS OF SUPERLATTICE NU2299

## 4.1 Introduction

Chapter 3 has examined superlattice NU2293 and has shown that our model produces a good match to the experimental  $I(V)$  data. The semiclassically calculated  $v_d(F)$  curves show resonant peaks which correspond to  $r = 2$  and 3 (fig. 3.20). However, the  $G(V)$  curves only show a peaks due to  $r = 1$  and not  $r = 2$  (figs. 3.26, 3.33, 3.34, 3.35, 3.36 and 3.37). This is because the electric field gradient is large for  $F(r = 2)$  and  $F(r = 3)$  etc (figs. 3.29, 3.30 and 3.31). Therefore, the proportion of the superlattice for which  $r = 2$  or  $r = 3$  is very small and there will only be a negligible overall current enhancement due to electrons moving faster through this region (see section 3.3).

Therefore, to see  $G(V)$  peaks corresponding to  $r = 2$ , we need to stop  $F$  varying so rapidly about  $r = 2$ . Therefore, we need to reduce or eliminate the high electric field domain that forms near the collector contact in superlattice NU2293 (31).

In this chapter, we investigate superlattice NU2299 which has a different bandgap between the first and second minibands to that of superlattice NU2293. The bandgap for superlattice NU2299 is 66.1 meV compared to 201.5 meV for sample NU2293. The structural differences between the two superlattice are covered in section 1.4. It is hoped that this smaller bandgap will allow interminiband tunnelling which should enable the electrons to move more freely. This should reduce electron buildup and prevent a high electric field domain forming.

We use the same semiclassical model for this superlattice that we used for superlattice NU2293 but with different parameters. This basic model does not account for interminiband tunnelling so the smaller miniband gap will have no effect on the electron dynamics. We will suggest modifications to allow this tunnelling later in the chapter.

## 4.2 Electron Dynamics for Superlattice NU2299

The semiclassical electron orbits for superlattice NU2299 are calculated in exactly the same way as they were for superlattice NU2293. The only parameters that differ between the two superlattices for this calculation are the superlattice period,  $d$ , and the form of the dispersion curve,  $E(k)$ . Figure 4.1 shows electron orbits calculated for superlattice NU2299 with  $B = 14$  T,  $\theta = 30^\circ$  and a range of  $r$  values. These figures are very similar to those in figure 3.3 which were calculated for superlattice NU2293. Likewise, figure 4.2 shows that the change in electron orbit with varying  $\theta$  for  $B = 14$  T and  $r = 1$  is very similar to the change for superlattice NU293 (fig. 3.5). Therefore, we refer the reader to the

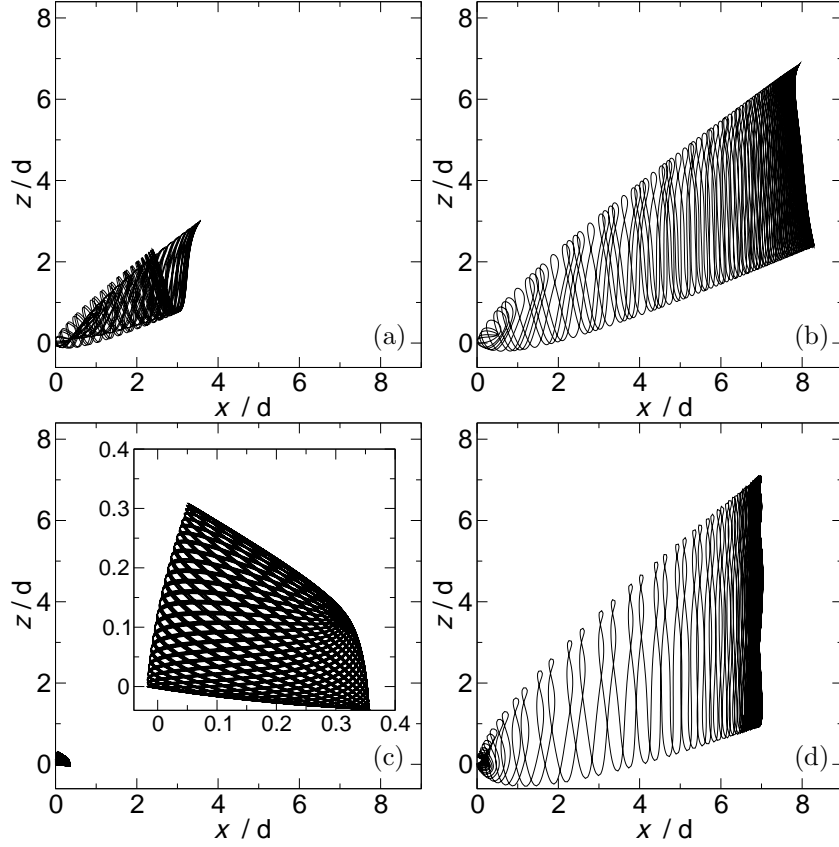


Fig. 4.1: Electron trajectories calculated over 20 ps starting from rest for  $\theta = 30^\circ$  and  $B = 14$  T in superlattice NU2299. The electric field is chosen such that (a)  $r = 0.5$ , (b)  $r = 1$ , (c)  $r = \frac{1+\sqrt{5}}{2}$  and (d)  $r = 2$ .

discussions in section 3.2 for an explanation of these results.

Figure 4.3 shows a selection of Poincaré sections calculated for  $B = 14$  T,  $\theta = 30^\circ$  and a range of  $r$  values. These sections are very similar to those shown for superlattice NU2293 (section 3.2.4). Therefore we will not examine them in any greater detail and the discussions in chapter 3 apply.

Figure 4.4(a) plots the drift-velocity as a function of electric field,  $v_d(F)$ , for  $B = 14$  T, a range of  $\theta$  values and superlattice NU2299. This figure shows that the resonance enhanced peaks in  $v_d(F)$  are much stronger for superlattice NU2299 than those found for superlattice NU2293 (figure 4.4(b)). To explain this increase we consider the following.

In section 3.2.10 we saw that the resonance peaks in  $v_d(F)$  calculated for superlattice NU2293 at 300 K were smaller than those calculated at 4.2 K. We explained this change with reference to the higher initial energies at 300 K com-

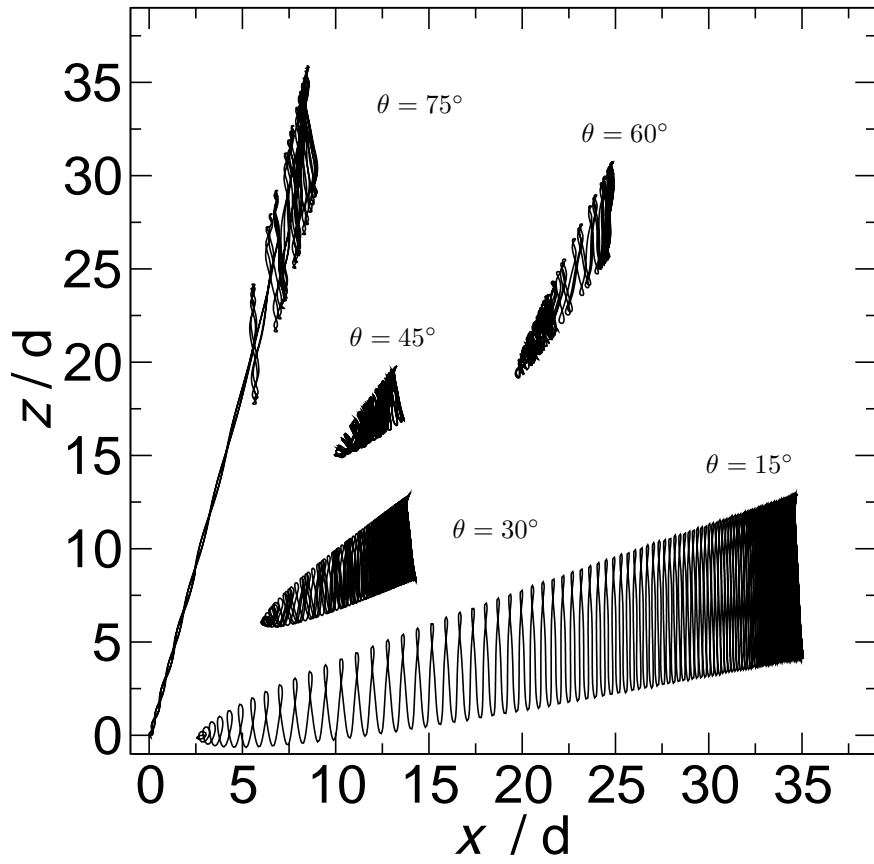


Fig. 4.2: Variation in electron orbit with  $\theta$  values as specified. These orbits are shown on the same scale and calculated over 20 ps starting from rest with  $B = 14$  T and  $r = 1$  in superlattice NU2299.

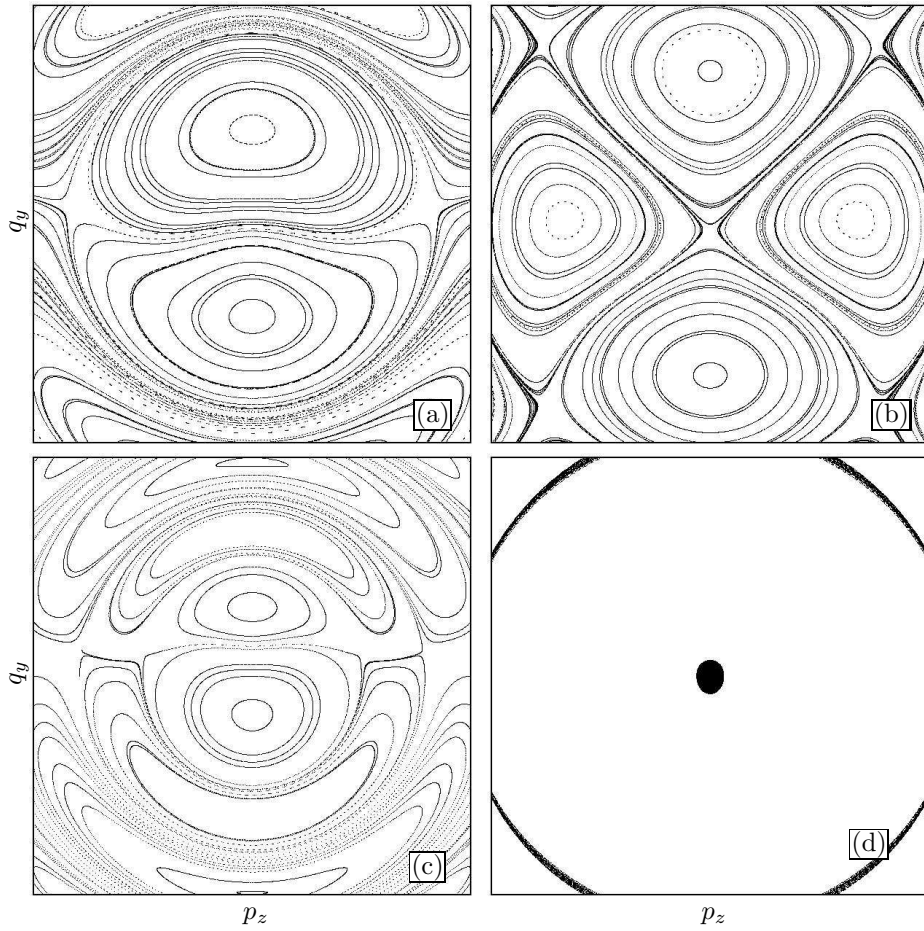


Fig. 4.3: Stroboscopic Poincaré sections calculated for superlattice NU2299 with  $\theta = 30^\circ$  and  $B = 14$  T. The electric field is such that (a)  $r = 1$ , (b)  $r = 2$ , (c)  $r = 0.5$  and (d)  $r = \frac{1+\sqrt{5}}{2}$ . Both axes range from  $(-2 \rightarrow 2) \times 10^{-25}$  kg ms $^{-1}$ . Note that (d) has fewer starting points than the other Poincaré sections.

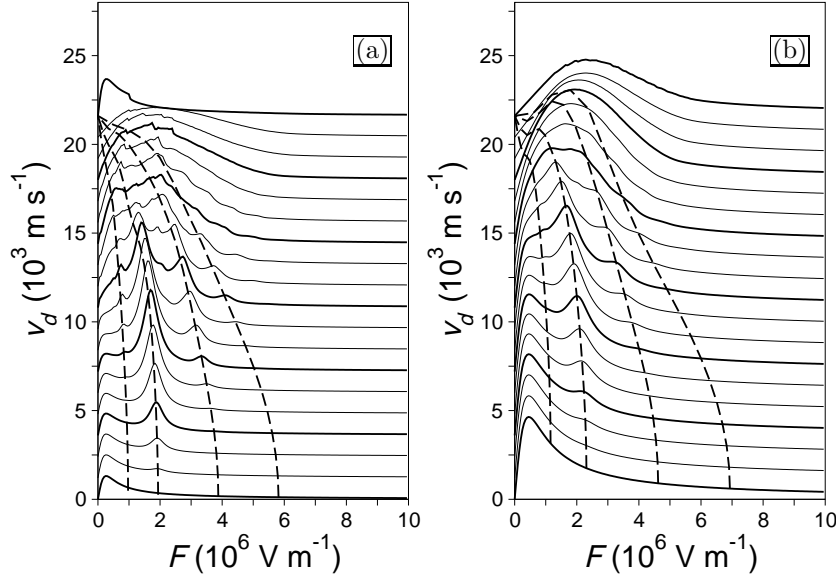


Fig. 4.4: Drift velocity vs. electric field curves calculated at 4.2 K for  $B = 14$  T in (a) superlattice NU2299 and (b) superlattice NU2293. In each panel  $\theta$  increases from  $0^\circ$  to  $90^\circ$  in  $5^\circ$  intervals from bottom to top. Adjacent curves are offset vertically by  $1.2 \times 10^3 \text{ ms}^{-1}$  for clarity. Curves for  $\theta = 0^\circ, 15^\circ, 30^\circ, 45^\circ, 60^\circ, 75^\circ$  and  $90^\circ$  are shown in bold. The dashed lines pass through the points on each curve where  $r = 0.5, 1, 2, 3$  from left to right respectively.

pared to those at 4.2 K. This means that more of the band is occupied at  $t = 0$  at the higher temperature. When considering the difference between superlattices NU2293 and NU2299 at fixed temperature, we note that the miniband width is smaller for superlattice NU2299. This means that a greater proportion of the band will be occupied at  $t = 0$  for superlattice NU2299 and we would therefore expect a reduction in the intensity of the resonance peaks in  $v_d(F)$ . However, the opposite result is found and another explanation must apply.

Unlike the results calculated at two different temperatures in superlattice NU2293, changing to superlattice NU2299 does affect the single electron dynamics. Therefore, the changing dynamics are the cause of the increased intensity resonant peaks in  $v_d(F)$ .

### 4.3 Electrostatics for Superlattice NU2299

We can use the drift-diffusion model (sec. 1.5) to calculate the transport properties,  $I(V)$  and  $G(V) = \frac{\partial I(V)}{\partial V}$ , and the electrostatic properties of a real superlattice system.

Figure 4.5(a) show  $I(V)$  curves calculated using this model for  $B = 14$  T and a range of  $\theta$  values and figure 4.5(b) shows the corresponding experimen-

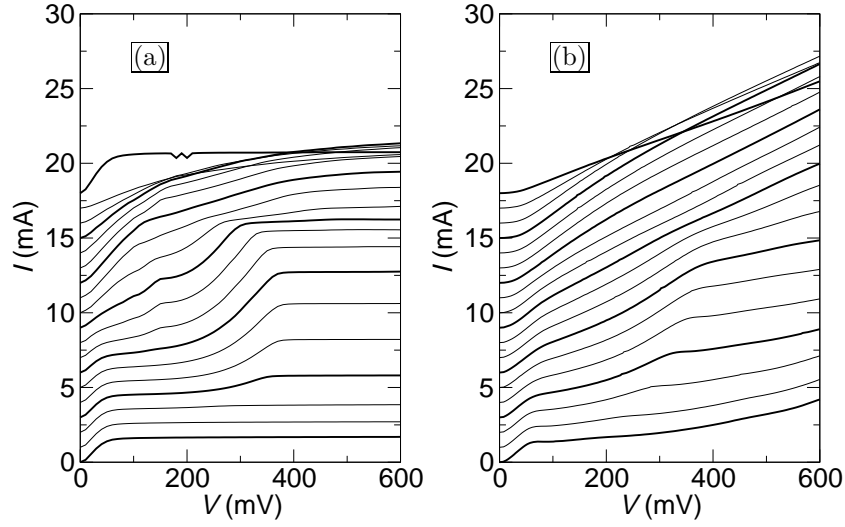


Fig. 4.5: Comparison of (a) theoretical and (b) experimental plots of  $I(V)$  at  $B = 14$  T.  $\theta$  increases from  $0^\circ$  to  $90^\circ$  in  $5^\circ$  intervals from bottom to top. Adjacent curves are vertically offset by 2 mA for clarity. These results are calculated using the model described in chapter 1 with no corrections made for interminiband tunnelling. All experimental data in this chapter are provided by Dr D. Fowler and Dr A. Patanè.

tally measured  $I(V)$  curves. Figure 4.6 shows the  $G(V)$  curves for these same parameters. The experimental and theoretical data does not compare well.

The theoretical data (fig. 4.5(a)) shows that, at  $\theta = 0^\circ$ ,  $I(V)$  is constant above 70 mV. This effect is due to negative differential velocity in  $v_d(F)$ : as voltage is increased, the average electric field increases which causes the electron drift velocity to decrease and so the current remains constant. However, the experimental data (fig. 4.5(b)) shows a rise in current for  $V > 70$  mV. Therefore, either the degree of negative differential velocity in the calculated  $v_d(F)$  curves has been overestimated, or the drift-diffusion model does not work for this superlattice.

As mentioned previously, the main difference between our superlattice samples is that interminiband tunnelling can occur more readily in superlattice NU2299. Because this is the only major difference between the samples, it is the most likely reason why our theoretical results for superlattice NU2299 do not reproduce the experimental results accurately. Therefore, we need to modify either the drift-diffusion model or the form of  $v_d(F)$  to obtain accurate theoretical results. However, to be able to do this, we need to know what the probability of interminiband tunnelling is.

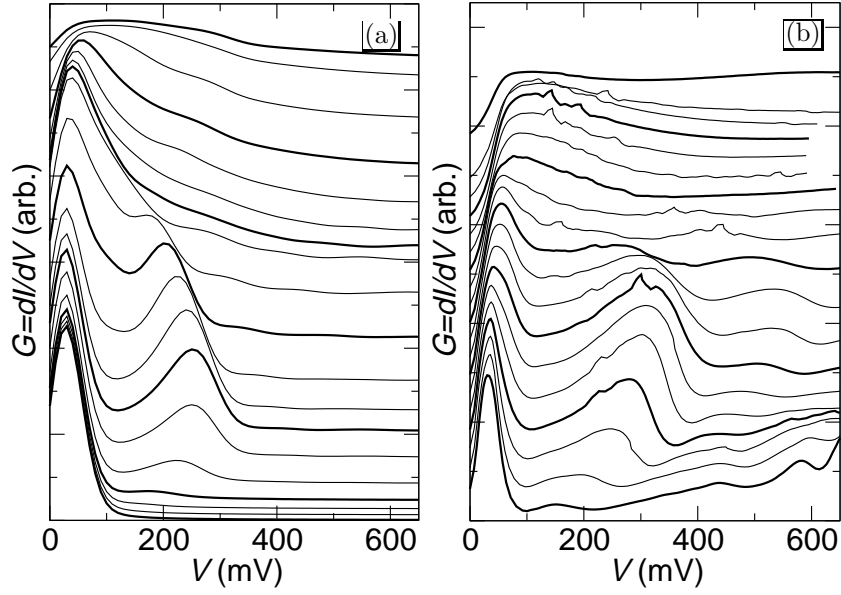


Fig. 4.6: Comparison of (a) theoretical and (b) experimental plots of  $G(V) = dI(V)/dV$  at  $B = 14\text{ T}$ .  $\theta$  increases from  $0^\circ$  to  $90^\circ$  in  $5^\circ$  intervals from bottom to top. Adjacent curves are vertically offset by a varying amount for clarity. These results are calculated using the model described in chapter 1 with no corrections made for interminiband tunnelling.

#### 4.3.1 Probability of Interminiband Tunnelling

To move between the  $\alpha = 0$  and  $\alpha = 1$  minibands, the electrons must tunnel through the triangular barrier shown in figure 4.7. In addition, the wavefunctions must match at the top and bottom of the  $\alpha = 1$  and  $\alpha = 0$  minibands respectively or else the transition will be disallowed. The tunnelling probability can now be calculated(32)(33) by evaluating:

$$T = \exp\left(-2 \int_B^C |\Im k(x)| dx\right) \quad (4.1)$$

where  $B$  and  $C$  are the left and right hand edges of the barrier respectively (see figure 4.7) and  $\Im k(x)$  indicates the imaginary part of the function  $k(x)$ . This equation is essentially an integral over the imaginary dispersion curve in the miniband gap. Zener(32) makes the nearly free electron assumption and obtains a tunnelling probability of:

$$T = \exp\left(-\frac{maE_{gap}^2}{4\hbar^2|eF|}\right) \quad (4.2)$$

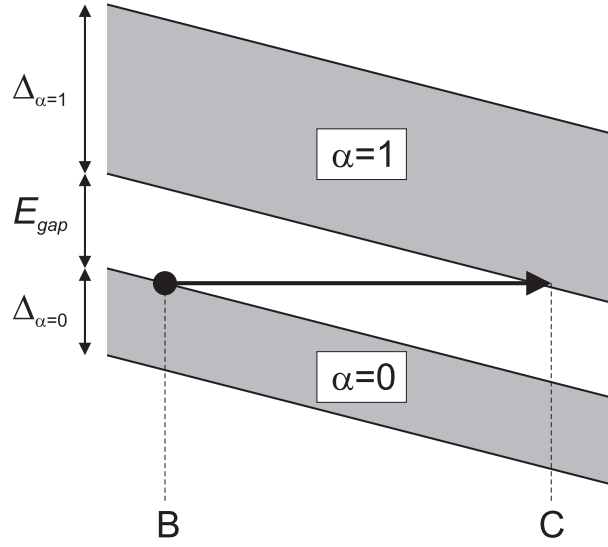


Fig. 4.7: Superlattice with an applied electric field showing tilted minibands. The arrow indicates the Zener tunnelling transition.  $E_{gap}$  is the minibandgap and  $\Delta_\alpha$  are the miniband widths.

where  $a$  is the lattice period,  $E_{gap}$  is the bandgap and  $m$  is the free electron mass. This probability can also be expressed more generally using the reduced electron mass(34)(35):

$$T = \exp\left(-\frac{\sqrt{m^*}\pi E_{gap}^{3/2}}{2\hbar|eF|}\right) \quad (4.3)$$

which does not make the nearly free electron approximation. An overview of this second method is given by Glutsch(36).

In this thesis, we will make the nearly free electron assumption and take the Zener or interminiband tunnelling probability in a superlattice to be:

$$T = \exp\left(-\frac{m^* d E_{gap}^2}{4\hbar^2 |eF| \cos\theta}\right) \quad (4.4)$$

where  $m^*$  is the semiconductor reduced electron mass, i.e. the free electron mass for the superlattice, and  $d \cos\theta$  is the superlattice period along the magnetic field direction. We will further restrict this tunnelling to occur only when the electron is at the top of the  $\alpha = 0$  miniband. Figure 4.8 show the form of  $T(F)$  for (a) superlattice NU2293 and (b) superlattice NU2299. These plots clearly show that the probability of interminiband tunnelling is insignificant for superlattice NU2293 but is  $> 10\%$  for  $F \gtrsim 5 \text{ MVm}^{-1}$  in superlattice NU2299.

We can calculate  $v_d(F)$  for electrons in the  $\alpha \geq 1$  minibands simply by

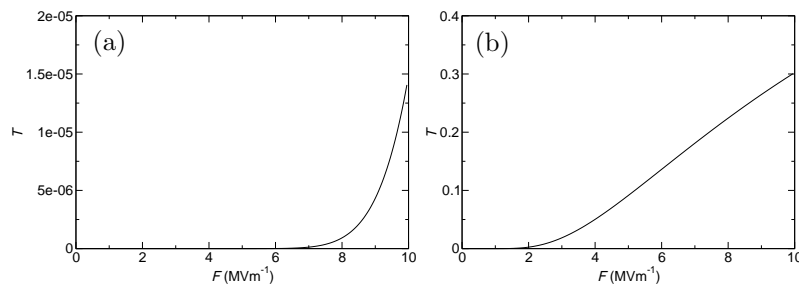


Fig. 4.8: Probability of tunnelling between the first and second minibands in (a) superlattice NU2293 and (b) superlattice NU2299. This probability is calculated using equation 4.4 and the minibandgaps are 66.1 mV and 201.5 mV respectively.

changing the dispersion curve and distribution of initial conditions. In addition, electrons whose  $E(p_x)$  energy component is greater than the superlattice barrier height will behave as if they were free. From figures 1.12 and 1.13 we can see that only the first two minibands have energies lower than the superlattice barriers. Therefore an electron reaching the third miniband will behave as if free and its kinetic energy will increase linearly with distance travelled along  $x$ .

#### 4.4 Modifying the Drift-Diffusion Model

The drift-diffusion model discussed in chapter 1 works very well for superlattice NU2293 (see section 3.3) but not superlattice NU2299. We will attempt to incorporate Zener tunnelling into the model to make it work for this second superlattice. This tunnelling can be added by using two conduction channels. Figure 4.9 shows this model schematically, we use two sets of current continuity equations, one for the  $\alpha = 0$  miniband and one for the  $\alpha = 1$  miniband. The current continuity equations also reflect the possibility of tunnelling between the minibands. Because Zener tunnelling is an elastic transition, the electron changes position rather than energy when tunnelling. Therefore, the electrons in section  $M$  of the second miniband come from both section  $M - 1$  and a section of the first miniband whose position depends on the electric field. Figure 4.9 shows this process diagrammatically. Therefore, each current continuity equation involve more superlattice sections than the single miniband model and the non-linearity of the equation set is substantially increased.

Therefore, the set of equations that must be solved to determine  $I(V)$  now has  $3N + 4$  equations: the original  $2N + 4$  equations and an additional  $N$  equations for current continuity in the second miniband. This set of equations is also more non-linear than the set for the single miniband transport model and we find it impossible to obtain a valid solution to the problem. The most

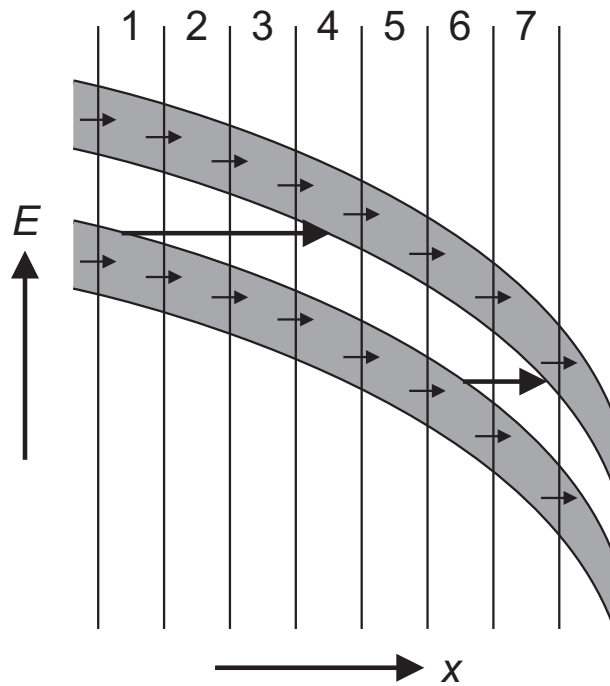


Fig. 4.9: Two conduction channel drift-diffusion model. The shaded areas represent minibands in a non-linear electric field and the bold arrows show Zener tunnelling between them. The small arrows show the direction of electron flow along the minibands. It is clear that this tunnelling can move an electron several superlattice sections (which are delineated by vertical lines). Therefore, the electrons in section four of the higher miniband come from section three of the same miniband as well as region one of the lower miniband. All of these electrons then flow into region five of the upper miniband.

likely reason for this problem is the increased complexity and non-linearity of the equations. Testing has shown that the problem is not due to the choice of initial conditions. Therefore, the two miniband drift-diffusion model has not resulted in an  $I(V)$  curve which incorporates interminiband tunnelling.

#### 4.5 Modifying Drift-Velocity

Because it is not possible to use a two miniband drift-diffusion model, we must use the original single-channel model and modify  $v_d(F)$  to account for interminiband tunnelling. There are two points at which this modification can be made. The first method is to calculate  $v_d(F)$  as normal and then make an addition to it. We do this as follows.

##### 4.5.1 Directly Modifying the $v_d(F)$ Curves

The simplest way to reduce the effects of negative differential velocity (NDV) on  $I(V)$  is to remove NDV from  $v_d(F)$  by adding some function. This function need to account for interminiband tunnelling and the simplest form is to assume that the electron can tunnel from the first to the second miniband in which it behaves as if it were free. We also assume that this tunnelling is only attempted once before an electron scatters. Therefore, the modified electron drift velocity,  $v_{d,mod}(F)$ , is given by:

$$v_{d,mod}(F) = (1 - T(F))v_{d,\alpha=0}(F) + T(F)v_{d,free} \quad (4.5)$$

where  $v_{d,\alpha=0}(F)$  and  $v_{d,free}$  are the electron drift velocities in the first miniband and free space respectively and  $T(F)$  is the probability of an electron tunnelling between these regions. The electron drift velocity in free space is given by:

$$\begin{aligned} v_{d,free} &= \frac{1}{\tau} \int_0^\infty \frac{eF \cos^2 \theta}{2m^*} t e^{-t/\tau} dt \\ &= \frac{eF\tau \cos^2 \theta}{2m^*} \end{aligned} \quad (4.6)$$

assuming that the electron starts from rest at  $t = 0$ . Figure 4.10 plots the modified  $v_d(F)$  relation given by equation 4.5 for  $B = 14$  T and  $\theta = 30^\circ$ . The addition of tunnelling has two effects: firstly, NDV is totally absent except for a small region after the  $r = 1$  peak and secondly, the  $r = 2$  peak now has a similar maxima to the  $r = 1$  peak. These two effects should mean that the current will continue to increase at high voltages and the effect of  $r = 2$  should be more pronounced on the  $I(V)$  results. Note that we scale the  $v_d(F)$  curves by the height of the main superlattice peak so that they can be compared easily and a

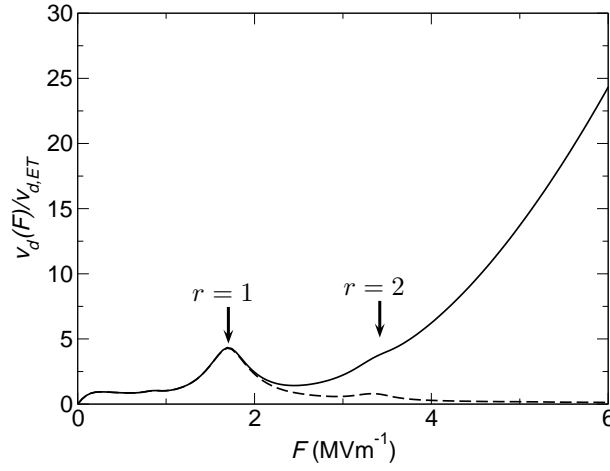


Fig. 4.10: Comparison of electron drift velocity calculated for  $\theta = 30^\circ$  and  $B = 14$  T with (solid) and without (dashed) Zener tunnelling to a free electron state as described by equation 4.5.

similar scaling is made when calculating  $I(V)$  curves (see section 3.2).

It is also possible to add more layers of complexity onto this simple model. The first of these modifications is to assume that the electron can attempt to tunnel multiple times before it is scattered. For example, the tunnelling probability changes to:

$$T_2(F) = T(F) + (1 - T(F))T(F) \quad (4.7)$$

for two tunnelling attempts. A more sophisticated form of this modification is to assume that the number of tunnelling attempts is given by the Bloch frequency because the electron reaches the top of the band once per Bloch oscillation. Therefore the number of tunnelling attempts,  $n_{tun}$ , made before scattering is:

$$n_{tun} = \frac{\tau e F d}{\hbar} \quad (4.8)$$

and the probability of tunnelling is:

$$T_{n_{tun}}(F) = 1 - (1 - T(F))^{n_{tun}}. \quad (4.9)$$

Figure 4.11 shows the  $v_d(F)$  relations for these modifications.

We can also use the full set of minibands and calculate  $v_d(F)$  allowing the electron to tunnel from the first to the second miniband and from there to free.

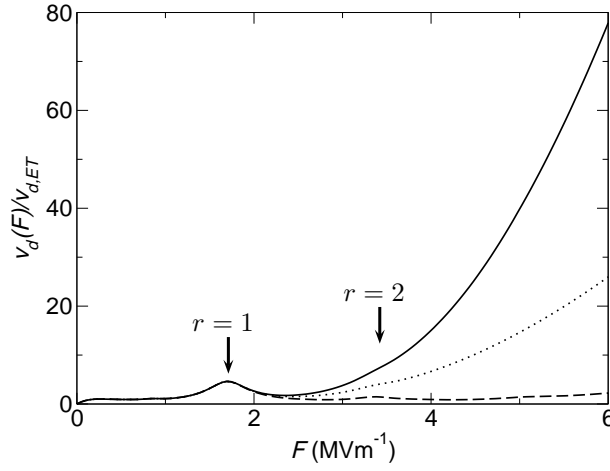


Fig. 4.11: Comparison of electron drift velocity calculated for  $\theta = 30^\circ$  and  $B = 14$  T for a variety of tunnelling probabilities. The dashed line assumes a single tunnelling attempt occurs before scattering (equation 4.5), the dotted line assumes two tunnelling attempts (equation 4.7) and the solid line assumes that the number of tunnelling attempts is given by the Bloch frequency (equations 4.8 and 4.9).

This drift velocity,  $v_{d,2\text{bands}}(F)$ , is given by:

$$\begin{aligned} v_{d,2\text{bands}}(F) &= (1 - T(F))v_{d,\alpha=0}(F) \\ &\quad + T(F)(1 - U(F))v_{d,\alpha=1}(F) \\ &\quad + U(F)T(F)v_{d,\text{free}}(F) \end{aligned} \quad (4.10)$$

where  $U(F)$  is the probability of tunnelling from the second miniband to free. Figure 4.12 shows  $v_{d,2\text{bands}}(F)$  for a variety of tunnelling attempt models. These results show that the rise in drift velocity is much slower than for the simpler miniband to free model, but the  $r = 2$  resonant peak is more intense and the  $r = 3$  peak can also be seen.

The three major problems with directly modifying  $v_d(F)$  are:

1. It cannot account for the increasing number of electrons at increasingly larger  $x$ . This increase occurs because the probability of tunnelling to a lower miniband is small so electrons gradually accumulate in the higher minibands towards the collector contact. Because  $v_d(F)$  is independent of  $x$ , it cannot account for this effect.
2. Directly modifying the  $v_d(F)$  curve doesn't allow the number of tunnelling attempts to be directly determined because this information is contained in  $v_x(t)$  and we must estimate this.

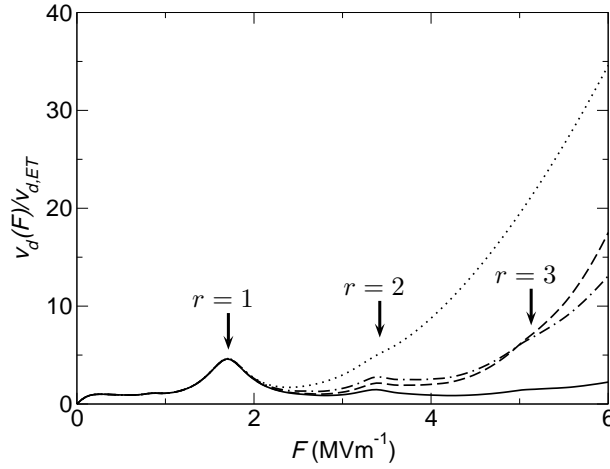


Fig. 4.12: Comparison of electron drift velocity calculated for  $\theta = 30^\circ$  and  $B = 14$  T for a variety of tunnelling probabilities in a two miniband to free model. The solid line assumes a single tunnelling event before scattering, the dot-dashed line assumes three tunnelling events and the dashed line assumes that the number of tunnelling events is given by the Bloch frequency. The dotted line shows  $v_{d,2\text{ bands}}(F)$  for the single miniband to free model with a single tunnelling event for comparison.

3. Finally, because we are taking a linear combination of different drift-velocity curves, we are assuming that all the tunnelling attempts occur at  $t = 0$  which is not true.

#### 4.5.2 Modifying $v_x$

An alternative approach to account for interminiband tunnelling is to modify the electron's velocity before scattering is applied. To do this, we incorporate tunnelling into the calculation of  $v_x$  and then calculate drift velocity using:

$$v_d = \frac{1}{\tau} \int_0^\infty v_x \exp(-t/\tau) dt \quad (4.11)$$

as normal. This method accurately models the number of tunnelling events because the number of times the electron reaches the top of the miniband can be determined. It also does not assume that tunnelling occurs at  $t = 0$ . However, it still suffers from the first deficiency in the list in the previous section. This model also introduces an additional deficiency because scattering is applied after tunnelling. This means that the scattered electrons relax to their equilibrium position in the first miniband, rather than remaining in the same miniband which is the correct behaviour.

Figure 4.13 shows how this model works. When  $v_x$  changes sign from positive to negative, the electron has reached the top of the miniband and a tunnelling

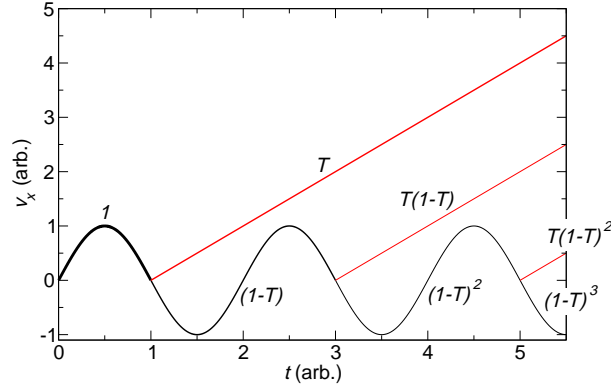


Fig. 4.13: Change in  $v_x$  with time at  $\theta = 0^\circ$  for the first miniband (black) and free (red). A tunnelling event occurs when  $v_{x,\alpha=0}$  changes from positive to negative. The thickness of the lines in this plot is a measure of the probability of the electron following that path (also see labels). The average electron velocity along  $x$  can be calculated using equation 4.12.

attempt can be made. The average electron velocity,  $\bar{v}_x$ , is then calculated from:

$$\bar{v}_x(t) = \sum_{paths} P_{path} v_{x,path}(t) \quad (4.12)$$

which is the sum over all the electron velocities,  $v_{x,path}(t)$ , that the electron could have at time  $t$  weighted by  $P_{path}$ , the probability of the electron having that particular velocity. The paths to consider are motion through the first miniband, motion through the second miniband if using a two miniband model and free electron behaviour.

Figure 4.14 compares  $v_d(F)$  calculated using this model to the unmodified  $v_d(F)$  curve. We show results for both the first miniband to free model and the first miniband to second miniband to free model. The rise in  $v_d(F)$  at high  $F$  for these results is slightly lower than the corresponding rises found when directly modifying  $v_d(F)$ .

### 4.5.3 Other Methods of Calculating $v_d$

There are a number of other ways in which interminiband tunnelling can be accounted for.

Zener tunnelling is often directly incorporated into current calculations without an explicit drift-velocity step(37) and this is a typical feature of  $I(V)$  calculations(8). However, such a method could not be applied to our complex system without making extreme simplifications.

$v_d(F)$  can also be extracted from experimental  $I(V)$  data(38) and this method could potentially be applied to our superlattice system. Another approach in-

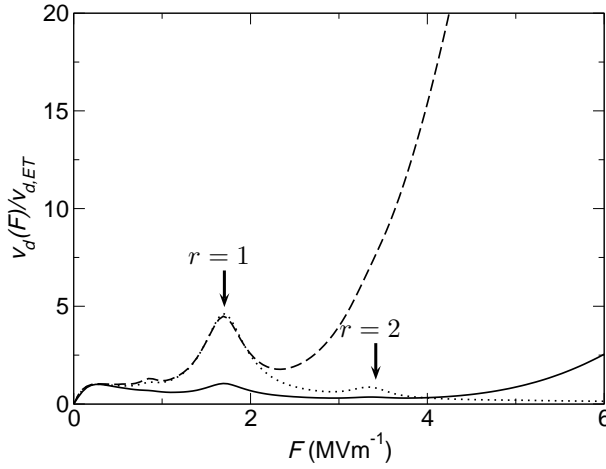


Fig. 4.14: Comparison of electron drift velocity calculated for  $\theta = 30^\circ$  and  $B = 14$  T by modifying  $v_x$  as described in equation 4.12. The dashed line uses a miniband to free model while the solid line uses a first miniband to second miniband to free model. The dotted line shows the unmodified electron drift-velocity.

volves using a quantum mechanical wavepacket model to calculate  $v_d(F)$  which will implicitly include interminiband tunnelling. Such an approach was used by S. Naylor(12) and this produces results that have the same form as those that Sibille *et al*(38) extracted from experimental data. Figure 4.15 shows a  $v_d(F)$  curve calculated for  $\theta = 0^\circ$  and  $B = 14$  T in superlattice NU2299 using this wavepacket method and an increase in  $v_d(F)$  at high  $F$  is clearly seen.

#### 4.6 Choice of Model

We decided to use an empirical approach to determine the form of  $v_d(F)$  because of the wide variety of differing models presented above. This involved matching the calculated  $I(V)$  data at  $\theta = 0^\circ$  to the experimental results by varying  $v_d(F)$ .

We used:

$$v_{d,m}(F) = v_d(F) + A(F) \quad (4.13)$$

as the modified electron drift velocity where  $A(F)$  is some function of electric field used to modify the original  $v_d(F)$  relation. We tried a variety of exponential and power functions for  $A(F)$  and found that there were a range of different additions that produced a relatively good match for  $I(V, \theta = 0^\circ)$ . The best match was achieved for:

$$A(F) = \frac{15}{2} v_{d,ET} \left( \frac{F}{10^7} \right)^{1.4} \quad (4.14)$$

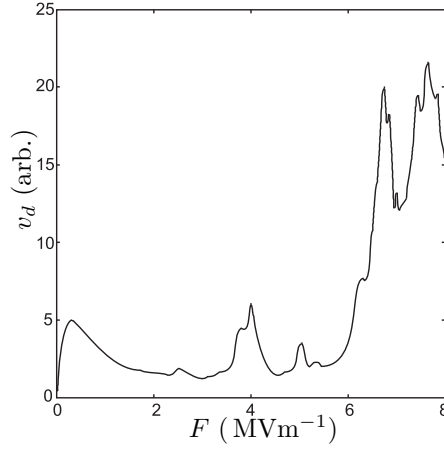


Fig. 4.15: Electron drift-velocity calculated using a wavepacket model for superlattice NU2299 with  $B = 14$  T and  $\theta = 0^\circ$ . Reproduced by kind permission of S. Naylor(12).

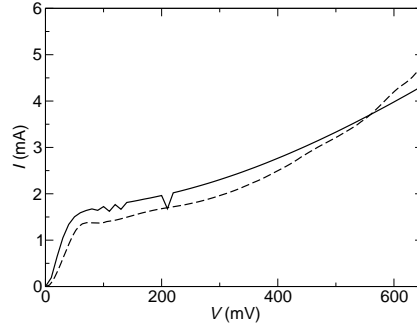


Fig. 4.16: Comparison of  $I(V)$  relation calculated from  $v_{d,m}(F)$  (eqns. 4.13 and 4.14) (solid curve) to experimentally measured data (dashed curve). These curves are for  $B = 14$  T,  $\theta = 0^\circ$  and superlattice NU2299.

where  $v_{d,ET}$  is the height of the Esaki-Tsu drift velocity peak at  $\theta = 0^\circ$ . Figure 4.16 compares  $I(V)$  calculated using this empirical function to experimental data.

A similar procedure was also carried out for  $\theta = 45^\circ$  and the best form of  $A(F)$  was found to be:

$$A(F) = 15v_{d,ET} \left( \frac{F}{10^7} \right)^{1.4}. \quad (4.15)$$

Figure 4.17 shows these modified  $v_d(F)$  curves. In general, the best function for

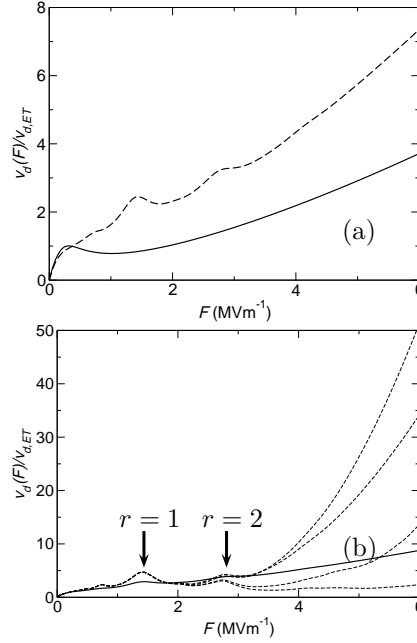


Fig. 4.17: (a) shows electron drift velocity calculated for (solid)  $\theta = 0^\circ$ , (dashed)  $\theta = 45^\circ$  and  $B = 14\text{ T}$  using equations 4.13, 4.14 and 4.15. (b) compares the  $\theta = 45^\circ$  curve to corresponding  $v_d(F)$  curves calculated for a variety of the theoretical models. The rise over the first  $4\text{ MVm}^{-1}$  is similar but the theoretical models tend to predict a high gradient for  $v_d(F > 4\text{ MVm}^{-1})$  which our empirical results do not reflect. However, the electrostatic results that will be shown later (fig. 4.20(b')) will show that the electric field is usually  $< 4\text{ MVm}^{-1}$  when using the empirical  $v_d(F)$  curve.

$A(F)$  is:

$$\begin{aligned}
 A(F) &= \left(15/2 + \frac{15\theta}{90}\right) v_{d,ET} \left(\frac{F}{10^7}\right)^{1.4} & (\theta \leq 45^\circ) \\
 A(F) &= \left(15 - \frac{15(\theta - 45)}{90}\right) v_{d,ET} \left(\frac{F}{10^7}\right)^{1.4} & (\theta > 45^\circ)
 \end{aligned} \quad (4.16)$$

where  $\theta$  is measured in degrees. This formula states that the prefactor varies linearly from  $15/2 \rightarrow 15$  for  $\theta = 0 \rightarrow 45^\circ$  and from  $15 \rightarrow 15/2$  for  $\theta = 45 \rightarrow 90^\circ$ . From this point, the term ‘‘empirical model’’ or ‘‘modified model’’ will refer to adding  $A(F)$  from equation 4.16 to the original  $v_d(F)$  curves. The ‘‘unmodified model’’ will set  $A(F) = 0$ .

The  $v_{d,m}(F)$  curves calculated using this empirical model have a different form to those calculated using most of the theoretical models for interminiband tunnelling (fig. 4.17(b)). However, the rises in  $v_{d,m}(F)$  for the different models are broadly similar to the empirical rise and there are no other obvious features of superlattice NU2299 that would account for this rise. We will

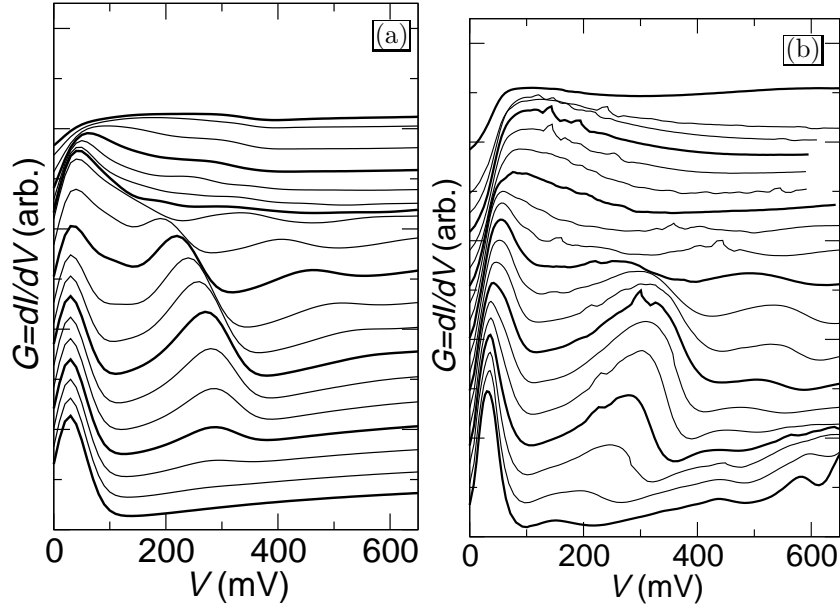


Fig. 4.18: Comparison of (a) theoretical and (b) experimental plots of  $G(V) = dI(V)/dV$  at  $B = 14$  T.  $\theta$  increases from  $0^\circ$  to  $90^\circ$  in  $5^\circ$  intervals from bottom to top. Adjacent curves are vertically offset by a varying amount for clarity. These results are calculated using the model described in chapter 1 and the empirical modification to  $v_d(F)$  outlined in the previous section is used.

therefore attribute the increase in the empirically determined  $v_{d,m}(F)$  curves to interminiband tunnelling.

#### 4.7 Electrostatics Including Interminiband Tunnelling

Figure 4.18(a) compares the  $G(V)$  curves calculated using the empirically model (eqns. 4.13 and 4.16) to the experimentally measured results (fig. 4.18(b)). Our calculated results now show peaks due to  $r = 1$  and  $r = 2$ . This is in contrast to the unmodified model (fig. 4.6(a)) which only shows an  $r = 1$  peak. The calculated results underestimate the voltage at which the  $r = 1$  peak appears and overestimate it for the  $r = 2$  peak. The amplitudes of the peaks are also not exact. However, this is the best overall match to the experimental data that we can produce without significantly varying  $A(F)$  for different  $\theta$ .

Figures 4.19 and 4.20 display the electrostatics calculated for  $B = 14$  T and  $\theta = 0^\circ$  or  $\theta = 45^\circ$  respectively. (a) plots  $r(x, V)$  as contours, (b) plots  $F(x, V)$  as a 3D surface and (c) plots  $n(x, V)$  also as a surface, the bold contours on all three plots correspond to integer values of  $r$ . The left hand columns of figures are calculated using the unmodified  $v_d(F)$  curves and the right hand column use the

empirically modified  $v_{d,m}(F)$  curves (eqns. 4.13 and 4.16). These figures show that the electrostatics undergo a profound change when the empirical model is used to account for interminiband tunnelling.

Comparing  $F(x, V)$  at high  $x$  and  $V$  for  $\theta = 0^\circ$  (fig. 4.19(b,b')), we can see that incorporating interminiband tunnelling prevents the formation of high electric field domains. This means that the electric field only rises to approximately half the value that it did in the unmodified model. The form of the rise in  $F(x, V = \text{const})$  also changes. In the modified model, the steepest electric field gradient occurs at low  $x$  and the variation in  $F$  at high  $x$  is relatively slow, this is in complete contrast to the  $F(x, V)$  behaviour in the unmodified model. However,  $\frac{\partial F}{\partial x}$  in the modified model is much smaller than in the high electric field domain of the unmodified model results. The electron density variation (fig. 4.19(c,c')) also mirrors this change and the modified model produces no charge buildup towards the collector contact (high  $x$ ).

The results for  $\theta = 45^\circ$  (fig. 4.20) show similar behaviour. We again see that  $\frac{\partial F}{\partial x}$  is largest at low  $x$  in the modified model (fig. 4.20(b')) compared to high  $x$  in the unmodified model (fig. 4.20(b)). This change has a large impact on the shape and size of the plateaux in  $F(x, V)$  which directly lead to increases in current (see sec. 3.4 on superlattice NU2293 for an explanation). From the contours on figure 4.20(b'), we can see that  $r = 1$  and  $r = 2$  are both achieved when  $\frac{\partial F}{\partial x}$  is relatively large. We find that the  $r = 1$  plateau initially occurs for  $V = 0.28$  V where it extends across  $\sim 50\%$  of the superlattice (fig. 4.20(a')). However, because  $\frac{\partial F}{\partial x}$  is relatively large, the plateau that forms for  $r = 1$  is much narrower than the corresponding plateau in the unmodified model, which appears when  $\frac{\partial F}{\partial x}$  is small. Because the plateau is narrow, it only extends across a significant proportion of the superlattice for  $0.28 < V < 0.32$  V. In contrast, the  $r = 1$  plateau in the unmodified model extends across a significant proportion of the superlattice length for all  $V > 2.5$  V. These results explain why the  $r = 1$  peak in  $G(V)$  for  $\theta = 45^\circ$  is different in the modified (fig. 4.18(a)) and unmodified (fig. 4.6(a)) models.

The main difference between the models can be seen for  $r = 2$ : the  $G(V)$  curve for  $\theta = 45^\circ$  in the unmodified model (fig. 4.6(a)) shows no  $r = 2$  peak but that for the modified model (fig. 4.18(a)) does. The  $r = 2$  plateau in the unmodified model (fig. 4.20(a)) occurs in the high electric field domain when  $\frac{\partial F}{\partial x}$  is very high. This causes the plateau to be very narrow, and, because it occurs at high  $V$  and  $x$ , the proportion of the superlattice over which  $r = 2$  is very small. Therefore, no appreciable increase in current occurs. Conversely, the the plateaux in the modified model (fig. 4.20(a')) are very similar except that the  $r = 2$  plateau is slightly narrower than the  $r = 1$  plateau and extends over a similar proportion of the superlattice for all  $V > 0.5$  V. It is also possible

to see the  $r = 2$  plateau in the  $F(x, V)$  surface for the modified model (fig. 4.20(b')). This means that a peak due to  $r = 2$  forms in the  $\theta = 45^\circ$   $G(V)$  curve for the modified model (fig. 4.18(a)). We can see that this peak is wider and less intense than the  $r = 1$  peak on the same curve. This is because the  $r = 2$  plateau is narrower than the  $r = 1$  plateau but varies in width more slowly with  $V$ . Therefore, we see a smaller current enhancement that extends over a wider range of  $V$ .

In summary, we see a peak due to  $r = 2$  when using the modified model because of the suppression of the high electric field domain. This suppression occurs because interminiband tunnelling causes a significant rise in  $v_d(F)$  at high  $F$  because the electrons can move faster in higher minibands. This effect is not significant for superlattice NU2293 which has a much larger minibandgap than superlattice NU2299 so the probability of interminiband tunnelling is negligible.

#### 4.8 Conclusion

This chapter has considered superlattice NU2299 whose first minibandgap is a third of the size of the corresponding gap for superlattice NU2293. We can attempt to incorporate this effect into our models by either modifying  $v_d(F)$ , modifying  $v_x(t)$ , or modifying the drift-diffusion model. We found that the latter approach proved unusable and that there are many levels of sophistication that can be included when modifying  $v_d(F)$  or  $v_x$  which give widely varying  $v_d(F)$  curves.

Therefore, we used an empirical approach to calculate a modified  $v_d(F)$  curve by matching the resulting  $I(V)$  curves to experimentally measured data. This approach resulted in a  $v_d(F)$  curve that was broadly similar to, but did not exactly match, the theoretical models for this modification. The curves were similar enough to be able to attribute the change in  $v_d(F)$  to interminiband tunnelling.

Making the modification to  $v_d(F)$  had a dramatic effect on the superlattice electrostatics. We found that high field domain formation was completely suppressed and that the electric field gradient was highest near the injector contact. This caused the  $r = 2$  plateau in  $F(x, V)$  to increase in width which means that the electron drift velocity is enhanced across more of the superlattice. This enhancement causes a visible peak in  $G(V)$  which is in agreement with the experimental data.

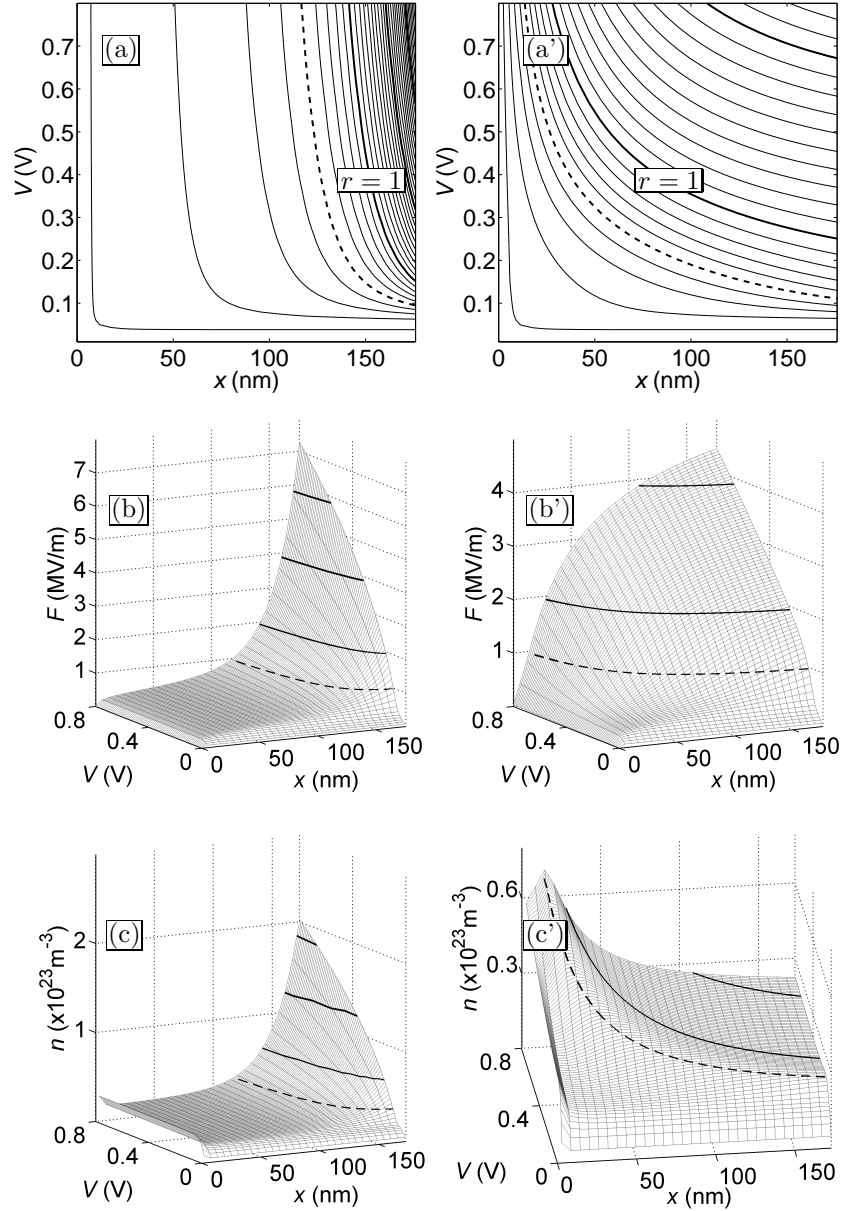


Fig. 4.19: Contour plots (a) showing  $r$  as a function of  $x$  and  $V$ . The contours are in steps of 0.1 with the broken contour indicating  $r = 0.5$  and the bold contours indicating when  $r$  is an integer. (b-c) show 2D surface plots of  $F$  and  $n$  respectively as functions of  $x$  and  $V$ . The solid contours indicate when  $r$  is an integer and the broken contour indicates  $r = 0.5$ . This data is calculated for  $B = 14 \text{ T}$  and  $\theta = 0^\circ$  with the unmodified (left) and modified (right)  $v_d(F)$  curves.

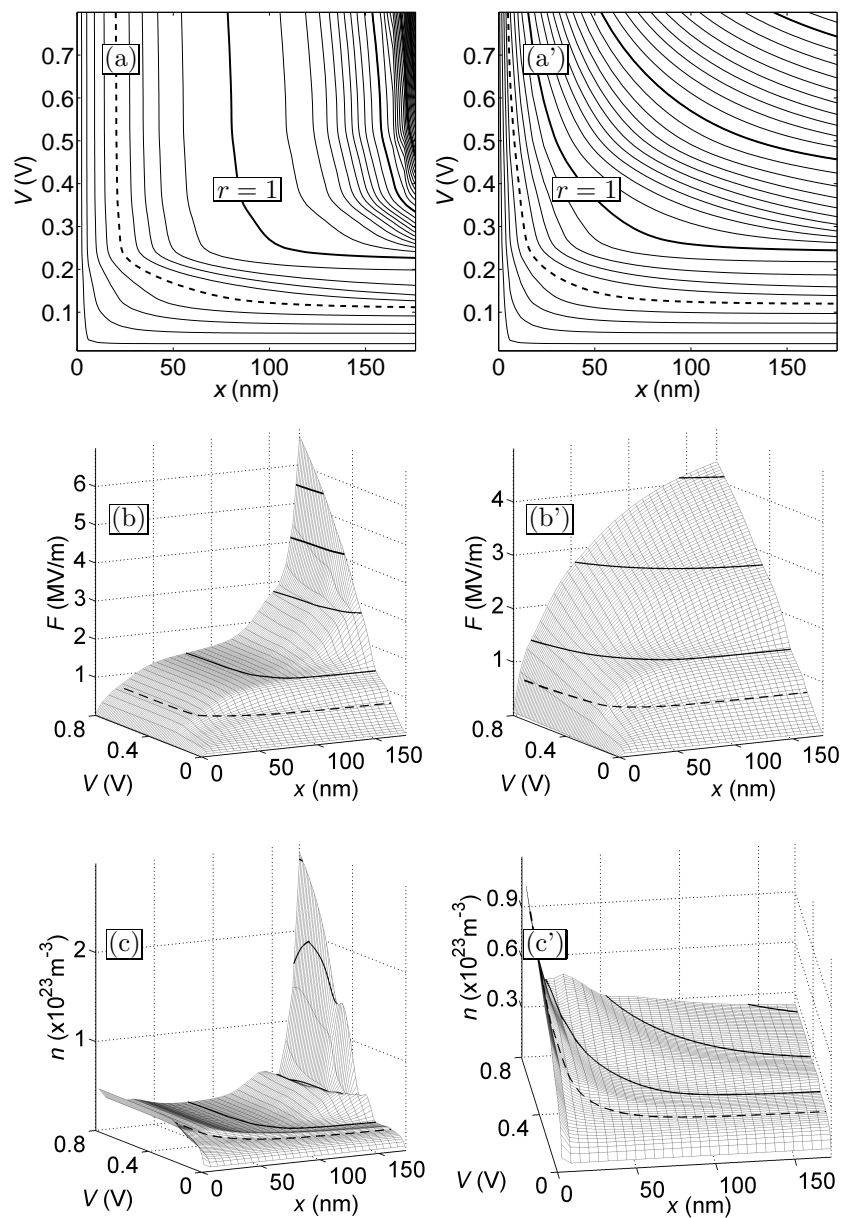


Fig. 4.20: Contour plots (a) showing  $r$  as a function of  $x$  and  $V$ . The contours are in steps of 0.1 with the broken contour indicating  $r = 0.5$  and the bold contours indicating when  $r$  is an integer. (b-c) show 2D surface plots of  $F$  and  $n$  respectively as functions of  $x$  and  $V$ . The solid contours indicate when  $r$  is an integer and the broken contour indicates  $r = 0.5$ . This data is calculated for  $B = 14 \text{ T}$  and  $\theta = 45^\circ$  with the unmodified (left) and modified (right)  $v_d(F)$  curves.

## 5. QUANTUM ANALYSIS OF SUPERLATTICE NU2293

## 5.1 Introduction

The semiclassical method for determining electron behaviour for our system, characterised by the Hamiltonian derived in section 1.3, has been explored in the previous chapters. This chapter will focus on obtaining the quantum-mechanical energy eigenstates of the system. To obtain these eigenstates, we solve Schrödinger's equation for the full Hamiltonian, which includes the superlattice periodic potential and the applied electric and magnetic fields. We can then calculate the electron probability density functions from which we can obtain Wigner functions. The probability density plots can be compared to semiclassical electron orbits and the Wigner functions to Poincaré sections. The exact procedure for determining these probability density and Wigner functions will be developed later in this chapter.

This chapter will examine the correlation between the quantum-mechanical and semiclassical systems and chapter 6 will look at the quantum system in more detail.

Systems that exhibit quantum chaos have been studied for a number of systems previously(39). These include cold atom(40)(41), semiconductor (42; 43; 44; 45; 46; 47; 48; 49; 50) and optical(51) systems whose chaotic behaviour arises from direct confinement in a quantum well. However, our system is substantially different in that we need to use quantum mechanics to find even classical chaos because we use superlattice minibands in the semiclassical model.

## 5.2 Quantum Mechanical Formulation of the Tilted Field System

To determine the quantum mechanical electron probability distributions, we solve the Schrödinger equation:

$$\hat{H}\Psi_g = E_g\Psi_g \quad (5.1)$$

which has an infinite number of solutions each labelled with the index  $g$ . We will use the matrix method outlined in appendix A to find these solutions.

The quantum Hamiltonian operator is similar to the semiclassical Hamiltonian 1.70. However, it explicitly contains the superlattice potential rather than the miniband dispersion curve:

$$\hat{H} = -\frac{\hbar^2}{2m^*} \left( \frac{\partial^2}{\partial x^2} + \frac{\partial^2}{\partial z^2} \right) + V_{eff}(\mathbf{r}), \quad (5.2)$$

where

$$V_{eff}(\mathbf{r}) = V_{SL}(x) - eFx + \frac{1}{2}m^*\omega_C^2(x \sin \theta - (z - z_0) \cos \theta)^2, \quad (5.3)$$

$z_0 = p_y/eB \cos \theta$  and  $V_{SL}$  is shown in figure 1.12. This Hamiltonian is derived in the same way as the semiclassical Hamiltonian in Chapter 1 except that  $V_{SL}(x)$  and the operator  $-\frac{\hbar^2}{2m^*} \frac{\partial^2}{\partial x^2}$  for motion in the  $x$  direction are not replaced by the dispersion curve  $E(k)$ . The Hamiltonian can be written in the form

$$\hat{H} = \hat{H}_0 + \Delta\hat{H}, \quad (5.4)$$

where

$$\hat{H}_0 = -\frac{\hbar^2}{2m^*} \left( \frac{\partial^2}{\partial x^2} + \frac{\partial^2}{\partial z^2} \right) + V_{SL}(x) + \frac{1}{2} m^* \omega_C^2 z^2 \cos^2 \theta \quad (5.5)$$

and

$$\Delta\hat{H} = -eFx + \frac{1}{2} m^* \omega_C^2 x^2 \sin^2 \theta - m^* \omega_C^2 xz \sin \theta \cos \theta. \quad (5.6)$$

We will use the solutions of the eigenequation  $\hat{H}_0 \Psi_g^0 = E_g \Psi_g^0$  as our basis set for constructing the full Hamiltonian matrix. The following procedure is used to obtain this basis set.

Because  $\hat{H}_0$  contains no  $xz$  cross terms, it can be separated into  $x$  and  $z$  components:

$$\hat{H}_0 = \hat{H}_x + \hat{H}_z \quad (5.7)$$

where

$$\hat{H}_x = -\frac{\hbar^2}{2m^*} \left( \frac{\partial^2}{\partial x^2} \right) + V_{SL}(x) \quad (5.8)$$

and

$$\hat{H}_z = -\frac{\hbar^2}{2m^*} \left( \frac{\partial^2}{\partial z^2} \right) + \frac{1}{2} m^* \omega_C^2 z^2 \cos^2 \theta. \quad (5.9)$$

These components are separable so a product wavefunction can be defined:

$$\Psi_g^0 = \psi_{k,\alpha}^0(x) \varphi_n^0(z) \quad (5.10)$$

where  $\psi_{k,\alpha}^0(x)$  is the  $\alpha^{\text{th}}$  solution to  $\hat{H}_x \psi_{k,\alpha}^0 = E_{k,\alpha} \psi_{k,\alpha}^0$  for a given  $k$  and  $\varphi_n^0(z)$  is the  $n^{\text{th}}$  solution to  $\hat{H}_z \varphi_n^0 = E_n \varphi_n^0$ .

Each eigenfunction,  $\psi_{k,\alpha}^0(x)$ , can be determined by expanding the superlattice potential as a Fourier series and using Bloch's theorem as described in appendix A. We use a numerical method in preference to an analytical method, such as the Krönig-Penny model, because our numerical method can be easily adapted to different superlattice potentials.

Because the Bloch functions obtained by the above procedure have infinite extent along the  $x$ -direction, they are not ideal basis states for the full wavefunctions of a finite system. An alternative orthogonal basis set that can be constructed from the Bloch function set consists of Wannier functions(52). These Wannier functions extend over only a few superlattice periods and are

therefore ideal for modelling a finite structure. The general form of a Wannier function is:

$$\phi_{m,\alpha}(x) = N_{m,\alpha} \frac{d}{2\pi} \int_{-\pi/d}^{+\pi/d} e^{-imkd} \psi_{k,\alpha}(x) dk \quad (5.11)$$

where  $N_{m,\alpha}$  is a normalising factor,  $m$  defines which quantum well the Wannier function is centred on and  $\alpha$  defines the “band” index. There are a large number of possible sets of Wannier functions which depend on the phase chosen for the Bloch functions. It is important to choose this phase correctly because a poor choice will not lead to localised Wannier functions. The maximally localised Wannier functions, known as the Wannier-Kohn functions(53)(54), are created using the following rules for phase:

1. If  $\psi_{k=0,\alpha}(0)$  and  $\psi_{k=\pi/d,\alpha}(0)$  are non-zero, then the phase should be chosen such that the Bloch function  $\psi_{k,\alpha}(0)$  is real.
2. If  $\psi_{k=0,\alpha}(0)$  and  $\psi_{k=\pi/d,\alpha}(0)$  are zero, then the phase should be chosen such that the Bloch function  $\psi_{k,\alpha}(0)$  is imaginary.
3. Otherwise, the  $x$  coordinate should be shifted by  $d/2$  which will result in one of the above situations.

Using these rules, the Wannier-Kohn functions can be determined and figure 5.1 shows the  $m = 0$  and  $\alpha = 0, 1, 2, 3$  functions for superlattice NU2293. The  $m \neq 0$  Wannier functions for a given  $\alpha$  are simply obtained by shifting the  $m = 0$  function by integer multiples of  $d$  along the  $x$ -axis. We will replace  $\psi_{k,\alpha}^0(x)$  with  $\phi_{m,\alpha}^0(x)$  in equation 5.10 and we have added a 0 superscript to indicate that it is being used as a basis state.

Eigenfunction  $\varphi_n^0(z)$ , the second term in equation 5.10, is obtained from the solutions to  $\hat{H}_z \varphi_n = E_n \varphi_n$  which is a simple harmonic oscillator Schrödinger equation (55). These solutions are:

$$\varphi_n^0(z) = N_n h_n(\beta z) \exp\left(-\frac{1}{2}\beta^2 z^2\right). \quad (5.12)$$

Here,

$$\beta = \sqrt{m^* \omega_C \cos \theta / \hbar}, \quad (5.13)$$

$N_n$  is a normalising constant,  $h_n$  are the Hermite polynomials and  $n = 0, 1, 2, \dots, \infty$ .

We now have our basis states and the final solutions to Schrödinger’s equation 5.1, which contains Hamiltonian 5.2, have the form:

$$\Psi_g^0(x, z) = \sum_{m,n,\alpha} C_{g(m,n,\alpha)} \phi_{m,\alpha}^0(x) \varphi_n^0(z) \quad (5.14)$$

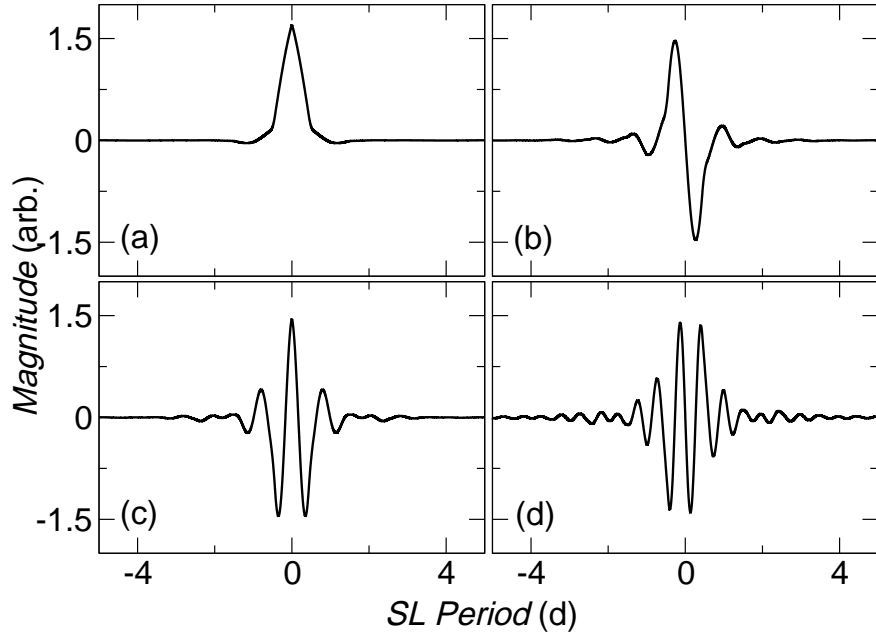


Fig. 5.1: Locally maximised Wannier functions (Wannier-Kohn functions) for superlattice NU2293 and (a)  $\alpha = 0$ , (b)  $\alpha = 1$ , (c)  $\alpha = 2$  and (d)  $\alpha = 3$ . Therefore, the Wannier functions are mostly localised to a single superlattice period for low energies (low  $\alpha$ ).

where the index  $g$  is some combination of the  $m$ ,  $n$  and  $\alpha$  indices and the  $C_{g(m,n,\alpha)}$  coefficients will be obtained from the solution to the Hamiltonian matrix equation. In full:

$$\hat{H} \sum_{m,n,\alpha} C_{g(m,n,\alpha)} \phi_{m,\alpha}^0(x) \varphi_n^0(z) = E \sum_{m,n,\alpha} C_{g(m,n,\alpha)} \phi_{m,\alpha}^0(x) \varphi_n^0(z). \quad (5.15)$$

### 5.3 Construction of the Hamiltonian Matrix

As previously noted, a simple numerical solution of Schrödinger's equation can be obtained by diagonalising the Hamiltonian matrix (see appendix A). The elements of this matrix are:

$$H_{g,g'} = \langle \Psi_g^0 | \hat{H} | \Psi_{g'}^0 \rangle \quad (5.16)$$

where  $\Psi_g^0$  and  $\Psi_{g'}^0$  are basis states of the form 5.14. To construct the actual matrix, it will be easiest to use the three minor indices,  $m$ ,  $n$  and  $\alpha$ , from equations 5.11 and 5.12 and combine them into the major index  $g$ . In addition, the full Hamiltonian will be divided into parts to simplify the construction of

the Hamiltonian matrix. The final matrix elements are given by:

$$H_{m,n,\alpha,m',n',\alpha'} = \left\langle \phi_{m,\alpha}^0 \varphi_n^0 \left| \hat{H} \right| \phi_{m',\alpha'}^0 \varphi_{n'}^0 \right\rangle. \quad (5.17)$$

To evaluate the matrix elements, the Hamiltonian will be divided into three parts,  $\hat{H}_x$ ,  $\hat{H}_z$  and  $\Delta\hat{H}$ , described by equations 5.8, 5.9 and 5.6 respectively. The three following sections will each determine one of these matrix element parts.

### 5.3.1 Evaluation of Matrix Element due to $\hat{H}_x$

We define the matrix element relating to  $\hat{H}_x$  as:

$$H_{x;m,n,\alpha,m',n',\alpha'} = \left\langle \phi_{\alpha',m'} \left| \hat{H}_x \right| \phi_{\alpha,m} \right\rangle \quad (5.18)$$

which can be simplified to:

$$H_{x;m,n,\alpha,m',n',\alpha'} = \left\langle \phi_{\alpha',m'} \left| \hat{H}_x \right| \phi_{\alpha,m} \right\rangle \langle \varphi_{n'} | \varphi_n \rangle \quad (5.19)$$

$$= \left\langle \phi_{\alpha',m'} \left| \hat{H}_x \right| \phi_{\alpha,m} \right\rangle \delta_{n',n} \quad (5.20)$$

because the  $\varphi$  basis set is independent of  $x$  and orthonormal. Expanding out the form of the Wannier functions using equation 5.11 gives:

$$\begin{aligned} H_{x;m,n,\alpha,m',n',\alpha'} &= N_{m,\alpha}^2 \left( \frac{d}{2\pi} \right)^2 \int_{-\infty}^{\infty} \left[ \int_{-\pi/d}^{\pi/d} e^{im'k'd} \psi_{k',\alpha'} dk' \hat{H}_x \right. \\ &\quad \left. \times \int_{-\pi/d}^{\pi/d} e^{-imkd} \psi_{k,\alpha} dk \right] dx \delta_{n',n} \end{aligned} \quad (5.21)$$

$$\begin{aligned} &= N_{m,\alpha}^2 \left( \frac{d}{2\pi} \right)^2 \int_{-\pi/d}^{\pi/d} \int_{-\pi/d}^{\pi/d} e^{i(m'k'-mk)d} \\ &\quad \times \left\langle \psi_{k',\alpha'} \left| \hat{H}_x \right| \psi_{k,\alpha} \right\rangle dk dk' \delta_{n',n}. \end{aligned} \quad (5.22)$$

The bra-ket term in equation 5.22 simply equals the energy eigenvalues of a Bloch function in a periodic potential (Appendix A) so  $\left\langle \psi_{k',\alpha'} \left| \hat{H}_x \right| \psi_{k,\alpha} \right\rangle = E_{k,\alpha} \delta_{k,k'} \delta_{\alpha,\alpha'}$ . Therefore, the  $H_x$  matrix elements reduce to:

$$H_{x;m,n,\alpha,m',n',\alpha'} = N_{m,\alpha} \frac{d}{2\pi} \int_{-\pi/d}^{\pi/d} e^{-ik(m-m')d} E_{k,\alpha} dk \delta_{n',n}. \quad (5.23)$$

where one of the normalising constants has been lost because we now only have a single integral. This final point is not important to our calculations because  $N_{m,\alpha}$  is determined numerically.

5.3.2 Evaluation of Matrix Element due to  $\hat{H}_z$ 

We define the matrix element relating to  $\hat{H}_z$  as:

$$H_{z;m,n,\alpha,m',n',\alpha'} = \left\langle \phi_{\alpha',m'} \varphi_{n'} \left| \hat{H}_z \right| \phi_{\alpha,m} \varphi_n \right\rangle \quad (5.24)$$

which reduces to:

$$= \left\langle \varphi_{n'} \left| \hat{H}_z \right| \varphi_n \right\rangle \langle \phi_{\alpha',m'} | \phi_{\alpha,m} \rangle \quad (5.25)$$

$$= \left\langle \varphi_{n'} \left| \hat{H}_z \right| \varphi_n \right\rangle \delta_{m,m'} \delta_{\alpha,\alpha'} \quad (5.26)$$

where the bra-ket term is given by the eigenvalues of a simple harmonic oscillator (55). Therefore:

$$H_{z;m,n,\alpha,m',n',\alpha'} = \hbar\omega_C \cos \theta \left( n + \frac{1}{2} \right) \delta_{n,n'} \delta_{m,m'} \delta_{\alpha,\alpha'} \quad (5.27)$$

5.3.3 Evaluation of Matrix Element due to  $\Delta\hat{H}$ 

We define the matrix element relating to  $\Delta\hat{H}$  as:

$$\Delta H_{m,n,\alpha,m',n',\alpha'} = \left\langle \phi_{\alpha',m'} \varphi_{n'} \left| \Delta\hat{H} \right| \phi_{\alpha,m} \varphi_n \right\rangle \quad (5.28)$$

which can be reduced to:

$$\begin{aligned} &= \frac{1}{2} m^* \omega_C^2 \sin^2 \theta \langle \phi_{m',\alpha'} | x^2 | \phi_{m,\alpha} \rangle \delta_{n,n'} \\ &- \langle \phi_{m',\alpha'} | x | \phi_{m,\alpha} \rangle (eF \delta_{n,n'} + m^* \omega_C^2 \sin \theta \cos \theta \langle \varphi_{n'} | z | \varphi_n \rangle). \end{aligned} \quad (5.29)$$

The integrals  $\langle \phi_{m',\alpha'} | x | \phi_{m,\alpha} \rangle$  and  $\langle \phi_{m',\alpha'} | x^2 | \phi_{m,\alpha} \rangle$  will have to be determined numerically but this will only need to be done once per unique set of  $\psi_{k,\alpha}$  bases. The integral  $\langle \varphi_{n'} | z | \varphi_n \rangle$  has a known, analytical solution(56):

$$\langle \varphi_{n'} | z | \varphi_n \rangle = \frac{\sqrt{\hbar}}{\sqrt{2m^* \omega_C \cos \theta}} (\delta_{n-1,n'} \sqrt{n} + \delta_{n+1,n'} \sqrt{n+1}). \quad (5.30)$$

Therefore:

$$\begin{aligned} \Delta H_{m,n,\alpha,m',n',\alpha'} &= \frac{1}{2} m^* \omega_C^2 \sin^2 \theta \langle \phi_{m',\alpha'} | x^2 | \phi_{m,\alpha} \rangle \delta_{n,n'} \\ &- \langle \phi_{m',\alpha'} | x | \phi_{m,\alpha} \rangle \left( eF \delta_{n,n'} + m^* \omega_C^2 \sin \theta \cos \theta \right. \\ &\quad \left. \times \frac{\sqrt{\hbar}}{\sqrt{2m^* \omega_C \cos \theta}} (\delta_{n-1,n'} \sqrt{n} + \delta_{n+1,n'} \sqrt{n+1}) \right). \end{aligned} \quad (5.31)$$

### 5.3.4 The Full Hamiltonian Matrix

The full Hamiltonian matrix can now be constructed by adding the matrix elements defined in equations 5.23, 5.27 and 5.31:

$$\underline{H} = \underline{H}_x + \underline{H}_z + \underline{\Delta H}. \quad (5.32)$$

Due to the complexity of the elements of this matrix, it will not be written out in full here. The next section will consider the structure of this matrix.

## 5.4 Solving the Eigenvalue Problem

We can now solve the matrix problem:

$$\underline{H} \underline{C} = E \underline{C} \quad (5.33)$$

to give the  $C_{g(m,n,\alpha)}$  coefficients which are required by equation 5.14 to determine the energy eigenfunctions. These coefficients are obtained by diagonalising the Hamiltonian matrix and we use the DSBEVX LAPACK(57) routine to achieve this. The key issue is how to combine the  $m$ ,  $n$  and  $\alpha$  sub-indices into the main index  $g$  to arrange the full Hamiltonian matrix. In general, a matrix with its non-zero elements close to the diagonal is easiest to diagonalise and the form of  $g(m,n,\alpha)$  should reflect this.

To arrange the indices optimally, the points at which the matrix will be zero need to be considered:

- For given  $m$  and  $m'$  indices, the full Hamiltonian matrix will not have any guaranteed zeros because the  $\langle \phi_{m',\alpha'} | x | \phi_{m,\alpha} \rangle$  and  $\langle \phi_{m',\alpha'} | x^2 | \phi_{m,\alpha} \rangle$  integrals can take a finite value for any  $m$  and  $m'$ . Therefore  $m$  should be one of the “inner” indices, i.e. close to the diagonal.
- For given  $n$  and  $n'$  indices, the matrix will only be non-zero on the diagonal ( $n = n'$ ) and first sub- and super-diagonals ( $n = n' \pm 1$ ) (see eqn. 5.30). Therefore  $n$  is a good choice for the “outer” index.
- Like  $m$ , given  $\alpha$  and  $\alpha'$  values will not guarantee any zeros in the matrix and so should also be “inner” indices.

We will construct the full matrix with  $m$  as the inner index,  $\alpha$  as the middle index and  $n$  as the outer index. Thus the major index,  $g$ , is given by:

$$g(m,n,\alpha) = n((m_{max} + 1) \times (\alpha_{max} + 1)) + \alpha(m_{max} + 1) + m \quad (5.34)$$

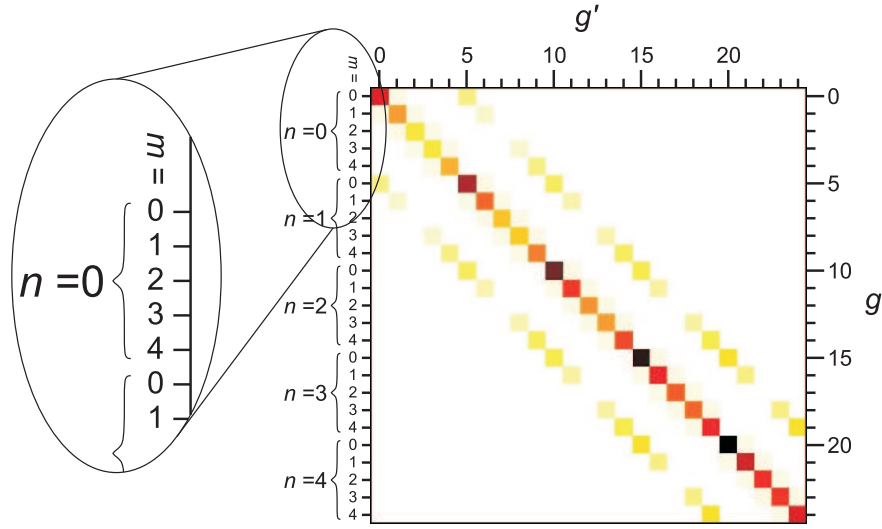


Fig. 5.2: Scaled colourmap intensity image of the absolute values of a Hamiltonian matrix. This matrix is for a 5 period superlattice with  $B = 11$  T,  $\theta = 60^\circ$  and  $r = 1$ . The basis has only 5  $n$  states and a single  $\alpha$  state to reduce its size. The decomposition of index  $g$  into  $m$  and  $n$  indices is also shown.

where the indices are numbered from zero. Index  $m$  is chosen in preference to index  $\alpha$  as the innermost index because it relates to the superlattice length which will tend to be constant. This choice of  $m$  as the innermost index means that the integrals  $\langle \phi_{m',\alpha'} | \phi_{m,\alpha} \rangle$ ,  $\langle \phi_{m',\alpha'} | x | \phi_{m,\alpha} \rangle$  and  $\langle \phi_{m',\alpha'} | x^2 | \phi_{m,\alpha} \rangle$  need only be constructed once for a superlattice of a given length (fixed  $m$  range). They can then be reused for different magnetic fields to reduce computational time. Figure 5.2 shows an example of such a matrix with 5  $m$  values, 5  $n$  values and a single  $\alpha$  value. This figure clearly shows a main diagonal and two off-diagonal peaks which correspond to  $m = m'$  and  $n - n' = 0, \pm 1$ . Matrix elements with  $m \neq m'$  are very small in comparison to the  $m = m'$  matrix elements and cannot be seen on this plot.

We now have all the information required to determine the energy eigenvalues and eigenfunctions for this system using equations 5.33 and 5.14.

## 5.5 Wigner Functions

We discussed a Wigner function method for generating a phase space map of a wavefunction in section 2.8. The basic form of a 1D Wigner function is:

$$W(x, p_x) = \frac{1}{\pi\hbar} \int_{-\infty}^{\infty} \Psi^*(x + \lambda) \Psi(x - \lambda) e^{2ip_x\lambda/\hbar} d\lambda \quad (5.35)$$

where  $W(x, p_x)$  is the Wigner quasi-probability distribution. For a 2D wavefunction, such as  $\Psi(x, z)$ , the Wigner function is four dimensional,  $W(x, z, p_x, p_z)$ , which needs to be reduced to a 2D function of different variables,  $W(p_z, q_y)$ , for comparison to the semiclassical Poincaré sections. A mapping between position and momentum can be obtained from the semiclassical Hamiltonian using the procedure described in section 3.2.4. We obtain the transformation equations (equations 3.9 and 3.14 in section 3.2.4):

$$x = \frac{1}{eF} \left( -H + \frac{q_y^2 + p_z^2}{2m^*} + E(p_x) \right) \quad (5.36)$$

and

$$z = \frac{1}{\cos \theta} \left( -\frac{q_y}{eB} + x \sin \theta \right), \quad (5.37)$$

where  $H$  is the energy of the particular eigenstate under consideration. It should be noted that since we are using the semiclassical Hamiltonian to derive transformation equations 5.36 and 5.37, the resulting Wigner functions will only be strictly accurate in the semiclassical limit and for an infinite superlattice. Therefore, the Wigner function of any wavefunctions which lie close to the edges of the spatial region spanned by our finite basis need to be considered with caution. We require that  $p_x$  is zero when calculating the Wigner functions to be compared with the  $p_x = 0$  Poincaré sections. Because it is not possible to produce a stroboscopic Wigner function without changing the form of the Hamiltonian, we will restrict our Wigner function vs. Poincaré section comparison to the  $p_x = 0$  plane of phase space.

A Wigner function comparable to the  $p_x = 0$  Poincaré sections can now be calculated by mapping  $(p_z, q_y)$  onto  $(x, z, p_x, p_z)$  using equations 5.36 and 5.37:

$$\begin{aligned} W(p_z, q_y) \rightarrow W(x, z, p_x = 0, p_z) &= \frac{1}{4\pi^2 \hbar^2} \int_{-\infty}^{\infty} \int_{-\infty}^{\infty} \Psi^*(x + \lambda_x, z + \lambda_z) \\ &\times \Psi(x - \lambda_x, z - \lambda_z) e^{2ip_z \lambda_z / \hbar} d\lambda_x d\lambda_z. \end{aligned} \quad (5.38)$$

The Wigner functions calculated using this method can be directly compared to  $p_x = 0$  Poincaré sections to see if quantum phase space patterns analogous to stochastic webs form. The Wigner functions will also be useful in determining if any scarring of wavefunctions occurs. Scarring is an effect whereby electron wavefunctions are localised along the paths of unstable periodic classical orbits(44)(58)(59). Such scars may manifest themselves as deviations from the usual form of the Wigner functions(60). Scarred states are most likely to be present in short superlattices where classical periodic orbits due to reflections

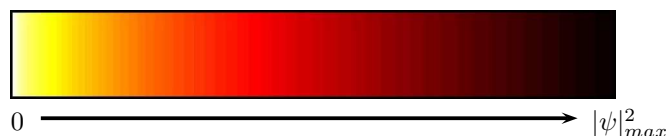


Fig. 5.3: Colourmap used for eigenstate probability density,  $|\Psi|^2$ , plots in this thesis. This colourmap is non-linear in RGB colourspace to allow low intensity features to be resolved. All figures are scaled to make full use of this colourmap.

off the ends of the superlattice are more probable.

## 5.6 Analysing the Quantum Data

There are three main pieces of data that we use to analyse the quantum eigenstates. Firstly, the energy eigenvalues of the Hamiltonian will be useful when looking at the distribution of energy levels and the transitions between them. The eigenvalues will be plotted as  $E(N)$  curves where  $N$  is the eigenstate index (starting at  $N = 0$  and ordered by increasing energy). Secondly, we will consider the probability density functions,  $|\Psi|^2$ , which show the spatial form of a particular eigenstate. These probability density plots will be shown as 2D colourplots using the colourmap defined in figure 5.3. For all the probability density figures,  $x$  is on the horizontal axis and  $z$  on the vertical. The axes values may vary between figures but the distance between the centres of two small antinodes in the  $x$  direction is always the superlattice period,  $d$ , and the  $x$ - and  $z$ -axes have the same scale. For each energy level, we can determine the position and width of the corresponding eigenstate along the  $x$ -axis. We can therefore plot where electrons with a particular energy are likely to be found in the superlattice. This information will be used to understand electron transport along the superlattice direction. Finally, Wigner functions will be plotted as 2D colour images using the colourmap defined in figure 5.4. These Wigner functions will have  $p_z$  on the horizontal axis and  $q_y$  on the vertical and the axis limits will both be  $(-2 \rightarrow 2) \times 10^{-25} \text{ kg ms}^{-1}$ , unless otherwise noted. These Wigner functions will be used to identify features that are hard to see in real space probability density plots - similar to how Poincaré sections were used in the semiclassical analysis.

In general, this chapter will look at two different systems. The first system will simulate a 61 period superlattice by using a basis with  $m = 0 \rightarrow 60$ . This long superlattice is designed to give results that are largely independent of the boundary conditions imposed by a limited basis set. We will compare an electron's behaviour in this system to the infinite semiclassical model. Our second superlattice system consists of only 14 periods, which is comparable to

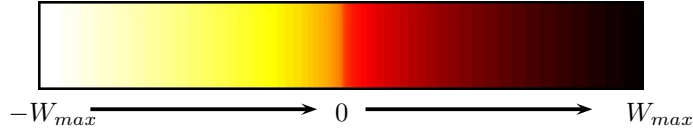


Fig. 5.4: Colourmap used for Wigner function quasi-probability plots,  $W(x, z, p_x = 0, p_z)$ , in this thesis. This colourmap is scaled so low intensity features can be seen, it is therefore non-linear in RGB colourspace. The Wigner functions are plotted so that the centre of the colourmap is zero and the positive and negative scaling is identical.

the NU2293 experimental system and will be used to examine electron transport. The main difference between this 14 period system and the real superlattice used in experiments is that the model doesn't account for the superlattice contacts in any way. Therefore the eigenstates will be those for a superlattice with infinite potential barriers at its ends rather than with finite barriers linked to a circuit. Because of this lack of contacts, we will not be able to calculate any currents directly using the quantum model. In both superlattices, unless otherwise noted, we use  $n = 0 \rightarrow 120$  and  $\alpha = 0$  to construct our Hamiltonian matrix.

We use a magnetic field of  $B = 11$  T for the long superlattice because this value is consistent with the majority of semiclassical and experimental results obtained. However, for the shorter system, we found it necessary to increase the magnetic field to keep more electron states away from the contacts. We generally use small  $\theta$  values of  $\theta = 15^\circ$  to  $30^\circ$  because these values lead to more regular semiclassical electron behaviour which is easier to match to quantum eigenstates. After examining general trends at these low angles, we look at some higher angles to see how they compare. The majority of this chapter will be concerned with resonant values of  $r$ , typically  $r = 1$ , because the semiclassical results have shown that novel behaviour occurs for these parameters. However, the effect of varying  $r$  on the quantum system will also be investigated.

## 5.7 Energy Eigenvalues of the Superlattice

In this section, we will explore the spectrum of energy eigenvalues to initially identify overall features and trends which we will examine in more detail later in the thesis.

Figure 5.5 shows the energy eigenvalues of a 14 period superlattice with  $B = 20$  T and (a)  $\theta = 0^\circ$ ,  $r = 1$ , (b)  $\theta = 30^\circ$ ,  $r = 1$ , (c)  $\theta = 30^\circ$ ,  $r = \frac{1+\sqrt{5}}{2}$  plotted as a function of eigenstate index  $N$ . All three plots show characteristic curving tails which are a consequence of the boundary conditions imposed by the finite number of basis states.

We previously noted that transitions between eigenstates can be mediated

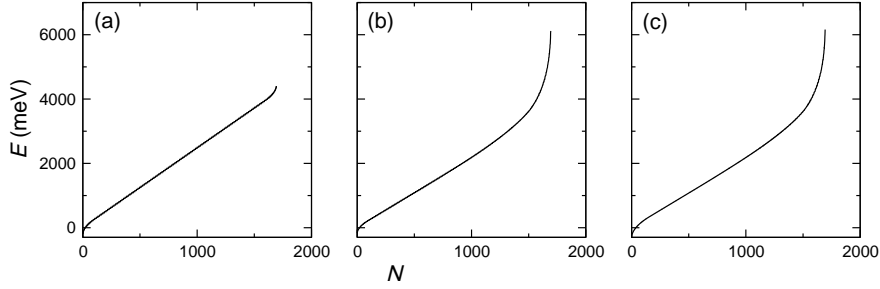


Fig. 5.5: Energy eigenvalues,  $E(N)$ , calculated for a 14 period superlattice with  $B = 20$  T and (a)  $\theta = 0^\circ$ ,  $r = 1$ , (b)  $\theta = 30^\circ$ ,  $r = 1$ , (c)  $\theta = 30^\circ$ ,  $r = \frac{1+\sqrt{5}}{2}$ . These plots are at each end, which is a consequence of the finite number of basis states used for the calculations.

by phonons with energies of tens of meV (section 1.2.2), therefore it is energy spectrum over this range that is important when considering electron transport. Figure 5.6 shows a magnification of the energy spectra for the 14 period superlattice calculated for a range of  $\theta$  values with  $B = 20$  T and  $r = 1$ . This figure shows a clear step structure, which implies that there is a repeating set of eigenstates with some periodic energy increase, i.e. a staircase function combined with some periodic function. At  $\theta = 0^\circ$  (upper curve), the eigenstates on a step are degenerate but this degeneracy is lost as soon as the magnetic field is tilted. This loss of degeneracy is the first evidence within the quantum model that tilting the magnetic field causes a fundamental change in an electron's behaviour. Electron probability distributions will be used to investigate these steps in section 5.9.

When the system is off-resonance, the distribution of energy eigenvalues changes dramatically. Figure 5.7 shows how the step structure changes for non-integer values of  $r$ . When  $r = \frac{1+\sqrt{5}}{2}$  (black curve) there is no obvious step structure for this irrational value of  $r$  and the energy eigenvalues increase approximately linearly with increasing  $N$ . However, an altered step structure exists for non-integer rational values of  $r$  and this is particularly strong at  $r = \frac{1}{2}$  (grey curve). We find that values of  $r$  within  $\sim 5\%$  of  $r = 1$  (green and blue curves) also exhibit a strong step structure which has the same size steps as the  $r = 1$  curve (red). We will continue analysing the effect of the resonance condition in section 5.10.

## 5.8 Electron Probability Distributions for the Superlattice

Figure 5.8 shows probability density plots for a range of energy eigenstates. These plots clearly show that there is a wide variety of electron density profiles for a single set of parameters - in this case a 61 period superlattice with  $B =$

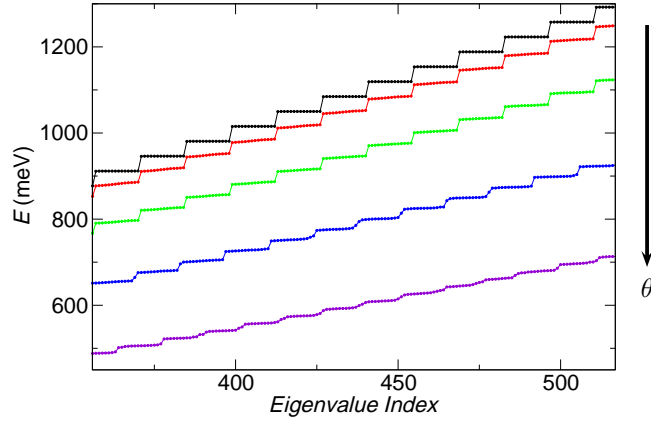


Fig. 5.6: Energy eigenvalues plotted as a function of eigenstate index  $N$  for a 14 period superlattice with  $B = 20$  T,  $\theta = 0^\circ, 15^\circ, 30^\circ, 45^\circ, 60^\circ$  from top to bottom and  $r = 1$ . These plots show the loss of degeneracy within each step as soon as  $\theta \neq 0^\circ$ . The step height gradually decreases as  $\theta$  increases because, for given  $r$  and  $B$ ,  $eFd \propto \cos \theta$ , and  $eFd$  determines the step height (see section 5.9).

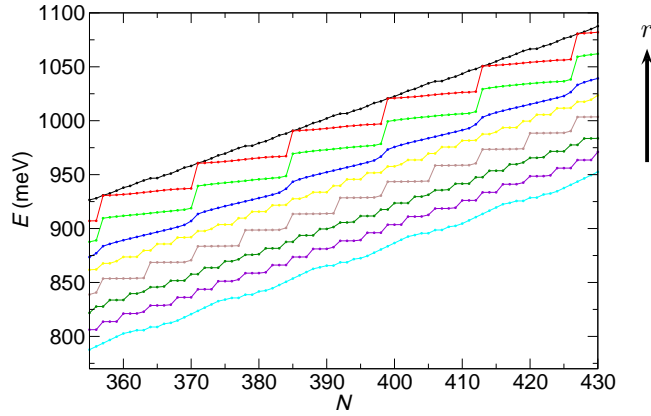


Fig. 5.7: Energy eigenvalues plotted as a function of eigenstate index  $N$  for a 14 period superlattice with  $B = 20$  T,  $\theta = 30^\circ$  and  $r = \frac{1+\sqrt{5}}{2}, 1, 0.99, 0.95, 0.6, 0.5, 0.4, 0.25$  and  $0.1$  from top to bottom. These plots show the variation in step function as  $r$  is altered. Adjacent curves are offset by 20 meV for clarity, with only the lower (cyan) curve having no offset.

11 T,  $\theta = 30^\circ$  and  $r = 1$ .

This figure shows that eigenstate probability density functions with similar energies can take very different forms. For example, eigenfunctions (b) and (c) occupy different regions of space while (d) overlaps both of these regions. Eigenfunction (e) is concentrated in the region where (b) and (c) overlap. Eigenfunctions (a) and (f) both occupy subsets of the region filled by (b). Much of this behaviour mirrors the semiclassical electron orbits seen in chapter 3. For example, the different regions occupied by eigenfunctions (b) and (c) are similar to the two regions of electron orbit density seen in figure 3.4(f). To explore this correspondence, in figure 5.9 we overlay a semiclassical electron orbit on the probability density plot of a quantum mechanical eigenfunction. This comparison shows that the semiclassical electron trajectory occupies almost exactly the same region of space as the electron probability density in figure 5.8(b). Finally, as expected, these plots show that the antinodes are located in the middle of the quantum wells rather than in the barriers.

If the real space behaviour of an electron in the semiclassical and quantum-mechanical models has some correspondence, it follows that there will also be a correspondence in phase space. Figure 5.10 shows Wigner functions (a-e) calculated for energy eigenfunctions (a-e) in figure 5.8, while (f) shows the semiclassical Poincaré section. Figure 5.10(d) in particular shows good correspondence to the Poincaré section because it has maxima along many of the stochastic filaments in the semiclassical web. In general, regions in the Wigner functions can be easily matched to stable islands in the Poincaré section. Within these regions, the quasiprobability repeatedly flips between positive and negative.

There is an upper limit of the real-space  $x$  spread of the wavefunction which is imposed by the finite length of the 61 period superlattice being modelled. The  $z$  spread of the wavefunction is limited by the number of  $n$  values used in the basis which also causes the  $x$  spread to be limited because the wavefunction takes a characteristic 2D shape. The dashed lines on figure 3.4(d) indicate the  $x$  spread limits, the left hand limit is imposed by the energy of the eigenstate and the right hand limit is, in this case, imposed by the finite number of  $n$  basis states used. Equation 5.36 can be used to translate this limit in  $x$  spread into a limit in  $\rho^2 = q_y^2 + p_z^2$  spread. Figure 5.10 shows this  $\rho$  limit as a dashed circle and it is clear that the Wigner functions have zero quasiprobability outside this limit.

The major difference between the quantum and semiclassical phase spaces is that the electron distribution in the quantum system is spread between both “stable” and “chaotic” regions - although of course these terms have no real meaning for a quantum system. However, in the semiclassical system, an electron trajectory is confined to either a single stable island or to the stochastic

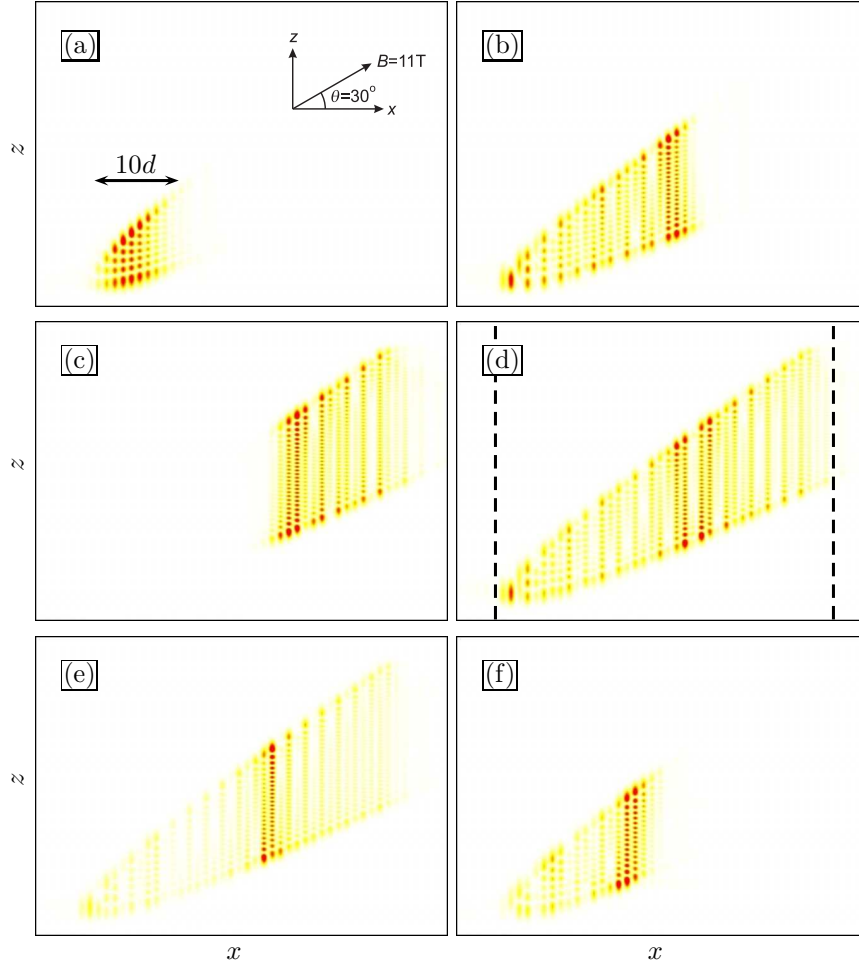


Fig. 5.8: Probability density plots,  $|\Psi(x, z)|^2$ , for six energy eigenstates of a 61 period superlattice calculated for  $B = 11$  T,  $\theta = 30^\circ$  and  $r = 1$ . The plots show the  $N =$  (a) 1182, (b) 1200, (c) 1201, (d) 1202, (e) 1206 and (f) 1219, eigenstates whose energies are 426.84 meV, 432.31 meV, 432.46 meV, 432.77 meV, 433.21 meV and 435.55 meV respectively. Each plot is shown on an identical set of axes so the real-space region covered by the different energy eigenstates can be easily compared. Plots (b) and (c) occupy different regions of space while (d) and (e) overlap both these regions to some degree. Plots (a) and (f) occupy subsets of the region filled by (b). The dashed lines on (d) indicate the  $x$  spread of the probability density function. The colourmap used is shown in figure 5.3 and varies from white to yellow to red to black from zero to  $(|\Psi|^2)_{\max}$ .

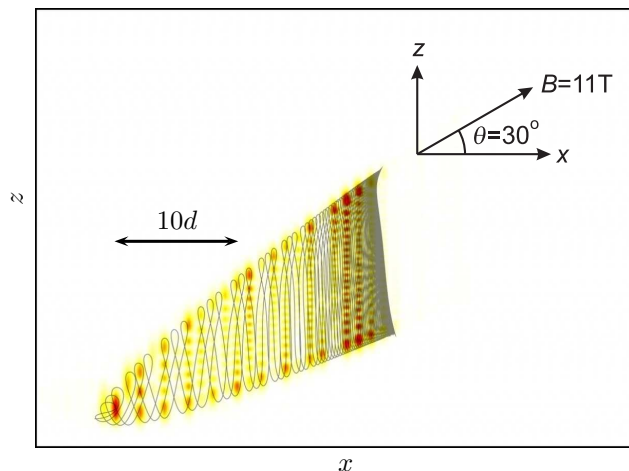


Fig. 5.9: Probability density plot for  $B = 11$  T,  $\theta = 30^\circ$  and  $r = 1$  with the corresponding semiclassical electron trajectory, starting from rest, overlaid on it. This probability density data is identical to that shown in figure 5.8(b).

web.

Figure 5.11 compares more Wigner functions and Poincaré sections, this time calculated for  $\theta = 30^\circ, 45^\circ$  or  $60^\circ$ ,  $B = 11$  T and  $r = 1$  or 2. We can clearly see a correspondence between the semiclassical and quantum data for these parameters. The Wigner functions show a number of regions whose location corresponds to that of the stable islands in the Poincaré sections. Therefore, some quantum analogue of the stochastic filaments exists. We will examine the effects of this confining potential and its effects on the realspace eigenstate probability densities in section 6.1.

As  $\theta$  increases, a chaotic sea forms at the centre of the Poincaré sections and this appears as a low intensity blurred region in the Wigner functions. The electron probability density can easily flow out of this region and be trapped in a stable island.

This thesis will not evaluate the correspondence between semiclassical and quantum phase spaces any further because this comparison has been carried out in detail by others. In particular, the PhD thesis of D. Sherwood(27) devotes a large section to this. However, we should note that the Poincaré sections correspond well to the Wigner functions in all cases that were studied in producing this thesis.

### 5.9 Explanation of the Steps in the On-Resonance $E(N)$ Curves

We will now examine why there is a step function component in  $E(N)$  when the system is on-resonance (figures 5.6 and 5.7). This section will not look at the different eigenstates on these steps but chapter 6 will investigate them in

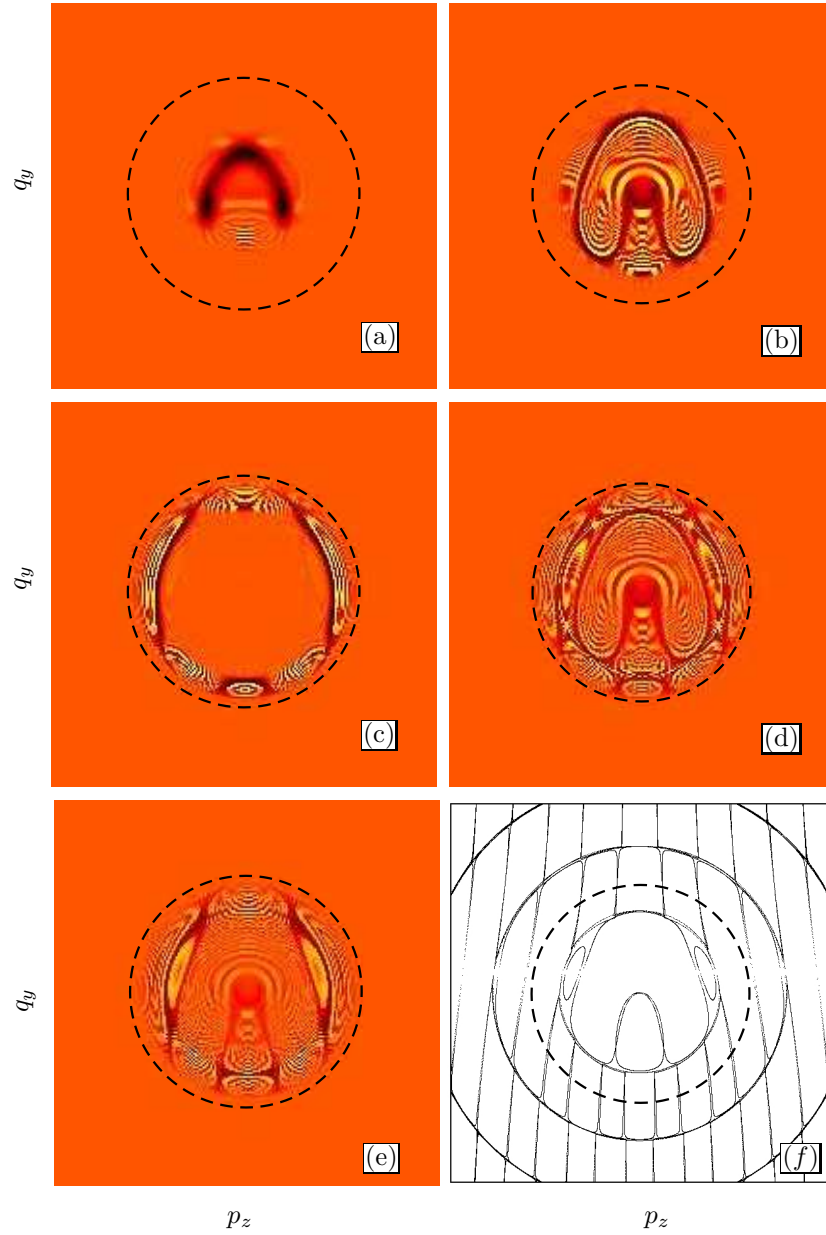


Fig. 5.10: (a-e) show Wigner functions corresponding to wavefunctions (a-e) in figure 5.8 calculated for a 61 period superlattice with  $B = 11$  T,  $\theta = 30^\circ$  and  $r = 1$ , (f) shows the semiclassical Poincaré section for the same parameters. We see that (b) covers a region of phase space corresponding to the first ring of the semiclassical stochastic web while (c) occupies some of the second ring. (d) and (e) both occupy a region equivalent to the first and some of the second rings of this web. The broken circles show the limits on the spread of the Wigner function caused by the finite superlattice. All plots have axes from  $(-2 \rightarrow 2) \times 10^{-25}$  kg ms $^{-1}$  and the colourmap in figure 5.4 is used which is white $\rightarrow$ yellow $\rightarrow$ orange $\rightarrow$ red $\rightarrow$ black from negative $\rightarrow$ positive and orange is zero.

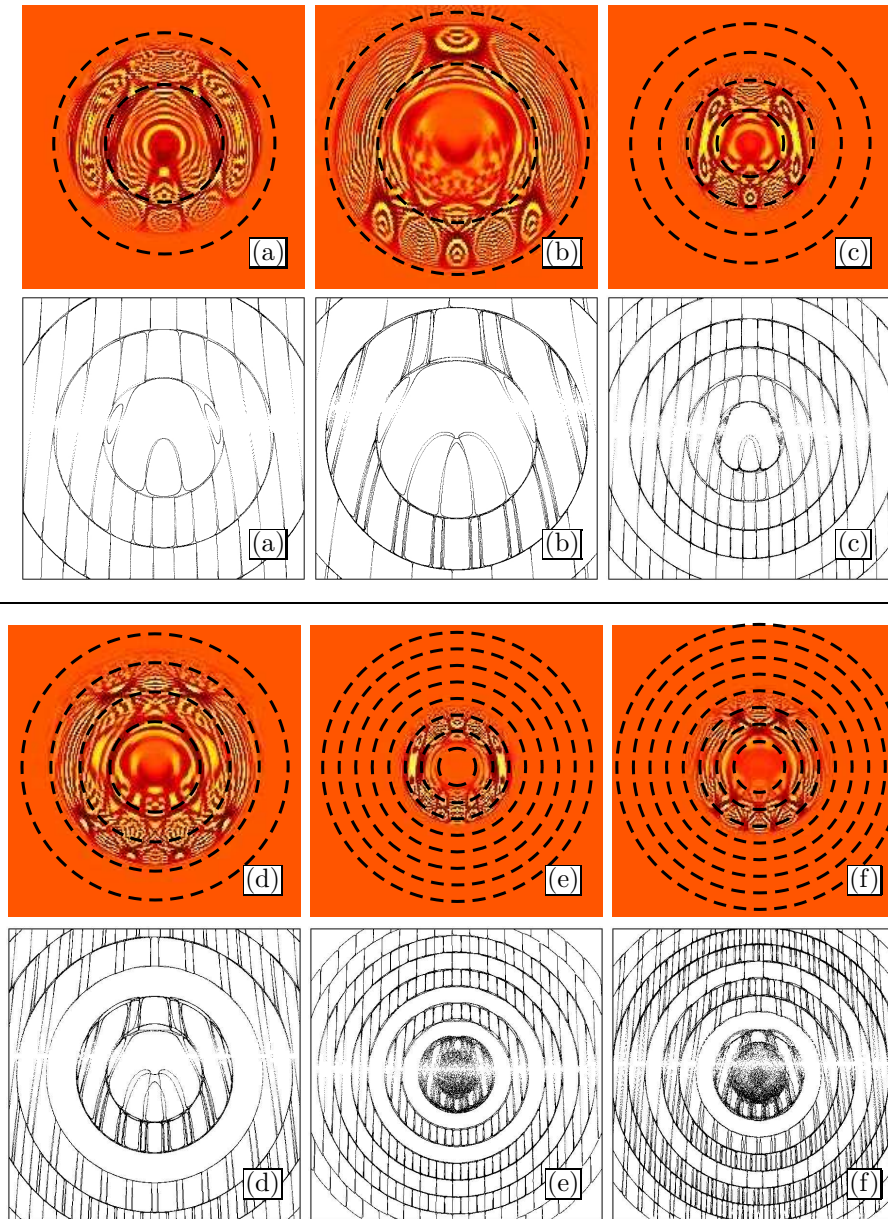


Fig. 5.11: Comparison of Wigner functions (upper) to Poincaré sections (lower).  $B = 11$  T and (a) is for  $\theta = 30^\circ$ ,  $r = 1$ , (b) is for  $\theta = 30^\circ$ ,  $r = 2$ , (c) is for  $\theta = 45^\circ$ ,  $r = 1$ , (d) is for  $\theta = 45^\circ$ ,  $r = 2$ , (e) is for  $\theta = 60^\circ$ ,  $r = 1$  and (f) is for  $\theta = 60^\circ$ ,  $r = 2$ . Wigner function (a) shows a number of ripple-like features which exist between the stochastic filaments of the corresponding Poincaré section (indicated by broken circles on Wigner plots). This region of the Poincaré section should contain stable islands but they are not shown because it would make the Poincaré sections too complex for these small figures (see figure 3.15 for example). The Wigner functions for other parameters also show this correspondence and (d) shows features which correspond to stable islands within the first three rings of the stochastic web.

detail.

Figure 5.12 shows the eigenvalues of the system when  $B = 11$  T,  $\theta = 15^\circ$  and  $r = 1$  and the inset clearly shows this step function in  $E(N)$ . We can explain this step by showing that a coordinate shift of  $(x, z) = (d, d \tan \theta)$  in Hamiltonian 5.2 leaves the Hamiltonian invariant save for an energy shift of  $-eFd$ (27). Shifting the Hamiltonian gives:

$$\begin{aligned} \hat{H}(x' - d, z' - d \tan \theta) &= -\frac{\hbar^2}{2m^*} \left( \frac{\partial^2}{\partial x'^2} + \frac{\partial^2}{\partial y'^2} \right) - eF(x' - d) \\ &+ V_{SL}(x' - d) + \frac{1}{2}m^*\omega_C^2 ((x' - d) \sin \theta - (z' - d \tan \theta) \cos \theta)^2 \end{aligned} \quad (5.39)$$

which can be simplified, due to the periodicity of the lattice, to:

$$\begin{aligned} \hat{H}(x' - d, z' - d \tan \theta) &= -\frac{\hbar^2}{2m^*} \left( \frac{\partial^2}{\partial x'^2} + \frac{\partial^2}{\partial y'^2} \right) - eF(x') \\ &+ V_{SL}(x') + \frac{1}{2}m^*\omega_C^2 (x' \sin \theta - z' \cos \theta)^2 + eFd. \end{aligned} \quad (5.40)$$

Therefore,

$$\hat{H}(x' - d, z' - d \tan \theta) = \hat{H}(x', z') + eFd \quad (5.41)$$

or

$$\hat{H}(x', z') = \hat{H}(x, z) - eFd. \quad (5.42)$$

So, if  $\hat{H}(x, z)\Psi_n(x, z) = E_n\Psi_n(x, z)$ , then:

$$\begin{aligned} \hat{H}(x' - d, z' - d \tan \theta)\Psi_n(x' - d, z' - d \tan \theta) \\ = E_n\Psi_n(x' - d, z' - d \tan \theta) \end{aligned} \quad (5.43)$$

substituting in for equation 5.41 and rearranging gives:

$$\hat{H}(x', z')\Psi_n(x' - d, z' - d \tan \theta) = (E_n - eFd)\Psi_n(x' - d, z' - d \tan \theta). \quad (5.44)$$

Finally, we remove the primes to leave

$$\hat{H}(x, z)\Psi_n(x - d, z - d \tan \theta) = (E_n - eFd)\Psi_n(x - d, z - d \tan \theta). \quad (5.45)$$

Therefore, shifting a wavefunction by  $(d, d \tan \theta)$  shifts the energy eigenvalue by  $-eFd$ . The form of the wavefunction is otherwise unchanged because both the effective potential,  $\frac{1}{2}m^*\omega_C^2(x \sin \theta - z \cos \theta)^2$ , and the periodic potential terms are unchanged by this shift. Therefore the energy shift is a result of the shift by  $d$  along the electric field in  $x$  and the shift of  $d \tan \theta$  along  $z$  is required to leave the magnetic potential unchanged. Therefore we see a series of steps in

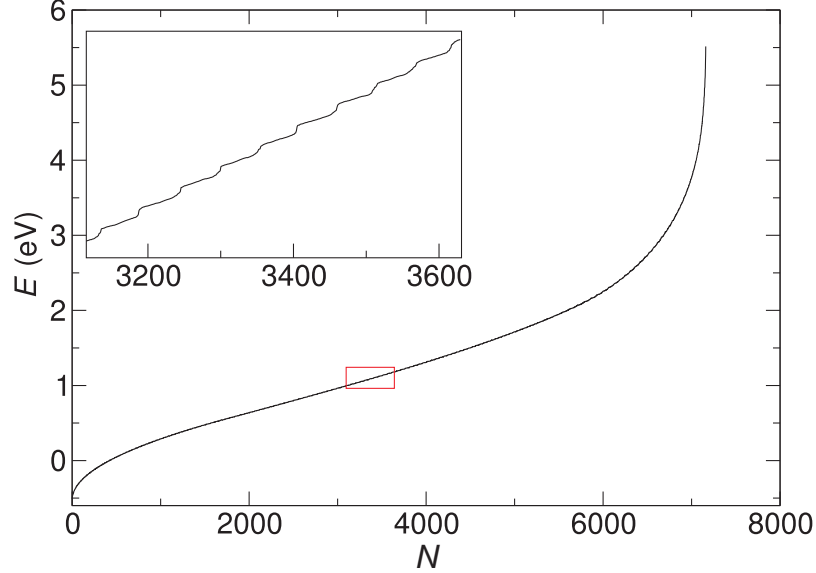


Fig. 5.12: Energy eigenvalue plotted as a function of state index,  $N$ , calculated for a 61-period superlattice with  $B = 11$  T,  $\theta = 15^\circ$  and  $r = 1$ . Closeup (inset) of the area inside the box on the main curve shows step-like behaviour.

$E(N)$  each shifted from the previous step by  $eFd$ .

To ensure that these steps are indeed due to shifts of wavefunctions, we overlay two electron probability densities for eigenstates that differ in energy by  $4eFd$  (figure 5.13). This figure shows that the wavefunction is shifted by  $4d$  in  $x$  and the shift follows the magnetic field direction as expected. Figure 5.14 shows four electron probability densities corresponding to energy levels which differ by  $eFd$  and also have a shift of  $(d, d \tan \theta)$  in  $(x, z)$  between each.

We use an autocorrelation method to confirm that the step height in  $E(N)$  is exactly  $eFd$ . The density of eigenstates,  $D(E)$ , is defined as:

$$D(E) = \sum_{N=0}^{\infty} \rho(E - E_N) \quad (5.46)$$

where  $\rho(E - E_N)$  is the intensity at  $E$  of a normalised Gaussian centred on  $E_N$ . This measure has a periodicity of  $eFd$  which can be clearly seen in figure 5.15(a) for  $B = 20$  T,  $\theta = 30^\circ$  and  $r = 1$ . The autocorrelation function of  $D(E)$ ,

$$A(\Delta E) = \int_{-\infty}^{\infty} D(E)D(E + \Delta E)d\Delta E, \quad (5.47)$$

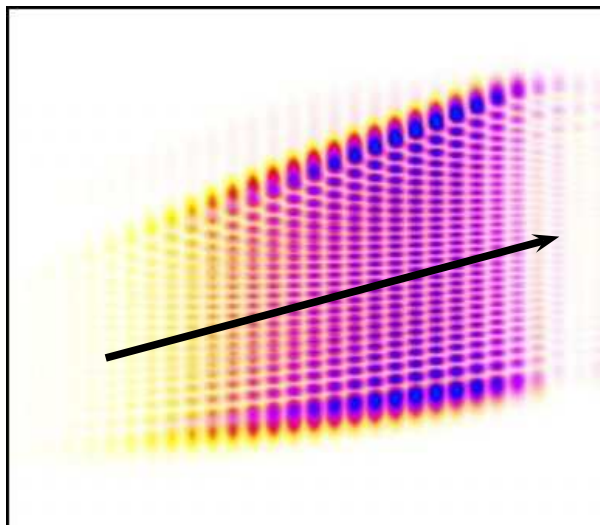


Fig. 5.13: Two overlaid eigenstates of the superlattice system with  $B = 11$  T,  $\theta = 15^\circ$  and  $r = 1.00$ . The eigenstates are separated by  $4eFd$  in energy which was chosen so the eigenstate shift in both  $x$  and  $z$  is clear. The arrow is aligned at  $\theta = 15^\circ$  to show that both states are positioned along the same magnetic field line. Note that this figure will not be clear in greyscale so use figure 5.14 instead.

is plotted in figure 5.15(b) which shows that the period is indeed  $eFd$ . Therefore the step height in  $E(N)$  is  $eFd$  as predicted.

### 5.10 Effect of $r$ on the Energy Eigenstates

This section examines the effect on the energy eigenstates of altering the electric field such that the resonance parameter  $r$  takes on a number of rational and irrational values. The associated variation in the probability density plots will be useful for qualitatively evaluating how electron transport changes with  $F$ . We have seen in figure 5.7 that  $E(N)$  exhibits a step structure for integer and rational, but not irrational, values of  $r$ . Figure 5.16 shows how the energy eigenstate probability density plots vary with  $r$  for a 14 period superlattice with  $B = 20$  T and  $\theta = 30^\circ$ .

We see that electron probability density is most widely spread (extended) for integer values of  $r$  (figs. 5.16(h,m,n,o)). When  $r$  is within  $\sim 5\%$  of  $r = 1$  (figs. 5.16(f,g,i,j)) the spatial extent of the state decreases with increasing  $|r - 1|$ . For non-integer rational values of  $r$  (figs. 5.16(a,b,c,d,e,k)), the probability density is localised in, and coherently couples, two or more quantum wells. This differs from when  $r$  is integer because the coupled quantum wells are no longer adjacent. When  $r$  is irrational (fig. 5.16(l)), the eigenstate probability density is localised

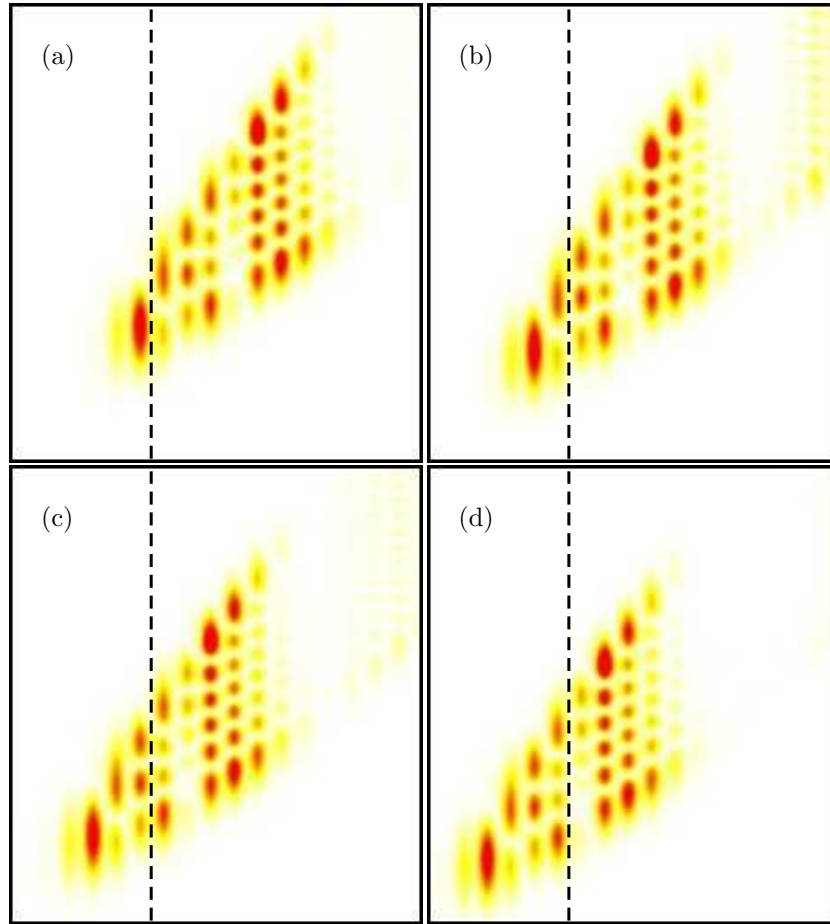


Fig. 5.14: Probability density plots of four eigenstates calculated for  $B = 11$  T,  $\theta = 45^\circ$  and  $r = 1.00$ . The energy eigenvalues are (a) 128.1 meV, (b) 141.6 meV, (c) 155.0 meV and (d) 168.4 meV which is a shift of  $eFd = 13.5$  meV between each. The broken lines are positioned at the same  $x$  value in each figure to show the shift of  $d$  in  $x$  position with an  $eFd$  increase in energy.

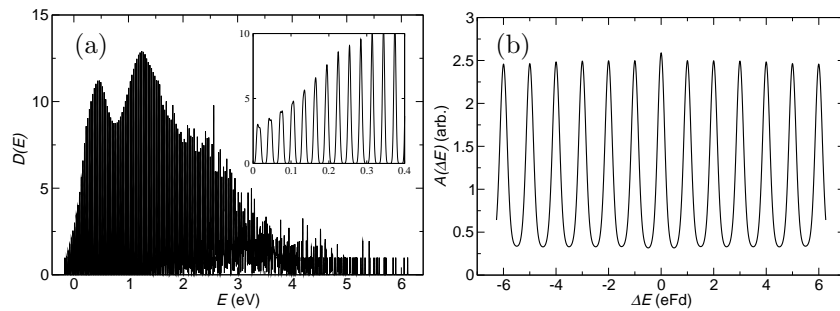


Fig. 5.15: (a) Density of eigenstates and (b) its associated autocorrelation function calculated for  $B = 20$  T,  $\theta = 30^\circ$  and  $r = 1$ . A periodicity of  $eFd = 0.188$  eV is clearly present.

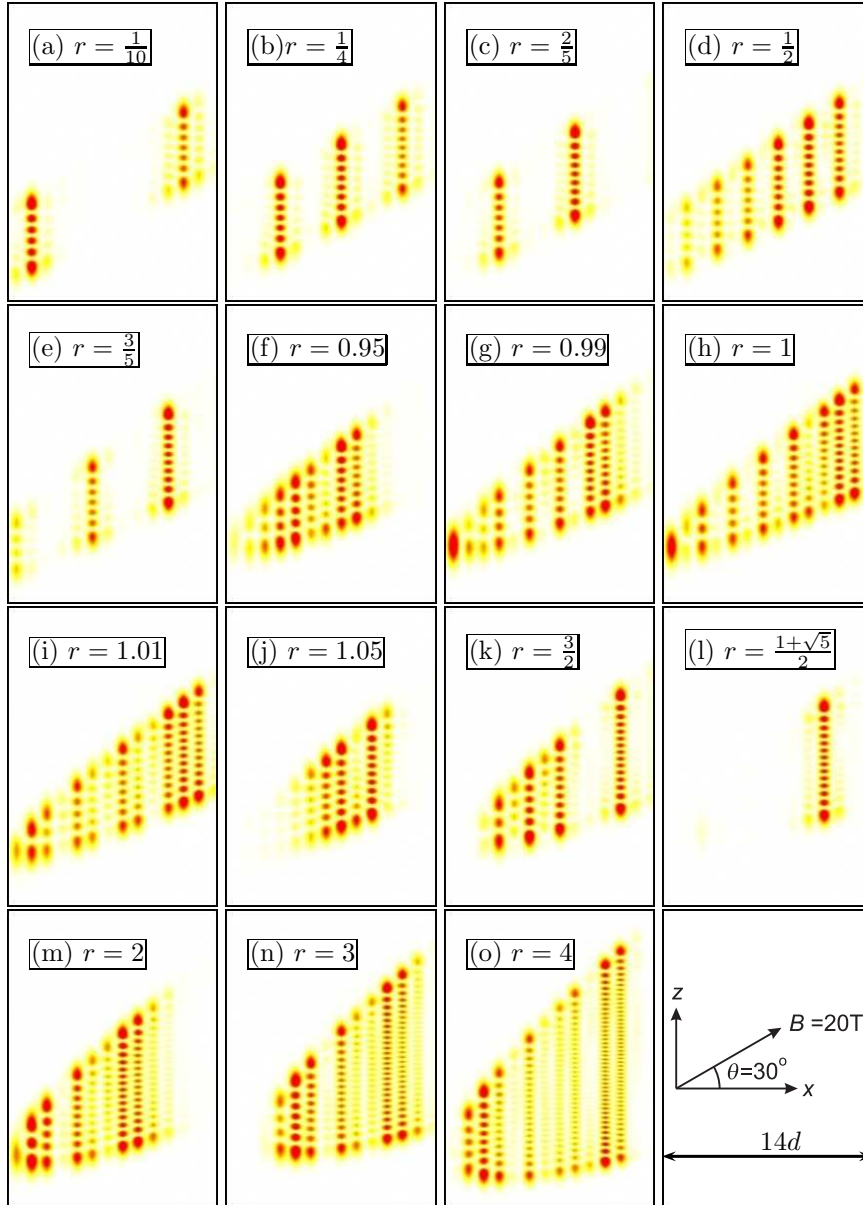


Fig. 5.16: Probability density plots calculated for a variety of integer [(h)  $r = 1$ , (m)  $r = 2$ , (n)  $r = 3$  and (o)  $r = 4$ ], near-integer [(f)  $r = 0.95$ , (g)  $r = 0.99$ , (i)  $r = 1.01$  and (j)  $r = 1.05$ ], rational [(a)  $r = \frac{1}{10}$ , (b)  $r = \frac{1}{4}$ , (c)  $r = \frac{2}{5}$ , (d)  $r = \frac{1}{2}$ , (e)  $r = \frac{3}{5}$  and (k)  $r = \frac{3}{2}$ ] and irrational [(l)  $r = \frac{1+\sqrt{5}}{2}$ ] values of  $r$ . The eigenfunctions are calculated for a 14 period superlattice with  $B = 20$  T and  $\theta = 30^\circ$ . Note that the wavefunctions extend over many superlattice periods for rational and integer values of  $r$  but not for irrational values. Extended electron states also exist when the system has an almost integer value of  $r$ . All panels are plotted on the same axes and  $x$  and  $z$  are to scale.

in a single quantum well.

Figure 5.17 shows the Wigner functions corresponding to the probability density plots shown in figure 5.16. These Wigner functions help to display the difference between eigenstates corresponding to integer, near-integer, rational and irrational values of  $r$ . As expected, the radial extent of the wavefunction is controlled by the resonance parameter  $r$ . For integer (figs. 5.17(h,m,n,o)) or near-integer (figs. 5.17(f,g,i,j)) values of  $r$ , the Wigner function extends from the origin to some fixed radius which is determined by the location of the rings in the semiclassical stochastic web. For non-integer rational values of  $r$  (figs. 5.17(a,b,c,d,e,k)), the momentum distributions of the Wigner functions is typically concentrated within a range of radial values, which does not necessarily encompass the origin. When  $r$  is irrational (fig. 5.17(l)), the Wigner function is confined to a single ring of phase space<sup>1</sup> as would be expected for this Landau level like state.

We will initially use a simple coherent coupling argument to explain the origin of the extended eigenfunctions. For  $r = 1$  and  $\theta \neq 0^\circ$ , shifting an eigenstate by  $(x = d, z = d \tan \theta)$  causes it to gain  $eFd$  kinetic energy. However, from the definition of  $r$  (equation 3.6):

$$r = \frac{\omega_B}{\omega_C \cos \theta} = \frac{Fdm^*}{\hbar eB \cos \theta}, \quad (5.48)$$

this energy is also equal to the Landau level spacing  $\hbar\omega_C \cos \theta$ . Therefore, the  $n^{\text{th}}$  Landau level in well  $m$  is isoenergetic with the  $(n + 1)^{\text{th}}$  level in well  $m + 1$ . Because these Landau levels are centred on  $z$  and  $z + d \tan \theta$  respectively, they are not orthogonal and a superposition state can form which coherently couples both Landau levels. This effect can be seen for  $r = 1$  in figure 5.16(h): the  $m = 1$  well has a single antinode of probability density, the  $m = 2$  well has two antinodes and so on, i.e. the probability densities within each quantum well are similar to a series of Landau wavefunctions.

When  $r$  is non-integer but rational, the energy difference between adjacent quantum wells is a fraction of the Landau ladder spacing so the Landau levels in non-adjacent quantum wells are isoenergetic. Therefore, the electron probability density plots show coherently coupled Landau levels in non-adjacent quantum wells and appear to “skip” a number of superlattice periods. For example, when  $r = 0.5$  (fig. 5.16(d)), the  $n^{\text{th}}$  Landau level in quantum well  $m$  is isoenergetic with the  $(n + 1)^{\text{th}}$  Landau level in quantum well  $m + 2$ , so a single superlattice period is “skipped”. For  $r = 2$  (fig. 5.16(m)), the  $n^{\text{th}}$  Landau level in well  $m$  is isoenergetic with the  $(n + 2)^{\text{th}}$  Landau level in well  $m + 1$  so only every other Landau level component is seen and the electron probability density becomes

<sup>1</sup> This does not mean a single ring of the stochastic web.

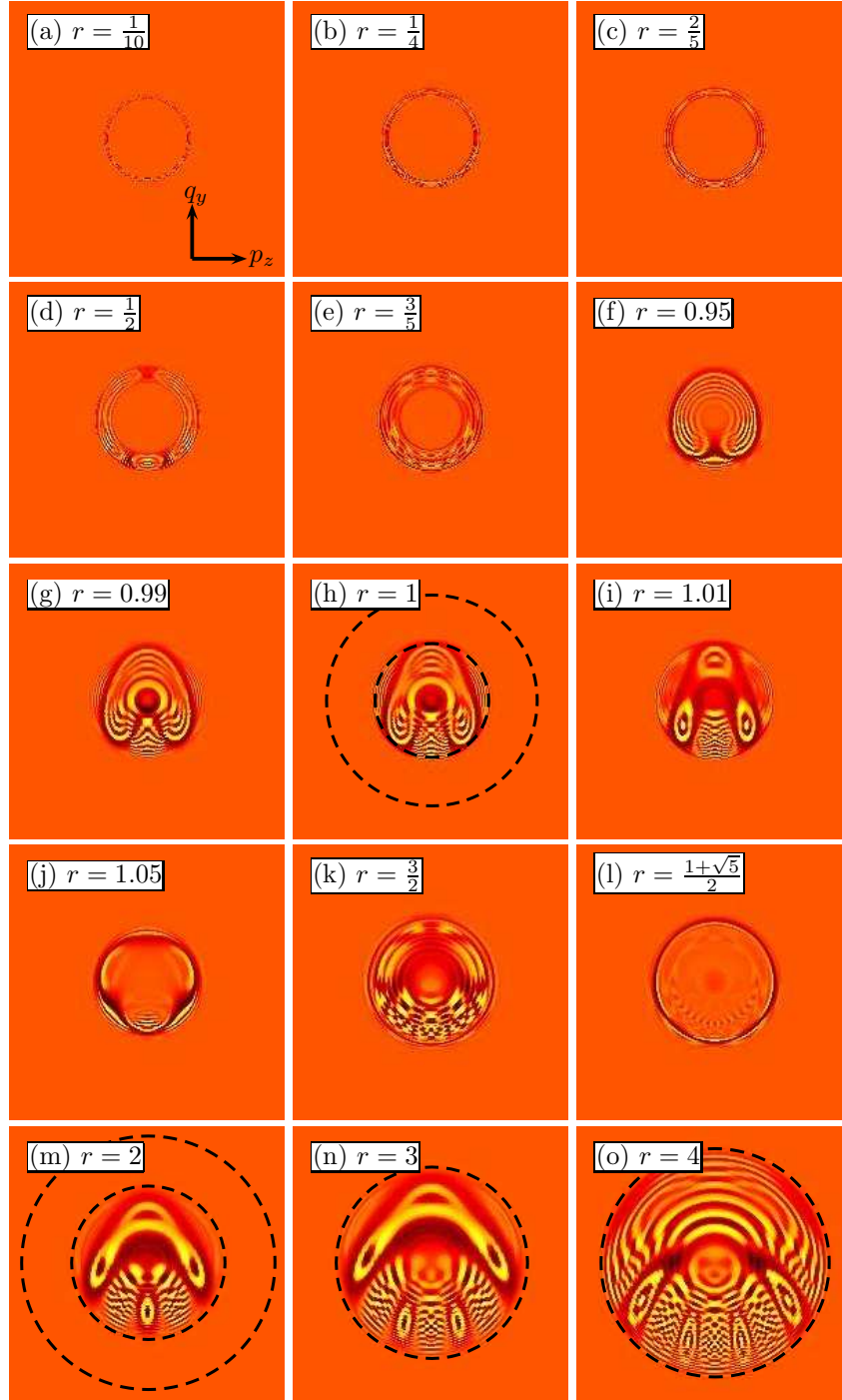


Fig. 5.17: Wigner functions for the energy eigenfunctions whose probability densities are plotted in figure 5.16 for a 14 period superlattice with  $B = 11$  T and  $\theta = 30^\circ$ . These plots show that integer and near-integer values of  $r$  produce the greatest spread in phase space followed by non-integer rational and finally irrational values of  $r$ . All panels are shown on the same axes with ranges of  $(-2 \rightarrow 2) \times 10^{-25}$  kg ms $^{-1}$ . The broken circles on (h,m,n,o) indicate the positions of the circular stochastic web filaments.

wider in  $z$  than it does for  $r = 1$  (figure 5.16(h)).

When  $r$  is irrational (fig. 5.16(l)), the energy difference between any pair of quantum wells is never equal to the Landau level spacing so coherent coupling will not occur. Therefore the electron probability density is always confined to a single quantum well.

This simple model helps explain the step structure seen for non-integer rational values of  $r$  in figure 5.7. For example, the steps in the energy eigenvalues for  $r = 0.5$  (grey curve in fig. 5.7) are half the length and half the height of those for  $r = 1$  (red curve). The steps are lower because  $eF(r = 0.5)d$  is half  $eF(r = 1)d$  and because every other period is skipped, there are only half as many states on a single step so the steps are half as long. The step structures for other rational values of  $r$  can be explained in a similar way.

However, the simple coherent coupling argument predicts infinitely extended states which we do not observe. We see additional long-range structure in the probability density plots which we also observed in the semiclassical dynamics. In the semiclassical picture we attributed this effect to the coupling between  $x$  and  $z$  which the above argument mostly ignores (other than noting that it removes the orthogonality of the  $n$  and  $n + 1$  Landau levels). Therefore, combining magnetic and electric fields and a superlattice potential produces eigenstates that cannot be explained simply.

### 5.11 Summary of Comparison between the Quantum and Semiclassical Models

We have seen that the frequency ratio  $r$  has a similar effect on the electron's real and phase space localisation in both the quantum and semiclassical systems. In addition, we have found a striking correspondence by directly comparing electron orbits to probability densities and Poincaré sections to Wigner functions. Therefore, there is a clear classical $\leftrightarrow$ quantum mapping between the two models as expected from the similar Hamiltonians.

However, directly calculating transport properties, such as drift-velocity, is not possible from the solutions of the time-independent Schrödinger equation. A more complex (and computationally intensive) wavepacket-based quantum model was used by S. Naylor(12) which showed that the mean position of a wavepacket undergoes dynamics comparable to the semiclassical results. This model was also used to investigate the effect of quantum specific behaviour on drift-velocity. Quantum-mechanical calculations of drift-velocity showed  $r = 1, 2, \dots$  resonant peaks as well as additional features caused by electrons tunnelling between quantum wells at high electric fields.

### 5.12 *The Search for Scarring*

As mentioned in section 5.5, scarring occurs when electron wavefunctions become localised along the paths of unstable periodic classical orbits. This effect has been previously discovered in single quantum well systems with tilted fields(44)(60). When our superlattice is large, we see long complex quasi-periodic electron orbits (section 3.2) and the electron probability density tends to be localised in a similar region to these orbits. But, because the semiclassical orbits are not periodic, this is not scarring. However, if the superlattice is shorter and enclosed by infinite potential barriers, there is a possibility that classical periodic orbits will occur similar to those seen in single quantum well systems. Figure 5.18 shows a number of electron probability density functions calculated for a five-period superlattice which appear to display scarring. Note that we had to use basis states involving Wannier functions associated with several minibands (i.e. many  $\alpha$  values in equation 5.14) to find these scarred states.

From this figure we can see that wavefunctions (c), (e) and (h) in particular show regions of enhanced probability density along a single path which extends over the whole length of the superlattice. If this effect is due to scarring then there should be a corresponding classical periodic orbit along this path. However, our semiclassical model does not use a finite superlattice so will not show such an orbit. Therefore it is not currently possible to compare these states to semiclassical electron orbits and we cannot definitely say that these are scarred states. The Wigner functions for these states (figure 5.19) do not show any unusual behaviour or peaks in particular regions, corresponding to scarring orbits, which is unusual in itself given the unusual form of the probability density functions.

Therefore, it is inconclusive whether or not scarred states exist in short superlattices. Although some electron probability density functions appear to show scars, there is no corresponding evidence in the Wigner functions. In addition, no classical analysis has currently been performed to see if periodic orbits do exist along these scars of enhanced electron probability density. Because of these issues, no further potentially scarred states will be examined in this thesis.

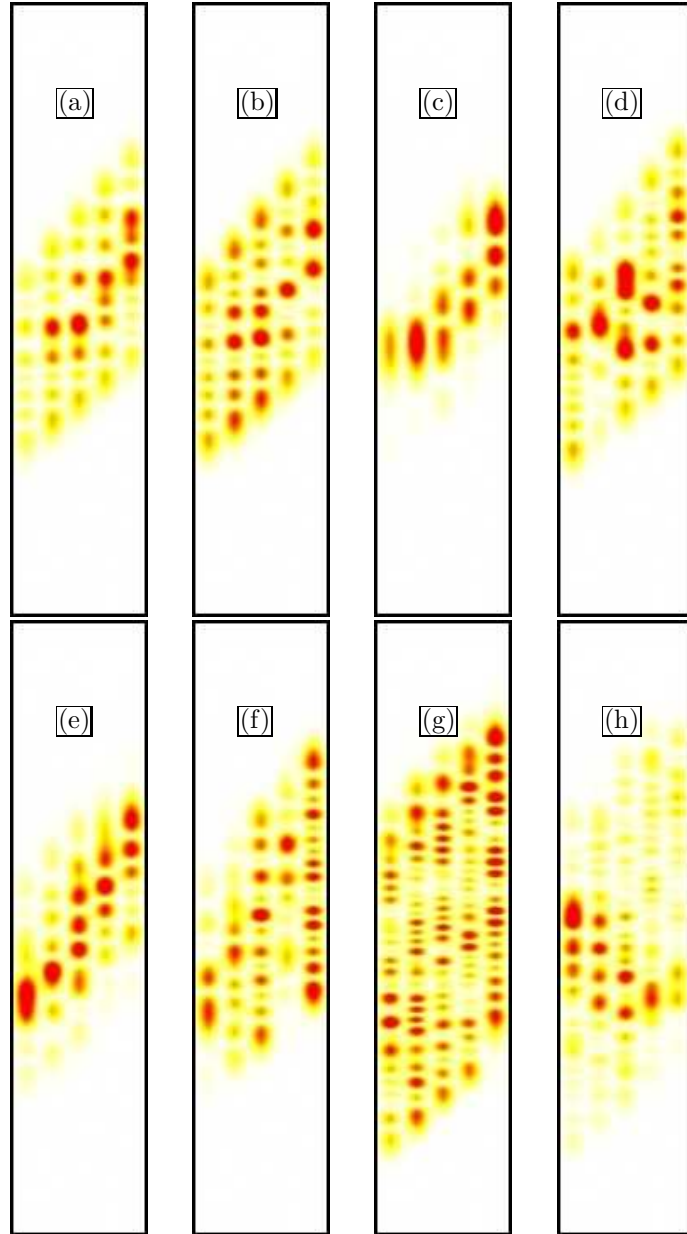


Fig. 5.18: Probability density plots of eigenfunctions calculated for a 5-period superlattice with  $B = 20 T$ ,  $\theta = 45^\circ$  and  $r = 1$  which show possible scarring. All these functions show regions of enhanced probability density which are dissimilar to those found for longer superlattices (e.g. figures 5.8 and 5.16). Panels (c), (e) and (h) in particular appear to show the electron localised along some single path which spans the full length of the superlattice.

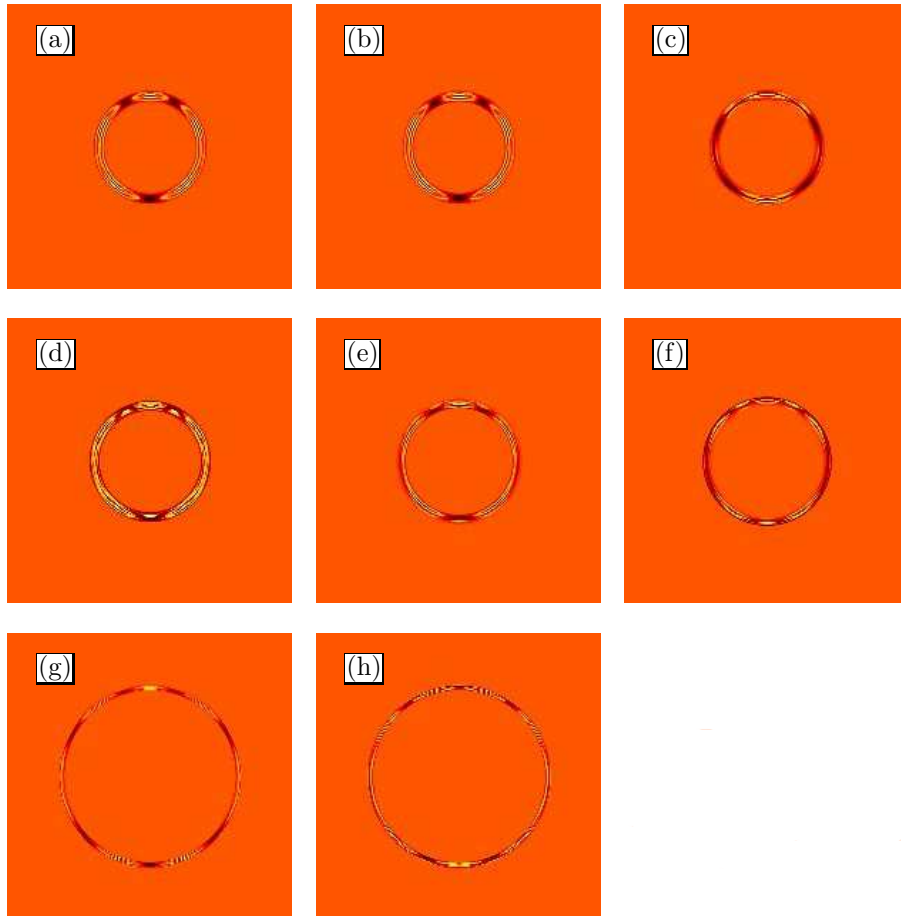


Fig. 5.19: Wigner functions for the eigenstates whose probability densities are shown in figure 5.18. These plots are calculated for a 5-period superlattice with  $B = 20 T$ ,  $\theta = 45^\circ$  and  $r = 1$ . Not hotspots which would indicate scarring are seen.

6. ANALYSIS OF LOCALISED BANDS IN SUPERLATTICE  
NU2293

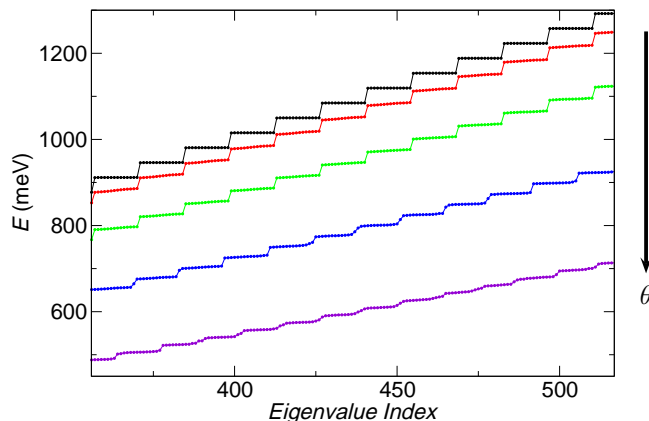


Fig. 6.1: Energy eigenvalues plotted as a function of eigenstate index  $N$  for a 14 period superlattice with  $B = 20$  T,  $\theta = 0^\circ, 15^\circ, 30^\circ, 45^\circ, 60^\circ$  from top to bottom and  $r = 1$ . These plots show the loss of degeneracy within each step as soon as  $\theta \neq 0^\circ$ . The step height gradually decreases as  $\theta$  increases because, for given  $r$  and  $B$ ,  $eFd \propto \cos \theta$ , and  $eFd$  determines the step height (see section 5.9). This is a repeat of figure 5.6 from chapter 5

In chapter 5, section 5.9 we saw that a step structure exists in the energy eigenstates of our superlattice system with applied electric and tilted magnetic fields when  $r$  takes a rational value. This chapter will examine the characteristics of the eigenstates on these steps and look at the consequences of having a repeating structure of energy shifted eigenstates.

### 6.1 Probability Density Plots for Eigenstates on a Single Step in $E(N)$

When  $\theta = 0^\circ$ , a plot of  $E(N)$  consists of a perfect staircase function with a number of degenerate eigenstates forming each step (fig. 6.1(black curve)). However, when  $\theta \neq 0^\circ$ , the degenerate eigenstates split and  $E(N)$  consists of a staircase function shaped by the addition of a second function with the same periodicity as the steps (fig. 6.1(non-black curves)). This section will examine in detail how the electron probability is distributed in real space for these eigenstates.

Figure 6.1 shows that the eigenstates on a single step in  $E(N)$  have a smoother energy variation at lower  $\theta$ . Thus we will initially investigate  $B = 11$  T,  $\theta = 15^\circ$  and  $r = 1$ . Chapter 5 has shown that there is a good correspondence between the semiclassical and quantum-mechanical systems. Therefore, we can use equation 5.36 to estimate the  $x$  limits that the eigenstate probability density is confined in. For  $\theta = 15^\circ$ , we can assume from the semiclassical results (fig. 3.4) that low energy eigenstates are localised within the first ring of the

stochastic web and this results in the electron wavefunction being delocalised over 93 superlattice periods in  $x$ . However, the quantum calculations only use a 61 period superlattice for these results so the superlattice will have a truncating effect on the eigenstate probability density in both real and phase space. A similar effect was seen in section 5.8. However, we will still examine these results because the  $\theta = 15^\circ$  step structure turns out to be the most regular.

Figure 6.2 shows probability density plots for the eigenstates which have the twelve lowest energy eigenvalues on the “flat” section of a single  $E(N)$  step, as shown in figure 6.3. These twelve wavefunctions all occupy much the same region of the superlattice. The number of nodes along the  $z$  direction in  $|\Psi|^2$  at a particular  $x$  value is the same for all the eigenstates. However, each of the eigenfunctions is modulated by a slower density fluctuation which generates regions of low probability density. The number and location of these regions vary amongst the eigenstates. We assume that these probability density functions are different subsets of some underlying function whose approximate form,  $\Psi_{meta}$ , is given by:

$$|\Psi_{meta}|^2 = |\Psi_{699} + \Psi_{700} + \Psi_{701} + \dots + \Psi_{710}|^2 \quad (6.1)$$

and is plotted in figure 6.4. This function resembles the probability density plots in figure 6.2 but does not have any regions of slowly fluctuating probability density.

We will introduce the following terminology to discuss this behaviour. The probability density of the summed eigenfunction will be known as the *meta-probability density function* and this meta-probability density function, weighted by some *envelope function*, will give a particular probability density function such as those plotted in figure 6.2.

We will refer to the set of eigenstates of a single  $E(N)$  step as a band because they are similar in both energy and position. Therefore a transition between any two of these states would only require a small amount of energy, which could be obtained from acoustic phonons for example.

As an aside, figure 6.5 compares the semiclassical electron orbit starting from rest calculated over 20 ps for  $B = 11$  T,  $\theta = 15^\circ$  and  $r = 1$  with (a) the probability density plot of the  $N = 702$  eigenstate (fig. 6.2(d)) and (b) the meta-probability density function (fig. 6.4). The semiclassical orbit encompasses the whole first ring of the stochastic web and these comparisons clearly show the truncation of the quantum eigenstates due to the finite length of the superlattice. However, taking this truncation into account, the semiclassical and quantum-mechanical models both show the electron covering the same characteristic area the the left of the end of the superlattice. Also the semiclassical electron has to travel for  $\sim 115\tau_{SL}$  before its average motion in the  $x$ -direction reverses so

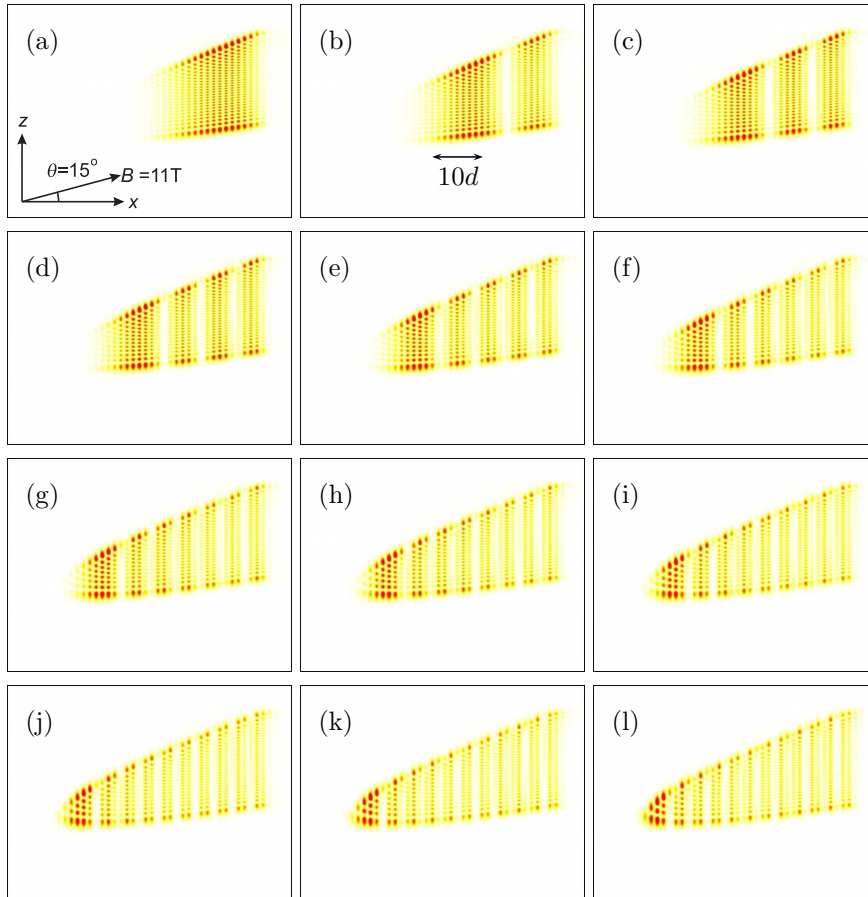


Fig. 6.2: Probability density plots of energy eigenfunctions with adjacent energy eigenvalues calculated for a 61 period superlattice with  $B = 11 \text{ T}$ ,  $\theta = 15^\circ$  and  $r = 1$ . These are the  $N = 699 \rightarrow 710$  eigenstates from (a) through (l). The RHS of the figures corresponds to the end of the superlattice which is modelled as a infinite potential barrier in our calculations. We only show these twelve states because the envelope period becomes comparable to the superlattice period for higher energy eigenfunctions. This makes the node structure hard to distinguish.

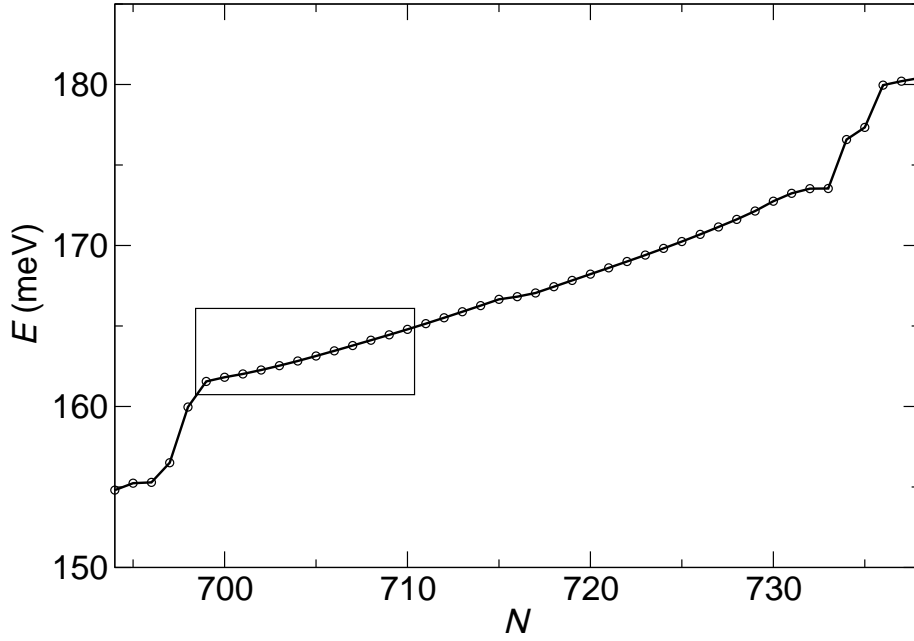


Fig. 6.3:  $E(N)$  plot showing the location of individual energy eigenvalues (circles) for  $B = 11$  T,  $\theta = 15^\circ$ ,  $r = 1$  and a 61-period superlattice. A new step begins on the  $E(N)$  curve at  $N \approx 699$ . The eigenvalues inside the box correspond to the eigenstate probability density plots shown in figure 6.2. Note that the energy eigenvalues inside the box vary smoothly with  $N$ .

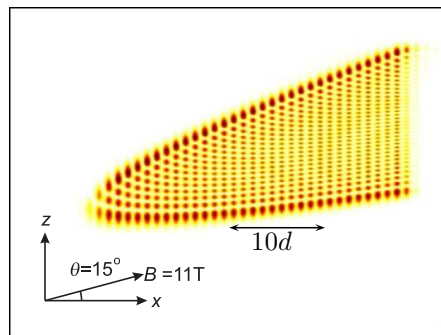


Fig. 6.4: Meta-probability density for the eigenstates in figure 6.2 created using equation 6.1.

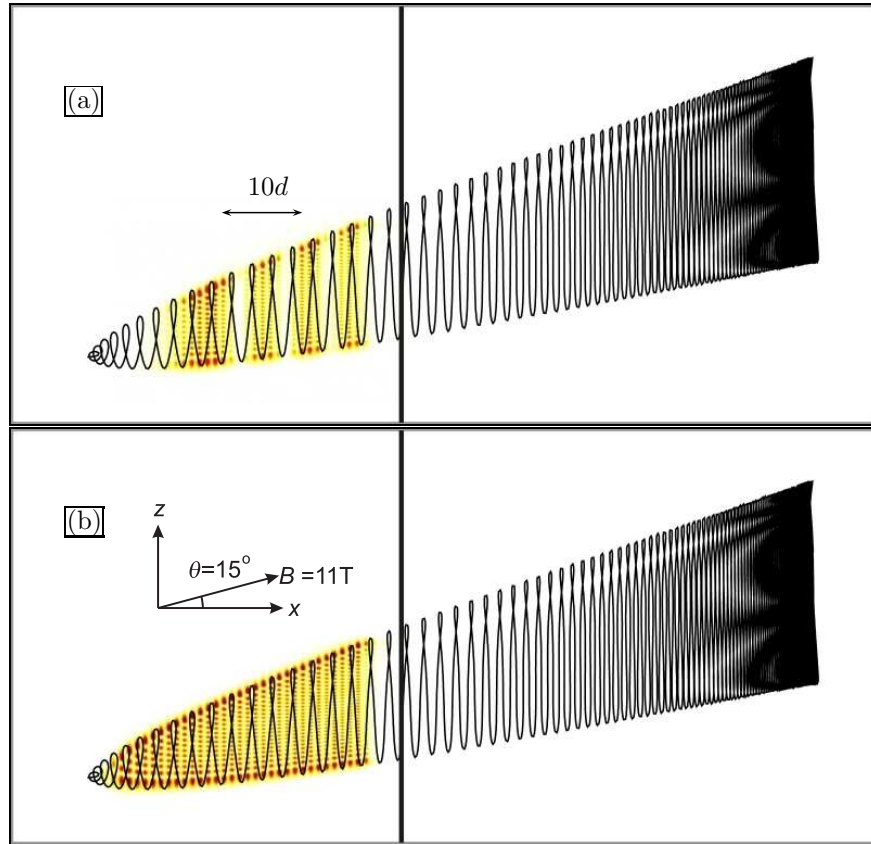


Fig. 6.5: Semiclassical electron trajectory calculated for  $B = 11$  T,  $\theta = 15^\circ$  and  $r = 1$  in an infinite superlattice overlaid on the corresponding (a) probability density plot of the  $N = 702$  eigenstate (b) meta-probability density plot, both calculated for a 61 period superlattice. The solid line indicates where the superlattice is truncated by the finite basis used to determine the quantum results, meaning that the probability density is zero to the right of this line.

truncation by the superlattice is unlikely to be important in the semiclassical model for these parameters.

We now return to the eigenstate probability density plots in figure 6.2 and use our new terminology to describe them. The envelope function corresponding to the lowest energy eigenstate (fig. 6.2(a)) appears to consist of a single antinode along one dimension which is roughly aligned with the  $x$ -axis. Increasing  $N$  by one (fig. 6.2(b)) adds an additional antinode to the envelope function which causes the eigenstate probability density to split into two regions. This pattern continues, with successively higher energy eigenstates having an additional antinode in their envelope function. Figure 6.6 plots  $\Psi(x, z)$  for the  $N = 702$  eigenstate (c.f. fig. 6.2(d)) which shows that there is a change in sign between adjacent antinodes. This behaviour is consistent with quantisation within a box

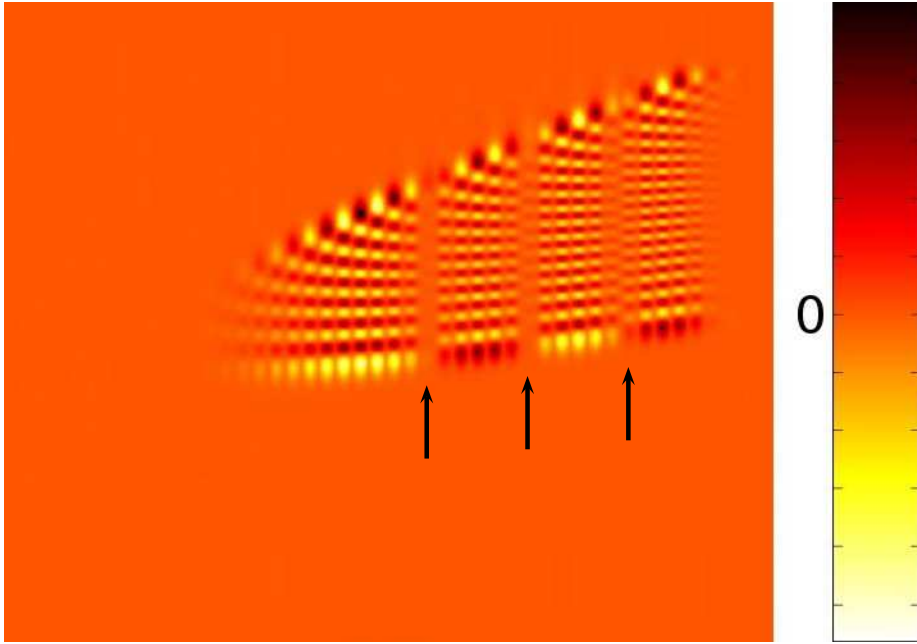


Fig. 6.6:  $N = 702$  eigenfunction of a 61 period superlattice with  $B = 11$  T,  $\theta = 15^\circ$  and  $r = 1.00$ . Note that the sign of the slowly varying envelope function changes as  $x$  passes through the (arrowed) antinodes.

created by the rising electric potential on the left hand side and the finite length superlattice on the right.

For completeness, figure 6.7 shows the Wigner functions of the twelve eigenstates studied. These functions show radial truncation due to the finite length of the superlattice as discussed in section 5.8, but also show an increasing number of antinodes with increasing  $N$ . The node structure in the Wigner functions is more complex than that in the real space probability density plots and consists of a separate set of nodes in each stable island of the corresponding semiclassical stochastic web.

Because our boxed state is partially formed by the end of the superlattice, we will now change the parameters of the applied fields to see if the same behaviour occurs when the electron eigenfunction is not truncated by the superlattice.

### 6.1.1 Shorter Eigenstates

From equation 5.36, we obtain the approximate eigenstate delocalisation in  $x$ ,  $\Delta x$ , to be:

$$\Delta x = \frac{\rho_{max}^2}{2m^*eF} = \frac{d\rho_{max}^2}{2\hbar B \cos \theta}. \quad (6.2)$$

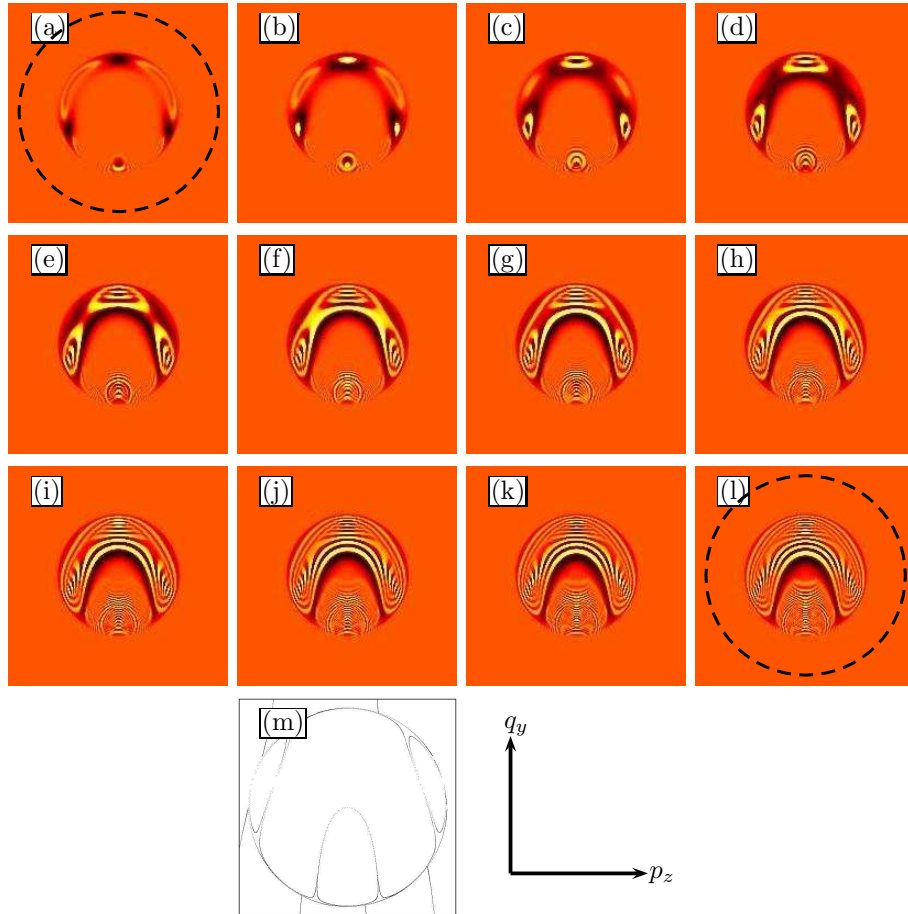


Fig. 6.7: Wigner functions corresponding to the twelve probability density plots shown in figure 6.2. These are for a 61 period superlattice with  $B = 11$  T,  $\theta = 15^\circ$  and  $r = 1$ . The number of antinodes clearly increases as energy increases. The broken line in (a) and (l) shows the location of the first circular stochastic filament in the corresponding Poincaré section (m). It is clear that the Wigner functions are truncated at a radial limit which is smaller than the radius of the first ring of the stochastic web. Both axes range from  $(-2 \rightarrow 2) \times 10^{-25} \text{ kg ms}^{-1}$ .

Furthermore, equation 3.7 states that the circular filaments in the stochastic web are located at the zeros of:

$$J_r \left( \rho \frac{d \tan \theta}{\hbar} \right). \quad (6.3)$$

If we choose a particular root of  $J_r$ , which corresponds to a particular circular filament of the stochastic web, we can combine these equations and obtain:

$$\Delta x = \frac{\hbar (J_r^0)^2}{2eBd \tan \theta \sin \theta} \quad (6.4)$$

where  $J_r^0$  is a zero  $J_r$ . Therefore, we find that  $\Delta x$  varies as:

$$\Delta x \propto \frac{1}{B \sin \theta \tan \theta}, \quad (6.5)$$

so the eigenstate's delocalisation along  $x$  decreases as both  $B$  and  $\theta$  increase. However, the semiclassical dynamics analysis in chapter 3 revealed that increasing  $\theta$  increases the chance that the electron will explore more rings of the stochastic web (see figs. 3.4 and 3.11). Therefore the probability density plots may show an increased delocalisation at large  $\theta$ .

Assuming that the electron remains confined to the first ring of the stochastic web, we find that keeping  $B = 11$  T and setting  $\theta = 30^\circ$  reduces the electron delocalisation to 22 superlattice periods. This is much shorter than our 61 period superlattice so it should be possible to obtain results that are not truncated by the end of the lattice.

However, it must be remembered that the quantum model produces results with a range of energy eigenvalues. This contrasts to the semiclassical electron orbits in seen section 3.2, which have a single energy. We therefore expect higher energy eigenstates to explore regions of phase space corresponding to larger rings of the stochastic web and therefore to possibly extend over more than 22 superlattice periods in real space. Figure 6.8 shows (a,b) probability density and (c,d) Wigner function plots for the  $N = 1197$  and  $N = 1198$  eigenstates respectively, calculated for  $B = 11$  T,  $\theta = 30^\circ$  and  $r = 1$ . These eigenstates clearly exist in different regions of real space which correspond to first and second rings of the stochastic web respectively. Note that the higher energy of eigenstate (fig. 6.8(b)) is limited by the end of the superlattice, but the lower energy eigenstate (fig. 6.8(a)) is not.

To look for behaviour similar to that seen for  $\theta = 15^\circ$ , we will examine the eigenstates on a single step in  $E(N)$  whose probability density is concentrated within the first ring of the stochastic web. We do this so our analysis is not initially confused by eigenstates which occupy a different region of space entirely.

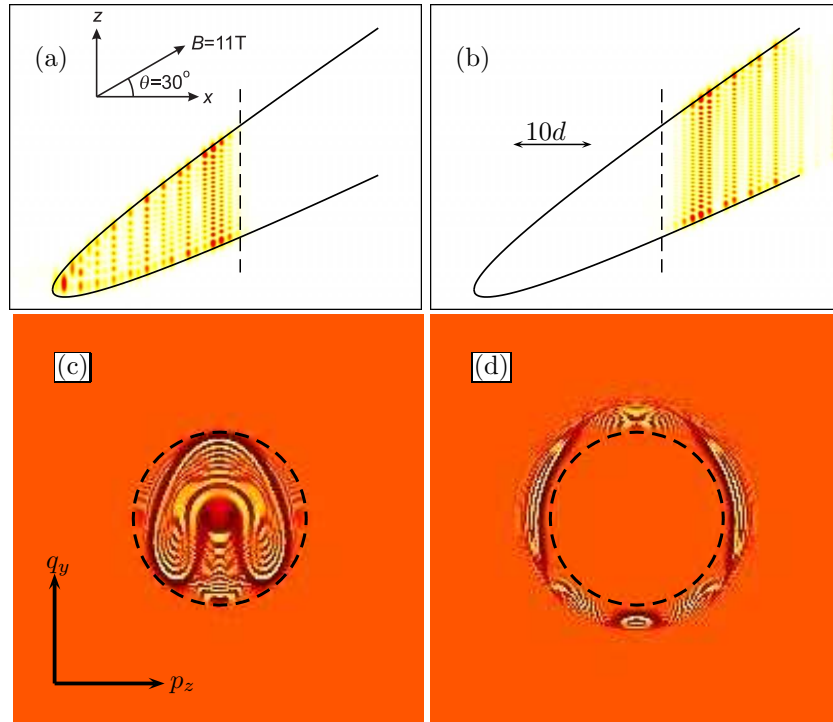


Fig. 6.8: (a) and (b) show probability densities plots for the  $N = 1197$  and  $N = 1198$  eigenstates in a 61 period superlattice system with  $B = 11\text{ T}$ ,  $\theta = 30^\circ$  and  $r = 1$ . Both plots are on the same scale and the right hand border of the plot corresponds to the end of the superlattice which is modelled by an infinite barrier. The solid line shows the semiclassical electron orbit locus given by equation 3.16 and the broken line shows the  $x$  limit corresponding to the first ring of the stochastic web. (c) and (d) show the corresponding Wigner function plots with the broken line again indicating the first ring of the stochastic web. The axes on the Wigner functions range from  $(-2 \rightarrow 2) \times 10^{-25} \text{ kg ms}^{-1}$ .

This restriction means that some eigenstates are ignored and hence the series of eigenstates chosen will not be contiguous in  $N$ . Figure 6.9 shows probability density plots of the ten eigenstates that were chosen, and figure 6.10 highlights their energy eigenvalues on the full  $E(N)$  curve. Finally, figure 6.11 plots the Wigner functions for these eigenstates. Note that figures 6.9(i) and 6.11(i) are identical to (a) and (c) in figure 6.8.

These probability density plots and Wigner functions show results similar to those obtained for  $\theta = 15^\circ$ . The probability density plots (fig. 6.9) again show an envelope function with a number of antinodes that increases by one with each successive energy increase. Figure 6.12 shows that the  $x$  position of the nodes varies with  $z$  which implies that the series of antinodes is not aligned along the superlattice axis and does not appear to show it aligned along  $\theta$  either. However, we will assume that the antinode series is aligned along the  $x$ -axis for simplicity. We can make this assumption because it is the  $x$  component of electron transport that is useful for determining  $I(V)$  relations.

The major difference between the probability density plots results at  $\theta = 30^\circ$  (fig. 6.9) and those at  $\theta = 15^\circ$  (fig. 6.2) is that the electron is no longer confined by the edge of the superlattice but by some other, shorter, limit. The Wigner function plots (fig. 6.11) confirm that this limit corresponds to the first ring of the stochastic web. The Wigner functions have a distinctive pattern which consists of a number of regions that correspond to the semiclassical stable islands. The number of antinodes inside each of these regions varies with the same sequence as that describing the number of antinodes in the probability density plots.

The electron is therefore bounded on all sides by three different barriers. The left hand barrier is due to the rising electric potential, which, in principle, can become infinitely high. The top and bottom barriers are created by the magnetic field gutter potential and can also become infinitely high. Finally, the right hand barrier has some connection with the semiclassical stochastic web and its form is non-obvious. We will refer to this barrier as a *dynamical barrier* because it appears to arise from the semiclassical electron dynamics of our tilted field system rather than from a potential energy increase.

We can easily estimate the width of the dynamical box produced by the dynamical barrier,  $\Delta x_D$ , using equation 6.2. We obtain:

$$\Delta x_D \approx \frac{\rho_{max}^2}{2meF} = \frac{\rho_{max}^2 dm^*}{r\hbar B \cos \theta} \quad (6.6)$$

where  $\rho_{max}$  is the radius of the first ring of the stochastic web given by the first root of equation 6.3. It should be emphasised that this dynamical box only exists if the electron wavefunctions are extended, which only occurs for rational

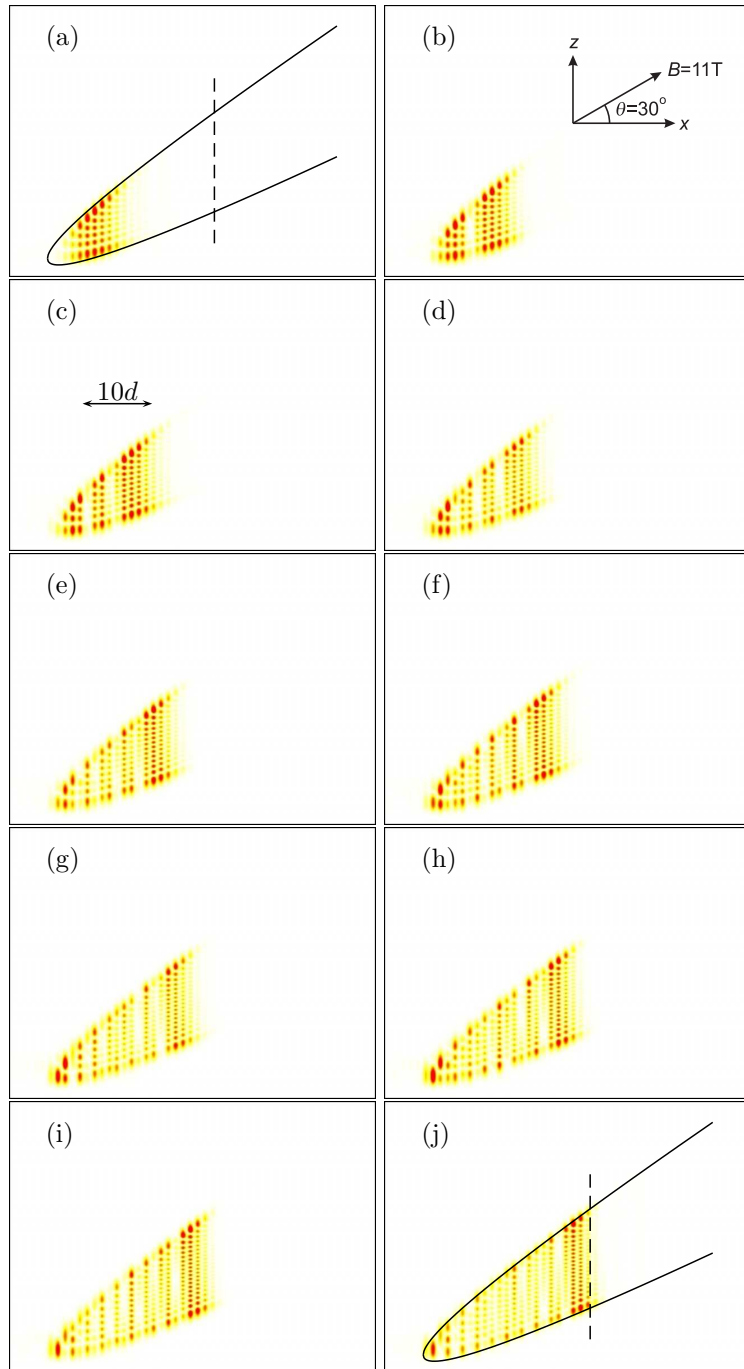


Fig. 6.9: Probability density plots for ten eigenstates localised in the same region of space calculated for a 61 period superlattice with  $B = 11 \text{ T}$ ,  $\theta = 30^\circ$  and  $r = 1.00$ . The energy eigenvalues of these eigenstates are similar but not necessarily adjacent (fig. 6.10). The solid lines in (a) and (j) show the semiclassical locus and the broken lines show the  $x$  limit corresponding to the first ring of the stochastic web.

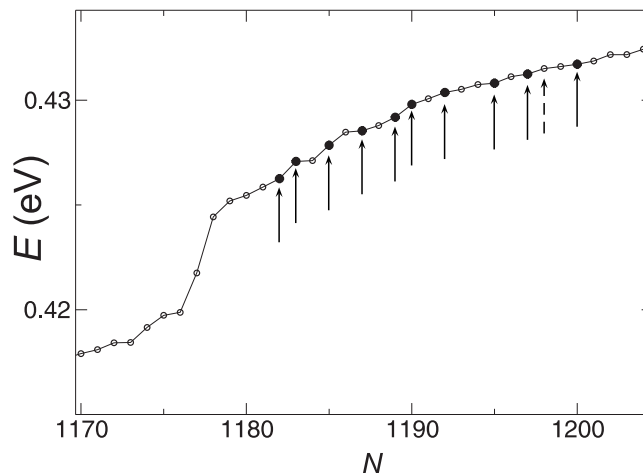


Fig. 6.10:  $E(N)$  plot showing the location of individual energy eigenvalues (circles). A new step begins on this  $E(N)$  curve at  $N \approx 1178$ . The solid points (arrowed) are the energy eigenvalues of the eigenstates shown in figure 6.9(a→j) from left to right respectively. The broken arrow indicates the energy eigenvalue of the eigenstate plotted in figure 6.8(b). Note that this step continues to  $N \approx 1222$ .

values of  $r$ . In addition,  $\rho_{max}$  can only be easily determined for integer values of  $r$ .

### 6.1.2 Form of the Dynamical Barrier and Box

We know the exact form of the potential energy function that gives rise to our dynamical box. This function consists of a magnetic gutter potential tilted at an angle  $\theta$  to a linearly varying electric potential (see figure 1.9) which is multiplied by a periodically varying superlattice potential aligned along the electric field. This potential is expressed by equation 5.3. However, this function is not useful to visualise because the interaction between the applied fields and the periodic potential is non-trivial and ultimately results in the complex dynamics seen in chapter 3. It would therefore be useful to obtain the form of an approximate dynamical potential which would explain the antinodes seen in figures 6.2 and 6.9. This dynamical potential will not attempt to describe the Landau level-like antinodes along the  $z$ -direction, which can be adequately described by the applied field potentials, nor will it attempt to explain the nodes spaced by  $d$  along  $x$ , which correspond to the superlattice barriers. However, it will attempt to describe the large scale node structure seen in this chapter.

Because we are looking for a potential which describes a series of antinodes along one direction, the magnetic field direction, we can simplify our search to 1D potentials. Two initial candidates for this potential are an infinite well

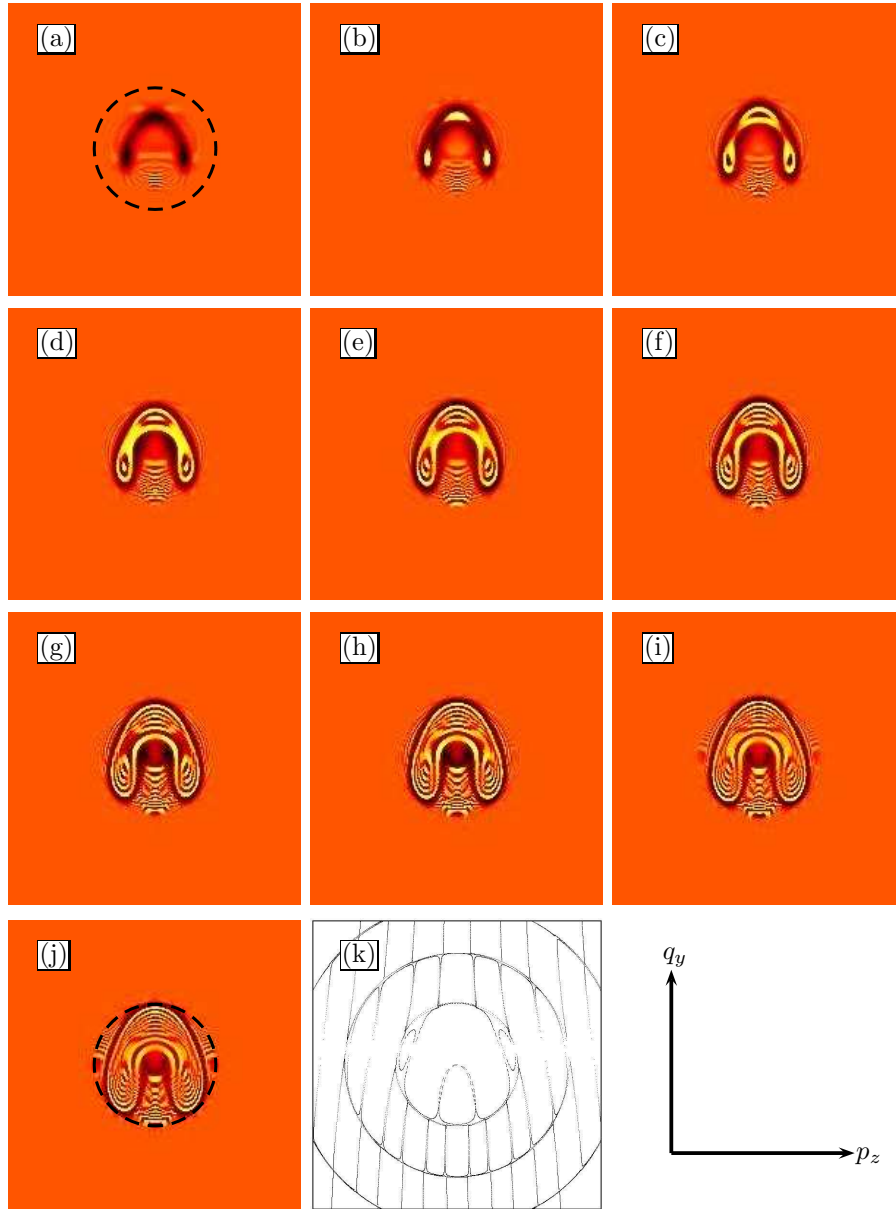


Fig. 6.11: Wigner functions corresponding to the ten probability density plots shown in figure 6.9. These are calculated for a 61 period superlattice with  $B = 11$  T,  $\theta = 30^\circ$  and  $r = 1$ . (k) shows the Poincaré section corresponding to these Wigner function and the broken line on (a) and (j) indicates the position of the first ring in the stochastic web.

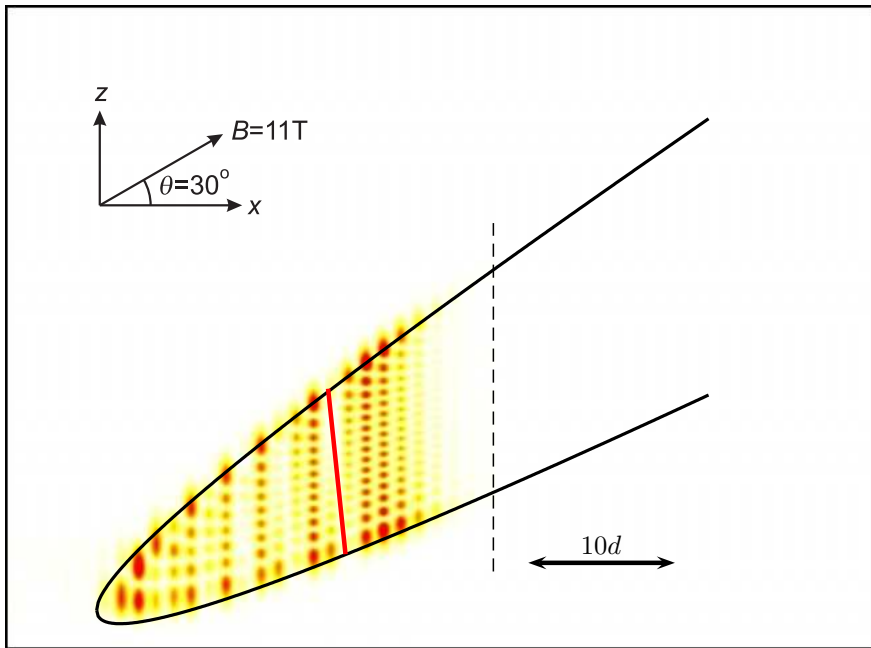


Fig. 6.12: Probability density plots for the  $N = 1190$  eigenstate calculated for a 61 period superlattice with  $B = 11 T$ ,  $\theta = 30^\circ$  and  $r = 1.00$ . This is an enlargement of figure 6.9(f). The solid lines in (a) and (j) show the semiclassical locus and the broken lines show the  $x$  limit corresponding to the first ring of the stochastic web. The red line shows the approximate node orientation which does not appear to correspond to either the superlattice axis or  $\theta$ .

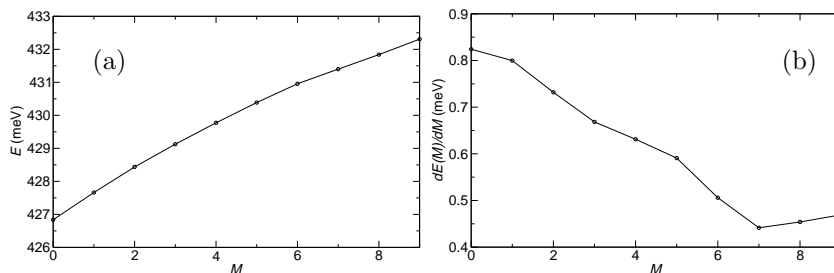


Fig. 6.13: (a) energy eigenvalues (circles) corresponding to the probability density plots shown in figure 6.9.  $M$  indexes the number of large nodes seen in these distributions which is one less than the number of antinodes. (b) plots the gradient of (a) and shows that the energy eigenvalues do not vary linearly with  $M$ .

with straight sides and a simple harmonic or parabolic potential, both of which produce a series of wavefunctions that have an increasing number of nodes with increasing energy. The energy eigenvalues of the straight walled and parabolic potentials vary as  $E(M) \propto M^2$  and  $E(M) \propto M$  respectively where the eigenfunction indexed by  $M = 0$  has a single antinode, that by  $M = 1$  has two antinodes and so on. We can therefore test these candidates by seeing how  $E(M)$  varies for the eigenstates pictured in figure 6.9 (identical to just plotting the solid points in figure 6.10). Figure 6.13 plots (a)  $E(M)$  and (b)  $\frac{dE(M)}{dM}$  and clearly shows that the eigenvalues increase sublinearly with increasing  $M$ ,  $E(M) \propto M^{<1}$ . This result means that a straight walled potential is ruled out. A parabolic potential is more likely because the variation of  $E(M)$  with  $M$  is close to linear and the deviation may arise from the more complex underlying potential that we are attempting to abstract. Note that the potential should also include a left hand barrier, which is formed from the rising electric potential.

Figure 6.14 plots  $x(t)$  for the semiclassical electron orbit calculated for  $B = 11$  T,  $\theta = 30^\circ$  and  $r = 1$  (fig. 3.3). There is a slow oscillation present in this result which has a period of  $\sim 11$  ps and an amplitude of  $\sim 23d$ . This slow oscillation therefore spans the entire dynamical box and is the semiclassical manifestation of our dynamical potential. We will use this  $x(t)$  data to estimate the form of the dynamical potential. At  $x = 0$ , we can see that the electron changes direction abruptly and the reflection resembles bouncing off a flat wall. Conversely, at  $x = 23d$ , the electron reverses direction more gradually which indicates that the potential change is also gradual. Therefore the potential of the dynamical box appears similar to half a parabolic potential (fig. 6.15). The left hand barrier in this potential is, of course, provided by the rising electric potential so its gradient is  $eF$  which an order of magnitude greater than that of the right hand parabolic barrier for these parameters.

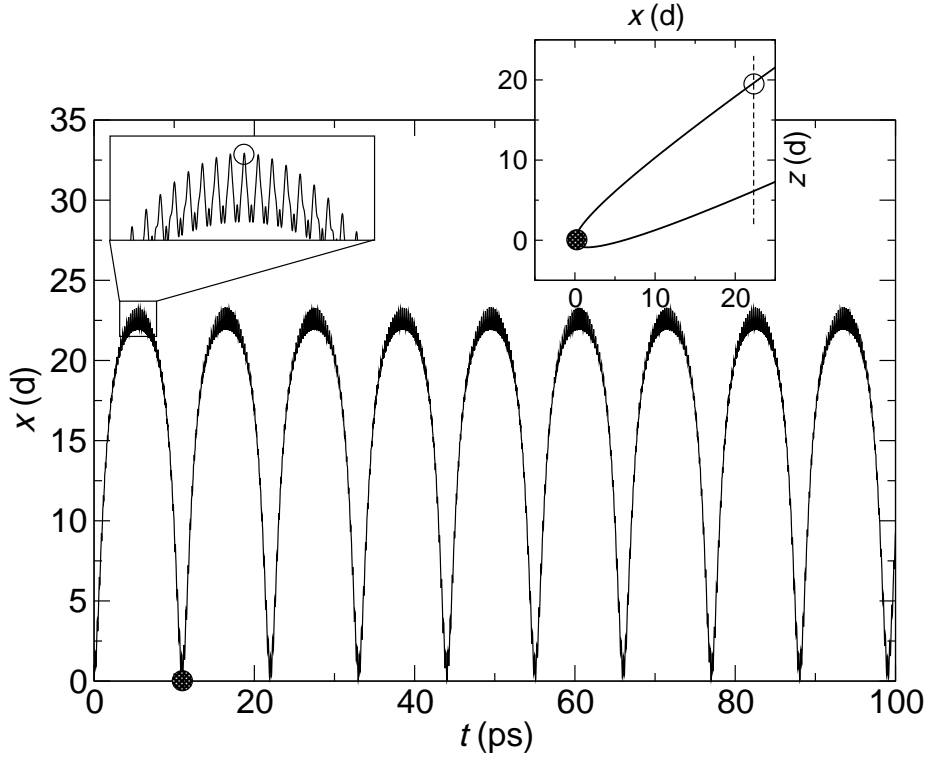


Fig. 6.14: Variation in semiclassical electron displacement along  $x$  with time calculated for  $B = 11\text{ T}$ ,  $\theta = 30^\circ$  and  $r = 1$ . The slow oscillation with a period of  $\sim 11\text{ ps}$  and length of  $\sim 23d$  is attributed to the dynamical box. The solid and open circles indicate where the electron is in  $(x, z)$  space (inset) at the bottom and top of this slow oscillation respectively.

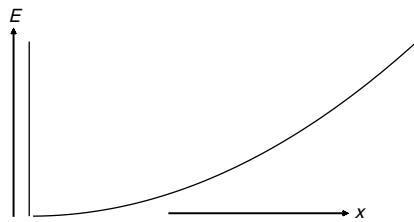


Fig. 6.15: Sketch of a half-parabolic potential. This is our first estimate of the form of the dynamical box which leads to the loss of degeneracy in the energy eigenvalues (fig. 6.13).

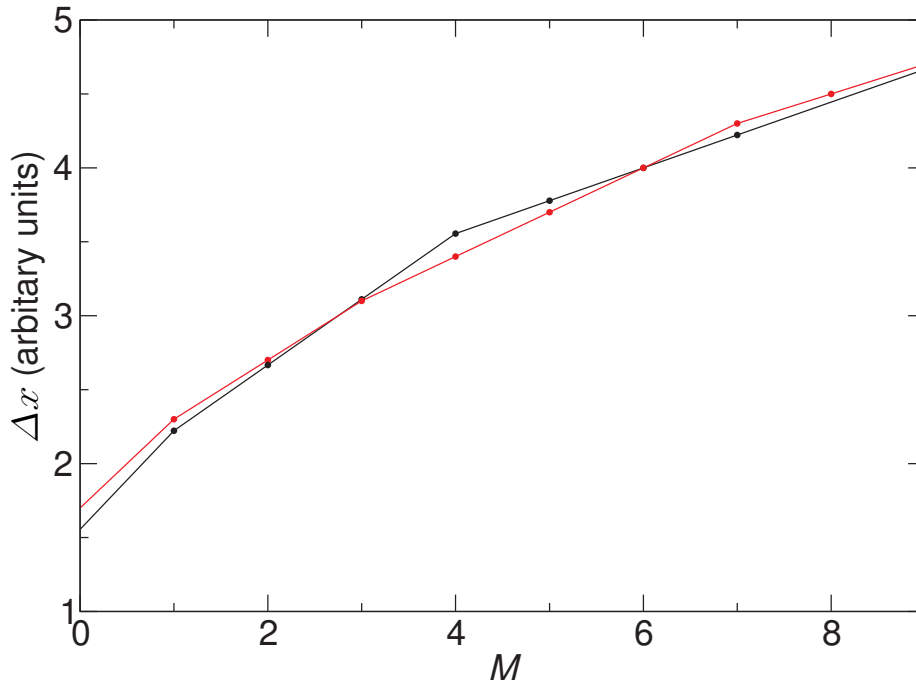


Fig. 6.16: Comparison of the widths of the eigenstate probability density functions,  $\Delta x$ , measured from figure 6.9 (black) to the widths of the eigenstates in a half-parabolic potential (red). These predicted widths were calculated from equation 5.12 and the curve is scaled to the same size as the black curve so we are only comparing *relative* widths rather than absolute widths.

We will now examine the quantum-mechanical probability density plots (fig. 6.9) to see if the eigenstates support this half-parabolic potential. This data shows that the left-hand sides of the eigenfunctions all begin at approximately the same  $x$  location. This is consistent with an abrupt barrier such as that formed by the rising electric potential. However, the right-hand side of these eigenfunctions shifts to higher  $x$  with increasing energy. This is consistent with a barrier whose energy varies slowly with position such as a parabolic potential. We can calculate how the widths of the eigenfunctions of a theoretical half-parabolic potential vary with  $M$  from equation 5.12. Figure 6.16 compares this predicted progression with the actual widths along  $x$  of the eigenstates in figure 6.9. This data shows that the increase in eigenfunction  $x$  width with increasing energy is exactly predicted by the half-parabolic potential.

We can also see that the size of the antinodes in figure 6.9 varies with position with the widest antinodes located at higher  $x$ . This is consistent with half-parabolic potential eigenfunctions which would be similar to half of figure 6.17. Finally, figure 6.13 has shown the the change in energy eigenvalue with  $M$  is not dissimilar to that expected for a parabolic potential.

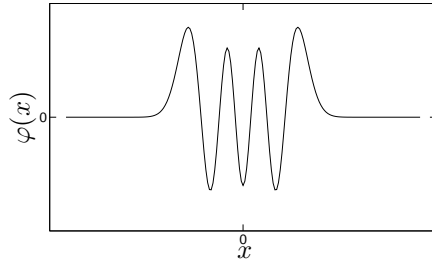


Fig. 6.17: Form of the  $n = 6$  simple harmonic oscillator (parabolic potential) wavefunction calculated from equation 5.12 where  $z$  has been replaced by  $x$ . A half-parabolic potential eigenfunction would resemble the  $x > 0$  part of this function.

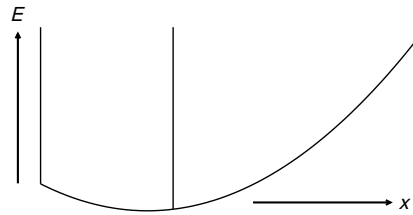


Fig. 6.18: Sketch of the dynamical potential experienced by an electron in a 61 well superlattice with  $B = 11$  T,  $\theta = 15^\circ$  and  $r = 1$ . The central vertical line indicates where the RHS of the superlattice truncates the potential with an infinite barrier. Since this truncation does not typically occur at higher  $\theta$  we include the remainder of the curved potential for reference.

Therefore, all the evidence gathered from the  $\theta = 30^\circ$  results indicates that the dynamical potential has a form similar to that shown in figure 6.15.

We will now return to the  $\theta = 15^\circ$  results (figs. 6.2, 6.3 and 6.7) to see if they can be explained by a similar dynamical potential. Figure 6.2 shows that the right hand edges of all twelve eigenstates are aligned which would appear to disagree with the half harmonic potential. However, it must be remembered that most ( $\sim 2/3$ ) of the dynamical box is inaccessible due to the finite length superlattice so our dynamical potential needs to have an infinite barrier added. We also find that the left hand edges of the eigenstates are not aligned which also disagrees with the potential sketched in figure 6.15. This conflict can be rectified by using more than half a harmonic potential such as that sketched in figure 6.18. The  $\theta = 30^\circ$  results (fig. 6.9) also show a slight shift in the LHS of the eigenfunction with increasing energy which is consistent with this change.

To clarify this explanation, figure 6.19 shows the general form of the dynamical potential for superlattices whose length (a) does not affect this potential and (b) does cause this potential to be truncated. We also plot a series of equally spaced energy levels in these potentials which show how the  $x$  width of the corresponding eigenfunctions would vary with energy. These levels help show how

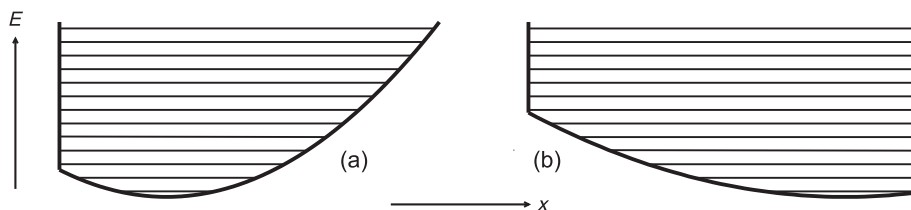


Fig. 6.19: Our second estimate of the form of the dynamical box potential including sample energy levels. (b) is truncated by the superlattice while (a) is not. These figures show how truncating the superlattice can lead to eigenstate probability density plots for different energies being aligned along opposite sides of the dynamical box. This potential is essentially a guess made from the  $x$  lengths of the eigenfunctions.

truncating the superlattice can cause the eigenstate probability density plots to be aligned along different sides of the dynamical box.

We can compare the probability density plots for  $\theta = 30^\circ$  (fig. 6.9) to the levels in figure 6.19(a). We see that the LH edges of the two lowest energy eigenfunctions are shifted to the right. We also see that RH edges of all the eigenfunctions shift right with increasing energy, this causes the overall width of the eigenfunctions to increase with energy. Therefore the potential shown in figure 6.19(a) appears to be a good choice for the dynamical potential when  $B = 11$  T,  $\theta = 30^\circ$  and  $r = 1$ . We can also compare the eigenstate probability density plots for  $\theta = 15^\circ$  (fig. 6.2) to the energy levels in figure 6.19(b). We see that the RH edges of all the eigenfunctions are aligned and the position of the LH edge shifts left with increasing energy until the barrier imposed by the electric potential is met.

Therefore, the potential shown in figure 6.19(b) is a good choice for the dynamical potential when  $B = 11$  T,  $\theta = 15^\circ$  and  $r = 1$ .

### 6.1.3 What About the States We Skipped?

In formatting the above picture of a dynamical box, we only considered states on a single step in  $E(N)$  that were concentrated in the region of  $(x, z)$  space corresponding to the first ring of the stochastic web. This section will briefly examine the form of *all* the eigenstates on a step in  $E(N)$ .

We will calculate the eigenstates for a 14-period superlattice to reduce the maximum number of states on a step to 14. For this shorter superlattice, we have to increase the magnetic field strength to  $B = 20$  T so that the first dynamical box for  $\theta = 30^\circ$  is not truncated by the end of the superlattice. With  $B = 20$  T and  $r = 1$ , the first dynamical box is  $12.3d$  long for  $\theta = 30^\circ$ ,  $5.0d$  long for  $\theta = 45^\circ$  and  $2.4d$  long for  $\theta = 60^\circ$ , which is shorter than the superlattice in all cases. The second reason for using a 14-period system is because we have experimental data

for such a system. We will use this short superlattice throughout the remainder of the chapter.

Figure 6.20 shows probability density plots of the 14 eigenstates on a single step in  $E(N)$  calculated for  $B = 20T$ ,  $\theta = 30^\circ$  and  $r = 1$ , while figure 6.21(a) shows  $E(N)$  for these parameters. From the results for the 61-period superlattice, we expect there to be a sequence of eigenfunctions with 1, 2, 3... antinodes. The arrows in figure 6.20 indicate the positions of these nodes. The number of antinodes in the sequence (a), (b), (c), (d), (e), (f) appears to increase by one each time, although two of the nodes are not obvious in (e). The nodes are harder to distinguish in this shorter superlattice because the nodes are proportionally shorter. Any regions of near-zero probability density shorter than  $d$  will be hard to identify unless they correspond with the centre of a quantum well. However, a dynamical box generated node in the same  $x$  position as a node caused by the superlattice barriers will be difficult to identify.

Although the number of antinodes increases by one through figures 6.20(a→f), it does not follow this trend for higher energy eigenstates. Instead, we find that the number of nodes decreases by one through the sequence (g), (h), (i), (j), (l), (m), (n) with (g) probably having 6 antinodes. The number of nodes in (g) is hard to determine because the probability density is concentrated towards the right of the superlattice. The eigenstate probability density plotted in figure 6.20(k) is not concentrated in the same region as the other eigenstates and only extends across a single superlattice period.

There are therefore 13 eigenstates which exist within the dynamical box corresponding to the first ring in to stochastic web. This is unsurprising because this box is  $12.3d$  width which means that there should be 13 degenerate eigenstates in it at  $\theta = 0^\circ$ , which then split in energy for  $\theta = 30^\circ$ .

We will now plot the eigenstates for  $\theta = 45^\circ$  and then go on to discuss the antinode sequences seen in both the  $\theta = 30^\circ$  and  $\theta = 45^\circ$  results.

Figures 6.22 and 6.21(b) plot the probability density and energy eigenvalues for the 14 eigenstates on a single step in  $E(N)$  for  $B = 20T$ ,  $\theta = 45^\circ$  and  $r = 1$ . In figure 6.22, eigenfunctions (a), (d), (g), (h), (j) and (n) exist within the first ring of the stochastic web although (g) and (h) also have a significant proportion of their probability density outside this region. For these six states, the number of antinodes follows the sequence  $1 \rightarrow 2 \rightarrow 3 \rightarrow 3 \rightarrow 2 \rightarrow 1$  with increasing energy. The remaining eigenstates exist within the second ring of the stochastic web which should extend to  $17.4d$  but is truncated by the superlattice. The number of antinodes in these states goes as (b) 1, (c) 2, (e) 3, (f) 4, (g) ?, (h) ?, (i) ?, (k) 3, (l) 2 and (m) 1, where ? indicates that the number of antinodes in (g), (h) and (i) is unclear, but is probably 5, 5 and 4 respectively. These series show that similar behaviour occurs in the first and second rings of the stochastic

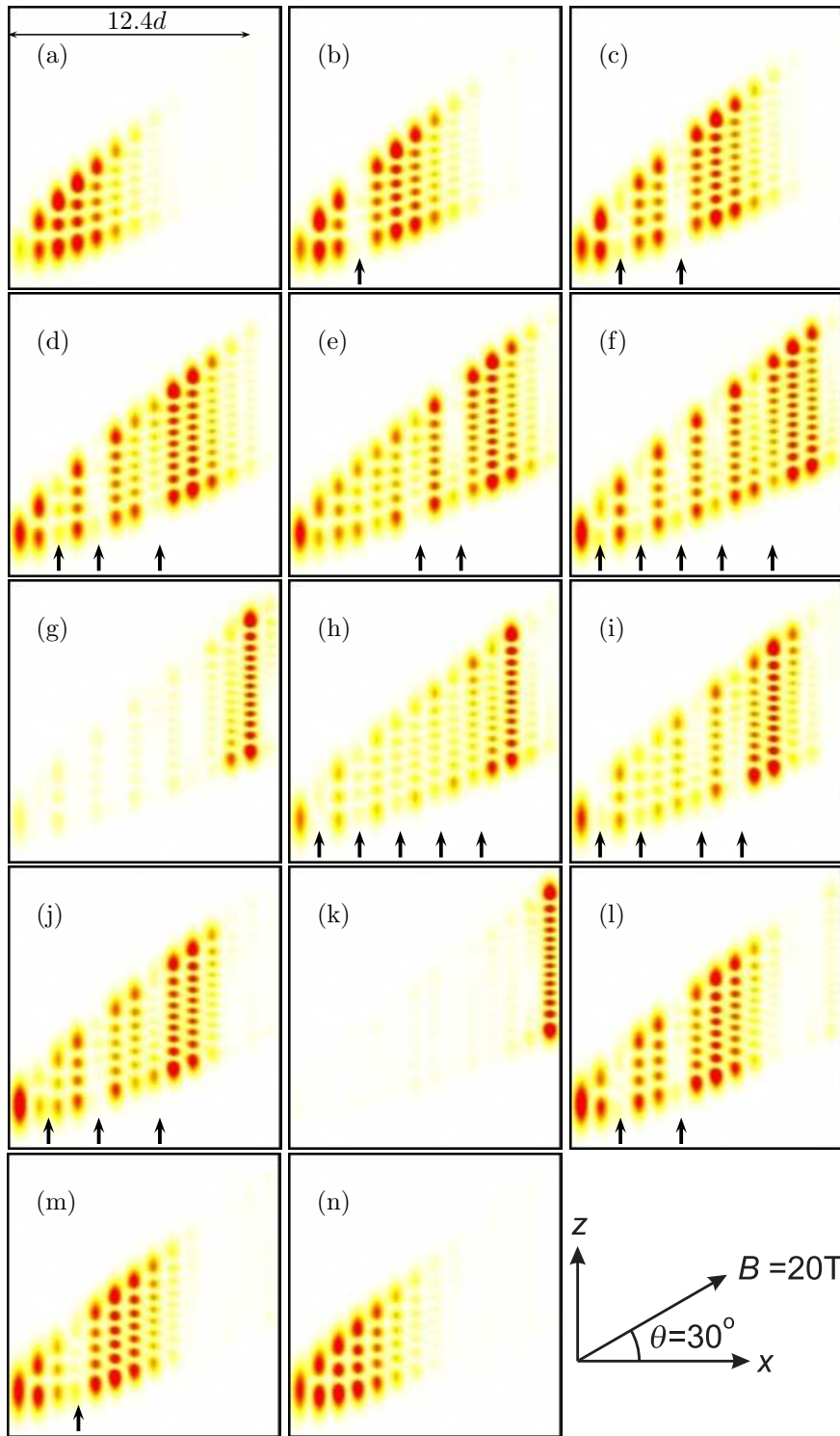


Fig. 6.20: Probability density plots for eigenstates  $N = 91 \rightarrow 104$  calculated for  $B = 20T$ ,  $\theta = 30^\circ$  and  $r = 1$  in a 14-period superlattice. The energy eigenvalues for these states are shown in figure 6.21(a). The arrows indicate the position of the more clearly visible nodes along  $x$  which are caused by confinement in the dynamical box. There are probably 4 nodes in (e) and 6 in (g) although these are hard to identify for the reason outlined in the text.

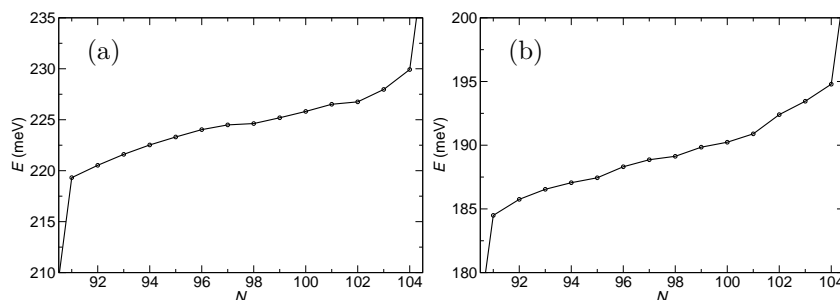


Fig. 6.21: A single step on the  $E(N)$  curves calculated for  $B = 20$  T,  $r = 1$  and (a)  $\theta = 30^\circ$ , (b)  $\theta = 45^\circ$  for a 14-period superlattice. These plots show the energies of the probability density plots in figures 6.20 and 6.22 respectively.

web so there should also be a dynamical box corresponding to the second ring. Eigenfunctions (g) and (h) cover both these dynamical boxes so some form of tunnelling between them is possible.

We can therefore modify our predicted form of the dynamical potential to account for these results. The  $1 \rightarrow 6 \rightarrow 1$  sequence of antinodes found for  $\theta = 30^\circ$  (fig. 6.20) implies that the potential is symmetric about some characteristic energy. Having such a closed potential would also place a finite limit on the spread of the eigenstates along  $x$ . Because we see a similar sequence of states in the region corresponding to the second ring of phase space for  $\theta = 45^\circ$  (fig. 6.22), a similar dynamical potential exists here as well. Presumably the series of dynamical boxes is infinite with one corresponding to each ring of the stochastic web. Figure 6.23 sketches this new form of the dynamical potential.

We can determine if this potential is accurate by plotting the spatial extents of the eigenfunctions against their energy eigenvalues. Figure 6.24 shows such a plot for  $B = 20$  T,  $\theta = 45^\circ$  and  $r = 1$  with an overlaid sketch of the dynamical potential. We can see that the form of the eigenstates is broadly consistent with the dynamical potential although the match is not exact. This is the final piece of evidence that our approximation of the dynamic box as a series of parabolic potentials mirrored about some energy is a good choice, and that the concept of a dynamical box is valid.

#### 6.1.4 Dynamical Potential Box Summary

In the previous sections we have suggested that the large scale antinode structure along  $x$  (figs. 6.20 and 6.22) can be explained by the dynamical potential wells shown in figure 6.23.

At this point, we should re-emphasise what this dynamical potential does and does not model. It is not intended as an addition to the three real potentials that define this system (electric, magnetic and superlattice), instead, it is

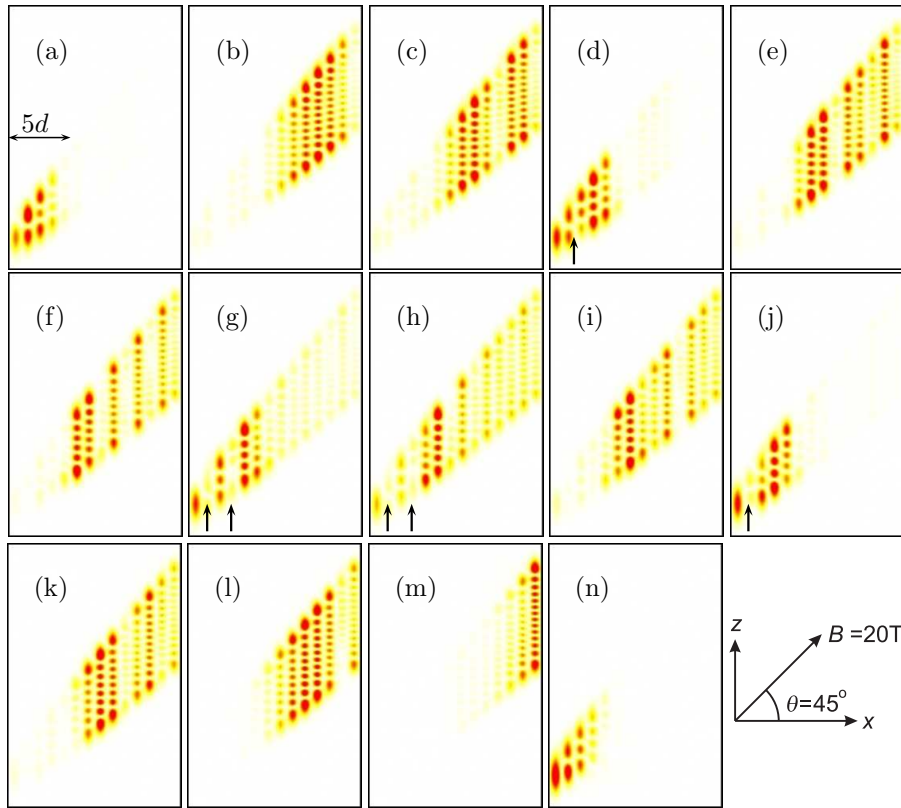


Fig. 6.22: Probability density plots for eigenstates  $N = 91 \rightarrow 104$  calculated for  $B = 20\text{ T}$ ,  $\theta = 45^\circ$  and  $r = 1$  in a 14-period superlattice. The energy eigenvalues for these states are shown in figure 6.21(b). The arrows indicate the position of the more clearly visible nodes along  $x$  which are caused by confinement in the dynamical box corresponding to the first ring of the stochastic web. Note that eigenfunctions (g) and (h) extend over two dynamical boxes both only the nodes in the region corresponding to the first dynamical box are arrowed.

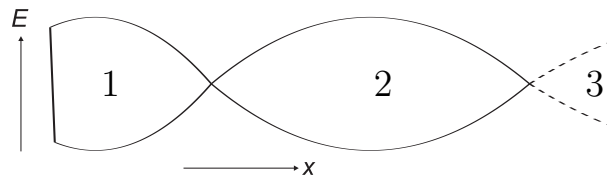


Fig. 6.23: Sketch of our final estimate of the form of the dynamical potential. The region inside the shape shows the allowed energy/position coordinates and the region outside is forbidden. The dynamical boxes corresponding to rings of the stochastic web that are progressively further from the centre (numbered) get progressively larger. This occurs because  $x$  varies as  $\rho^2$  where  $\rho$  is radial distance in phase space. This series of boxes is created from a number of curves with a  $E = B + (x - A)^2$  and  $E = B - (x - A)^2$  functional forms where  $A$  and  $B$  shift the position of the boxes.

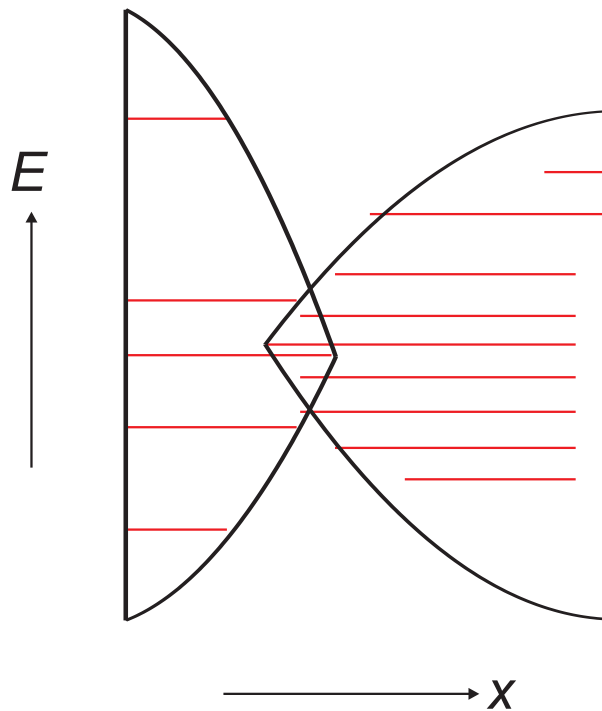


Fig. 6.24: (red) Plot of the  $x$  width of the eigenstates shown in figure 6.22 vs. their energy eigenvalues. This data is for  $B = 20 \text{ T}$ ,  $\theta = 45^\circ$  and  $r = 1$ . (black) Attempt to fit a parabolic dynamical potential similar to that shown in figure 6.23 around these states. The potential is truncated at high  $x$  by the finite superlattice length. It will not be possible to get a perfect match between the real eigenstates and the expected form of the dynamical box because the eigenfunction lengths are generally integer multiples of  $d$  because of the underlying superlattice potential while the dynamical box has no such restriction.

designed to account for the features only occur when these three real potentials are combined. Thus it does not attempt to model the small scale nodes along  $x$  which are an obvious effect of the superlattice potential. Nor does it attempt to describe the locus which confines the electron (eqn. 3.16) which, in a semiclassical model, is defined by the electric and magnetic field. However, it does attempt to account for the limit on  $x$  delocalisation which is caused by the stochastic web and is therefore due to a combination of all three potentials. It also attempts to describe the series of energy levels which form from the same underlying set of Landau levels.

The dynamical box model does not explicitly consider the stochastic filaments which exist around the edges of the stable regions of phase space. Therefore, the only mechanism for an eigenfunction to span multiple dynamical boxes in the dynamical box approximation is the tunnel between them.

The next section will compare the energy level spacing between adjacent  $N$  eigenstates to the spacing predicted from the large scale oscillations in the semiclassical electron trajectories. The remainder of the chapter will then look at the full spectrum of energy levels rather than just those on a single step in  $E(N)$ .

## 6.2 Semiclassical and Quantum Frequency Comparisons

The dynamical potential helps explain the large antinode structure seen in the eigenstate probability density plots (figs. 6.20 and 6.22). The corresponding semiclassical behaviour is a large scale orbit along the magnetic field direction (fig. 6.14). If this orbit is stable and periodic, it should be possible to relate the slow semiclassical frequency,  $\omega_S$ , to the quantum energy eigenvalue spacing,  $\Delta E$ , using:

$$\Delta E = \hbar\omega_S. \quad (6.7)$$

If this relation is true, it will provide further validity to our parabolic dynamical box approximation.

We can measure  $\omega_S$  by calculating the semiclassical electron trajectories in an identical manner to that performed in chapter 3 and Fourier transforming  $x(t)$ . Figure 6.25 shows an example Fourier transform corresponding to  $x(t)$  calculated for an electron starting from rest with  $B = 11$  T,  $\theta = 30^\circ$  and  $r = 1$  (fig. 6.14). As expected from the form of figure 6.14, we find two frequencies, the high frequency ( $\sim 4$  THz) corresponds to the frequency of the Bloch and cyclotron oscillations (remember that we are plotting  $f$  rather than  $\omega$ ) while the low frequency ( $\sim 0.091$  THz) corresponds to slow periodic oscillations within the dynamical potential. In this analysis of the dynamical box, we will ignore

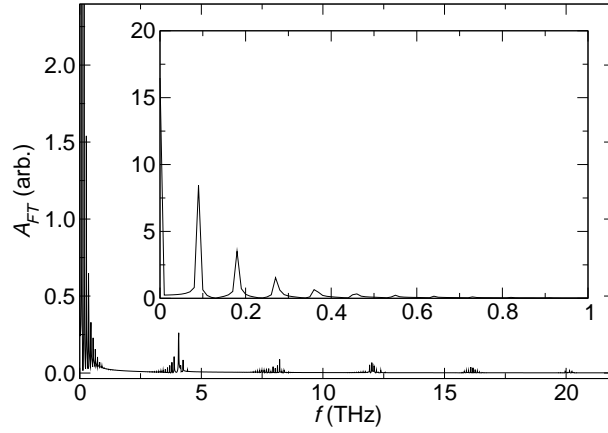


Fig. 6.25: Fourier transform,  $A_{FT}(f)$ , of the  $x(t)$  data shown in figure 6.14. The main plot shows high frequency peaks ( $\sim 4$  THz), and their harmonics, which correspond to Bloch and cyclotron oscillations. The inset shows lower frequency peaks ( $\sim 0.091$  THz), which are the large scale oscillations caused by the presence of the stochastic web.

the high frequency component for the same reason that we ignored the small scale node structure in the probability density plots. This reason is simply that the high frequency behaviour can be explained from either the magnetic potential (cyclotron oscillations) or a combination of the superlattice and electric potentials (Bloch oscillations). However, the low frequency behaviour arises from a combination of all three potentials which is the specific behaviour that the dynamical box is designed to model.

However, we cannot simply inset this value of  $\omega_S = 0.091$  THz into equation 6.7 because it is calculated for a single electron starting from rest. Therefore, this value of  $\omega_S$  only corresponds to a trajectory which exists on the stochastic web but does not cover any stable islands of the semiclassical phase space. In contrast, the Wigner functions (fig. 6.11 for example) incorporate both chaotic and stable regions. Therefore, we must calculate  $\omega_S$  for a number of different initial conditions and take some weighted average to compare to the quantum energy level spacing. Figure 6.26 plots electron trajectories and  $x(t)$  for a variety of stable orbits which show that slow frequencies also exist for these stable trajectories.

To calculate our average slow frequency,  $\bar{\omega}_S$ , we determine  $\omega_S$  for a grid of  $(q_y, p_z)$  values by calculating and Fourier transforming  $x(t)$  data calculated for these each of these starting momenta. This  $\omega_S(q_y, p_z)$  function is then weighted by the normalised quantum Wigner function,  $W(q_y, p_z)$ , and summed to give

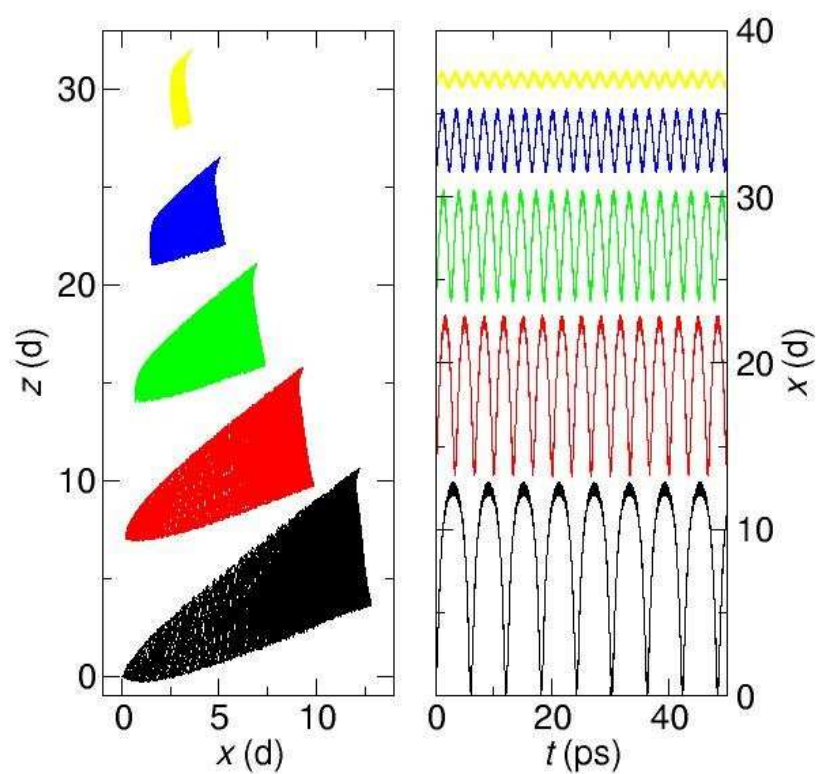


Fig. 6.26: Five semiclassical electron trajectories (left) whose initial momentum is (yellow) near the centre of a stable island, (black) on the stochastic web and (blue, green, red) a range of values in between. Adjacent plots have a variable offset in the  $z$ -direction for clarity. The right hand figures plot  $x(t)$  for these same electron trajectories and each orbit shows a differing slow frequency.

$\bar{\omega}_S$ . This can be expressed mathematically as:

$$\bar{\omega}_S = \sum_{q_y=-\infty}^{\infty} \sum_{p_z=-\infty}^{\infty} \omega_S(q_y, p_z) W(q_y, p_z). \quad (6.8)$$

Figure 6.27(a) shows plots  $\omega_S(q_y, p_z)$  for  $B = 20 \text{ T}$ ,  $\theta = 30^\circ$  and  $r = 1$ . The form of  $\omega_S(q_y, p_z)$  resembles the form of both the corresponding Poincaré section (fig. 6.27(b)) and a sample Wigner function (fig. 6.27(c)), which is unsurprising considering that  $\omega_S(q_y, p_z)$  is generated from the same information as the Poincaré section.

Figure 6.27(a) shows that  $\omega_S(q_y, p_z)$  is highest at the centre of the stable islands in the stochastic web and decreases towards the edges of these islands. The Wigner functions also tend to be concentrated in these areas (fig. 6.27(c)).  $\omega_S(q_y, p_z)$  is very low on the stochastic filaments and these small regions will not make a large contribution to  $\bar{\omega}_S$ . Therefore, it is the electron behaviour in the stable islands that will make the main contribution to  $\bar{\omega}_S$ . This is useful because equation 6.7 is only valid for stable orbits and orbits in stable islands are stable by definition. The three panels on the RHS of figure 6.27 plot example Fourier transforms for given  $q_y$  and  $p_z$  values. These Fourier transforms all show a single low frequency peak with associated harmonics. Therefore these low frequency orbits are stable.

The value of  $\bar{\omega}_S$  can now be calculated, using equation 6.8, for all the Wigner functions on a particular step in  $E(N)$ . Multiplying by  $\hbar$  should then give a measure of the quantum energy level spacing (eqn. 6.7). Figure 6.28 compares the energy level spectrum calculated from these spacings to  $E(N)$  calculated using the quantum model. The two sets of values compare fairly well although there is some deviation whose cause is unknown.

Figures 6.29 and 6.30 are identical to figure 6.27 but are calculated for  $\theta = 45^\circ$  and  $\theta = 60^\circ$  respectively. In both cases we see that the form of  $\omega_S(q_y, p_z)$  (figs. 6.29(a) and 6.30(a)) is reminiscent of the Poincaré sections (figs. 6.29(b) and 6.30(b)) and the Wigner functions (figs. 6.29(c) and 6.30(c)).

The form of  $\omega_S(q_y, p_z)$  changes as  $\theta$  is increased. For  $\theta = 45^\circ$ ,  $\omega_S(q_y, p_z)$  (fig. 6.29(a)) is very irregular and low valued within the first ring of the stochastic web. An example Fourier transform of this region (fig. 6.29(B)), shows that a large number of frequencies are present which is a signature of unstable behaviour. Fortunately, these unstable orbits will not make a significant contribution to  $\bar{\omega}_S$  because the calculated  $\omega_S$  is low for the unstable regions (our approach simply detects the lowest frequency peak in the Fourier transform). Additionally,  $W(q_y, p_z)$  also tends to be low in the unstable regions because stable regions “trap” the electron probability. We still see some stable orbits within

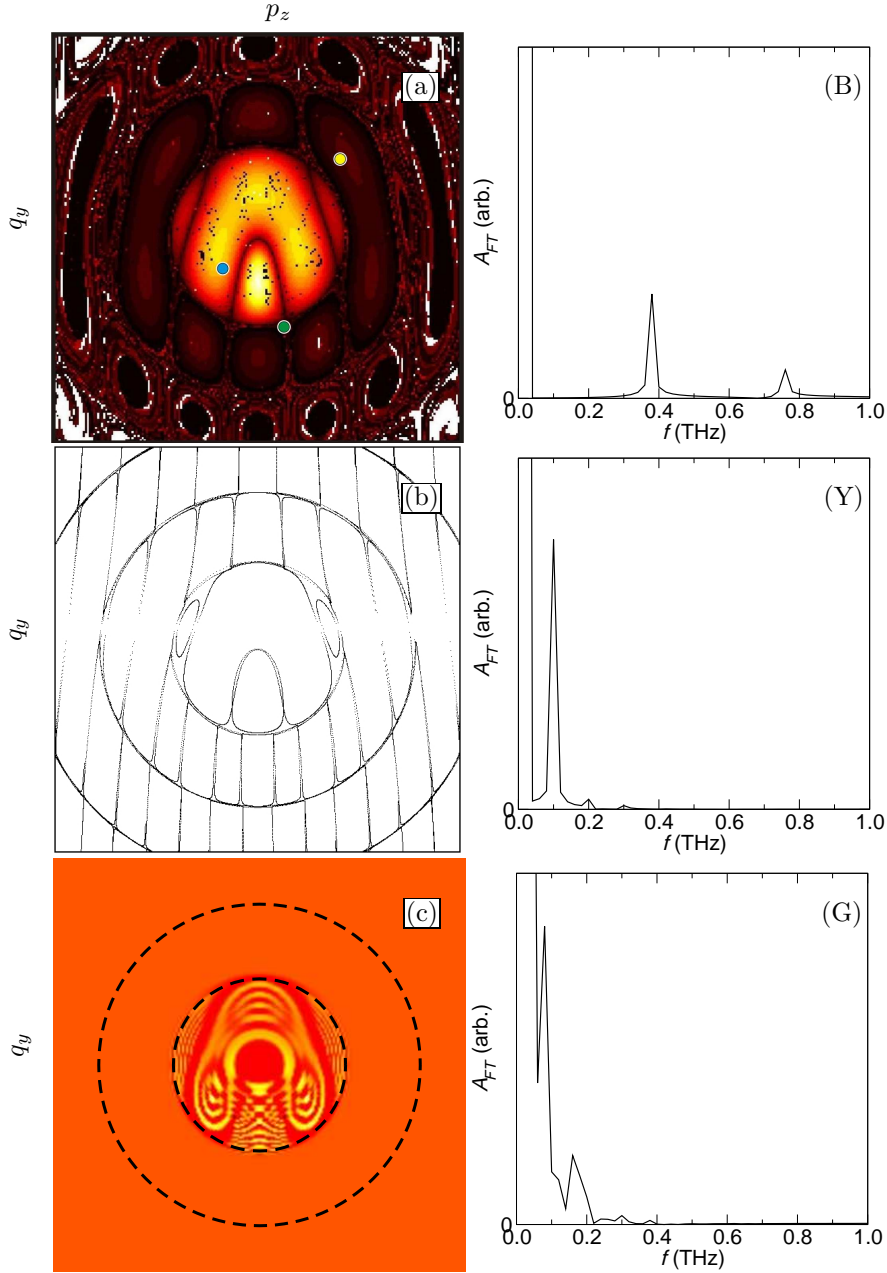


Fig. 6.27: Plots of (a)  $\omega_S(q_y, p_z)$ , (b) the Poincaré section and (c) an example Wigner function for  $B = 20$  T,  $\theta = 30^\circ$  and  $r = 1$ . All three plots are on the same axes which vary from  $(-2 \rightarrow 2) \times 10^{-25}$  kg ms $^{-1}$ . The three graphs on the right show Fourier transforms for electron orbits starting from the (B) blue, (Y) yellow and (G) green points on (a). Note that the  $\omega_B$  peak is off the scale at 7.2 THz. The large number of white points at the edges of (a) correspond to  $\omega_B$  which is  $\gg \omega_S$ .  $\omega_B$  is only detected if the resolution of the Fourier transform is too low to find a lower frequency peak which should always exist. The noise in the centre of (a) does not have a significant impact on any results calculated from this data and smoothing out the noise has no significant impact on  $\bar{\omega}_S$ . The colourmap for (a) varies linearly from black to yellow to red to white. The broken circles on the Wigner functions show the radius of the stochastic rings.

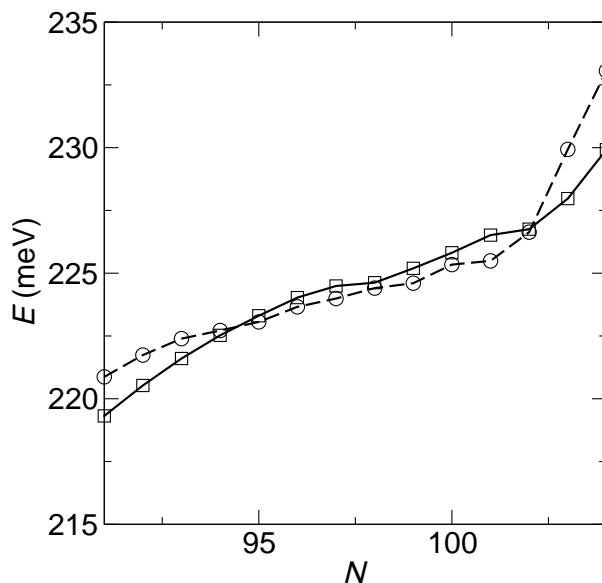


Fig. 6.28: Comparison between the quantum mechanical energy eigenvalues (circles) and the calculated semiclassical energies (squares) for a single step in  $E(N)$  for a 14 period superlattice.  $B = 20$  T,  $r = 1$  and  $\theta = 30^\circ$ .

the first ring of the stochastic web for  $\theta = 45^\circ$ , figure 6.29(Y) for example.

For  $\theta = 60^\circ$ , the unstable region in  $\omega_S(q_y, p_z)$  (fig. 6.30(a)) extends out to the second ring of the stochastic web and we can see the corresponding chaotic sea in the Poincaré section (fig. 6.30(b)). Again, these unstable orbits are characterised by a large number of low frequency peaks (figs. 6.30(B) and 6.30(Y)).

Figure 6.31 shows the comparison between  $E(N)$  calculated from the quantum model and  $E(N)$  calculated from  $\omega_S(q_y, p_z)$  using the semiclassical model for (a)  $\theta = 45^\circ$  and (b)  $\theta = 60^\circ$ . These results agree to a greater degree than those at  $\theta = 30^\circ$  and the  $\theta = 45^\circ$  match is especially good. For  $\theta = 60^\circ$ , there is a large deviation for  $N > 100$ . The  $N = 103$  and 104 eigenstates are part of the next step in the  $E(N)$  curve and are shifted by approximately  $eFd$  from the  $N < 100$  energy levels. Eigenstates 101 and 102 exist somewhere between these two steps. Therefore, the discrepancy in the two methods of calculating  $E(N)$  occurs because  $\hbar\omega_S$  can only predict the energy level spacings of eigenstates whose eigenfunctions are localised in a similar region of space. The  $eFd$  spacing arises from shifting the eigenfunction and so cannot be accounted for with  $\hbar\omega_S$ .

It is unclear why the match is much better for  $\theta = 45^\circ$  and  $\theta = 60^\circ$  than for  $\theta = 30^\circ$  because the electron orbits for  $\theta = 30^\circ$  are almost all stable and so equation 6.7 should work much better. However the match is still good and does not represent a significant failing in our model.

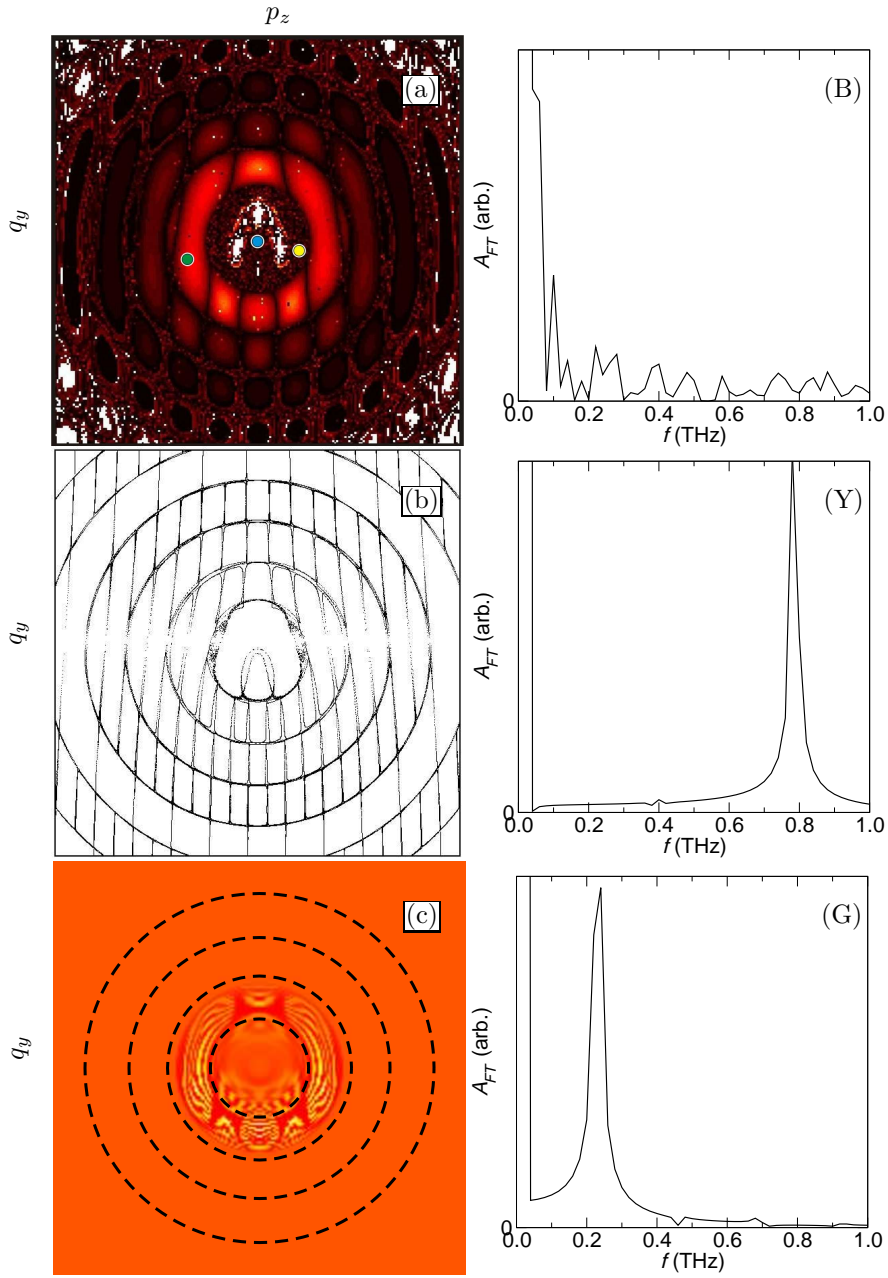


Fig. 6.29: Plots of (a)  $\omega_S(q_y, p_z)$ , (b) the Poincaré section and (c) an example Wigner function for  $B = 20$  T,  $\theta = 45^\circ$  and  $r = 1$ . All three plots are on the same axes which vary from  $(-2 \rightarrow 2) \times 10^{-25}$  kg ms $^{-1}$ . The three graphs on the right show Fourier transforms for electron orbits starting from the (B) blue, (Y) yellow and (G) green points on (a). Note that the  $\omega_B$  peak is off the scale at 5.9 THz. The noise in (a) is discussed in the caption of figure 6.27. The colourmap for (a) varies linearly from black to yellow to red to white. The broken circles on the Wigner functions show the radius of the stochastic rings.

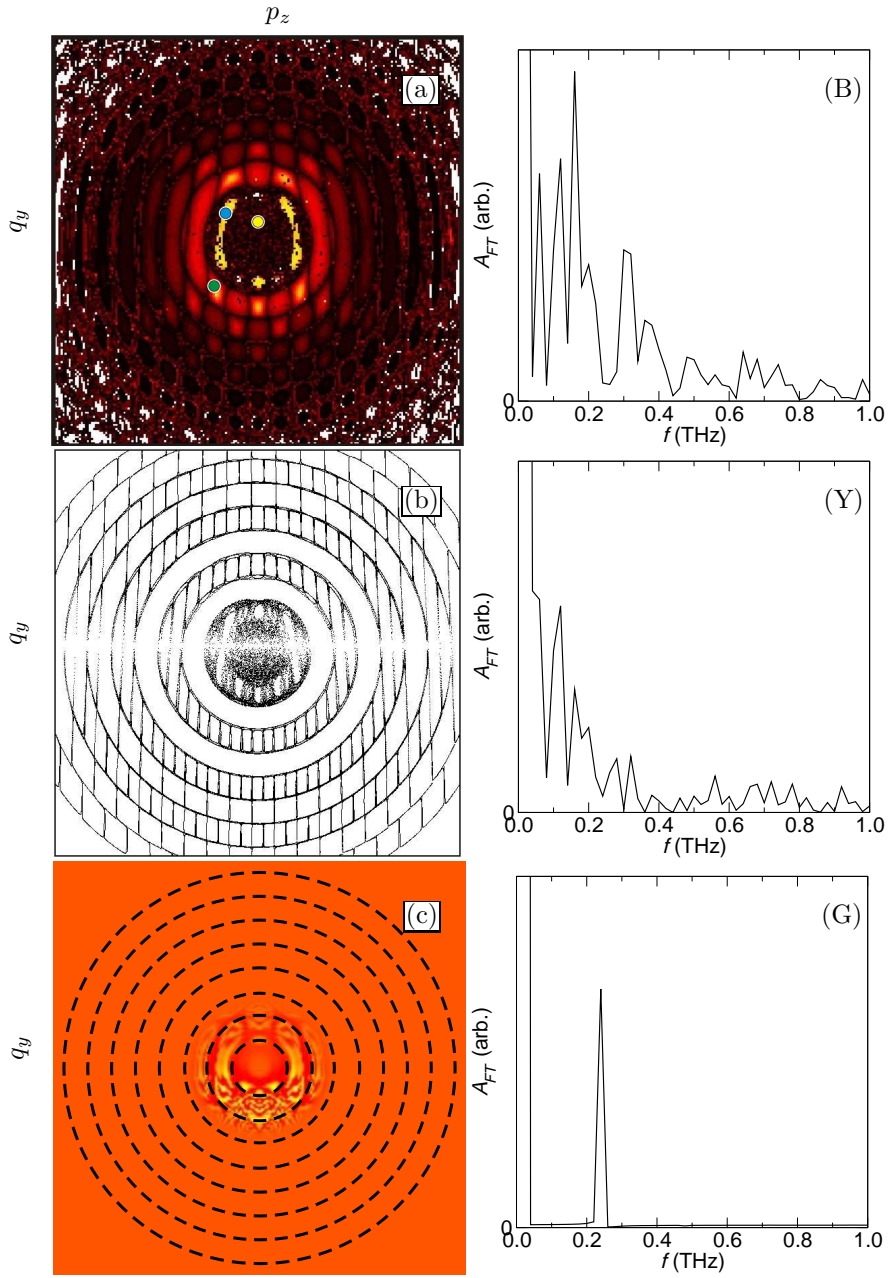


Fig. 6.30: Plots of (a)  $\omega_S(q_y, p_z)$ , (b) the Poincaré section and (c) an example Wigner function for  $B = 20$  T,  $\theta = 60^\circ$  and  $r = 1$ . All three plots are on the same axes which vary from  $(-2 \rightarrow 2) \times 10^{-25}$  kg ms $^{-1}$ . The three graphs on the right show Fourier transforms for electron orbits starting from the (B) blue, (Y) yellow and (G) green points on (a). Note that the  $\omega_B$  peak is off the scale at 4.2 THz. The noise in (a) is discussed in the caption of figure 6.27. The colourmap for (a) varies linearly from black to yellow to red to white. The broken circles on the Wigner functions show the radius of the stochastic rings.

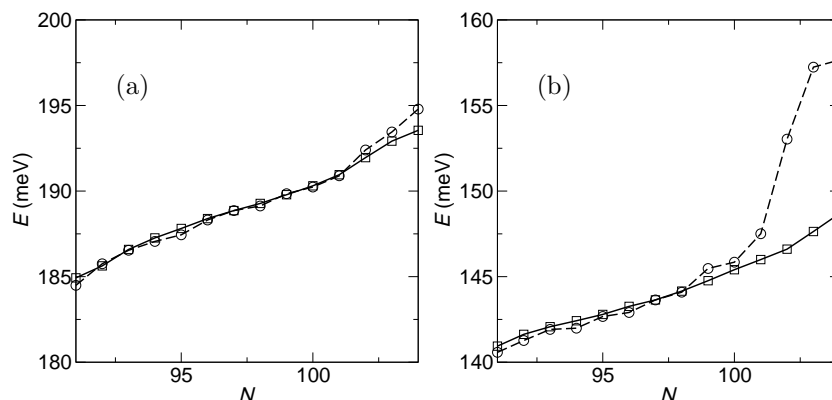


Fig. 6.31: Comparison between the quantum mechanical energy eigenvalues (circles) and the calculated semiclassical energies (squares) for a single step in  $E(N)$  for a 14 period superlattice.  $B = 20$  T,  $r = 1$  and (a)  $\theta = 45^\circ$ , (b)  $\theta = 60^\circ$ . The large deviation for  $\theta = 60^\circ$  and  $N > 100$  occurs because the energy eigenvalues of these states place them on a different step in  $E(N)$  to the  $N \leq 100$  eigenstates. The equation  $\Delta E = \hbar\omega_S$  can only account for the spacing between eigenstates that are positioned on the same step.

This energy correspondence is the final piece of evidence in verifying our hypothesis that the non-degenerate eigenstates on a single step in  $E(N)$  vary in energy due to quantisation in the box shown in figure 6.23. We have found that  $E(M)$  does not vary linearly with  $M$  as predicted by  $\Delta E = \hbar\omega_S$  because  $\omega_S$  varies with energy<sup>1</sup>.

### 6.3 Band Structure

The previous sections have shown that the degenerate set of localised eigenstates seen at  $\theta = 0^\circ$  split into non-degenerate levels when  $\theta > 0^\circ$ , which form short bands of states with spatially extended eigenfunctions (fig. 6.24). Continuing with our previous convention, we will refer to these bands as *dynamical bands* because they arise from the dynamical box and to distinguish them from semiconductor bands and superlattice minibands. This section will look at the structure of these dynamical bands and discuss their effect on electron transport through the superlattice. We will continue to look at the 14-period superlattice for which we have experimental  $I(V)$  data. When considering these bands, it is important to note that thermal broadening of energy levels will occur in a real system. This thermal broadening is of the order  $\hbar/\tau_{SL}$  which is typically a few meV.

<sup>1</sup> We use  $M$ , rather than  $N$  used earlier in the paragraph, because only the eigenstates in the same dynamical box should have a separation given by  $\Delta E = \hbar\omega_S$  but a full step in  $E(N)$  may contain eigenstates in different dynamical boxes.

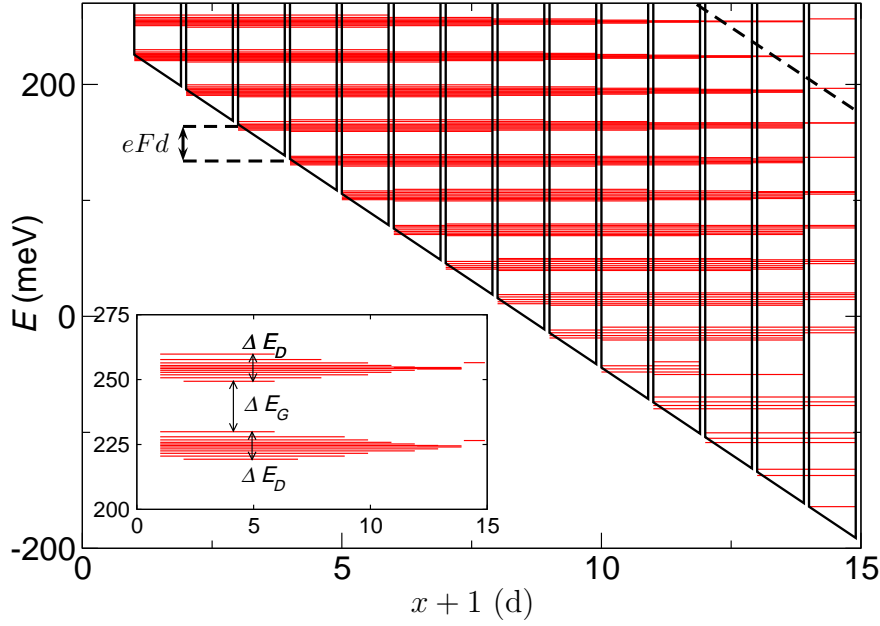


Fig. 6.32: Plot of the  $N = 0 \rightarrow 119$  energy eigenstates of a 14-period superlattice with  $B = 20 \text{ T}$ ,  $\theta = 30^\circ$  and  $r = 1$ . The height of each red line indicates each eigenstate's energy eigenvalue and the width of the line indicates the spatial extent of its eigenfunction along  $x$ . The superlattice and electric field potential (black) is also shown for reference. The inset shows a magnification of the top two bands indicating the dynamical bandwidth,  $\Delta E_D$ , and the dynamical bandgap,  $\Delta E_G$ . The broken line shows where the first dynamical box is expected to end so the majority of these states are confined to the first dynamical box.

The  $N = 0 \rightarrow 118$  eigenstates for  $B = 20 \text{ T}$ ,  $\theta = 30^\circ$  and  $r = 1$  are shown in figure 6.32. This figure represents each eigenstate by a horizontal line whose length shows the  $x$  width of the eigenfunctions and whose height shows the energy eigenvalue. We will refer to such a plot as the band structure. We generally find that the number of states in each dynamical box is equal to the number of superlattice periods that the dynamical box extends over. The shape of the bands in figure 6.32 resembles the expected form of the dynamical potential of the first dynamical box<sup>2</sup>. No band due to the second dynamical box can be seen because only a few states exist in this region (to the right of the broken line).

This type of band picture will only emerge when  $r$  takes an integer value. This is because the Landau levels in adjacent superlattice periods must be isoenergetic to allow the eigenfunctions to extend across adjacent superlattice periods. Extended eigenfunctions will still form for non-integer rational values of  $r$  but they will contain gaps (see fig. 5.16). This integer  $r$  condition is identical to the

<sup>2</sup> See figure 6.24 for an example of how this works

Stark-Cyclotron resonance condition that must be satisfied for Wannier-Stark hopping to occur when  $\theta = 0^\circ$  (section 1.2.2). The difference is that, for  $\theta = 0^\circ$ , an integer  $r$  enables scattering based transport but, for  $\theta \neq 0^\circ$ , it enables coherent coupling of adjacent quantum wells. This difference occurs because different Landau eigenfunctions,  $\varphi_n(z)$ , are orthogonal unless offset in space:

$$\langle \varphi_n(z) | \varphi_{n'}(z) \rangle = \delta_{nn'} \quad (\theta = 0^\circ) \quad (6.9)$$

$$\langle \varphi_n(z) | \varphi_{n'}(z + d \tan \theta) \rangle \neq 0 \quad (\theta \neq 0^\circ). \quad (6.10)$$

The offset is, in this case, caused by the tilted magnetic field.

Figure 6.33 confirms that dynamical bands form for other values of  $\theta$  and for other integer values of  $r$ . When  $r = 2$  (fig. 6.33(a)), two bands form per  $eFd$  energy range. These two bands occur because the extended eigenstates for  $r = 2$  combine every other Landau level-like state (see fig. 5.16(m)). Therefore, there are two possible basic eigenstates, one which combines the  $n = 0$  Landau level in superlattice period one with the  $n = 2$  level in period two and so on, the second combines the  $n = 1, 3, 5 \dots$  Landau levels in adjacent periods. The energy difference between these two possibilities is  $\hbar\omega_C$  which is  $\frac{1}{2}eFd$  for  $r = 2$ . These basic states then split into bands and a series of these bands, shifted in energy by  $eFd$  and in position by  $(x = d, z = d \tan \theta)$ , will occur.

When  $\theta = 45^\circ$ ,  $B = 20$  T and  $r = 1$  (fig. 6.33(b)), the bands are divided into two along the  $x$ -direction (thick lines). This splitting occurs because two dynamical boxes fit into the superlattice (the first is  $5d$  long and the second would be  $17.4d$  long if it were not truncated by the finite superlattice). The density of levels in these shorter dynamical boxes tends to be lower because there are fewer levels in each part of the dynamical band. However, there are also some eigenstates which extend across multiple dynamical boxes so tunnelling between them is possible (see fig. 6.22(g) for an example of an eigenfunction that spans multiple dynamical boxes).

When  $r$  is irrational, there are no Landau levels that are isoenergetic with Landau levels in a different superlattice period so no coherent coupling occurs. Therefore the eigenfunctions are localised to a single superlattice period (fig. 5.16(l)). Figure 6.34 plots the “band structure” for  $B = 20$  T,  $\theta = 30^\circ$  and  $r = \frac{1+\sqrt{5}}{2}$  which clearly shows that no dynamical bands form.

For non-integer rational values of  $r$ , the eigenstate probability density function “skips” some superlattice periods because Landau levels in adjacent periods are not isoenergetic, but those in non-adjacent periods may be (see fig. 5.16 for examples). Therefore the dynamical bands will contain periodic gaps along  $x$ . Figure 6.35 shows the band structure for  $B = 20$  T,  $\theta = 30^\circ$  and  $r = 0.5$  which appears to resemble that for  $r = \frac{1+\sqrt{5}}{2}$  (fig. 6.34). However, coherent coupling

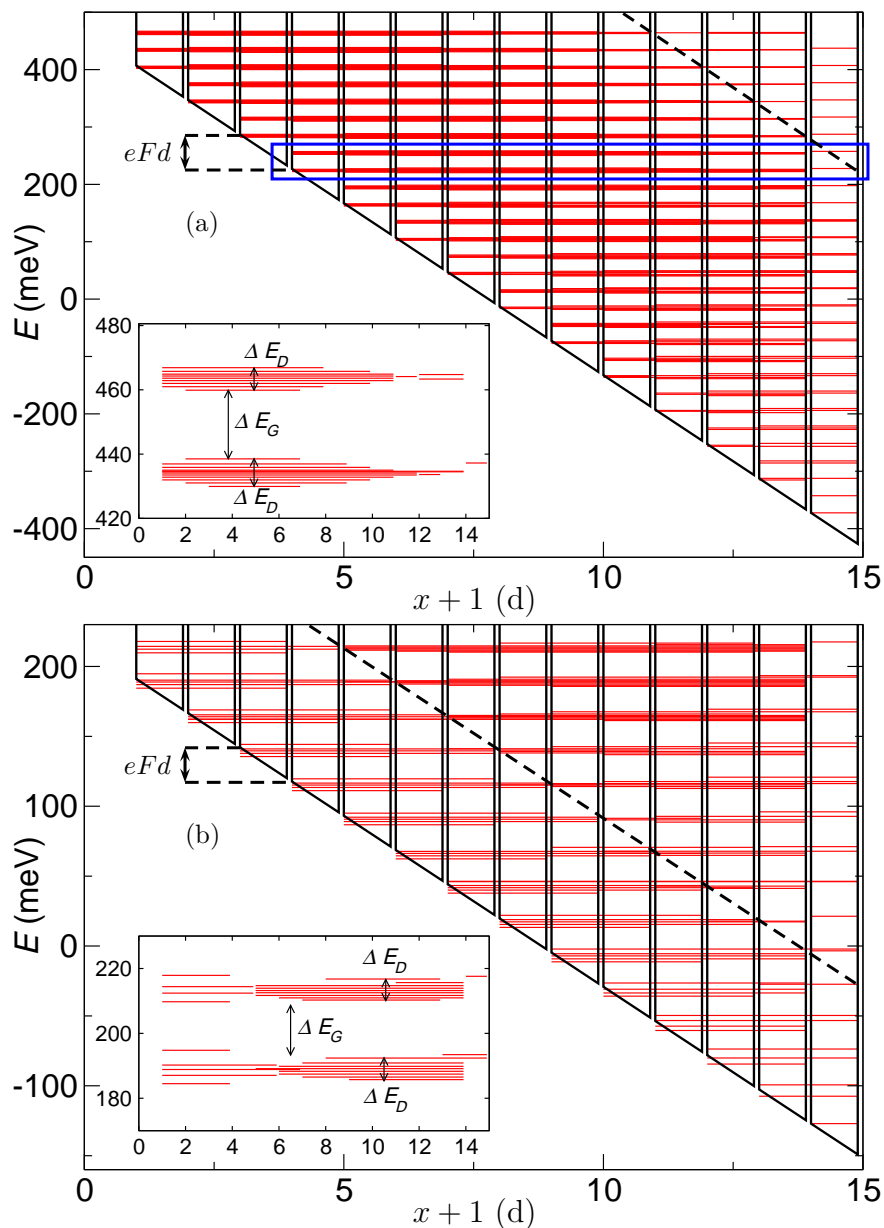


Fig. 6.33: Plot of the (a)  $N = 0 \rightarrow 239$  and (b)  $N = 0 \rightarrow 119$  energy eigenstates of a 14-period superlattice with  $B = 20$  T and (a)  $\theta = 30^\circ$ ,  $r = 2$ , (b)  $\theta = 45^\circ$ ,  $r = 1$ . The height of each red line indicates each eigenstate's energy eigenvalue and the width of the line indicates the spatial extent of its eigenfunction along  $x$ . The superlattice and electric field potential (black) is also shown for reference. The insets show a magnification of the top two bands indicating the dynamical bandwidth,  $\Delta E_D$ , and the dynamical bandgap,  $\Delta E_G$ . In (a), for  $r = 2$ , we see that there are two dynamical bands per shift of  $eFd$  in energy (e.g. the two bands inside the blue box). The broken lines show the limit of the first dynamical box and in (b) we can clearly see dynamical bands corresponding to both the first and second dynamical boxes (left and right of the broken line respectively).

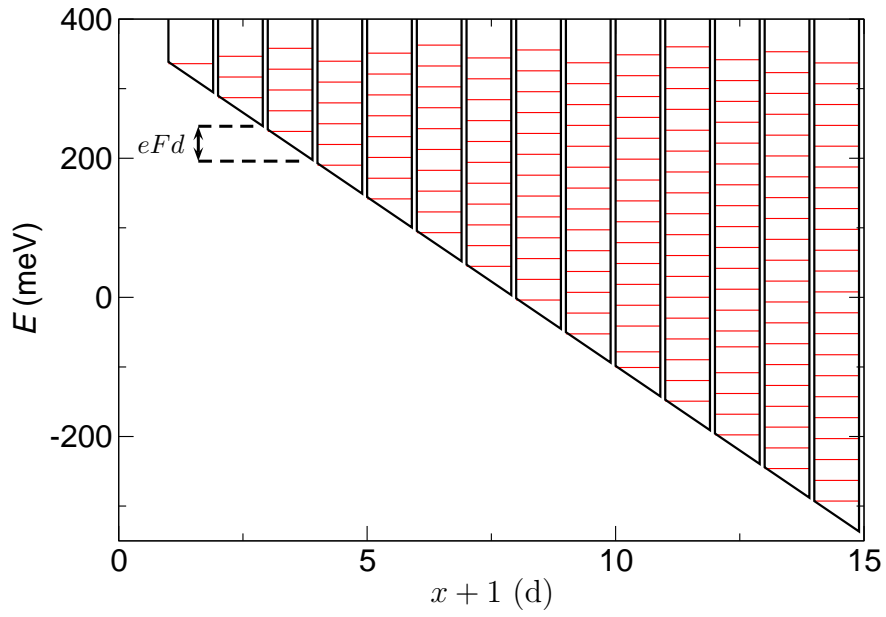


Fig. 6.34: Plot of the  $N = 0 \rightarrow 119$  energy eigenstates of a 14-period superlattice with  $B = 20$  T,  $\theta = 30^\circ$  and  $r = \frac{1+\sqrt{5}}{2}$ . The height of each red line indicates each eigenstate's energy eigenvalue and the width of the line indicates the spatial extent of its eigenfunction along  $x$ . The superlattice and electric field potential (black) is also shown for reference. It is clear that no bands form and the eigenstates are all localised to a single superlattice period.

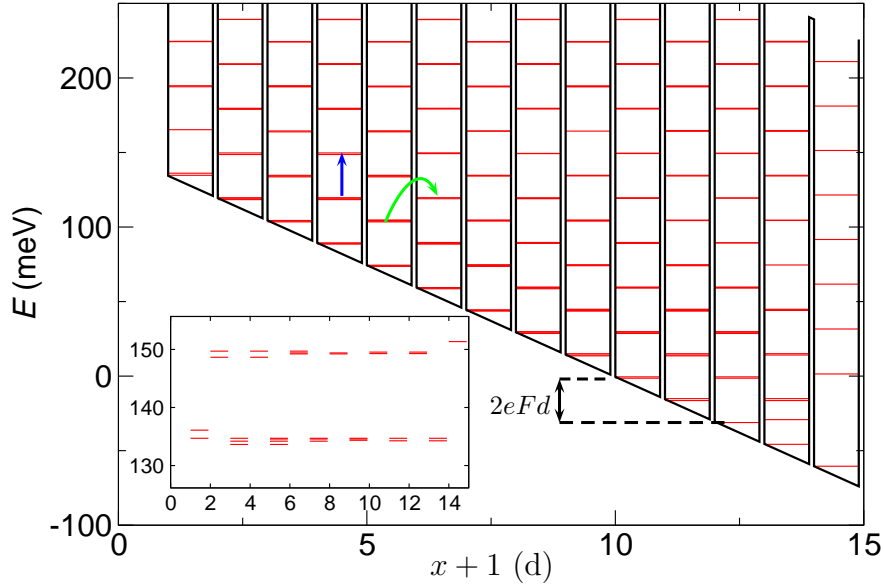


Fig. 6.35: Plot of the  $N = 0 \rightarrow 119$  energy eigenstates of a 14-period superlattice with  $B = 20$  T,  $\theta = 30^\circ$  and  $r = 0.5$ . The height of each red line indicates each eigenstate's energy eigenvalue and the width of the line indicates the spatial extent of its eigenfunction along  $x$ . The superlattice and electric field potential (black) is also shown for reference. Note that coherent coupling of non-adjacent superlattice period does occur. The blue arrow indicates a vertical transition which has an energy spacing of  $2eFd$ . The green arrow shows a transition which only has an energy spacing of  $eFd$  but requires a shift in position.

still occurs between non-adjacent periods so the electron probability density is not localised to a single superlattice period. Therefore, the bandgap for vertical transitions is  $2eFd$  and  $eFd$  for transitions that shift superlattice periods.

In summary, for rational values of  $r$ , we have found dynamical bands that extend across most of the 14 superlattice periods. However, there are few individual electron eigenfunctions that span this full distance, instead each band is formed from states that occupy a number of dynamical boxes whose widths are related to the radius of the rings in the semiclassical stochastic web. Therefore, an electron can only move a short distance through the superlattice without the influence of scattering. That said, this short distance is still much longer than the highly localised eigenfunctions which occur when the dynamical box does not exist (fig. 6.34). The next section will investigate the variation in the width of these dynamical bands as a function of both  $B$  and  $\theta$ .

### 6.3.1 Width of the Dynamical Bands

We will now investigate how the bandwidth,  $\Delta E_D$  of the dynamical bands varies with  $B$  and  $\theta$ . We can make two measures of this bandwidth. Firstly, if  $B$  and  $r$  are fixed and  $\theta$  is varied, then the absolute bandwidth can be plotted as a function of  $\theta$ . However, using this approach means that  $eFd$ , the energy spacing between the centres of adjacent bands, will decrease with increasing  $\theta$  because:

$$eFd = \frac{reB \cos \theta}{m^*}. \quad (6.11)$$

Thus, even if the absolute bandwidth stays constant with increasing  $\theta$ , the bandgap,  $\Delta E_G$ , will decrease and a plot of  $\Delta E_D$  will not reveal the full picture. Therefore, to see the true effect of varying  $\theta$ , we can either fix  $B \cos \theta$  or plot bandwidth as a fraction of  $eFd$ . This second measure of bandwidth will be referred to as *band spread*,  $\Delta E_S$  because it measures how much of the energy spectrum is covered by bands. The experimental data we have has fixed  $B$  or  $\theta$  so the best way to measure band spread is to calculate:

$$\Delta E_S = \frac{\Delta E_D}{eFd}. \quad (6.12)$$

The above discussion applies equally for investigating the effects of varying  $B$  rather than  $\theta$ .

The particular  $N$  states which form a band vary depending on  $\theta$  and  $B$ . For example, the fifteenth dynamical band for  $B = 20$  T and  $r = 1$  is made from  $N = 91 \rightarrow 104$  for  $\theta = 30^\circ$  and  $\theta = 45^\circ$ , but from  $N = 89 \rightarrow 101$  for  $\theta = 60^\circ$  (figure 6.36). This makes determining  $\Delta E_D$  for a wide range of parameters problematic because it is hard to automatically determine which states are actually in a single band. The problem is further compounded by the presence of interband eigenstates - eigenstates whose energy eigenvalue lies between two bands and the eigenfunction does not appear to belong to either band (see figure 6.37 and discussion). Figure 6.37 shows an example of these interband states and it is clear that they do not belong to a band. Therefore, for a 14-period superlattice, the maximum number of eigenstates in a dynamical band is 14 but will often be lower. We tend to find that high  $B$  and  $\theta$  values cause the number of eigenstates in a dynamical band to decrease as will be shown later.

To calculate the dynamical bandwidth automatically, we determine:

$$\Delta E_D = \min [E(N) - E(N - W + 1)] \quad (6.13)$$

where  $W$  is the number of states we expect to find in the dynamical bands. We

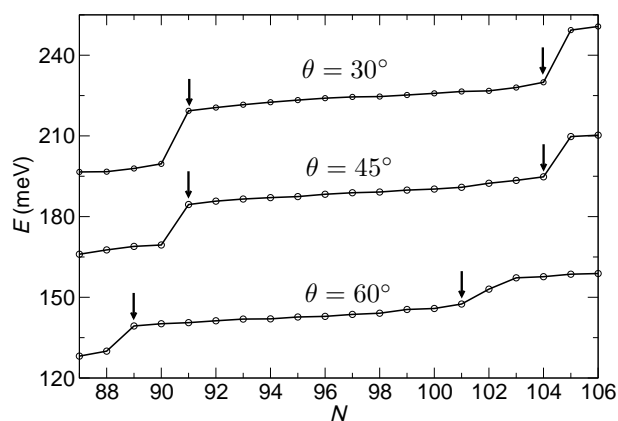


Fig. 6.36: Plot showing  $E(N)$  for  $B = 20$  T,  $r = 1$  and  $\theta$  as marked. The arrows indicate the lowest and highest energy eigenstates that form the fifteenth dynamical band. Therefore, which eigenstates form a particular band can change with  $\theta$ .

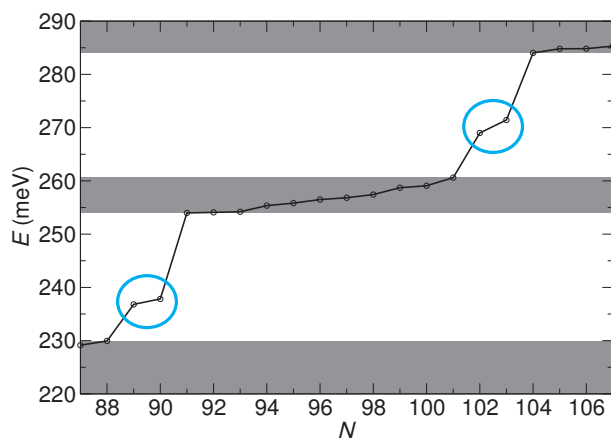


Fig. 6.37: Plot of  $E(N)$  for  $B = 35$  T,  $\theta = 60^\circ$  and  $r = 1$ . The dynamical bands are shown by the grey energy ranges and four interband states are highlighted by the blue circles. The interband states lie over 8 meV from the bands which is much further than the thermal energy broadening of  $\hbar/\tau \approx 3.75$  meV. Therefore, these interband states will never be part of the band.

will calculate  $\Delta E_D$  for  $W = 14, 13, 12$  and  $11$ . This will obtain the bandwidth assuming there are zero, one, two and three interband states which do not belong to a band that we want to ignore respectively. Figure 6.38 plots these four different bandwidths calculated for  $\theta = 45^\circ$ ,  $r = 1$  and  $B = 0 \rightarrow 50$  T. This figure shows that when  $B > 30$  T, the amplitude of the  $W = 14$  curve (black) is much larger than the other solid curves which indicates that a single interband state is present. The  $W = 13$  and  $W = 12$  curves also show a similar increase for  $B > 42$  T which implies that there are three interband states at these high magnetic fields. The bandwidth for a particular  $B$  should be taken from the up-most curve that doesn't show a large deviation from the curves below it. We therefore use the black curve for  $B \leq 30$  T, the red curve for  $30 < B < 42$  T and the blue curve for  $B \geq 42$  T.

The broken line in figure 6.38 shows how  $eFd$  varies with  $B$ . The energy spacing between  $E(N)$  and  $E(N + 14)$  should also be  $eFd$  so if the  $W = 14$  bandwidth (black curve) approaches  $13/14$  of  $eFd$  then the bands are merged. This is because the interband spacing is equal to, or less than, the spacing between levels within the bands. This occurs for  $B < 10$  T and, for these magnetic fields, something approaching a continuum of states exists.

The variation in  $\Delta E_D$  with  $\theta = 0 \rightarrow 60^\circ$  for  $B = 20$  T and  $r = 1$  is plotted in figure 6.39(a). We find that bandwidth increases with increasing  $\theta$  for  $\theta < 15^\circ$  and peaks at  $\sim 11$  meV. The bandwidth for  $\theta > 15^\circ$  decreases slightly with increasing  $\theta$ . Using the method outlined in the caption of figure 6.38, we can tell that the band consists of 14 eigenstates for  $\theta \leq 52^\circ$  and a single interband state is present for  $\theta > 52^\circ$ . We find that  $eFd$  is always much larger than  $\Delta E_D$  so distinct bands are always present.

Figures 6.39(b-d) show the variation in  $\Delta E_D$  with  $B = 0 \rightarrow 50$  T for  $r = 1$  and (b)  $\theta = 30^\circ$ , (c)  $\theta = 45^\circ$ , (d)  $\theta = 60^\circ$ . For all these values of  $\theta$ , the bands merge into a series of closely packed states for  $B \lesssim 10$  T. Above this low  $B$  limit, the bandwidth appears to rise with increasing  $B$  in some non-linear manner and varies between  $\sim 10$  meV and  $\sim 20$  meV. For high  $B$ , especially at high  $\theta$ , there are a large number of interband states and the dynamical bands only contain  $\sim 11$  levels for  $\theta = 60^\circ$  and  $B > 30$  T.

We can also determine the change in band spread,  $\Delta E_S = \Delta E_D/eFd$ , as  $\theta$  and  $B$  are varied. Figure 6.40 plots the change in  $\Delta E_S$  corresponding to  $W = 14$  for  $\theta = 0 \rightarrow 60^\circ$ ,  $B = 20$  T and  $r = 1$ . The band spread increases rapidly with increasing  $\theta$  for  $\theta < 15^\circ$  and then increases more slowly beyond this limit. Therefore, for varying  $\theta$ , decreasing the width of the dynamical box by increasing  $\theta$  causes the dynamical band spread to increase. By comparing with figure 6.39(a) we see this is because  $\Delta E_D$  is roughly constant for  $\theta > 15^\circ$  but  $eFd$  decreases with increasing  $\theta$ .

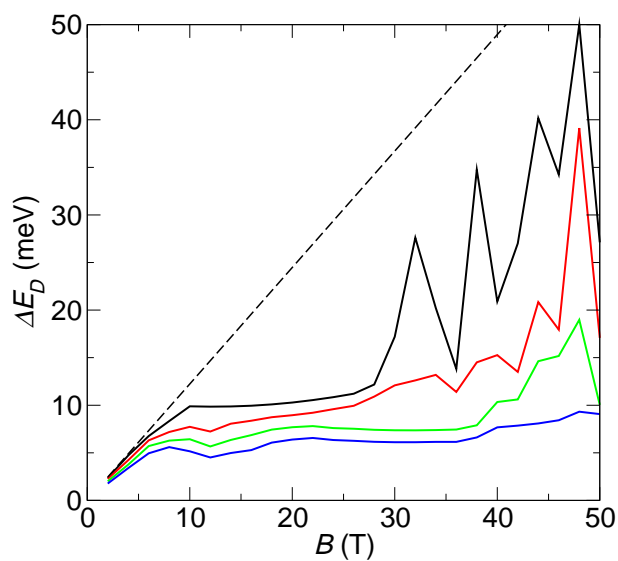


Fig. 6.38: Dynamical bandwidth as a function of  $B$ ,  $\Delta E_D(B)$ , calculated for  $\theta = 45^\circ$  and  $r = 1$ . The four curves correspond to setting  $W = 14, 13, 12$  and  $11$  in equation 6.13 from top to bottom. The broken line shows  $eFd$  and the bandwidth will always be below this value. This is because the largest bandwidth is the energy spacing between  $N$  and  $N + 13$  while  $eFd$  is the spacing between  $N$  and  $N + 14$  for a 14-period superlattice and  $r = 1$ . We select the bandwidth as being the amplitude of the solid line that isn't highly different to the amplitude of all the lines below it. We therefore use the black curve for  $B \leq 30$  T, the red curve for  $30 < B < 42$  T and the blue curve for  $B \geq 42$  T.

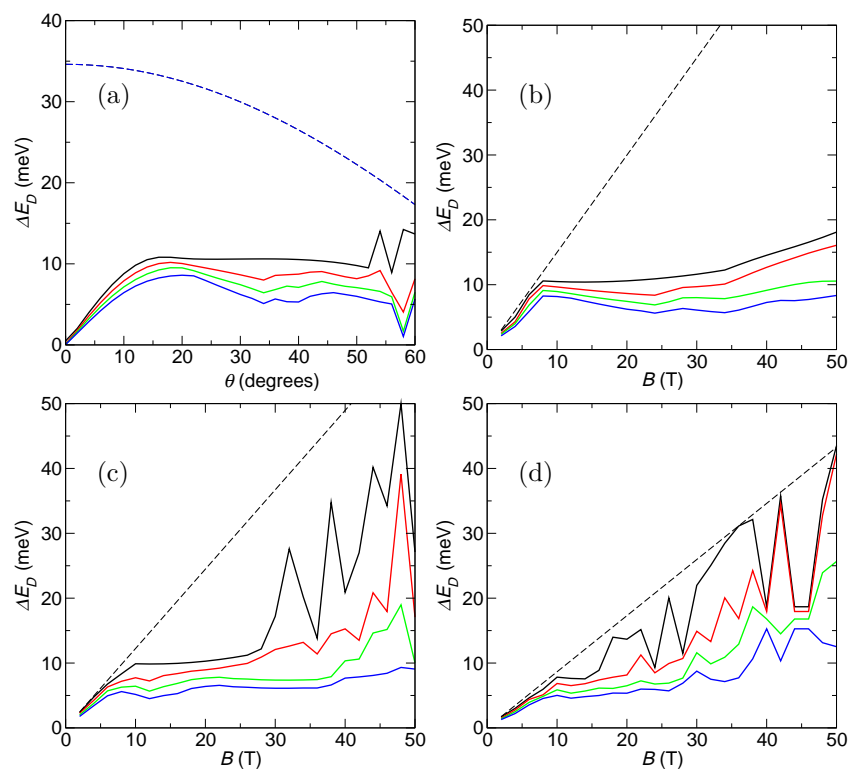


Fig. 6.39: Bandwidth of the dynamical bands for (a) varying  $\theta$  with  $B = 20$  T and (b-c) varying  $B$  with (b)  $\theta = 30^\circ$ , (c)  $\theta = 45^\circ$  and (d)  $\theta = 60^\circ$ .  $r = 1$  in all cases and the broken lines show the value of  $eFd$ .

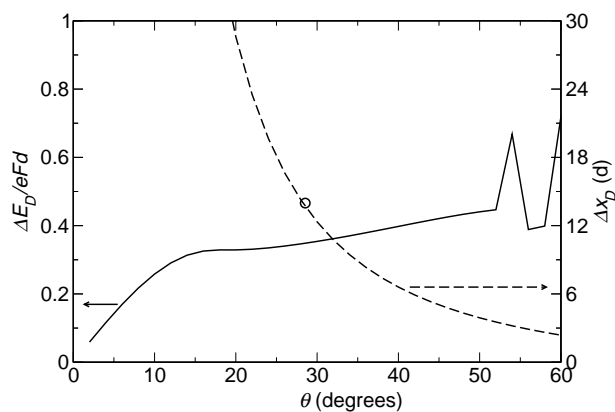


Fig. 6.40: Variation in bandwidth of the dynamical bands (solid line) as a fraction of  $eFd$ , known as band spread, for varying  $\theta$  at  $B = 20$  T and  $r = 1$ . The theoretical width of the dynamical box (broken line) is also shown. The circle shows where the dynamical box corresponding to the first ring of the stochastic web equals the length of the superlattice, therefore the dynamical box becomes truncated for  $\theta < 28^\circ$ .

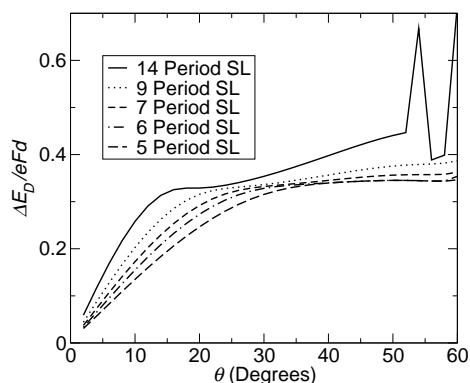


Fig. 6.41: Variation in band spread with  $\theta$  for  $B = 20$  T,  $r = 1$  and five different superlattice lengths (see legend). This figure shows that region of reduced band spread at low  $\theta$  increases in size as the superlattice is shortened. We therefore attribute this low  $\theta$  region of decreased band spread to band truncation caused by the finite superlattice.

From the broken line in figure 6.40, we can see that the dynamical box corresponding to the first ring of the stochastic web will fully fit into the superlattice when  $\theta \gtrsim 28^\circ$  and that the dynamical boxes for  $\theta < 20^\circ$  are highly truncated by the superlattice. When the dynamical box is truncated, the dynamical bands consist of fewer states than the untruncated band would and a reduction in band spread is unexpected. The  $\theta \lesssim 28^\circ$  region where the dynamical box is truncated and the  $\theta < 15^\circ$  region where the band spread is notably reduced do not totally overlap. It therefore appears that band truncation can slightly reduce the number of states in the dynamical bands without significantly affecting the band spread. However, the band spread is greatly reduced when the dynamical band only contains a few states because it is severely truncated.

Figure 6.41 plots the change in band spread with  $\theta$  for  $B = 20$  T,  $r = 1$  and a range of superlattice lengths. This figure shows that the  $\theta$  range over which the band spread is reduced becomes larger as the superlattice is shortened. This result shows that the reduction in band spread at low  $\theta$  is at least partially due to truncation of the dynamical box by the finite superlattice. Therefore, band spread increases approximately linearly with increasing  $\theta$  unless the dynamical box cannot fit into the superlattice. When this occurs, the band spread is decreased by an amount which depends on how much of the box is truncated.

Figure 6.42 plots the variation in band spread with changing  $B$ . We find that band spread is proportional to the width of the dynamical box. This is in contrast to the behaviour seen for varying  $\theta$  which showed that increasing the size of the box decreased band spread. The dynamical bands are truncated for  $B \lesssim 13$  T but no obvious variation in band spread is seen at this point. For  $B < 10$  T the band spread approaches one which means that the bands merge

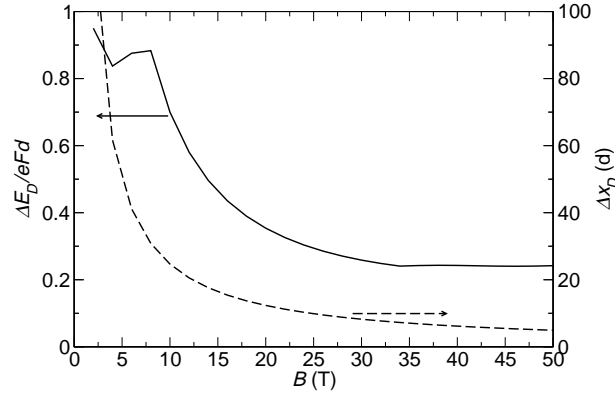


Fig. 6.42: Variation in bandwidth of the dynamical bands (solid line) as a fraction of  $eFd$ , known as band spread, for varying  $B$  at  $\theta = 30^\circ$  and  $r = 1$ . The theoretical width of the dynamical box (broken line) is also shown. It is clear that  $\Delta E_D/eFd$  is proportional to the dynamical box width for  $B > 10$  T. This  $B > 10$  T limit is the point at which the dynamical bands are not merged into a continuous sequence (see figure 6.39(b)).

together and our measurements of bandwidth and band spread are meaningless.

To understand the difference between the effects of  $\theta$  and  $B$  on the band spread, we need to consider the stochastic webs. Chapter 3 has shown that  $\theta$  has a large effect on the form of the stochastic webs (fig. 3.10 for example).  $\theta$  affects both the size of the stochastic web and the width of the stochastic filaments as well as controlling where a chaotic sea forms. In contrast, changing  $B$  has no effect on the stochastic web and  $B$  only affects the extent of the electron trajectories along  $x$  (fig. 3.7 and eqn. 3.12 where  $F \propto B$ ). Therefore, our result for band spread variation with  $B$  (fig. 6.42) have shown that the band spread is proportional to the dynamical box width because changing  $B$  changes nothing else. However, the result for band spread variation with  $\theta$  (fig. 6.40) shows that band spread is also dependant on other factors which are controlled by  $\theta$  but not  $B$ .

We can understand the changing band spread with dynamical box width as follows. If the dynamical box width doubles, then the number of states in that section of the dynamical band will double. However, the spacing between these states will halve because the characteristic frequency,  $\omega_S$ , of the dynamical potential is inversely proportional to the dynamical box width. This implies that the *bandwidth* will be constant with changing  $B$  and figures 6.39(c-d) support this theory to some degree. However, the band spread is  $\Delta E_D/eFd$  and  $F \propto B$ . Therefore, the band spread should be inversely proportional to  $B$  which we see in figure 6.42.

We would see a similar effect for  $\theta$  with band spread being inversely proportional to  $\tan \theta \sin \theta$  if  $\theta$  did not have additional effects which overshadow this

relationship.

### 6.3.2 Dynamic Band Summary

This chapter has shown that, when  $r$  is rational, the energy degenerate Landau-like eigenfunctions in different superlattice periods seen at  $\theta = 0^\circ$  combine into extended eigenfunctions for  $\theta \neq 0^\circ$ . The energy eigenvalues of the extended eigenfunctions are split into a range of non-degenerate values. We can understand the splitting between these eigenstates semiclassically via the concept of a dynamical box. See section 6.1.4 for a description of these dynamical boxes.

The non-degenerate eigenstates form dynamical bands whose states are localised in a number of regions along the superlattice axis. The length of these regions is determined by the size of the dynamical boxes which is in turn determined by the radius of the rings of the stochastic web.

We find that the band spread of the dynamical bands, which is defined as:

$$\Delta E_S = \frac{\Delta E_D}{eFd}. \quad (6.14)$$

where  $\Delta E_D$  is the bandwidth, varies with both  $\theta$  and  $B$  for  $r = 1$ . We find that  $\Delta E_S$  increases with increasing  $\theta$  (fig. 6.40) so long as the majority of the dynamical box can fit in the superlattice. We also find that  $\Delta E_S$  is directly proportional to  $1/B$  (fig. 6.42).

The variation in dynamical box width cannot be the sole reason for these trends because it varies as:

$$\Delta x_D \propto \frac{1}{B \tan \theta \sin \theta}. \quad (6.15)$$

Therefore, increasing both  $\theta$  and  $B$  decreases the dynamical box width which contrasts with the trends in  $\Delta E_S$  (figs. 6.40 and 6.42). Changing  $B$  only affects the width of the dynamical bands while changing  $\theta$  also affects the form of the corresponding semiclassical stochastic web. Therefore,  $\Delta E_S$  is proportional to  $\Delta x_D$ , but it is also affected by other parameters which are controlled by  $\theta$  and not  $B$ .

## 6.4 A Hybrid Transport Model for the Dynamic Bands

Finally, we propose a transport model for electrons moving through the dynamical band system with reference to experimental data.

The two models of superlattice transport discussed in chapter 1 are miniband transport and Wannier-Stark hopping. In general, miniband transport is valid at low electric fields where electrons are delocalised over many superlattice

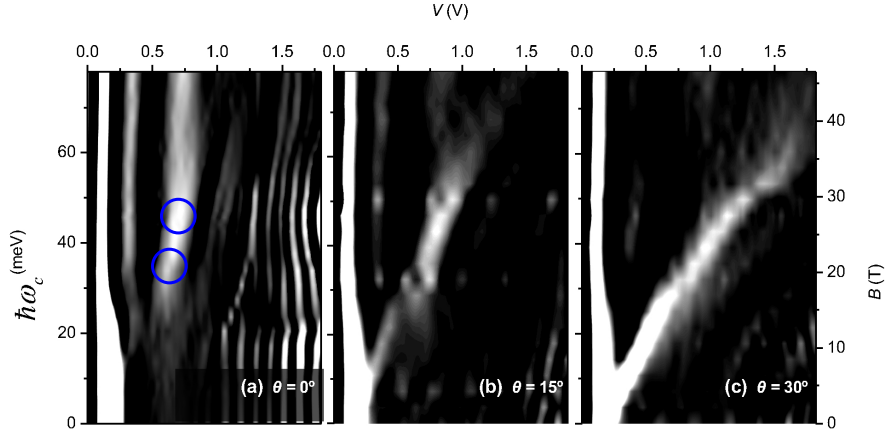


Fig. 6.43: Greyscale plots of experimental  $d^2I/dV^2$  data plotted as a function of  $V = 0 \rightarrow 1.8$  V and  $B = 0 \rightarrow 47$  T. The data is measured for (a)  $\theta = 0^\circ$ , (b)  $\theta = 15^\circ$  and (c)  $\theta = 30^\circ$ . (a) shows two hotspots at  $V \approx 0.7$  V for  $B = 21$  T and  $B = 27$  T (blue circles) which correspond to Wannier-Stark hopping transport mediated by the AlAs and GaAs phonons respectively. (b) and (c) show a diagonal feature which corresponds to current enhancement due to extended electron behaviour. Experimental data provided by Dr D. Fowler(61).

periods. Wannier-Stark hopping is valid when equivalent eigenstates in adjacent superlattice periods have an energy separation greater than thermal broadening. However, our dynamical bands already include the electric field and will therefore be valid for all electric fields for which  $r$  is rational.

When  $\theta = 0^\circ$  or  $r$  is irrational, no dynamical bands form and either the miniband transport or Wannier-Stark hopping model can be used depending on the electric field. However, when  $\theta \neq 0^\circ$  and  $r$  is rational, dynamical bands form and the transport picture is less clear.

Figure 6.43 shows experimental data for a 14-period superlattice system, plotting  $d^2I/dV^2$  as a function of  $B$  and applied voltage  $V$  for three different values of  $\theta$ . The aim of this section is to qualitatively formulate an electron transport model that explains the features in this data. It must be remembered that voltage does not directly correspond to electric field and the semiclassical work in chapter 3 showed that  $F(x)$  is often highly variable for a single value of  $V$ . Therefore, it is also possible for  $r$  to take an integer value across some of the superlattice for a range of  $V$ .

When  $\theta = 0^\circ$ , the experimental data (figure 6.43(a)) shows a number of features but the important points to note for this analysis are the hotspots (circled) at  $V = 0.7$  V for  $B = 21$  T and  $B = 27$  T. These hotspots correspond to the onset of Wannier-Stark hopping transport which is mediated by AlAs and

GaAs LO phonons for  $B = 21$  T and  $B = 27$  T respectively. Similar hotspots also occur for  $\theta = 15^\circ$  (figure 6.43(b)) but not for  $\theta = 30^\circ$  (figure 6.43(c)) where these features are obscured by a broad diagonal stripe.

This diagonal region of enhanced transport seen in figures 6.43(b) and (c) has two important properties. Firstly, it has a much larger amplitude than the hotspots seen for  $\theta = 0^\circ$  and secondly, it exists for all magnetic fields up to  $\sim 40$  T. The cause of this current enhancement was discussed in chapter 3 using the semiclassical model. This model showed that enhancing the distance the electrons travel leads to a current enhancement. We therefore attribute this diagonal stripe to be due to current enhancement corresponding to  $r = 1$ . We can use the range of  $B$  values over which the stripe exists to tell us something about the dynamical band structure.

The simplest electron transport model for this system is to use dynamical band transport when  $r$  is rational and Wannier-Stark hopping when  $r$  is irrational. This simple model has a number of problems. If the dynamical bands were split into a number of dynamical boxes then scattering would be required for electron transport along the whole superlattice. A pure miniband transport model would therefore predict zero current as soon as the dynamical bands were composed of more than one dynamical box. This should occur for  $B \gtrsim 13$  T at  $\theta = 30^\circ$  and is not observed in figure 6.43(c). Secondly, a non-linear electric field would cause  $r$  to vary across the superlattice, which would truncate the dynamical bands. It would therefore be impossible to choose a single model because  $r$  would be both irrational and rational for a single value of  $V$ . Finally, even if the electrons were confined to a single dynamical band and managed to move across the whole superlattice, they would enter the collector contact at a higher energy relative to the electric potential than it left the emitter contact. This could lead to a loss of current at high  $F$  depending on the width of the bands in the contacts. No such loss is seen in figures 6.43(b) and (c).

Because of these problems with the pure band transport model, we suggest the use of a mixed band and interband scattering based transport model when  $r$  is an integer. This model will allow transport along the dynamical bands, but also permit inter- and intraband phonon assisted scattering. Interband scattering will only be possible if a phonon of the correct energy exists.

Using our combined model, we can calculate the parameters for which phonon assisted interband scattering is possible. Wannier-Stark hopping at  $\theta = 0^\circ$  occurs when the spacing between Landau levels is equal the phonon energy, known as the magnetophonon resonance condition. In superlattice NU2293, there are two bulk longitudinal optic (LO) phonons which have energies of 36 meV and 47 meV for GaAs and AlAs respectively. The hotspots in figure 6.43(a) occur when the MPR condition is satisfied for these two phonon energies.

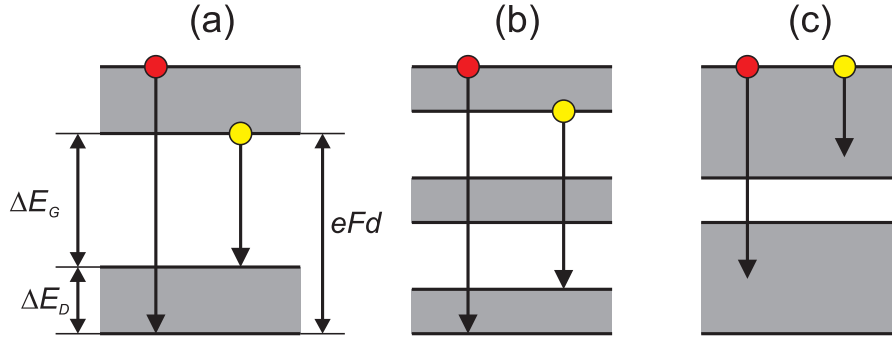


Fig. 6.44: (a) shows the maximum (red) and minimum (yellow) energy phonons that can cause transitions between two adjacent bands (equation 6.16). (b) shows the phonons that can cause transitions between non-adjacent bands (equation 6.17). (c) shows that transitions can be either intra- or interband if the bandgap is smaller than the bandwidth.

Dynamical bands form for  $\theta > 0^\circ$  which mean that the scattering condition is easier to satisfy because the bands provide a range of transition energies. In general, if the bandwidth,  $\Delta E_D$ , is smaller than bandgap,  $\Delta E_G$ , then the phonon energy,  $E_{LO}$ , must satisfy:

$$\Delta E_G \leq E_{LO} \leq \Delta E_G + 2\Delta E_D \quad (6.16)$$

for interband scattering to occur. There is also a possibility of scattering between non-adjacent bands and the condition for scattering between band  $\alpha$  and band  $\alpha + \beta$  is:

$$\beta\Delta E_G + (\beta - 1)\Delta E_D \leq E_{LO} \leq \beta\Delta E_G + (\beta + 1)\Delta E_D. \quad (6.17)$$

Finally, scattering will always be possible if  $\Delta E_D > \Delta E_G$  but this will be intraband scattering if  $E_{LO} \leq \Delta E_G$ . Figure 6.44 shows these three conditions graphically. The dynamical bands we have found so far are all narrower than the LO phonon energies so intraband scattering can only be caused by low energy acoustic phonons.

Figure 6.45 plots the magnetic fields for which phonons can cause interband scattering for  $\theta = 30^\circ$  and  $r = 1$ . This figure shows that the phonon resonance condition is satisfied for all  $B < 41$  T, which increases to  $B < 45$  T when thermal broadening of  $\hbar/\tau_{SL}$  is incorporated. These limits correspond well to the experimental data in figure 6.43(c) which shows a reduction in the enhanced current region for  $B > 40$  T.

Therefore, in figure 6.43(c), the enhancement in transport occurs when  $r = 1$  which causes the electrons to extend significantly further along the superlattice

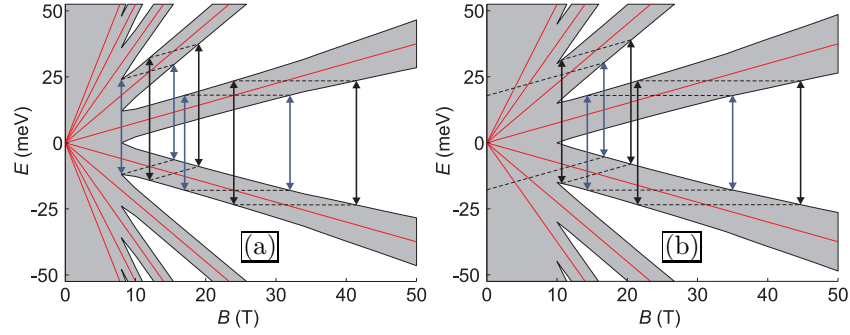


Fig. 6.45: Figure showing when the phonon resonance condition is satisfied (b) with and (a) without thermal broadening of  $\hbar/\tau$  applied. The grey regions show how the bandwidth varies with  $B$  for  $\theta = 30^\circ$  and  $r = 1$  while the gaps between these regions show how the bandgap varies. The red lines indicate the centres of the bands. The blue arrows, and the dotted lines joining them, show the range of  $B$  over which the 36 meV GaAs phonons can cause interband scattering events. The black arrows show the same for the 47 meV AlAs phonons. Where the bands merge ( $B = 8$  T in (a) and  $B = 10$  T in (b)) any phonon can cause a transition. The highest  $B$  value for which a phonon scattering event can cause an interband transition is 41 T and 45 T if thermal broadening is considered.

axis. However, when the magnetic field reaches a critical value of  $B \approx 40$  T, the current enhancement drops off because it is no longer possible for LO phonons to cause interband scattering. This second limit is essentially a magnetophonon resonance condition. Therefore, interband scattering is a requirement for transport through our dynamical band system. The  $B$  value at which our model predicts that the enhanced enhanced current will terminate is similar to the measured value which suggests that our calculated bandwidths are of the correct magnitude. However, the lack of extensive experimental data means it is not possible to further validate our transport model.

There are two further points to consider. Firstly, the rate of electron transport across the short dynamical bands has not been calculated. Therefore, no quantitative measure of current enhancement can be made using the quantum model. Secondly, this model has assumed that the electric field is fixed at  $r = 1$  across much of the superlattice. The results in chapter 3 support this assumption to some degree but use the semiclassical approximation and so may not apply to this quantum result. Therefore, our transport model can only be qualitatively compared to the limited range of experimental data available.

## APPENDIX

## A. GENERATION OF BLOCH STATES

The Bloch wavefunctions,  $\psi$  for a particular superlattice can be determined by solving:

$$\hat{H} |\psi\rangle = E |\psi\rangle \quad (\text{A.1})$$

where

$$\hat{H} = -\frac{\hbar^2}{2m^*} \frac{\partial^2}{\partial x^2} + V_{SL}. \quad (\text{A.2})$$

If the wavefunction  $\psi$  is expanded as a linear combination of basis states:

$$|\psi\rangle = \sum_n A_n |\phi_n\rangle \quad (\text{A.3})$$

then the eigenvalue problem may be rewritten as:

$$\begin{aligned} \hat{H} \sum_n |\phi_n\rangle A_n &= E \sum_n A_n |\phi_n\rangle \\ &= \sum_n \langle \phi_m | \hat{H} | \phi_n \rangle A_n = E \sum_n \langle \phi_m | \phi_n \rangle A_n. \end{aligned} \quad (\text{A.4})$$

This can be represented in matrix form by:

$$\underline{\underline{H}} \underline{\underline{A}} = E \underline{\underline{I}} \underline{\underline{A}} \quad (\text{A.5})$$

where  $\underline{\underline{H}} = \langle \phi_m | \hat{H} | \phi_n \rangle$  and  $\underline{\underline{I}}$  is the identity matrix because  $\langle \phi_m | \phi_n \rangle = \delta_{nm}$  due to the orthogonal basis set. Therefore, solving this matrix equation by diagonalisation will give the required  $A_n$  coefficients to construct the Bloch wavefunction  $\psi$  from bases  $\phi_n$ .

### A.1 Construction of the Hamiltonian Matrix for Bloch States

$\psi$  obeys Bloch Theorem (eqn. 1.3) for a superlattice:

$$\psi_k(x) = e^{ikx} \sum_n A_n e^{iNx} \quad (\text{A.6})$$

where  $u_k(x)$ , is expanded as a series of plane waves,  $n$  is an integer,  $A_n$  are the coefficients required by equation A.3 and  $N$  is a reciprocal lattice vector defined by:

$$N = \frac{2\pi n}{d}. \quad (\text{A.7})$$

The basis states are now be defined as:

$$\phi_n = \exp\left(i\left(k + \frac{2\pi}{d}n\right)x\right). \quad (\text{A.8})$$

The Hamiltonian matrix,  $\underline{H}$ , can be constructed by substituting equation A.8 into A.2. Dividing the Hamiltonian into the kinetic,  $\hat{K}$ , and potential,  $\hat{P}$ , terms will simplify the construction of the final matrix:

$$\hat{H} = \hat{K} + \hat{P}. \quad (\text{A.9})$$

The kinetic energy component to the Hamiltonian matrix is,

$$\begin{aligned} K_{n,m} &= \int_{-\infty}^{\infty} e^{-i\left(k + \frac{2\pi}{d}m\right)x} \left(-\frac{\hbar^2}{2m^*} \frac{\partial^2}{\partial x^2}\right) e^{i\left(k + \frac{2\pi}{d}n\right)x} dx \\ &= \frac{\hbar^2}{2m^*} \left(k + \frac{2\pi}{d}n\right)^2 \int_{-\infty}^{\infty} \exp\left(i\frac{2\pi}{d}(n-m)x\right) dx \\ &= \frac{\hbar^2}{2m^*} \left(k + \frac{2\pi}{d}n\right)^2 \delta_{n,m}. \end{aligned} \quad (\text{A.10})$$

The potential energy component is given by:

$$\begin{aligned} P_{n,m} &= \int_{-\infty}^{\infty} e^{-i\left(k + \frac{2\pi}{d}m\right)x} V_{SL} e^{i\left(k + \frac{2\pi}{d}n\right)x} dx \\ &= \int_{-\infty}^{\infty} e^{-i\left(k + \frac{2\pi}{d}m\right)x} a_l e^{i\left(\frac{2\pi}{d}lx\right)} e^{i\left(k + \frac{2\pi}{d}n\right)x} dx \end{aligned} \quad (\text{A.11})$$

$$(\text{A.12})$$

where  $V_{SL}$  is expanded into a series of Fourier terms weighted by  $a_l$  (for details of determination of  $a_l$  see reference (11) for example). Therefore,

$$P_{n,m} = a_l \delta_{n+l,m}. \quad (\text{A.13})$$

Summing  $\underline{K}$  and  $\underline{P}$  gives the full Hamiltonian matrix  $\underline{H}$  whose size is determined by the number,  $n$  of basis states used. This matrix is banded and has a width determined by the number of Fourier terms used in the expansion of the periodic potential. Typically, 1001 basis states and 2001 Fourier terms produce a dense matrix of a sufficient size to accurately account for  $V_{SL}$  and to produce accurate Bloch states. A matrix of this size can be diagonalised swiftly using modern

computers.

In practice, this matrix was solved using NAG routine F02HCF, although an equivalent LAPACK routine such as ZHEEVR could also be used.

## BIBLIOGRAPHY

- [1] L. Esaki and R. Tsu. Superlattices and Negative Differential Conductivity in Semiconductors. IBM J. Res. Develop., 1970.
- [2] R. Tsu. Superlattices to Nanoelectronics. Elsevier, 2005.
- [3] G.K. Rasulova, M.V. Golubkov, A.V. Leonov, P.N. Brunkov, A.E. Zhukov, V.M. Ustinov, S.O. Usov, and S.G. Konnikov. Domain boundary instability in weakly coupled GaAs/AlGaAs superlattices. Superlattices and Microstructures, 37(2):139, 2005.
- [4] N. W. Ashcroft and N. D. Mermin. Solid State Physics. W. B. Saunders Company, 1976.
- [5] R. G. Scott. Cold Atoms in Optical Lattices. PhD thesis, University of Nottingham, 2003.
- [6] N. Mori, C. Hamaguchi, A. Patanè, T. M. Fromhold, and L. Eaves. Resonant Transport in Semiconductor Superlattices in a Tilted Magnetic Field. International Journal of Modern Physics B, 18:3617, 2004.
- [7] A. A. Ignatov, E. P. Dodin, and V. I. Shashkin. Transient Response Theory of Semiconductor Superlattices: Connection with Bloch Oscillations. Mod. Phys. Lett. B, 5(16):1087–1094, 1991.
- [8] A. Wacker. Semiconductor Superlattices: a model system for nonlinear transport. Physics Reports, 357:1–111, 2002.
- [9] E. Schomburg, J. Grenzer, K. Hofbeck, T. Blomeier, S. Winnerl, S. Brandl, A. A. Ignatov, K. F. Renk, D. G. Pavel'ev, Yu. Koschurinov, V. Ustinov, A. Zhukov, A. Kovich, S. Ivanov, and P. S. Kop'ev. Millimeter wave generation with a quasi planar superlattice electronic device. Solid-State Electronics, 42:1495, 1998.
- [10] A. S. Raspopin, A. A. Zharov, and H. L. Cui. Spectrum of electromagnetic excitations in a dc-biased semiconductor superlattice. Journal of Applied Physics, 98:103517, 2005.

- 
- [11] D. Sherwood. Effect of Stochastic Webs on Electron Transport in Semiconductor Superlattices, Appendix A. PhD thesis, University of Nottingham, 2003.
- [12] S. L. Naylor. Stochastic Dynamics in Periodic Potentials. PhD thesis, University of Nottingham, 2006.
- [13] S. M. McMurry. Quantum Mechanics. Prentice Hall, 1996.
- [14] R. Amca, Y. Ergün, I. Sökmen, and H. Sari. Electronic energy spectra in a multiple quantum well within external electric and tilted magnetic fields. Semicond. Sci. Technol., 15(11):1087–1092, 2000.
- [15] A. Patanè, D. Sherwood, L. Eaves, T. M. Fromhold, M. Henini, and P. C. Main. Tailoring the Electronic Properties of GaAs/AlAs Superlattices by InAs Layer Insertions. App. Phys. Lett., 81(4):661–663, 2002.
- [16] C. Rauch, G. Strasser, K. Unterrainer, W. Boxleitner, and E. Gornik. Transition Between Coherent and Incoherent Electron Transport in GaAs/GaAlAs Superlattices. Phys. Rev. Lett., 81(16):3495–3498, 1998.
- [17] H. G. Schuster and W. Just. Deterministic Chaos: An Introduction. Wiley-VCH, 4th edition, 2005.
- [18] R. L. Ingraham. A Survey of Non-linear Dynamics. World Scientific, 1991.
- [19] G. M. Zaslavsky. Chaos in Dynamic Systems. Harwood Academic Publishers, 1987.
- [20] G. M. Zaslavsky. Physics of Chaos in Hamiltonian Systems. 1998.
- [21] H-J Stöckmann. Quantum Chaos: An Introduction. Cambridge University Press, 1999.
- [22] E. P. Wigner. On the quantum correction for thermodynamic equilibrium. Physics Reports, 40:749–759, 1932.
- [23] M. Hillery, R. F. O’Connell, M. O. Scully, and E. P. Wigner. Distribution Functions in Physics: Fundamentals. Physics Reports, 106(3):121–167, 1984.
- [24] M. Berry. Semiclassical Mechanics in Phase Space: A Study of Wigner’s Function. Philosophical Transactions of the Royal Society of London A, 287(1343):237–271, 1977.
- [25] J. S. Hutchinson and R. E. Wyatt. Quantum Ergodicity and the Wigner Distribution. Chemical Physics Letters, 72(2):378–384, 1980.

- 
- [26] P. A. Dando and T. S. Monteiro. Quantum surfaces of section for the diamagnetic hydrogen atom: Husimi functions versus Wigner functions. Journal of Physics B, 27(13):2681–2693, 1994.
- [27] D. Sherwood. Effect of Stochastic Webs on Electron Transport in Semiconductor Superlattices. PhD thesis, University of Nottingham, 2003.
- [28] T. M. Fromhold, A. Patanè, S. Bujkiewicz, P. B. Wilkinson, D. Fowler, D. Sherwood, S. P. Stapleton, A. A. Krokhin, L. Eaves, M. Henini, N. S. Sankeshwar, and F. W. Sheard. Chaotic electron diffusion through stochastic webs enhances current flow in superlattices. Nature, 428:726–730, 2004.
- [29] W. H. Press, S. A. Teukolsky, W T Vetterling, and B P Flannery. Numerical Recipes in C, chapter 16, page 710. Cambridge University Press, 2nd edition, 1992.
- [30] NAG Fortran Library. E04UNF. NAG.
- [31] D. P. A. Hardwick, S. L. Naylor, S. Bujkiewicz, T. M. Fromhold, D. Fowler, A. Patanè, L. Eaves, A. A. Krokhin, P. B. Wilkinson, M. Henini, and F. W. Sheard. Effect of inter-miniband tunneling on current resonances due to the formation of stochastic conduction networks in superlattices. Physica E, In Press, 2005.
- [32] C. Zener. A Theory of Electrical Breakdown of Solid Dielectrics. Proc. Royal Soc. London A, 145(855):523–529, 1934.
- [33] M. Holthaus. Bloch Oscillations and Zener Breakdown in an Optical Lattice. J. Opt. B, 2:589–604, 2000.
- [34] E. O. Kane. Zener Tunneling in Semiconductors. J. Phys. Chem. Solids, 12(2):181–188, 1960.
- [35] E. O. Kane. Theory of Tunneling. Journal of Applied Physics, 32(1):83–91, 1961.
- [36] S. Glutsch. Nonresonant and Resonant Zener Tunneling. Phys. Rev. B., 69:235317, 2004.
- [37] A. Di Carlo and P. Vogl. Theory of Zener tunnelling and Stark ladders in semiconductors. Semicond. Sci. Technol., 9:497–499, 1994.
- [38] A. Sibille, J. F. Palmier, and F. Iruelle. Zener Interminiband Resonant Breakdown in Superlattices. Phys. Rev. Lett., 80(20):4506–4509, 1998.

- 
- [39] T. E. Judd, A. Henning, D. P. A. Hardwick, R. G. Scott, A. G. Balanov, P. B. Wilkinson, D. Fowler, A. M. Martin, and T. M. Fromhold. Chaotic Transport in Semiconductors, Optical and Cold-Atom Systems. Progress in Theoretical Physics Supplement, 166:169, 2007.
- [40] W. K. Hensinger, H. Häffner, A. Browaeys, N. R. Heckenberg, K. Helmer-son, C. McKenzie, G. J. Milburn, W. D. Phillips, S. L. Rolston, H. Rubinsztein-Dunlop, and B. Upcroft. Dynamical tunnelling of ultracold atoms. Nature, 412:52, 2001.
- [41] C. Ryu, M. F. Andersen, A. Vaziri, M. B. d’Arcy, J. M. Grossman, K. Helmer-son, and W. D. Phillips. High-Order Quantum Resonances Observed in a Periodically Kicked Bose-Einstein Condensate. Phys. Rev. Lett., 96:160403, 2006.
- [42] S. Tomsovic and D. Ullmo. Chaos-assisted tunneling. Phys. Rev. E, 50:145, 1994.
- [43] K. Nakamura and T. Harayama. Quantum Chaos and Quantum Dots. Oxford University Press, Oxford, 2003.
- [44] T. M. Fromhold, P. B. Wilkinson, F. W. Sheard, L. Eaves, J. Miao, and G. Edwards. Manifestations of Classical Chaos in the Energy Level Spectrum of a Quantum Well. Phys. Rev. Lett., 75(6):1142–1145, 1995.
- [45] P. B. Wilkinson, T. M. Fromhold, L. Eaves, F. W. Sheard, N. Miura, and T. Takamasu. Observation of ‘scarred’ wavefunctions in a quantum well with chaotic electron dynamics. Nature, 380:608, 1996.
- [46] D. L. Shepelyansky and A. D. Stone. Chaotic Landau Level Mixing in Classical and Quantum Wells. Phys. Rev. Lett., 74(11):2098–2101, 1995.
- [47] G. Müller, G. S. Boebinger, H. Mathur, L. N. Pfeiffer, and K. W. West. Pre-cursors and Transition to Chaos in a Quantum Well in a Tilted Magnetic Field. Physical Review Letters, 75:2875, 1995.
- [48] E. E. Narimonov and A. D. Stone. Origin of Strong Scarring of Wave Functions in Quantum Wells in a Tilted Magnetic Field. Phys. Rev. Lett., 80(1):49–52, 1998.
- [49] T. S. Monteiro and P. A. Dando. Chaos in a quantum well in tilted fields: A scling system. Phys. Rev. E, 53(4):3369–3373, 1996.
- [50] T. M. Fromhold, L. Eaves, F. W. Sheard, M. L. Leadbeater, T. J. Foster, and P. C. Main. Magnetotunneling Spectroscopy of a Quantum Well in the Regime of Classical Chaos. Phys. Rev. Lett., 72(16):2608–2611, 1994.

- 
- [51] J. U. Nöckel and A. D. Stone. Ray and Wave Chaos in Asymmetric Resonant Optical Cavities. Nature, 385:45, 1997.
- [52] G. H. Wannier. The Structure of Electronic Excitation Levels in Insulating Crystals. Phys. Rev., 52:191–197, 1937.
- [53] W. Kohn. Analytic Properties of Bloch Waves and Wannier Functions. Phys. Rev., 115(4):809–829, 1959.
- [54] F. B. Pedersen, G. T. Einevoll, and P. C. Hemmer. Wannier functions for the Kronig-Penny model. Phys. Rev. B, 44(11):5470–5475, 1991.
- [55] S. M. McMurry. Quantum Mechanics, chapter 5. Prentice Hall, 1996.
- [56] R. W. Robinett. Quantum Mechanics. Cambridge University Press, 1997.
- [57] E. Anderson, Z. Bai, C. Bischof, S. Blackford, J. Demmel, J. Dongarra, J. Du Croz, A. Greenbaum, S. Hammarling, A. McKenney, and D. Sorensen. {LAPACK} Users' Guide. Society for Industrial and Applied Mathematics, third edition, 1999.
- [58] M. Gutzwiller. Chaos in Classical and Quantum Mechanics. Springer-Verlag, 1990.
- [59] E. J. Heller. Bound-State Eigenfunctions of Classically Chaotic hamiltonian Systems: Scars of Periodic Orbits. Phys. Rev. Lett., 53(16):1515–1518, 1984.
- [60] T. M. Fromhold, P. B. Wilkinson, R. K. Hayden, L. Eaves, F. W. Sheard, N. Miura, and M. Henini. Tunneling Spectroscopy of Mixed Stable-Chaotic Electron Dynamics in a Quantum Well. Phys. Rev B, 65:155312, 2002.
- [61] D. Fowler, D. P. A. Hardwick, A. Patanè, M. T. Greenway, A. G. Balanov, T. M. Fromhold, L. Eaves, and M. Henini. Magnetic field-induced miniband conduction in semiconductor superlattices. Phys. Rev. B, to be published, 2007.